Analysis of scattering by urban areas in the frame of NLOS target detection in SAR images.

Azza Mokadem

Thèse de Doctorat

Domaine : Sciences physiques pour l'ingénieur
Spécialité : Électromagnétisme

École Doctorale ≪ Sciences et Technologies de l'Information des Télécommunications et des Systèmes ≫

Présentée par :

Azza MOKADEM

Sujet :

Analyse de la diffusion par les scènes urbaines dans le cadre de la détection des cibles en visée non directe du radar dans les images SAR

Soutenue le 4 Février 2014 devant les membres du jury :

Yves Lostanlen, Toronto University	Rapporteur
Bernard Uguen, INSA Rennes	Rapporteur
Jean-Marie Nicolas, Télécom ParisTech	Examinateur
Carlos Lopez-Martinez, PUC	Examinateur
Lionel Pichon, LGEP	Examinateur
Régis Guinvarc'h, SONDRA/SUPELEC	Examinateur
Elise Colin-Koeniguer, ONERA	Encadrante
Laetitia Thirion-Lefevre, SONDRA/SUPELEC	Directrice de Thèse

2014-04-TH

Acknowledgments

It would not have been possible to write this thesis without the help and support of the kind people around me, to only some of whom it is possible to give particular mention here.

Above all, I would like to thank my parents and brother for the unequivocal support they gave me all my life, for which my mere expression of thanks likewise does not suffice.

This thesis would not have been possible without the help, support and patience of my two supervisors, Dr. Laetitia Thirion-Lefevre and Dr. Elise Colin-Koeniguer. They have been invaluable on both an academic and a personal level, for which I am extremely grateful. They gave me the opportunity to discover the world of research in the best conditions and supported me to achieve this work until the last second. Their guidance helped me in all the time of research, writing of the thesis and preparing the defence. I could not have imagined having better advisors for my Ph.D study. I will always remember their generosity,m sympathy and kindness.

I would like to thank also the people of SONDRA for the beautiful environment I have been during these last three years. A special thank for my office colleagues Israel for his friendship and support and Jerome for the moments of fun.

Last but not the least, I would like to thank the friends I met in SUPELEC, Laila, Mircea, Aymen, Zina, Pierre and Takis.. I will always remember the beautiful moments we spend together..

Contents

Foreword

Earth observation from space through various remote sensing instruments has provided a big knowledge concerning the monitoring of land surface dynamics, natural resources management, and the overall state of the environment itself [Joseph 2005]. There are many possible definitions about what remote sensing actually is. One of the most common definitions is "the collection and interpretation of information about an object, area, or event without being in physical contact with the object". According to Canada Center for Remote Sensing, it is: "a group of techniques for collecting image or other forms of data about an object from measurements made at a distance from the object and the processing and analysis of the data".

Based on these two definitions, we can propose another definition of remote sensing as "the technology to identify, measure and analyze the characteristics of an object of interest without a direct contact." Electromagnetic radiation which is reflected or emitted from an object is the usual source of remote sensing data. The device to detect the electromagnetic radiation reflected from an object is called a "remote sensor" or "sensor". Cameras or scanners are examples of remote sensors. A vehicle to carry the sensor is called a "platform". Aircraft and satellites are the common platforms for remote sensing of the earth. The development and deployment of satellites has enhanced the collection of remotely sensed data and offers a way to obtain information over large areas. The capacity of remote sensing to identify and monitor land surfaces and environmental conditions has expanded greatly over the last few years. Moreover, the gathered data is an essential tool in natural and urban resources management. Remote sensing imagery has many applications in mapping land-use and cover, agriculture, soils mapping, forestry, city planning, archaeological investigations, military observation, and geomorphological surveying, among other uses. For example, foresters use aerial photographs for preparing forest cover maps, locating possible access roads, and measuring quantities of trees harvested [Trewartha 1961]. Specialized photography using color infrared film has also been used to detect disease and insect damage in forest trees.

The remote sensing systems can be classified into two groups depending on the operating wavelength:

- The optical and infrared remote sensing,
- The microwave remote sensing.

The optical remote sensing satellites carry passive sensors meaning that they require the illumination of the sun for imaging. The corresponding operating wavelengths extend usually from the visible and near infrared (0.7 μm to 1.5 μm) to the short-wave infrared (1.5 μm to 3 μm). Different materials such as water, soil, vegetation, buildings and roads reflect visible and infrared light in different ways. They have different colours and brightness when seen under the sun. The interpretation of optical images require the knowledge of the spectral reflectance signatures of the various materials (natural or man-made) covering the surface of the earth. The first optical satellite devoted to remote sensing, named LANDSAT-1, was launched by the NASA in 1972 [Longshaw 1976]. It allows to collect information about agricultural resources, geography, cartography, environmental pollution, oceanography and me-

teorological phenomena. SPOT-1, the first french satellite dedicated to earth observation was launched in 1986. It is an optical imaging system initiated by the CNES (the french space agency) to improve the knowledge and management of the earth by exploring the earth's resources, detecting and forecasting phenomena involving climatology and oceanography, and monitoring human activities [Berry 1988].

The microwave remote sensing satellites carry active sensors that emit pulses of microwave radiation to illuminate the areas to be imaged (the wavelength varying from 1 mm to 1 m). Images of the earth surface are formed by measuring the microwave energy scattered by the ground or sea back to the sensors. As they are active systems, these satellites carry their own "flashlight" emitting microwaves to illuminate their targets. The images can thus be acquired day and night. Microwaves have an additional advantage as they can penetrate clouds. Therefore, images can be acquired even when the weather is cloudy. Indeed, radar microwaves are less affected by atmospheric constituents (rain, clouds, snow..) than optical waves. As long as the size of the particles is small than the wavelength, they can be considered as invisible. Nevertheless, if the relative size grows up, interactions between the particles and the waves increase and the signal is significantly disturbed.

An example of a microwave imaging system which can produce high resolution image of the earth is the Synthetic Aperture Radar (SAR). The interest of SAR systems comparing to conventional radar systems is explained in [Cumming 2004]. The intensity in a SAR image depends on the amount of microwave backscattered by the target and received by the SAR antenna. Since the physical mechanisms responsible for this backscatter is different for microwave, compared to visible/infrared radiation, the interpretation of SAR images requires the knowledge of how microwaves interact with the targets.

The first spaceborne SAR system, named SEASAT, was designed for remote sensing of the oceans [Monaldo 2003]. SEASAT, launched on the 27 th of June 1978, was initiated by NASA's Jet Propulsion Laboratory. It was designed to achieve a twofold mission. The first objective was to demonstrate the feasibility of global satellite monitoring of oceanographic phenomena and the second objective was to help determining the requirements for an operational ocean remote sensing satellite system. The first European Remote Sensing satellite ERS-1, launched in 1991 by the European Space Agency (ESA), carried a payload including an imaging SAR, a radar altimeter and other instruments to measure ocean surface temperature and winds at sea [Johannessen 1995].

The operating mode of SAR system is based on the interactions between the scene elements and the emitted waves. Depending on the characteristics of the illuminated object, the scattering signal differs. This difference between the emitted signal and the received one is used, as for every radar system, to get information of the illuminated objects in the scene. Unless the scene is composed by simple elements with simple geometry (sphere, dihedral, ..), the returned radar signal is not so easy to interpret. An example of a complex environment to study using SAR images is the urban areas.

In this thesis, the main topic is the detection of NLOS (Non Line Of Sight) targets inside a simple and representative scene (the urban canyon), using SAR images for military and civilian purposes. Applications in the area of detecting hidden targets using radar systems are numerous: the global reconnaissance is done

mainly by satellite systems, aircrafts and high flying platforms carrying sensors for wide area observation. In addition, there are miniaturized SAR equipments which are integrated into drones for battlefield surveillance. The resolution of SAR systems has been improved over the last decades up to the order of a centimeter [Brenner 2013]. Advanced classification algorithms are now able to identify some military objects in the scene which is of great interest [Berens 2006].

In this context, our primary goal is not to develop images processing techniques to investigate the detection of NLOS targets but rather to gain knowledge about the electromagnetic (EM) phenomenology of propagation inside urban canyons. Once the relation between the radar parameters (frequency, polarization, incidence angle,..), the scene composition (geometry and materials) and the returned signal established, the accurate prediction of the possible detection or not of a NLOS target would be possible.

This present thesis is composed by three main parts. The first part is dedicated to a general introduction to the problematic based on a study of the state-of-art works to point out our contribution comparing to the current achievements. Our methodology to deal with this new topic is also presented (chapter 1). In addition, a description of the reference data that we have at our disposal to analyze the EM phenomenology of scattering inside urban canyons for both indoor and outdoor environments, is given in chapter 2. The second part of this thesis deals with the EM knowledge concerning the propagation inside the canyon acquired through the analysis of indoor data. In the third chapter, we give a presentation of the different EM commercial tools tested to select a reliable tool to investigate about the EM propagation inside real urban canyons. In chapter 4, we give a detailed presentation of the anechoic chamber data we performed the simulations of the EM codes on. In the last chapter of this part, the results of the simulations of the selected EM tools are presented with the main analysis we derived concerning the EM phenomenology of propagation for both controlled and real case urban canyons. The third part of the thesis is a presentation of our developed and validated in-house code to investigate the detection of NLOS point and extended targets inside urban canyons (chapter 6 and 7). Finally an example of application of this in-house code to interpret InSAR data is proposed in the last chapter .

Part I

General introduction

Chapter 1

Problematic and methodology

Contents

1.1 Introduction to the problematic

Application of remote sensing to urban areas requires a challenging effort to be carried out in the future. The use of remote sensing data for urban areas monitoring is highly desired for regular maintenance ([Johnson 2008], [Codjoe 2007]) as well as emergency occurrences ([Montoya 2002], [Van Westen 2000]). From the regular maintenance point of view, important information for economic development planning and best natural resources use can be provided by the analysis of land use, the estimation of population growth and its spatial distribution or movements. From the emergency situations management point of view, a fast and synoptic data acquisition of the areas affected by natural disasters would provide a rapid estimation of the damages and hence guarantee an adequate intervention.

This heavy demand on remote sensing applications related to urban areas leads to the development of imaging systems that are alternative to optical imagery. In particular, in the last few decades, there has been an increasing interest in SAR imagery, since some of its properties are favorable to optical imagery. In fact, the use of centimetric to millimetric wavelengths turns the SAR technique into an "all-weather" system able to work under adverse weather conditions and has a day night capability to obtain images. Moreover, the resolution is independent of the sensor's height.

In the past decades, due to the poor spatial resolutions of the provided images by the existing sensors, the earth mapping by satellite imagery has been mainly limited to natural landscapes. Often, the phenomena to be observed did not need high image resolution as they could be monitored using a resolution of many ten meters. But, this is not sufficient for urban areas where the main structures of the

objects of the scene (buildings, streets, etc..) have dimensions that are often in the scale of tens meters while many other items are even smaller (windows, balconies, cars and so on). Consequently, high resolution is an important requirement for an adequate description of this kind of scene.

So far, new technologies have been developed to this aim for high resolution sensors working in optical and radar domain. The ability of new SAR sensors to provide fine resolution imagery of the urban areas leads to new urban remote sensing applications such as: reconnaissance, surveillance, and targeting. Consequently, the extraction and recognition of very small structures in crowded environment is now possible. In dense urban areas the detection of structures from building to car is expected. These applications are driven by civilian needs of security such as reconnaissance and surveillance tasks. Currently, surveillance in urban areas is dominated by optical devices. Sensitive areas inside a city are covered by a large network of cameras. Optical images are the best means of surveillance for an operator because they do not need interpretation. However, they work only in Line Of Sight (LOS) with the presence of a light source. In order to prevent blind areas, it is necessary to employ a dense network of cameras whose performance degrades in conditions such as smoke and low light. Moreover, cameras in public areas bring up issues of privacy. Many of these issues are mitigated through the use of radar, specially SAR systems.

In fact, the use of urban SAR data for military applications such as detecting the underground pipes, inspecting the tanks below the canopy, searching and rescuing the crashed aircraft, etc.., has received increasing attention during last years [Mattar 2003]. Researchers are now improving the ability to detect and resolve targets in urban clutter [Mitra 2001]. The intent is to deliver persistent and accurate information to military and law enforcement agents so they may make rapid and suitable decisions.

However, the complexity of the urban environment makes the detection of targets a very challenging problem. Indeed, with the increase of the SAR sensor resolution, High Resolution (HR) SAR images could include a wide diversity of man-made structures (buildings, antennas, roads, lights, ground vehicles, etc), that have various shapes and sizes, different materials (metallic, asphalt, etc) and varying orientations from the sensor. This leads to a complex EM scattering environment characterized by a variety of single and multiple scattering mechanisms with a wide range of amplitudes.

Specifically, challenges such as multipath returns, building obscuration, and high clutter have to be overcome in order to maintain acceptable performance accuracy levels for target detection, estimation and tracking.

Typical SAR systems are designed for imaging targets with a direct line of sight of the SAR sensors. However, in an environment where the intended target (for example, man-made objects such as a tank or a truck) is hidden or surrounded by many scatterers (for example, buildings), the detection of the target in the corresponding SAR image can be wrong due to the absence of a LOS response. An example of this typical problem of target detection in urban SAR images is illustrated in Fig.B.1. This figure describes a SAR artifact preventing the accurate detection of the target: a target located in reality in front of the building, is synthesized at the shadow area located behind the building on the corresponding SAR

image. This is due to the existence of NLOS response that leads to a corresponding range distance different from the real one and hence the target is synthesized at a wrong position on the image.

Figure 1.1: (Left) Real building of interest with a target located in front of it (the green point indicates the position of the target). (Right) Corresponding SAR image acquired and processed by ONERA through a measurement campaign involving the BUSARD motor glider platform equipped with the Drive radar. The frequencies band is [33-37] GHz and the incidence angle is 60°. This image contains an artifact: a target located in front of the building is synthesized at the shadow area located behind the building (see the red rectangle).

1.2 Problematic statement

The example in Fig.B.1 has been selected to introduce the problematic of this thesis. The main objective is to investigate the detection of a target which can be in NLOS of the radar, in order to provide an explanation of the origin of some artifacts in the SAR image. This investigation will include the prediction for a specific urban scene of the cases where a target can be detected and the corresponding response in the range profile.

Our approach to begin with this new topic is to select a simple canonical but representative structure of an urban area to perform the detection of targets inside it. Our canonical structure of interest is the urban canyon which can be defined as two buildings separated by a street (see Fig.1.2). This is obviously the most common structure of an urban scene. The choice of this urban structure decreases significantly the complexity of the problem since we have reduced the size of the propagation environment. As a long term perspective, the results of this study could be used to propose a SAR imaging mode that may avoid these artifacts as well as a new SAR processing technique to correct them. To analyze the origin of some artifacts in SAR images, the interaction of the signal with the components of the urban scene has to be mastered. To this end, the image analysts proposed

Figure 1.2: Illustration of a real urban canyon: two buildings separated by a street.

EM models in order to understand the EM phenomenology of propagation inside the urban canyon. In [Franceschetti 2002], Franscetti *et al.* stated that there is an acknowledged lack of EM and radar models that are able to quantitatively predict and explain the SAR effects relevant to urban scenes. This is due to the high variability of urban landscapes, its complex combination with natural and man made elements, in addition to the wide variety of materials, object forms and size. Comprehensive and detailed EM models are advisable. The models published in the literature can be classified in two types:

- Numerical models that can give possible solutions to the backscattering problem. If the scene is properly specified, the numerical techniques may provide more precise results with respect to analytical methods. However, numerical methods are difficult to use in the case where surfaces of different dielectric properties are defined. Indeed, these methods do not show the functional dependence between the scattered electromagnetic field and the scene parameters. In addition, they are not efficient and are time-consuming if the numerical evaluation has to be repeated for an extended urban scene,
- Analytical models that allow an easy surface management with a possibility to include any scene parameters. In addition, these models allow a fast evaluation of the reradiated field. It is important to underline that a fast computation is a crucial requirement if the evaluation procedure has to be performed several times; this is the case if the electromagnetic return from an entire radar scene including several buildings has to be evaluated. Unfortunately, such an analytical methods is not available in the current literature.

According to Franscetti *et al.*, there is no existing EM model that achieves a trade-off between the level of accuracy of the simulated results and the need to minimize the huge calculation time required by an exact EM method specially for the case of an extended urban scene. However, as our objective is to study the detection of NLOS targets in a simple urban structure (the canyon), we expect to find in the literature a developed method dedicated to similar canonical structures where the scattering is not so complex to understand and to simulate.

The approach we followed to address the state-of-art of our subject is based on the following alternatives:

- Either to use directly the results of the current methods investigating the detection of static targets or even moving targets in urban areas and to adapt them to our specific case of study,
- Or to perform our own analysis of the possible cases of target detection inside the urban canyon using an EM simulator. Therefore, we would have to study the specificities of the existing simulators of urban areas in order to choose the simulator that fits the best to our final goal.

Hence, the state-of-art will be organized in two parts: in the first part, we present the works dealing with the detection of targets that can be static or moving in urban areas whatever the used imaging mode (SAR, GMTI,..). Then, in the second part, we present the different SAR simulators applied to the specific case of urban analysis. The objective of this state-of-art is to have an idea about the current approaches applied to the problem of detecting NLOS targets in urban areas in order to find the best method that fits to our final objective or the method that we can rely on or adapt to achieve our goal.

1.3 Review of the state-of-art

1.3.1 Detection of the NLOS targets

In the literature, works dealing with the detection of targets in urban areas can be classified into two groups. The first group of works investigates the detection of moving targets (or tracking) and the second group performs the detection of static target. In the following, we start by presenting the works concerning the tracking of moving targets in simple urban environments.

1.3.1.1 Detection of the NLOS moving targets

Surveillance of ground targets has traditionally been performed by SAR, ground moving target indication (GMTI) radar, and/or electrooptical (EO) systems. Typically, these systems are effective in open areas where LOS propagation from the sensing platform to the target is available. So far, there is a critical need for wide surveillance areas in urban scenes where the LOS detection of moving target is usually obscured by buildings and others urban structures. This makes the detection of moving targets a challenging task. Nevertheless, some recent studies demonstrated that it is possible to design systems exploiting the NLOS propagation to provide improved radar coverage and track accuracy in simple urban structures (the urban canyon). The first work evaluating the feasibility of exploiting multipath propagation for improved moving target detection in simple urban environments was performed in [Krolik 2006]. In this work, a quasi-analytical model for NLOS propagation assuming multiple specular reflections between buildings is derived. This model evaluates the radar coverage as a function of the scene parameters (target range, relative target position on a street, building height and separation) and the sensor altitude to assess airborne GMTI system. The potential of exploiting multipath was demonstrated through a set of simulations. Another approach to demonstrate the contribution of multipath propagation in the frame of NLOS targets tracking is proposed in [Tahmoush 2012] using radar measurements in various urban canyon environments. The experimental data was collected using an ISAR imaging system. In fact, the detection and tracking of NLOS moving objects using multiple bounces was attempted across a variety of urban buildings materials.

Based on the demonstrated performance that could be achieved by exploiting NLOS multipath propagation, some works proposed a model to help tracking targets in simple urban environments. In [Linnehan 2009], the authors developed a 2D geometrical model allowing to study the detection of moving targets through an urban canyon in the case of far field. This geometrical model simulates the range/Doppler intensity plots for canyons with walls of different roughness. To validate their approach and to gain knowledge about the EM phenomenology needed to develop GMTI radar techniques that exploit the multipath propagation, they performed some outdoor experiments of a moving vehicle inside a canyon in the monostatic case, and they validated their proposed model in terms of velocity and range prediction of the multipath responses [Linnehan 2010]. Nevertheless, the amplitude of the derived responses has not been validated.

In [Chakraborty 2011], Chakraborty *et al.* proposed a target tracker based on a waveform probabilistic data dedicated to multiple interactive motion models.

The new adaptive tracker computes the different probability detection values for a validated set of measurements in the case of LOS and NLOS returns from the target moving between three buildings, and then, select the simulated transmitted waveform that minimizes the mean-squared error (MSE) at each time step. The performance of this model has been evaluated in terms of MSE for the range position and the velocity of the different responses. However, as for the previous works, the performance of the proposed tracker to predict the amplitude of the responses has not been evaluated.

We can conclude that the multipath propagation can be exploited to investigate the detection of moving targets. Thus, based on this assumption, several models have been developed to investigate the target detection and the accuracy of these models has been evaluated in terms of the geometric velocity and range predictions for the multipath responses. Nevertheless, even if these models have shown satisfying results for accurate target tracking, we can not totally rely on them in the sense of using similar approaches and adapt them to our case of static target detection. The reason is that the validation of the proposed models is not complete as the validation of the amplitude is missing. The amplitude is an important parameter in the specific frame of target detection as it is possible to predict accurately the position in range and velocity of a response that may not exist. In fact, the response of a mechanism may disappear due to a huge loss in the amplitude caused by multiple interactions as well as the dielectric properties of the materials composing the scene. Therefore, to adopt a model for our specific application of detection, the phase as well as the amplitude parameters should be necessarily validated. In the following, we will present some of the current studies belonging to the second group of works investigating the detection of NLOS static targets.

1.3.1.2 Detection of the NLOS static targets

For the specific case of NLOS static target detection, the current state-of-art works did not investigate yet neither the detection of targets in the specific configuration of NLOS, nor the detection inside the specific urban structure of the canyon. They focused rather on the detection of LOS targets in a created scattering environment that induces multiple NLOS responses of the target. Then, the purpose of these works is to propose a SAR processing technique to remove the undesirable effects of NLOS responses in the image, named ghost images. Nevertheless, we will present these works in order to have a complete state-of-art of the problematic.

On the contrary of the previous works that exploit the multipath propagation as a useful information to correctly track the target, the approach is not the same for the works investigating the static target detection. In fact, for the case of a static target located in a rich scattering environment, the resulting SAR image will contain several NLOS responses due to the target in addition to the primary response (the LOS response). Hence, the detection task will be difficult to perform as it is difficult to distinguish the LOS response from the ghost images. The multipath propagation is no more exploited as it represents an obstacle to an accurate detection. Therefore, the current works focus on developing dedicated SAR image processing tools to remove the artifacts due the NLOS effects. TR-SAR (Time-Reversal) SAR is the most well known algorithm for target focusing and ghost image removal. It improves

automated target recognition and aids image analysts in identifying targets in dense multipath environment. Jin *et al.* developed this SAR algorithm for removing ghost images that are caused by multipath scattering when imaging two types of targets: the point target ([Yuanwei 2007a], [Yuanwei 2007b]) and the extended target ([Jin 2009]). The performance of this developed algorithm has been evaluated through a set of tests on experimental data and the results of removing ghost artifacts are satisfying.

After this first study of the state-of-art, we concluded that our work can not take advantages of the previous techniques investigating the detection of static and moving targets inside an urban scene for the following reasons:

- The validation of the proposed models to track NLOS targets is not completed for the the first group,
- Our first objective is not to propose an image processing technique to correct artifacts in SAR images of urban areas but rather, to understand the EM phenomenology of propagation inside the urban canyons that may explain the origin of some artifacts. So, our work does not belong to the second group.

Hence, the solution is to perform our own technique to investigate the detection of NLOS targets. Thus, we have to study a huge number of canyon configurations with different targets dimensions and positions inside the canyon in addition to different acquisition conditions related to the sensor. To do so, we need a huge urban data collection for various scene configurations, which is not available. To overcome this constraint, an approach would be to use a SAR simulator to be able to investigate all the possible tests needed to perform our analysis.

In the following, the second part of the state-of-art concerning the existing SAR simulators dedicated to urban areas analysis is presented. The main objective of this state-of-art study is to gain knowledge about the used simulation techniques and the corresponding applications to eventually select one of the simulators to assess the detection of NLOS targets in the urban canyons. In the case where this alternative is not possible, we can choose to develop our own tool referring to the used techniques of the existing SAR simulators.

1.3.2 SAR simulators of urban areas

The simulation process is in general a trade-off between an achievement of an approximation as close as possible to the reality and the minimization of the computational load and processing time. The simulation of SAR data is a widely used technique in radar remote sensing. Using simulations, the SAR data from sensors still under development can be synthesised. This provides data for developing image interpretation algorithms before the real sensor is launched. Moreover, the simulators can deliver images of any object of interest from various orbits, for a wide range of angles, using different radar wavelengths. In the long history of SAR simulation, many variants tools have been developed for different applications. In urban areas, SAR simulators are primarily used for mission planning, for the scientific analysis of the complex backscattering, and for geo-referencing. More broadly, simulators are used for sensor design, algorithm development, and for training and education. The different applications and their different requirements have lead to the development

of several SAR simulation techniques. In the following, we will present the most common techniques implemented in the SAR simulators and the main applications for which these SAR simulators have been designed for.

1.3.2.1 Techniques for SAR simulations

To determine how the simulated sensor and the virtual scene interact, two common methods are used: the ray tracing and the rasterization.

Ray tracing

Concept

Many SAR simulators use ray tracing or a derived technique. Ray tracing has been developed for the visualization of scenes in the optical dimension of light, based on the geometrical optics (described in Sec.3.4). In ray tracing, the path of each "ray" is followed from the SAR sensor, throughout the scene, and eventually back to the sensor. The number of rays launched on the scene depends on the implementation and the trade-off between the desired degree of realism and the need to minimize the computational load. At least one ray per slant-range resolution cell has to be ensured, but many simulators divide the scene into smaller cells, thus leading to a huge number of simulated rays throughout the scene. This method allows:

- The superposition of signal contributions into an individual cell,
- The automatic consideration of multiple reflections, shadows, and occlusions.

Validity domain

Standard ray tracing has the drawback that the rays are only reflected in the specular direction, which is a valid assumption for very smooth surfaces. This implies that the non specular scattering contributions from rough surfaces are neglected.

Acceleration methods for ray tracing

Unfortunately, the ray tracing approach is rather computational time consuming, because for each pixel of the simulated image, one ray has to be traced. For this reason, this technique is normally not used for real time applications. However, by optimizing the data organization for a fast search, the calculation speed of ray tracing can be drastically increased ([Glassner 1984]). Typically, Octrees ([Kyu-Young 1995]), binary space partitioning ([Paterson 1990]) and Kd-trees ([Wald 2006]) are the most known methods to optimize the ray tracing method in terms of computation time and computer resources consumption.

RCS target simulation using ray-tracing method

For target RCS simulation, the shooting and bouncing rays technique ([Hao 1989]) is often applied. In shooting and bouncing rays, each ray is traced through a target, according to the law of geometrical optics, until it leaves the target. Afterwards, physical optics is applied in order to address diffraction, refraction, etc. This technique is used in the SAR simulator (SE-Ray-EM) developed by Mametsa *et al.* ([Mametsa 2002]).

Rasterization

Besides ray tracing, a second technique, known by many as rasterization, can be used to visualize scenes with a lower computational load. This technique is widely used in real-time visualization applications, even though producing less realistic

results. Rasterization does not rely on tracing rays. It is based on meshing each 3D component into a set of elements, normally triangles that are transformed from world coordinates to image coordinates before rasterization. Each resulting 2-D triangle is rasterized to a collection of pixel fragments, called fragments. In subsequent fragment operations, the final intensity for each pixel is calculated. The final pixel value of an image can be determined by one or more fragments, either by combining the fragments or by determining a single fragment representing the pixel value, for example, by depth sorting [Balz 2009]. Today, specialized graphics hardware is used to accelerate the coordinate transformations and rasterization of the vector data. When compared to ray tracing, this process is usually faster, because instead of tracking millions of rays, only thousands of objects have to be transformed by a series of multiplication operations. Recently, this process has been accelerated using a dedicated hardware configuration, in addition to an increase of the visualization speed. The radar target simulation GRECO (Graphical Electromagnetic Computing) relies on rasterization to determine the visible parts of a target in order to speed up the RCS calculation ([Rius 1993b]). GRECO visualizes a 3D model using Graphics Processing Units (GPU). The concept was later extended for the SAR simulator GRECOSAR ([Margarit 2006]). Today, the graphics hardware is even more powerful, allowing for the GPU to be exclusively used for both the calculation and visualization of SAR images ([Balz 2009]).

Once the different interactions between the simulated sensor and the simulated elements of the scene are established, the second step is to evaluate the effects of every interaction of the travelling rays on the transmitted power. The goal is to calculate the backscattering intensity of each element of the scene under study. Some physical models, differing by their complexity, have been proposed for this goal. They will be presented in the following.

Ray tracing vs Rasterization in SAR simulation

For SAR simulations, the rasterization approach is less feasible, due to the numerous multiple reflections occurring in SAR images. Ray tracing is a standard technique and despite the higher computational effort involved, it is approaching real-time speed capability in some computer graphics applications. For SAR simulation, ray tracing is established as a standard technique used by a variety of software systems. Furthermore, Ray tracing and especially raw data simulators deliver more realistic simulation results than rasterization based simulators. This is due to the missing multi-bounce reflections and to the simplified backscattering model implemented in the rasterization-based simulators.

1.3.2.2 Physical models to calculate the backscattering intensity

A wide variety of different physical models are applied, ranging from the simplest to the most realistic possible. The desired complexity depends on the application.

Simplified physical model

In the following, we present some examples of simplified physical models to calculate the backscattering intensity.

1. Simplified simulations based on geometric constraints:

These simulations are used for layover and occlusion calculation that do not need a physical model and may rely on geometric constraints alone. After implementing the SAR geometry, simple layover and occlusion detection can be realized by setting the basic reflection value of each "ray" or each "fragment-interaction" to a basic constant reflection value r, such as $r = 1$ as an example. In the final image, shadow regions will have a reflection value of $r = 0$, whereas layover areas will have values such as $r > 1$,

2. Simplified simulations based on the Lambertian reflection model:
In this model, the backscattering is always supposed to be of Lambertian nature meaning that the backscatter has the same strength in all directions ([Jutzi 2006]). Under this assumption the observed backscattering intensity σ depends only on the local incidence angle θ_i and the reflectivity, r, determined for example, by look-up tables. σ is calculated as follows:

$$\sigma = r \cos \theta_i \tag{1.1}$$

3. Simplified simulations based on the Lambertian and specular reflection model:
Similar to Phong shading model ([Phong 1975]), the backscattering can be divided into the sum of two contributions: a Lambertian part and a specular part. Calculating diffuse and specular reflections separately and combining them to obtain a total reflection coefficient has been done before by Arnold Bos *et al.* ([Arnold-Bos 2007]).

"More elaborated" physical model

Other simulators implement a complete physical model. There is a wide variety of EM models used for this purpose ([Fung 1992]; [Fung 1994]). To calculate the backscatter, various variables are needed to describe the interaction of the signal and the materials such as the dielectric properties and the parameters describing the surface roughness. The backscattering of different objects do influence each other. However, in rasterization, as well as in ray tracing, the contribution of each ray or pixel is calculated separately. Therefore, the effects of the mutual influence of the SAR scatterers have to be calculated in a post-processing step. As this step is time consuming and depends on the number of scatterers included in the calculation for each SAR image pixel, it is often neglected by simulators requiring fast simulation results.

In order to make the simulated SAR image looks as realistic as possible, the proper treatment of SAR speckle noise is also an important issue. This is to avoid situations where image analysis algorithms perform well on simulated data but fail in their actual application to real SAR data.

Speckle simulation

The characteristic speckle effect of SAR images results from the destructive and constructive interferences coming from the contribution of the different scatterers within a resolution cell. Therefore, the resultant pixel can differ extremely from its average gray value. These gray values variations between adjacent pixels lead to the physical grainy appearance of SAR images [Bolter 1996]. The speckle simulation is often simplified by assuming Rayleigh-distributed speckle. It can be obtained

by multiplying the calculated backscatter intensity with a number generated randomly according to the Rayleigh distribution ([Hammer 2008]). For high-resolution SAR images, the basic assumption for a Rayleigh distribution can be wrong, especially for the case where high number of independent scatterers belong to the same resolution cell. Depending on the surface of study, various other probability distribution functions, including the Rician inverse Gaussian distribution ([Eltoft 2005]), K-distribution ([Jakeman 1976]), and many others ([Nadarajah 2008]), can describe the speckle more precisely. Besides approximating the appropriate probability density function, the multiplication of the random value with the calculated backscatter intensity is an additional simplification of the speckle calculation.

1.3.2.3 Applications of SAR Simulations in Urban Areas

Analysis of the complex radar backscattering of buildings
By comparing the simulated SAR images with the real ones, the interpretation of the real SAR data can be improved. Due to various disturbing effects in SAR images, such as speckle, layover and shadows, the interpretation is usually difficult. Simulations can help to:

- Explain the origin of certain artifacts in the SAR images,
- Verify assumptions about the image content ([Guida 2008]),
- Investigate separately some combined effects and their mutual influence.

SAR Data Acquisition Planning
SAR simulations can assist the mission planning and can determine the best acquisition parameters. This is extremely important for time critical operations in urban areas as for the disaster management [Yonezawa 2002].

SAR Image Geo-referencing
SAR sensors hold a strong potential for change detection studies, especially thanks to their all weather mapping capability and can also guarantee operational systems in the presence of crucial circumstances and night conditions illumination. To detect whether or not a change has occurred, two images are taken of the same scene, but at different times. These images are then geometrically registered to be cross correlated after. The step of geometric registration of the images is called geo-referencing. However, due to geometrical properties of the SAR sensor, SAR images suffer from occlusions and ambiguities especially in urban areas. Additionally, layover and shadow effects disturb the geo-referencing of SAR images in urban areas, which is a prerequisite for a successful change detection analysis. An improved geo-referencing can be achieved by simulating 3D-city models using a SAR simulator and comparing the simulated image to the real image. Correspondences between simulated and real images can be used for geo-referencing the image according to the coordinates of the 3D-city model and street datasets. The geo-referenced dataset can afterwards be used for change detection analysis ([Balz 2004]).

Training and Education
SAR simulators are important tools for training and education and can increase knowledge of the physical mechanisms of SAR ([Nunziata 2008]). SAR simulators

offer a cost-effective way to generate thousands of simulated SAR images of certain objects as it allows for a multitude of looking and azimuth angle combinations to be demonstrated at low or no cost. SAR simulations further offer the possibility to produce or not certain SAR effects, such as speckling. These possibilities make SAR simulations a huge advantage both for the training and education of students as well for the analysis and interpretation of SAR data.

1.3.2.4 Classification of SAR simulators

Different types of SAR simulators are used for different applications. To differentiate between them, SAR simulators can be classified according to different schemes. Up to now, there is no available standard for the classification of SAR simulators. We present in the following some proposed classification models in the literature for urban SAR simulators.

Classification based on the outputs

An output based classification has been proposed by Francescetti *et al.* [Franceschetti 1995]. They classified the different simulators into two groups based on the final output:

- SAR raw data simulators: they simulate the raw data of a sensor which has to be processed in order to get a SAR image. They are mostly used for the design of sensors or SAR processors, or to improve the scientific understanding of the complex radar backscattering behavior. Raw data simulation process is rather slow. To improve the speed, Rius *et al.*[Rius 1993b] developed a radar-cross-section simulation system GRECO, which used graphics hardware to accelerate the geometric processing. Radar-Cross-Section (RCS) is a measure of the detectability of an object by the radar. It is explained more in details in Subsection.2.2.1,
- SAR image simulators: they produce a final SAR magnitude image. They are designed for applications like interactive mission planning, training using interactive tools, or assisting the interactive interpretation and analysis of SAR data. These simulators provide their results fast, comparing to the SAR raw data simulators, but are less realistic.

Classification based on the inputs

Simulators can be distinguished by the input they use to estimate the RCS σ. The input-based classification from [Leberl 1990] distinguishes between three types of simulators according to the way they calculate σ:

- σ is calculated using look-up tables [Balz 2009],
- σ is derived from the real SAR image [Auer 2010],
- σ is calculated using physical models ([Franceschetti 1992], [Mametsa 2002]).

A second input classification proposed by Balz in [Soergel 2010], is based on the model implemented in the simulation tool. Four types can be identified:

- Radar target simulators: calculating the RCS of single targets,
- SAR background simulators: simulating natural landscapes, often based on 2.5 D Digital Elevation Model (this model describes a surface rather than the

volume of a feature, for further details, see [Schön 2009]) data and look up tables,

- SAR target-background simulators: separating the background from the target. The model applied to the background is often simplified and the model applied to the target may or may not be based on radar target simulators using shooting and bouncing rays,
- Integrated SAR simulators: not differentiating between the background and the targets. All objects are simulated in 3D and both inter and intra-object interactions are supported, covering multiple objects in an extended scene.

A combined classification of SAR simulators using the inputs of the previous classification and the outputs of the classification of Francescetti *et al.* in [Franceschetti 1995] is proposed also by Balz in [Soergel 2010] (see Tab.1.1). In this classification, for simplification and coherency, Balz stated that only the simulation of the target is taken into account for SAR target-background simulators.

Table 1.1: SAR classification proposed by Balz in [Soergel 2010].

	simulation outputs				
		SAR raw data simulator		SAR image simulator	
		look-up tables	physical model	look-up tables	physical model
simulation inputs	SAR background simulator	[Holtzman 1978]	SARAS [Franceschetti 1992]	SARViz [Balz 2006b]	
	SAR target background simulator		GRECOSAR [Margarit 2006]		
	Integrated SAR simulator			SARViz [Balz 2009]	SE-RAY-EM [Mametsa 2002]

Classification based on the radiometric/geometric correctness

Auer *et al.* proposed in [Auer 2010] another SAR simulators classification based on two approaches:

- Approach focusing on the radiometric correctness:
  This approach uses formulas to calculate a high-quality intensity values of the scattered field. These models take into account the roughness parameters (i.e., rms height and correlation length) and dielectric properties of the surfaces in the scene to calculate the scattering. However, the level of detail of 3-D models to be used is limited. For example, Franceschetti *et al.* [Franceschetti 1992] developed a SAR raw signal simulator (SARAS) and added reflection models for describing multiple-bounce effects at buildings modelled by a parallelepiped ([Franceschetti 2002], [Franceschetti 2003]). Dellière *et al.* [Delliere 2007] developed a SAR raw signal simulator using finite-difference time domain (FTDT) technique in order to quantitatively evaluate the EM return of a rectangular parallelepiped (placed either on smooth or

rough surface). Even if this simulator is able to predict fine EM effects, the FTDT technique is very demanding in terms of computation time and memory. It is therefore limited in its practical ability to represent very large areas,

- Approach focusing on the geometric correctness: This approach focuses on representing the geometric effects of a detailed scene. The radiometric quality is of less importance in this approach. Balz [Balz 2006a] used programmable graphics card units for generating single-bounce SAR images in real time. Margarit *et al.* analyzed reflection effects by including multiple reflections and SAR polarimetry for detailed 3-D models of vessels [Margarit 2006] and buildings [Margarit 2007], in addition, they preserved high radiometric quality by using a RCS simulator [Rius 1993a] named GRECO. Indeed, GRECO method is regarded as one of the most effective methods for RCS calculation, so it is used to calculate the scattering map of complex targets. In fact, simulation results using GRECO on complex radar targets can be found in [Rius 1993b], [Rius 1990] and show good agreement with the measurements. Brunner *et al.* [Brunner 2011] demonstrated that their simulator based on a simplified radiometric model is sufficient to calculate many various effects related to the scene geometry such as layover, shadowing, multi bounces scattering and diffuse corner reflection. In [Hammer 2008], Hammer *et al.* proposed a comparison between three simulators focusing on the geometric correctness. This comparison is based on the SAR geometric effects they are able to perform on a simple and complex urban structure.

In order to choose between the simulators dedicated to urban areas, the one that fits more to our application of NLOS target detection inside urban canyons, we have summarized into two groups the most common simulators of urban areas based on the radiometric and geometric correctness like in the Auer's classification. For each group of simulator, we have specified the inputs, the outputs, the simulation techniques, the EM method for backscattering calculation, the validity domain and applications (see Tab.1.2 and Tab.1.3).

To measure how far from the reality are the results, the validation step is required. It is an indicator of the performances achieved by a simulator. The validation process concerns these three steps:

- Comparison between simulation results and analytical formulation,
- Cross-comparison between simulators or "bechmarking",
- Comparison of simulation results with measurement.

The wide variety of SAR simulators types and their corresponding applications makes comparisons between them difficult. Thus, a cross comparison between simulators is not feasible. Therefore, the validity domain of a simulator would concern rather the first and the third steps. Even if we have chosen the same classification scheme as Auer *et al.*, there is a point of difference with them concerning the classification of GRECOSAR. In fact, we have included GRECOSAR in the group of simulators based on the radiometric correctness as it has been used (for the specific case of urban SAR simulations) to evaluate the scattering of a simple target (a box of gypsum over a perfectly conducting flat plane). Moreover, we have added in this group a new simulator developed by Nguyen *et al.* that proposed a 3D model to characterize the EM scattering by an urban area which is composed by a group of buildings for both monostatic and bistatic radar configurations

[Nguyen 2011]. They assessed a **quantitative** evaluation of the scattered field according to the polarization of the incident wave, the geometry and the materials composing the scene. We mean by quantitative evaluation, the validation of the expected theoretical effects by a set of simulations of the proposed model. Whereas, the **qualitative** evaluation is usually based on the validation of the proposed model with experimental measurements. Even if this simulator deals with a higher level of urban structures complexity by involving the scattering of multiple buildings, these considered buildings are composed by simple structures (the parallelepiped) without any additional features (building balconies, trees, cars..). So, we included this simulator in the group of simulators based on the radiometric correctness.

1.3.2.5 What is the best simulator to apply for our application?

At the end of this state-of-art study, we can say that all the simulators based on the geometric correctness achieved good results in simulating high level of detailed and extended urban scenes. However, as the radiometric quality is limited, we can not rely on the approximated amplitude of the scatterers to investigate the detection. For the second group of simulators based on the radiometric correctness, huge efforts have been made on the EM calculation of the scattered fields of simple urban structures. So, these simulators may achieve our goal as we are dealing also with simple canonical structures (the urban canyon). However, even if the calculated intensity of the scatterers is well performed, it has not been validated with experimental data as far as we know according to the literature. So, we can not rely also on radiometric accuracy based simulators for our purpose.

As we can conclude through this state-of-art, there is a wide variety of methods investigating the detection of NLOS moving and static targets inside simple urban scenes, in addition to a large variety of simulators trying to model the EM propagation inside different urban environments varying by their complexity. However, even if these works achieved satisfying results in detecting targets or simulating correctly the most important effects occurring inside an urban scene, their validation is not totally achieved yet. Specifically, the amplitude parameter has not been validated by current state-of-art works dealing with the EM modelling of urban areas. As mentioned before, this parameter is important in the specific framework of target detection as it determines the possible detection or not of a target.

1.4 Specifications of the objective

1.4.1 Requirements

As an ideal SAR simulator dedicated to urban areas, that addresses both the geometric and radiometric accuracy, and that has been validated in terms of amplitude and phase, is not achievable for the moment, we have first to define the requirements of our simulator and the followed strategy to validate it. As our ultimate objective is to investigate the possible detection of NLOS targets inside urban canyons, our proposed tool should be:

- Dedicated to urban canyon configuration,
- Fast in terms of computation time,

- Efficient for phase and amplitude simulation of the scatterers responses,
- Validated both in terms of phase and amplitude.

1.4.2 Approach

Regarding the specificities of our final application, we agreed that there is no need of a full detailed SAR image to detect the possible presence of a NLOS target inside an urban canyon. It is better to first understand the EM phenomenology of propagation inside the canyon to build then the dedicated tool for this purpose. The simulating tool should be able to analyze all the possible canyon configurations (empty canyon and canyon with a target included) and to determine automatically if a return back to the radar is possible. Considering the large variety of the configurations to be analyzed, we cannot develop a complex tool that will be obviously time-consuming.

Consequently, the approach is to develop a simulation tool with a specific output, fast to compute, and at the same time efficient to investigate about the detection of NLOS targets inside the canyon. This output will not be a full image but rather a radar range profile. Indeed, the comparison between the range profiles with or without a NLOS target (change detection) will help in determining if a NLOS target is present in the canyon. Moreover, in this case, a deeper analysis of the range profiles gives information about the possible location of the target, and we could also make assumptions on the nature of the target. For instance, we can have clues concerning the directivity of the target, as well as its orientation.

After building this tool, the validation process is required. So for this purpose, some indoor measurements are needed.

At the end of this work, we should have at our disposal an efficient and validated tool dedicated to the detection of NLOS targets inside a simple but representative structure of an urban area.

1.4.3 Methodology

To develop our simulation tool dedicated to NLOS target detection inside urban canyons, we adopted the following methodology based on two-steps validation process. First, we have conducted some measurements in the anechoic chamber to study the EM propagation inside a canyon with and without the presence of the target. An EM theoretical study has been carried out to help understanding the scattering phenomena for a canyon with a ratio between the typical dimension d of the object of interest and the wavelength λ imposed by the technical constraints of the anechoic chamber that does not correspond to the real case. Once the theoretical EM scattering investigated, a benchmarking between different EM commercial codes has been performed to select the EM code that best reproduces the EM indoor phenomenology of propagation inside the canyon. In fact, different comparisons between the simulation results of two codes (FEKO and CST) and the experimental data have shown a good agreement both for the phase and amplitude. Then, they have been used to simulate the scattering of more realistic configurations (in terms of d/λ ratio). All this study concerning the validation of the EM code is presented in the second part of this thesis.

The third part deals with the second step of validation. It concerns the valida-

tion of a fast and simple developed in-house EM code dedicated to NLOS target detection inside urban canyons. In fact, based on the simulation results of the EM validated commercial tool applied to real case configurations, we have developed our own EM tool. This tool predicts for any canyon configuration, the detectability areas where a NLOS target can be detected, and for the case where the target is present if it can be detected or not and the corresponding range signature. As a direct validation (direct comparison with the experimental data) is not possible due to the fact that the d/λ ratio can not be respected in the anechoic chamber, we validated our code with one of the selected EM codes. Indeed, a good agreement between the simulation results has been found for both phase and amplitude. An application of the results of our EM code to interpret real InSAR data is proposed in the last chapter.

In Fig.B.2, we propose a block diagram summarizing the different steps of the proposed methodology.

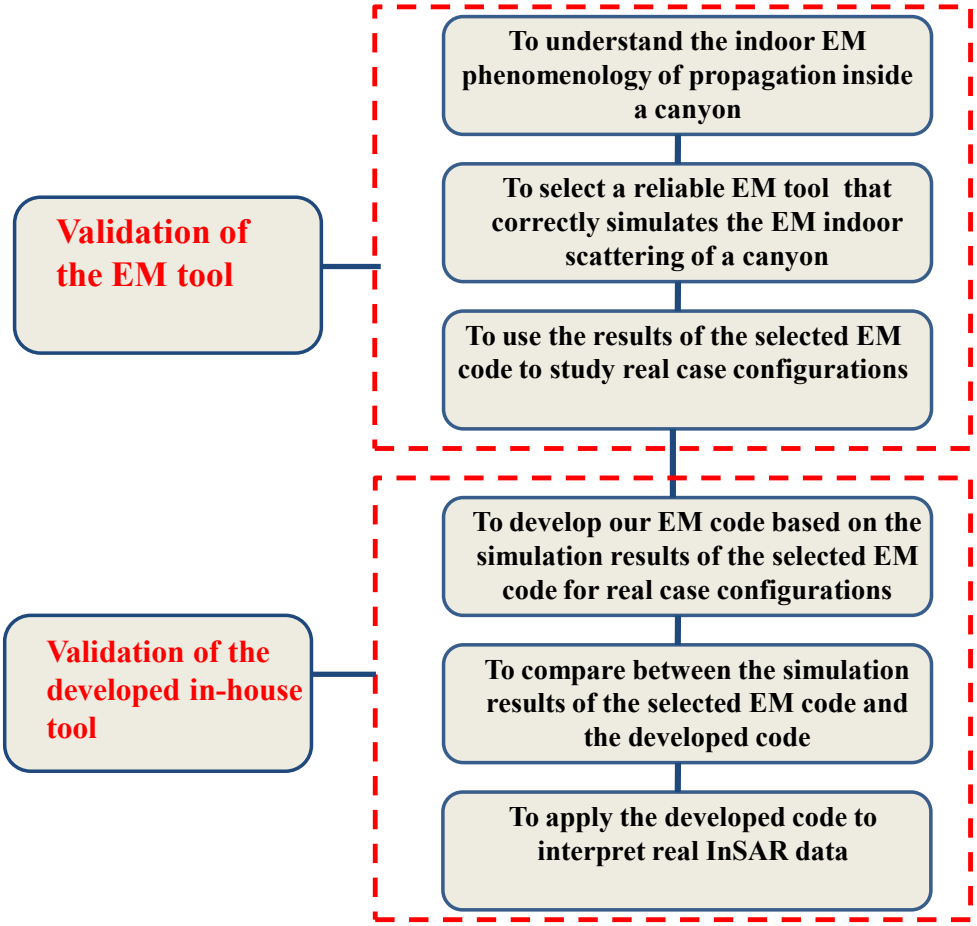

Figure 1.3: A block diagram summarizing the different steps of the followed methodology to develop and validate our EM simulation tool dedicated to the detection of NLOS targets inside urban canyons.

Table 1.2: Examples of SAR simulators based on the radiometric correctness.

SAR simulator	Input	Output	Simulation principle	Backscattering calculation	Validation	Applications
SARAS [Franceschetti 1992]	Simple canonical structures	SAR raw data simulator	Ray tracing	Kirchoff approach for PO / GO approximations [Franceschetti 2003]	-Quantitative validation of the expected theoretical EM effects produced by simple urban structures (a parallelepiped)	-Quantitative assessment of the effects of achievable SAR images according to the SAR sensor parameters for a fixed urban scene -Quantitative assessment of the effects of the scene geometry on the SAR images for a fixed SAR sensor
Dellière *et al.* simulator [Delliere 2007]	Simple canonical structures	SAR raw data simulator	Not mentioned	FTDT technique	-Quantitative validation of the expected theoretical EM effects produced by simple urban structures	-Quantitative evaluation of the EM return of a parallelepiped using a geometric and EM developed model
Nguyen *et al.* simulator [Nguyen 2011]	Simple canonical structures	SAR raw data simulator	Ray tracing	UTD	-Phase and amplitude validation of the simulated scattering of a right-angled wedge with an EM software (XGTD) -Phase validation of the simulated scattering of a canyon configuration (with target) with indoor measurements in the case of near field	-3D model to characterize high frequency scattering by simple urban structures in the monostatic and bistatic case
GRECOSAR [Margarit 2007]	Simple canonical structures	SAR raw data simulator	Rasterization	High frequencies methods implemented in RCS simulation system GRECO: PO/MEC/PTD/IBC [Rius 1993b]	-Validation of the scattering behaviour of simple urban targets via polarimetric simulations	-Support of different imagery modes: POLSAR/POLISAR/POLInSAR -Exploitation of POLINSAR data for urban identification procedure: discrimination of different kinds of targets (buildings, parks..)

Table 1.3: Examples of SAR simulators based on the geometric correctness.

SAR simulator	Input	Output	Simulation principle	Backscattering calculation	Validation	Applications
FERMAT [Mametsa 2002]	Complex urban scene	SAR raw data simulator	Ray tracing	High frequencies methods: GO, PO, PTD, ECM	Not mentioned	-Deals with complex objects, complex environments and complex targets in a complex 3D scene, -Handles various propagation effects: reflection, scattering, diffraction and transmission, -Implement dedicated models for clutter materials simulation including speckle effects.
SARVIZ [Balz 2009]	Complex urban scene	SAR image simulator	Rasterization	Specular and diffuse reflection	-Validation of the SAR effects (layover, shadow)	-Supports only single and double bounces effects -Fast time simulation of extensive urban areas
POV ray [Auer 2009]	Complex urban scene	SAR image simulator	Ray tracing	Specular and diffuse reflection	-Validation of the 3D localisation of the scatterers	- Investigates the intensity contribution in azimuth, range and elevation
Brunner *et al.* [Brunner 2011]	Complex urban scene	SAR image simulator	Extended Ray tracing	Lambertian-specular mixture model	-Validation of the SAR geometry effects (layover, shadowing, multi bounces scattering and diffuse corner reflector)	-Simulates the geometric effects of complex urban structures

Chapter 2

Reference data

Contents

2.1 Introduction

In this chapter, the goal is to present all the reference elements at our disposal to be used later for the validation process. This process concerns the validation of the EM commercial codes as well as the in-house code by a comparison between the elements of reference and the simulation results. When any agreement is found, we can assess about the accuracy of the tool. The reference elements consist of some existing data related to previous works in SONDRA and ONERA investigating the NLOS target detection inside a canyon as well as new data acquired during this thesis. We have also considered theoretical results available in the current literature. Thus, the first existing element that we referred to is the theoretical response value of canonical targets. This theoretical response is evaluated in terms of Radar Cross Section (RCS). The RCS is a parameter to measure the degree of the target's visibility to a radar. It is usually used to calibrate the indoor data as well as to validate the results of any EM code to correctly simulate the amplitude of the scatterer's response.

The second existing element of reference is a dataset of indoor measurements collected in the frame of a collaboration between SONDRA and the radar system group from Temasek Lab of NTU (Singapore). The goal was to investigate the NLOS target detection inside a metallic canyon in the anechoic chamber at Ka-band [SAR 2011]. The last existing element of reference is a set of outdoor SAR data acquired through a measurement campaign operated by ONERA to investigate the NLOS responses of different targets in SAR images of various urban scenarios at Ka-band [Nouvel 2011]. One of the proposed scenarios, containing an urban canyon,

has been analysed and presented in the last chapter of this thesis. Concerning the new measurements carried out during the thesis, they have been performed in one of the anechoic chambers of ONERA to gain knowledge about the EM phenomenology of propagation inside the canyon in a controlled environment. A complete study, devoted to the analysis of these data, is presented in the fourth chapter.

This chapter is organized as follows: in the first section, we present the existing elements that we referred to. The first subsection deals with the theoretical study concerning the EM evaluation of the amplitude of a response using the RCS parameter: the calculation principle of RCS as well as the expressions of some RCS of typical targets are presented. Then, the following subsections deal with the existing indoor and outdoor measurements. In fact, a general description is given including the scene geometry and the radar parameters, followed by the main conclusions about the analysis results of the measurements. In addition, we present the advantages and difficulties of every set of measurements. In the third section, we give a description of the new indoor data acquired during this work following the same scheme of presentation as for the existing elements of reference. Finally, we end up this chapter by a conclusion.

2.2 Existing elements

Before investigating our study of the NLOS target detection inside urban canyons, reference data have been at our disposal from previous works that helped in starting this new topic. These data consist of some measurements datasets (indoor and outdoor) and some theoretical references to use for validation. In this section, we introduce all these elements.

2.2.1 Theoretical Radar Cross Section (RCS)

The first reference serving to every study that investigates the calculation of the EM response of a target is the radar cross section (RCS). It is a measure of the target's ability to reflect radar signals in the direction of the radar receiver. It is a function of some parameters (frequency, material of the target, permittivity, the polarization of the incident wave..). The RCS, usually denoted σ, can be defined as the ratio between the energy scattered back and the energy intercepted by the target ([Knott 2004]):

$$\sigma = \lim_{R \to +\infty} 4\pi R^2 \frac{||\overrightarrow{E_s}||^2}{||\overrightarrow{E_i}||^2} \tag{2.1}$$

where:

- $\overrightarrow{E_s}$ and $\overrightarrow{E_i}$ are the scattered and incident electric fields respectively,
- R is the distance from the antenna to the object under illumination.

σ is an area and is expressed in m^2. It is used for point targets, whereas the backscattering from areas is described by the backscattering coefficient σ^0. σ^0 has no dimension and is defined as the radar cross section, normalized by the illuminated surface A ([Ulaby 1989]):

$$\sigma^0 = \frac{\sigma}{A} \tag{2.2}$$

The RCS parameter is used to validate the amplitude levels of the collected responses (by simulations or by measurements). Since, for some typical targets, the theoretical expression of the RCS is established, these targets are usually used to calibrate the indoor measurements. In addition, in the specific framework of NLOS target detection, the RCS has been used to validate the simulation results of the commercial EM tools to correctly evaluate the amplitude of the responses of the targets. In fact, the RCS parameter is a fundamental prerequisite that serves to validate any study involving the EM calculation of the scattered field inside the scene. In the following, some of the theoretical expressions corresponding to the RCS of typical targets are given. But before, we give an explanation of the theoretical formulas that are established.

2.2.1.1 RCS formula calculation

The RCS of the target depends on the wavelength, the polarization, the permittivity and the aspect angles. The aspect angles are defined by the incident wave vector $\overrightarrow{k_i}$ and are defined in the coordinate system relative to the target. This means that the aspect angles are only affected by the position of the radar and are independent of the radar's orientation. These two aspect angles are denoted θ_a and ϕ_a in Fig.2.1. To determine the RCS variation with the aspect angles and polarization, an aspect

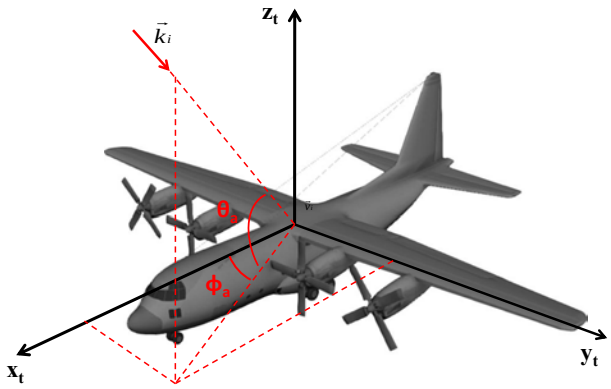

Figure 2.1: Target aspect angles. $\overrightarrow{k_i}$ is the incident wave vector.

factor is first calculated for the desired range of azimuth and elevation angles. Then, the resulting value of RCS is obtained by a multiplication between the aspect factor denoted F, the maximum value of RCS denoted σ_{max} and a scattering matrix S describing the EM behaviour of the target according to the polarization of the incident wave so that:

$$\begin{bmatrix} \sigma_{Hh} & \sigma_{Hv} \\ \sigma_{Vh} & \sigma_{Vv} \end{bmatrix} = F \times \sigma_{max} \times \begin{bmatrix} S_{Hh} & S_{Hv} \\ S_{Vh} & S_{Vv} \end{bmatrix} \tag{2.3}$$

Nevertheless, due to the geometry of the typical targets we will present (sphere, trihedral corner reflector and plate) and their material properties (metallic case), the cross polarization responses do not exist and the co polarization responses are

identical. Thus S will be defined as:

$$S = \begin{bmatrix} 1 & 0 \\ 0 & 1 \end{bmatrix} \tag{2.4}$$

Therefore:

$$\begin{cases} \sigma_{Hh} = \sigma_{Vv} \\ \sigma_{Hv} = \sigma_{Vh} = 0 \end{cases} \tag{2.5}$$

In the following, the RCS denoted σ_{pp} refers to the RCS for the co polarization channels (Hh and Vv) as they are equal such as:

$$\sigma_{pp} = F \times \sigma_{max} \tag{2.6}$$

Based on the formula in Eq.2.6, we will give in the following the expressions of the RCS of some typical targets.

2.2.1.2 RCS of a sphere

The RCS of a sphere [Gallman 2005] is defined as:

$$\sigma_{pp}^{sphere} = F_{sphere} \times \pi r^2 \tag{2.7}$$

The factor F_{sphere} is independent of the aspect angles and the wavelength. Its value is set to 1 as the target has an isotropic scattering. r is the radius of the sphere.

2.2.1.3 RCS of a flat plate

The RCS of a flat plate [Gallman 2005] is defined as:

$$\sigma_{pp}^{plate} = F_{plate} \times 4\pi \frac{(ab)^2}{\lambda^2} \tag{2.8}$$

a and b are the dimensions of the flat plate, λ is the radar wavelength and F_{plate} is defined as follows:

$$F_{plate} = \left[\cos\theta_a \frac{\sin x}{x} \frac{\sin y}{y} \right]^2 \tag{2.9}$$

x and y are defined in the following equations:

$$x = ka \sin\theta_a \cos\phi_a \tag{2.10}$$

$$y = kb \sin\theta_a \sin\phi_a \tag{2.11}$$

with:

- $k = 2\pi/\lambda$,
- θ_a and ϕ_a are the aspect angles. For the specific case of the plate orientation in the left part of Fig.2.2, $\phi_a = 0$ so that:

$$F_{plate} = \left[\cos\theta_a \frac{\sin(ka \sin\theta_a)}{ka \sin\theta_a} \right]^2 \tag{2.12}$$

2.2.1.4 RCS of a trihedral corner reflector

The RCS of a trihedral corner reflector [Gallman 2005] is defined as:

$$\sigma_{pp}^{trihedral} = F_{trihedral} \times \frac{4\pi L^4}{3\lambda^2} \tag{2.13}$$

L is the length of the the edge of the trihedral corner reflector (see the right part of Fig.2.2) and $F_{trihedral}$ is defined as follows:

$$F_{trihedral} = \left[2\cos\theta_a \frac{J_1(x)}{x}\right]^2 \tag{2.14}$$

with:

- J_1 is the Bessel function of the first order,
- $x \simeq 1.617 \frac{\sin\theta_a}{\sin 20°}$,
- θ_a is the aspect angle illustrated in the right part of Fig.2.2.

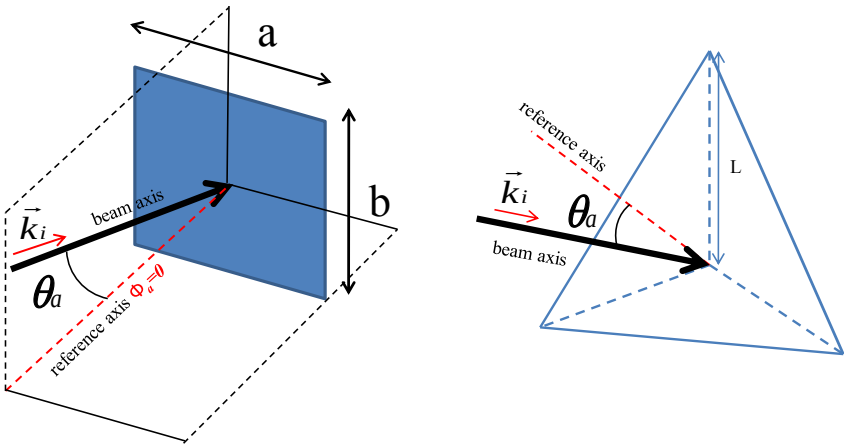

Figure 2.2: Parameters used for the RCS calculation of the flat plate and the trihedral corner. The beam axis corresponds to the incidence axis and the reference axis illustrated in dashed red line corresponds to the axis where the RCS is maximum. For the trihedral corner reflector, the reference axis corresponds to the symmetry axis.

For further details concerning the RCS calculation of the previous targets and others examples of typical targets, see [Gallman 2005].

2.2.2 Indoor measurements

2.2.2.1 General description

Before starting this work, a first preliminary study concerning the feasibility of detecting the NLOS targets inside an urban canyon has been investigated using a first set of indoor measurements. These data have been acquired in the frame of a collaboration with Singaporean scientists from the Radar Systems group from TL@NTU using DSO anechoic chamber.

Scene geometry:
The object of interest is a PEC (Perfect Electric Conductor) canyon with different types of included targets. The measurements setup and the canyon configuration are illustrated in Fig.2.3.

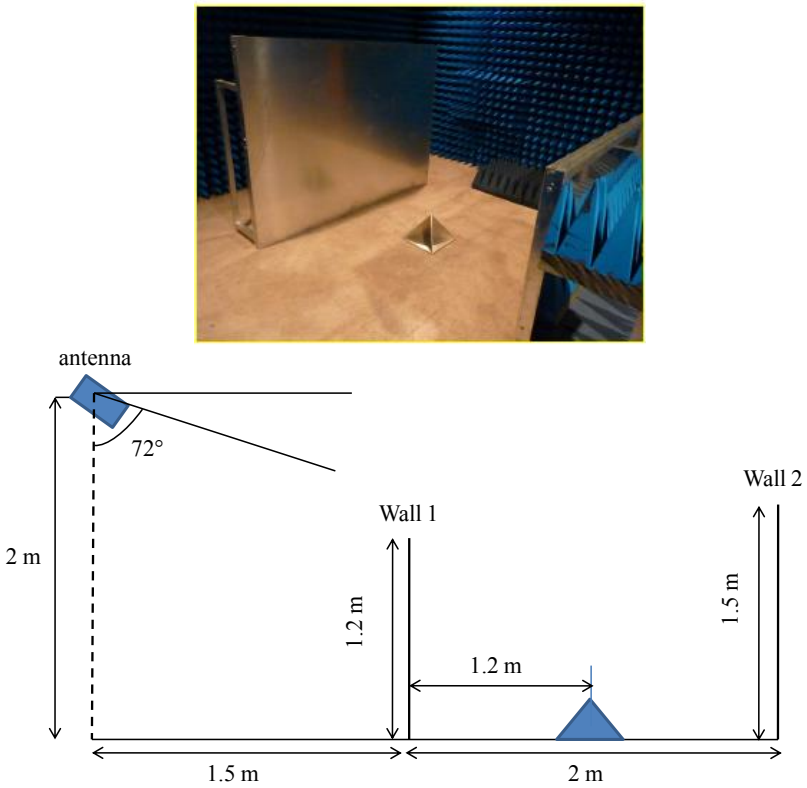

Figure 2.3: Measurement setup in the anechoic chamber of NTU at Ka-band. An example of targets (the 4-in-1 corner reflector) is located between the walls of the canyon.

Radar parameters
The used antenna is a of type horn antenna located at a distance of 1.5 m from the first wall of the canyon (see Fig.2.3). The incidence angle is 72°. The frequencies band is ranged between [33-37] GHz and the antenna supports a full polarimetric mode.

Urban object of interest
The urban canonical structure of interest for these indoor measurements consists of a canyon with different types of included targets.

- The canyon is composed of a two PEC (Perfect Electric Conductor) walls of 1.2 m and 1.5 m height and 2 m length. The first wall is located at a distance of 1.5 m of the antenna (see Fig.2.3),
- The used targets are:
  - A sphere to calibrate the system of radius $r = 15$ cm,
  - Two trihedral corner reflectors of different size to ensure the backscattering mechanism without changing the polarization of the incident waves,

– A 4-in-1 corner reflector which is composed by 4 trihedral corners forming a pyramid.

Scenarios setting

Three types of scenarios have been proposed to investigate the detection of NLOS targets depending on the illuminated object in the scene:

- The first object consists of a single wall (wall 1),
- The second object consists of an empty canyon,
- The third object consists of a canyon with different types of targets at different positions.

2.2.2.2 Measurements analysis

The experimental data have been analyzed using a radar range profile. The radar range profile allows to localize all the scatterers using a complex received signal $\underline{H}$ defined in Eq.4.8. It is a representation of the different responses of the scatterers according to their range positions. The methodology to extract a radar range profile from these complex signal outputs will be explained later (Subsec.4.2.5). To understand the process of generating the final outputs of the anechoic chamber used in the calculation of the radar range profile, we propose in Fig.2.4 an organigram describing the radar acquisition chain.

Radar acquisition chain

The organigram of Fig.2.4 presents the different steps leading to the received signal from its emission, its interaction with the scene elements, its reception and its processing to extract the radar range profile or the SAR image. Therefore there are 4 main blocks:

- The first bloc is the **transmission block**. The initial signal $\underline{E}_0(f)$ is multiplied by the transmitter complex antenna gain depending on the polarization, frequencies and the incidence angle (denoted $\underline{G}_T^{\theta,pol}(f)$). The obtained signal, denoted $\underline{E}_1(f)$, is defined as:

$$\underline{E}_1(f) = \underline{E}_0(f)\underline{G}_T^{\theta,pol}(f) \tag{2.15}$$

  Then, depending on the application, a radar waveform is chosen to transmit the signal. But before, a frequency modulation is usually established to the initial signal. It exists two types of radar differing by the way they transmit the signals:
  – The continuous wave radar: these radar transmit a continuous wave with a carrier frequency f_0, modulated in frequency by a sinusoid signal. The signal form can be expressed as:

$$\begin{cases} A\cos(2\pi f_0 t + \Phi(t)) \\ \frac{d\Phi(t)}{dt} = km(t) \end{cases} \tag{2.16}$$

  $m(t)$ is the initial signal to be modulated, k is a constant.

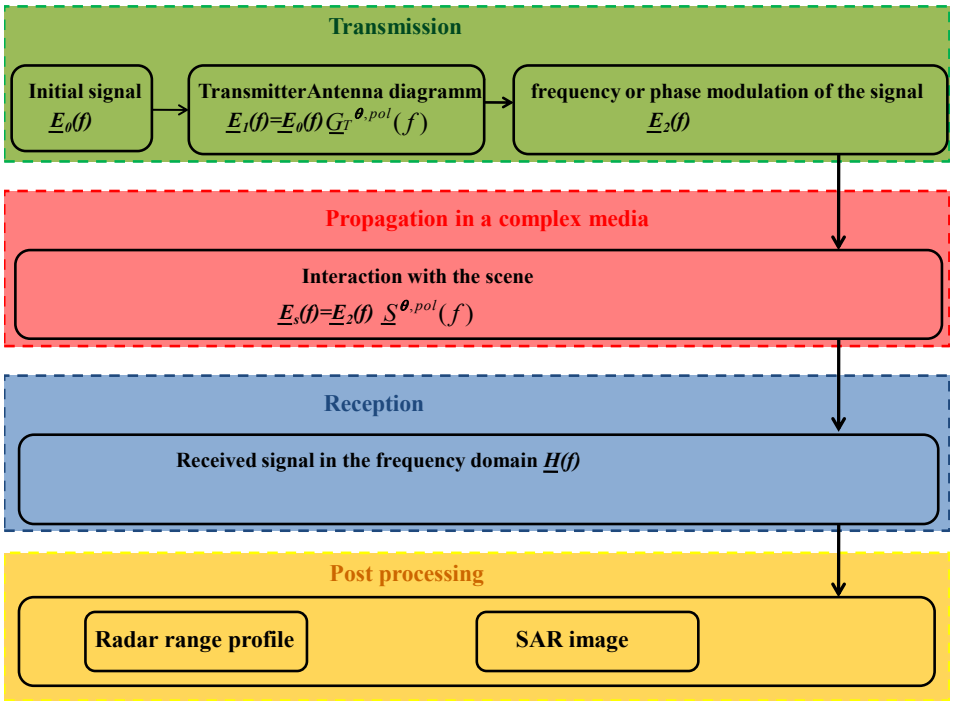

Figure 2.4: Radar acquisition chain in the anechoic chamber.

– The pulse radar are the most common radar systems including the SAR system. These radars transmit periodically pulses of duration T_x. These pulses are repeated with a frequency named PRF (Pulse Repetition Frequency), meaning that they are equally spaced by a time interval denoted T_1. The most simple waveform for pulse radar is the truncated sinusoid (not modulated in frequency). Indeed, the pulses contain sinusoid signals with a frequency f_s and an amplitude A such as:

$$\underline{E}^{sin,f_s}(t) = \begin{cases} Ae^{2j\pi f_s t} \text{ if } KT_1 < t < KT_1 + T_x,\ K \in \mathbb{N} \\ 0 \text{ else} \end{cases} \tag{2.17}$$

However, it exists various waveforms offering better performances such as the chirp waveform where the pulse has a linear modulation in frequency:

$$\underline{E}^{chirp,f_0,\Delta_f}(t) = \begin{cases} Ae^{2j\pi\left[(f_0-\frac{\Delta_f}{2})t+\frac{\Delta_f}{2T_x}t^2\right]} \text{ if } KT_1 < t < KT_1 + T_x,\ K \in \mathbb{N} \\ 0 \text{ else} \end{cases} \tag{2.18}$$

f_0 is the carrier frequency and Δ_f is the total bandwidth. Hence many modulated frequency waveforms can be defined, depending on the function $f(t, f_0, \Delta_f)$:

$$\underline{E}^{f(t,f_0,\Delta_f)}(t) = \begin{cases} Ae^{2j\pi f(t,f_0,\Delta_f)t} \text{ if } KT_1 < t < KT_1 + T_x,\ K \in \mathbb{N} \\ 0 \text{ else} \end{cases} \tag{2.19}$$

In the anechoic chamber, the used radar system is a pulse radar system with a frequency modulation. The obtained signal $\underline{E}_2(f)$ is defined as follows:

$$\begin{cases} \underline{E}_2(f) = \mathcal{F}(\underline{E}_2(t)) \\ \underline{E}_2(t) = \underline{E}_1(t)e^{2j\pi f(t,f_0,\Delta_f)t} \\ \underline{E}_1(t) = \mathcal{F}^{-1}(\underline{E}_1(f)) \end{cases} \tag{2.20}$$

$\mathcal{F}$ and $\mathcal{F}^{-1}$ are the Fourrier Transform and the Inverse Fourrier Transform, respectively.

- The second block is **the propagation block**. It describes the interactions of the emitted signal with the different elements of the scene. The resulting signal $\underline{E}_s(f)$ is defined as follows:

$$\underline{E}_s(f) = \underline{S}^{\theta,pol}(f)\underline{E}_2(f) \tag{2.21}$$

$\underline{E}_s(f)$ is the scattered signal. $\underline{S}^{\theta,pol}(f)$ is the scattering matrix describing how the scene elements impact on the electric field of the incident waves to obtain the scattered electric field.

$$\begin{bmatrix} \underline{E}_s^h(f) \\ \underline{E}_s^v(f) \end{bmatrix} = \begin{bmatrix} \underline{S}_{Hh} & \underline{S}_{Hv} \\ \underline{S}_{Vh} & \underline{S}_{Vv} \end{bmatrix} \times \begin{bmatrix} \underline{E}_2^h(f) \\ \underline{E}_2^v(f) \end{bmatrix} \tag{2.22}$$

Where
  - $\underline{E}_s^h(f)$ and $\underline{E}_s^v(f)$ are the horizontal and vertical components of the scattered electric field, respectively.
  - $\underline{E}_2^h(f)$ and $\underline{E}_2^v(f)$ are the horizontal and vertical components of the incident electric field, respectively.
- The third block is **the reception block**. The received signal is a complex matrix $\underline{H}$ containing complex reflection coefficients that each element of the matrix is defined as follows:

$$\underline{H}(f_i,\theta_i) = \underline{E}_s(f_i,\theta_i)\underline{G}_R^{\theta_i,pol}(f_i) \tag{2.23}$$

The process to obtain the matrix $\underline{H}$ is explained later in Subsec.4.2.5.
$\underline{G}_R$ is the receiver antenna pattern. f_i the i^{th} frequency of the bandwidth Δ_f and θ_i is the i^{th} incidence direction.
- The last block is **the post processing block**. The final output $\underline{H}$ is processed to extract a radar range profile or a SAR image (Subsec.4.2.5). The radar range profile can be calculated using two different methods:
  - It can be extracted directly of the spacial representation of the SAR image. It corresponds to a range line,
  - It can be calculated from the frequency representation of the measured signal.

  The experimental range profile is calculated using the second method.

In Fig.2.5, an example of an experimental range profile measured in the case of the empty canyon (extracted from [SAR 2011]). Multitude of peaks are observed due to many mechanisms occurring inside the canyon. The main conclusions drawn at the end of this experimental study are ([SAR 2011]):

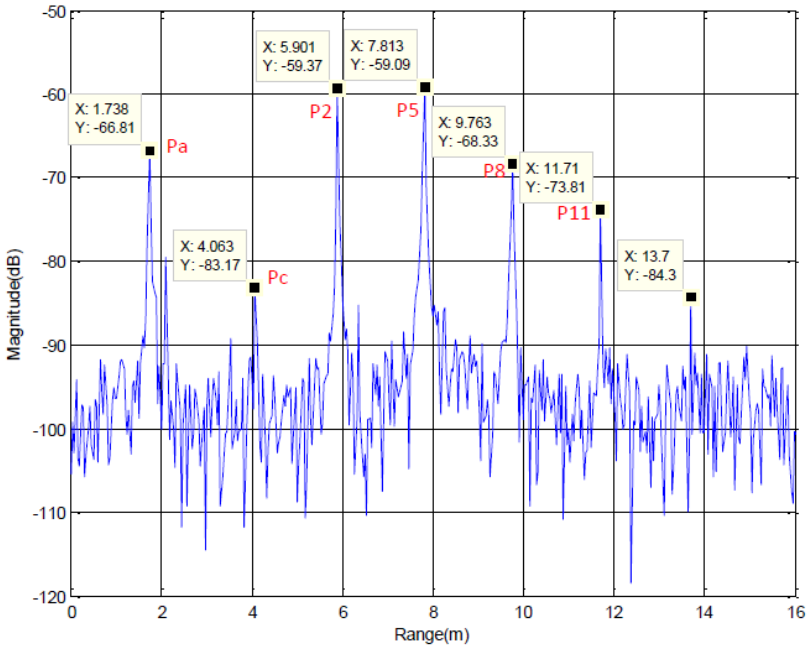

Figure 2.5: Experimental range profile extracted for an empty canyon.

- "The analysis of the different range profiles shows that the target is detectable for all the configurations provided it is located at the antenna boresight",
- "In this specific framework of NLOS target detection, the contribution of the polarimetry is not significant. Efforts should be investigated to validate the radiometric and polarimetric calibration process".

2.2.2.3 Advantages and difficulties

Advantages

The configuration of the anechoic chamber has a ratio between the dimensions and the used wavelength, that is near the real case ratio. Indeed, using the dimensions of the canyon understudy and the available frequencies band in the anechoic chamber, the ratio between the dimensions and the wavelength is preserved with respect to the real case one. In fact, if we consider a real SAR system operating at a frequency of 10 GHz (with a corresponding wavelength denoted λ_{rc}, rc for real case) where the average height of the buildings denoted d_{rc} is about 5 m, then, the ratio denoted r_{rc} will be:

$$r_{rc} = \frac{d_{rc}}{\lambda_{rc}} = \frac{5m}{0.03m} = 166.66 \tag{2.24}$$

Whereas in the anechoic chamber, if we consider the average height denoted d_{ac_1} of 1.2 m (height of the first wall of the canyon configuration of Fig.2.3) and a wavelength denoted λ_{ac_1} (ac_1 for the first anechoic chamber measurements propossal) corresponding to a center frequency of 35 GHz, the ratio denoted r_{ac_1} will be:

$$r_{ac_1} = \frac{d_{ac_1}}{\lambda_{ac_1}} = \frac{1.2m}{0.0086m} = 139.5349 \tag{2.25}$$

Even if the two ratios do not really correspond, we can assume that r_{ac_1} tends to r_{rc} so that we expect with these indoor measurements to study the main effects that occur in a real case urban canyon.

Drawbacks
Despite the fact that the ratio between the dimensions and the used wavelength is preserved for the canyon of the anechoic chamber, the condition of far field is no more respected. Consequently, the effects of near field appear in the anechoic chamber data outputs due to the angular variation in incidence. Therefore, to perform an accurate study of the canyon in near field, the antenna pattern must be carefully taken into account. Moreover, as the operating wavelength is too small, the positioning of the targets and the walls of the canyon must be very precise.

2.2.3 Outdoor measurements

2.2.3.1 General description

A second data set to investigate the NLOS phenomena at Ka-band concerns some outdoor data acquired during a measurement campaign. A part of these data will be analyzed in the last chapter of this thesis. Indeed, a measurement campaign has been realized during spring 2011, involving the ONERA BUSARD motor glider platform equipped with the DRIVE radar.

Six measurements flights have been done over urban and commercial areas, with two different incidence angles configurations. Ka-band SAR images have been generated and are available for studies and analysis.

Radar geometry configuration
Two flights have been conducted using two different incidences angles. In Tab.2.1, the radar parameters corresponding to each flight are summarized, where:

- The swaths refer to the on-ground swaths,
- The off-track distance is the distance from nadir to swath centre,
- The used frequencies band is ranged between [33-37]GHz,
- The radar antenna supports a single polarization mode (Vv).

Table 2.1: Radar geometry parameters for the two flights of the outdoor measurements campaign corresponding to two different incidence angles.

Incidence (deg)	Depression (deg)	Altitude[ft]	Range(m)	Off-track[m]	Swath[m]
45	45	2000	860	600	620
60	30	1400	850	740	950

Areas of interest
In the frame of this campaign dedicated to the characterization of urban signatures, flights were performed over urban and commercial areas. For the measurement flights, different urban areas in the vicinity of Salon de Provence were selected:

- Some in the northern part of the city (Fig.2.6),
- Main building of Air Force Base area (Fig.2.7),

- Commercial area at about 10 km west from Salon de Provence (Fig.2.8).

Figure 2.6: Zoom over the urban area.

Figure 2.7: Main building of Air Force Base area.

Scenarios setting

Among the sets of data, two configurations have been studied in particular involving different types of targets. They are illustrated in Fig.2.9 and are described as follows:

- The first scene is defined with a target facing a single wall (the wall of the Air Force Base) of 16 m high. The target can be a corner reflector, a car or a van (see the left part of Fig.2.9),
- The second scene involves the same targets located inside a canyon of 35 m width formed by two buildings, the first one is used as a reflector and the

Figure 2.8: Zoom over the commercial area.

second one is used as a mask (see the right part of Fig.2.9). This canyon is located in the commercial area and delimited with a red rectangle, in Fig.2.8.

2.2.3.2 Measurements analysis

For each of the two scenes of study, the delivered SAR images were analyzed and the feasibility of detecting the NLOS responses of the targets has been investigated using an additional theoretical study to compute the expected target location. Referring to the first scene of interest, the NLOS response of the corner reflector is expected to be observed in the shadow area behind the building of the Air Force Base. This is confirmed in the corresponding SAR image illustrated in Fig.2.10. The urban structure of interest is located inside the red rectangle and the target is detectable by a brilliant point synthesized in the shadow area. The analysis of the InSAR data corresponding to the second scene of study will be presented in the last chapter of this thesis as an example of application of our in-house developed EM code to interpret real SAR data.

The main conclusions drawn at the end of this campaign are summarized as follows [Nouvel 2011]:

- "The feasibility of NLOS target detection was largely confirmed considering the overall analysed radar dataset",
- "Through the analysis of the SAR images, the NLOS response corresponding to a reflection mechanism on the metallic surfaces is more distinguishable than the NLOS response corresponding to a reflection mechanism on the concrete surfaces",
- "The NLOS signature may be more or less spread in azimuth, depending on the geometry and on the shape of the reflecting wall",
- "NLOS phenomenon has been tested with a large variety of targets, with different RCS ranging from 6 to 37dBm^2. Results indicated that the corresponding NLOS RCS are higher at 45° than at 60° incident angle whatever

Figure 2.9: (Left) First scene of study: an example of a corner reflector (in red circle) facing the reflector wall of the Air Force Base. (Right) Second scene of study: three corner reflectors and a vehicle (in red circle) are located inside the canyon of interest in the commercial area.

Figure 2.10: SAR image of the first scene of study corresponding to a corner located in front of the building of the Air Force Base. Zoom on the area of interest (red rectangle).

is the type of target."

2.2.3.3 Advantages and difficulties

Advantages
This measurement campaign allowed to highlight the feasibility of detecting NLOS targets in SAR images using different kind of targets in different urban structures (single wall or a canyon) involving different materials. This variety of urban scenarios enables to study the impact of different parameters on the targets detection. For example, the dependance of the RCS value of the targets on the materials of the reflective wall, its nature (smooth surface or corrugated) and on the incidence angle has been pointed out. Our study won't focus on these aspects, nevertheless, they have been partly investigated in the last chapter of the thesis, where the impact of the building materials on the interferometric signature is highlighted.

Drawbacks
Some drawbacks related to this measurements campaign have to be noticed. The first disadvantage is related to the technical constraints of every airborne system such as: the platform susceptibility to wind and the narrow azimuth beamwidth.. Moreover, there is a lack of an exact knowledge of the dimensions of the scenes under study which is an important condition to investigate all the occurring effects. In addition, the use of such high frequencies (Ka-band) makes the system sensitive to small details in the scene leading to a difficult interpretation of all the EM effects observed in the images. From a polarimetric point of view, the use of a single polarization prevents the investigation of a complete polarimetric study that can help in the interpretation of the different interactions occurring.

2.3 New measurements

2.3.1 General description

The second study performed to investigate the NLOS target detection inside urban canyon using indoor measurements has been carried out in June 2012 in the frame of this thesis. These measurements have been conducted in the anechoic chamber BABI of ONERA in order to gain knowledge about the EM phenomenology of propagation inside a canyon in the case of far field. In chapter 4, we will give a detailed description of these measurements. In fact, our EM scattering study concerning the multipath propagation inside an urban canyon for a controlled environment with a d/λ ratio different from the real one will be based on the outputs of these measurements, therefore, a detailed description is required.

Scene geometry
The goal of the experiment is to study the propagation inside a PEC scaled canyon in the case of far field. The measurement setup and the canyon configuration are illustrated in Fig.2.11.

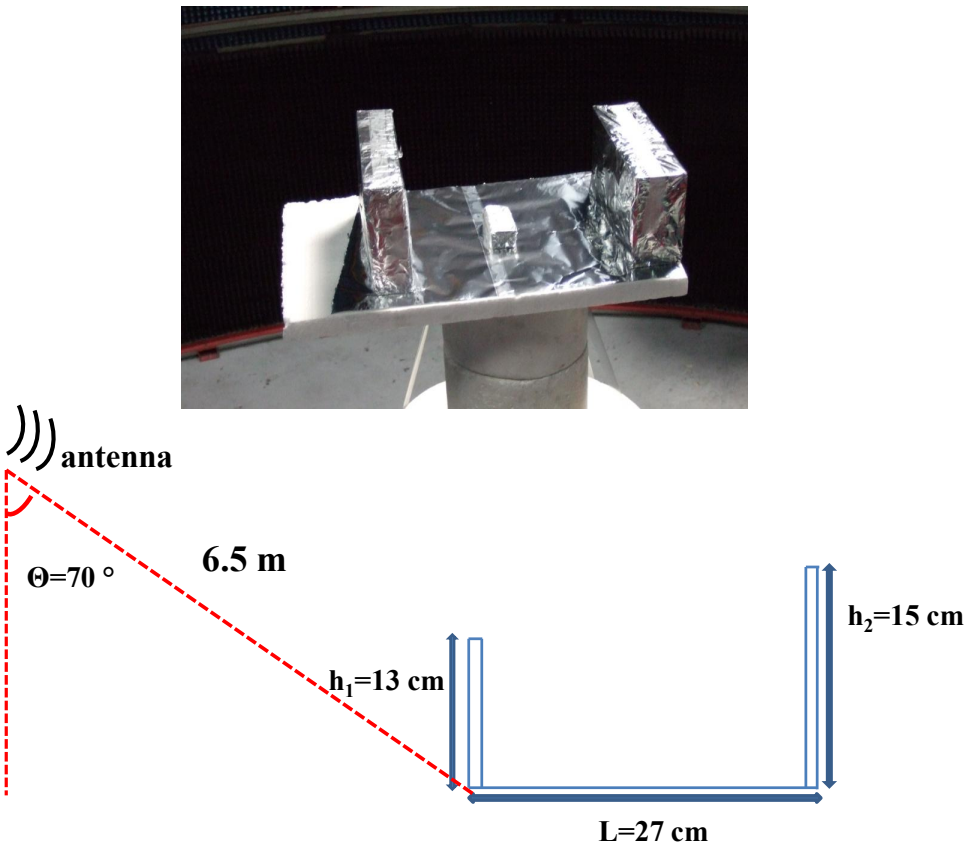

Figure 2.11: Measurement setup in the anechoic chamber BABI of ONERA. The canyon and the target (a parallelepiped) are covered with aluminium to ensure the PEC case. The canyon dimensions, the antenna location and the used frequencies ensure the case of far field.

Radar parameters
The used antenna is a horn antenna. The incidence angle is 70°. The frequency band is ranged between [6-18]GHz and the antenna supports a full polarimetric mode.

Urban object of interest
The urban canonical structure of interest for these indoor measurements consists of a canyon with different types of included targets:

- The canyon is composed of two PEC walls of 13 cm and 15 cm height and 22 cm length,
- The used targets are:
  - A toy modelling a car,
  - A parallelepiped target covered with aluminium.

Scenarios setting
As for the first indoor measurements, different types of scenarios have been proposed depending on the illuminated scene:

- The first scene consists of a single wall,
- The second scene consists of an empty canyon with parallel walls,
- The third scene is an empty canyon where the parallelism of the walls is no more preserved (the second wall is tilted of 1°),
- The fourth scene consists of a canyon with different types of included targets at different positions.

2.3.2 Measurements analysis

The experimental data have been analyzed using both SAR images and radar range profiles. Fig.2.12 shows an example of an experimental range profile and a SAR image for an empty canyon. The main conclusions drawn at the end of this study that will be presented in more details in the next part of the thesis are:

- In the anechoic chamber, it is not possible to ensure in the same time the case of far field and a ratio between the dimensions and the wavelength that tends to the real one. Consequently, additional scattering effects appear,
- The target is detected with a low amplitude.

2.3.3 Advantages and difficulties

2.3.3.1 Advantages

- The analysis of the anechoic chamber data allows to gain knowledge about the EM scattering inside the canyon in the anechoic chamber where the d/λ ratio is different from the real one,
- Based on these experimental data, a bechmarking between EM codes and a validation of a reliable EM tool have been investigated.

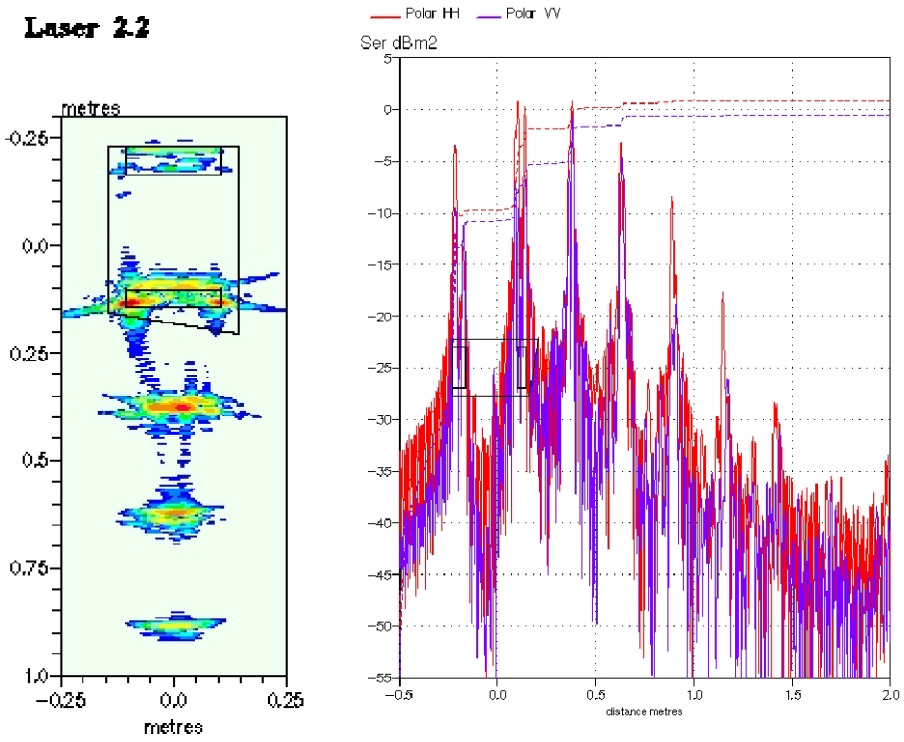

Figure 2.12: (Left) SAR image corresponding to an empty canyon. (Right) Experimental range profile calculated for an empty canyon.

2.3.3.2 Drawbacks

To ensure the case of far field with the best range resolution, a very low ratio between the dimensions and the wavelength is obtained. In fact, if we consider an average height denoted d_{ac_2} (ac_2 for the second anechoic chamber measurements proposal) of 10 cm and a wavelength denoted λ_{ac_2} corresponding to a center frequency of 12 GHz, the ratio denoted r_{ac_2} will be:

$$r_{ac_2} = \frac{d_{ac_2}}{\lambda_{ac_2}} = \frac{10cm}{2.5cm} = 4 \tag{2.26}$$

As we can notice, the obtained ratio is different from the real one (r_{rc} equal to 166.66 defined in Eq.2.24). Unless using a very high operating frequency which is technically not achievable, the real ratio can never be ensured in the anechoic chamber. Therefore, the EM effects occurring inside a canyon for real case configurations can never be analyzed using indoor data. In addition, the used low frequencies with respect to the canyon dimensions induced an angular variation in diffusion that leads to a complex scattering environment inside a simple canonical structure (presented in details in chapter 4). These effects are difficult to predict without using EM tools based on exact methods to calculate the EM scattered field.

2.4 Conclusion

This chapter is a general presentation of the different data that have been acquired before and during this work, to investigate the detection of NLOS targets inside urban canyons for both a controlled and real case environments. The reference data consist of two data sets of indoor and outdoor measurements on urban canyon configurations in addition to theoretical formulas of the RCS of typical targets to validate the amplitude of the different retrieved responses. All these data served at first to explain the EM phenomenology of propagation inside a controlled environment as well as for an outdoor environment and to validate a commercial EM tool in order to study further real cases. The main constraint to ideally fulfill in the case of indoor measurements is to preserve the ratio of real case between the dimensions and the wavelength in order to reproduce the outdoor main effects. This constraint has been fulfilled for the first indoor measurements, however, the far field condition of real case has not been ensured. To overcome this difficulty, we proposed new indoor measurements, reducing the dimensions of the canyon and setting a distance between the antenna and the canyon so that the far field condition is respected. Nevertheless, the ratio between the dimensions and the wavelength could not be respected due to the technical limitations of the anechoic chamber to achieve high frequencies. Therefore, the main conclusion is that ensuring a real case ratio between the dimensions and the wavelength and at the same time fulfill the condition of far field is not possible in the anechoic chamber. Nevertheless, these indoor data have been used to understand the EM phenomenology of propagation and to validate the results of some EM commercial codes. The results of this analysis is provided in the second part of the thesis. Concerning the outdoor data that we had at our disposal, the far field condition is ensured so that there is no angular variation in incidence. Hence, the complexity of the EM scattering is reduced. However, the lack of an exact knowledge of the ground truth (geometry and materials of the urban scene) in addition to the use of high frequency that is sensitive to small details in the scene can make the interpretation of the corresponding SAR images difficult. A deep analysis of these outdoor interferometric data are proposed in the last chapter of this thesis.

Summary

The first part of the thesis was a general introduction to the main topic. We stated in the first chapter the problematic and proposed a methodology to follow to investigate the NLOS target detection inside urban canyons. The second chapter presented the reference data at our disposal that helped to derive the urban EM phenomenology of propagation, then to validate the EM tools and finally to test the performance of our proposed in-house tool. After a deep study of the state-of-art works dealing with our topic, we concluded that even if current works achieved satisfying results in detecting NLOS static and moving targets or in developing high-performance SAR simulators of very detailed urban scenes, the validation process has not been completed. Indeed, according to the literature, even if the main SAR geometric effects have been successfully retrieved, their amplitude has never been validated. In this specific framework, the amplitude is a crucial parameter to investigate the detectability of the target. Based on this ascertainment, we decided to focus our work essentially on developing a validated tool to detect NLOS targets inside urban canyons. Our main contribution compared to the state-of-art is the achievement of a full validation process for some commercial tools, but also for a simple developed EM tool dedicated to NLOS targets detection.

As mentioned before, our approach is to understand the EM phenomenology of propagation inside urban canyons before developing the EM tool. For this reason, reference data are required for the first phase of analysis of the EM scattering effects before providing an explanation based on a theoretical study. The data at our disposal consist of some indoor and outdoor SAR data as well as theoretical references to calibrate the measurements and to validate the accuracy of any EM tool to correctly simulate the amplitude. Outdoor data have been used to test the validity of our tool to interpret InSAR data whereas indoor data have been used at the beginning of this study to gain knowledge about the EM phenomenology of propagation for two canyon configurations with two different ratios between the dimensions of the object of interest and the used wavelength. The main conclusion is that a canyon configuration ensuring both a real case ratio and the condition of far field would not be possible in the anechoic chamber. Therefore, the expected EM effects occurring in real case can never be investigated in a controlled environment. Thus, the need of validated EM tools to simulate canyon configurations with a real case ratio.

The next part of this thesis will be a presentation of the different EM commercial tools used to simulate the configuration of the anechoic chamber BABI where the condition of far field has been respected, but the ratio between the dimensions of the object of interest and the wavelength is different from the real case ratio. The simulations results as well as the EM knowledge acquired through the different tests will be also presented. A benchmarcking between EM tools have been carried out to select the EM tools that correctly simulate the experimental results both in terms of phase and amplitude. Even if at the end, two EM tools have been selected and validated, we decided to present the advantages of the non retained tools as well as the drawbacks, for three reasons. The first reason is that some

coming works may use an EM tool for a specific goal that does not require a full validation process, so that some of the summarized capabilities may be useful for their specific application. The second reason is that the review we made concerning the difficulties encountered for the validation of an EM tool may be useful for any user aiming to test this tool as it allows him to gain time. The third reason is that the simulation results of all the tested codes were not available when writing this manuscript.

Part II

EM codes benchmarking and analysis

Chapter 3

EM codes presentation

Contents

3.1 Introduction

This chapter is an overview of the EM commercial tools used to simulate the canyon configuration of the anechoic chamber BABI (described in Sec.2.3). The goal of this benchmarking is to select the EM tools that are able to correctly simulate the EM phenomenology of scattering inside this controlled environment both in terms of phase and amplitude. These EM tools, once validated, will be used to model the scattering at higher frequencies ensuring a d/λ ratio tending to the real one, so that we can study the EM phenomenology of propagation in real case and build consequently our dedicated EM tool based on these simulation results. Four EM tools have been used, nevertheless, only two of them have been retained. The first one that has been rejected is MOCEM as it has a limited number of interactions so that it can not model the scattering of a rich multipath propagation environment (as for the urban canyon). For the second rejected EM tool Wireless Insite, we encountered some difficulties in the validation process. Concerning the

selected EM tools, we present the EM methods implemented that may explain some characteristics of the corresponding simulations such as the calculation time (presented in the next chapter).

This overview will be useful for users who aim to perform EM simulations on urban canyons as they have now an idea about the capabilities and limitations of each tool.

This chapter is organized as follows: it contains four sections describing the EM tools. In each section, we give a general description of the EM tool, the different tests performed and for the non selected EM tools, the difficulties we encountered in the validation process. We end up this chapter by a conclusion.

3.2 Wireless Insite

3.2.1 General description

Wireless InSite (WI) is an EM tool composed by ray-tracing models and EM solvers for the analysis of radio propagation and wireless communication environments. The software provides predictions of propagation and communication channel characteristics in complex urban indoor, rural and mixed path environments. Applications range from military defense to commercial communications:

- Wireless communication links,
- Antenna orientation and coverage,
- Interference from multiple transmitters.

Even if WI is a tool that takes into account the multipath propagation, it has been initially designed for the telecommunication environment and not for the radar. This may explain the difficulties encountered thereafter.

3.2.2 Radar acquisition chain

Similarly to the radar acquisition chain built for the measurements in Fig.2.4, we present in Fig.3.1 the WI radar acquisition chain.

3.2.3 Tests with WI

WI has been tested on two canonical objects of validation: the trihedral corner reflector and the plate. Nevertheless, even if the phase is correct, the simulated amplitude used to calculate the RCS parameter has not been validated. This is due to two main difficulties:

- The definition of the waveform,
- The extraction of the radar range profile from the proposed outputs.

3.2.3.1 Difficulty 1: waveform definition

Depending on the domain, time or frequency, the used techniques to define the waveform are different.

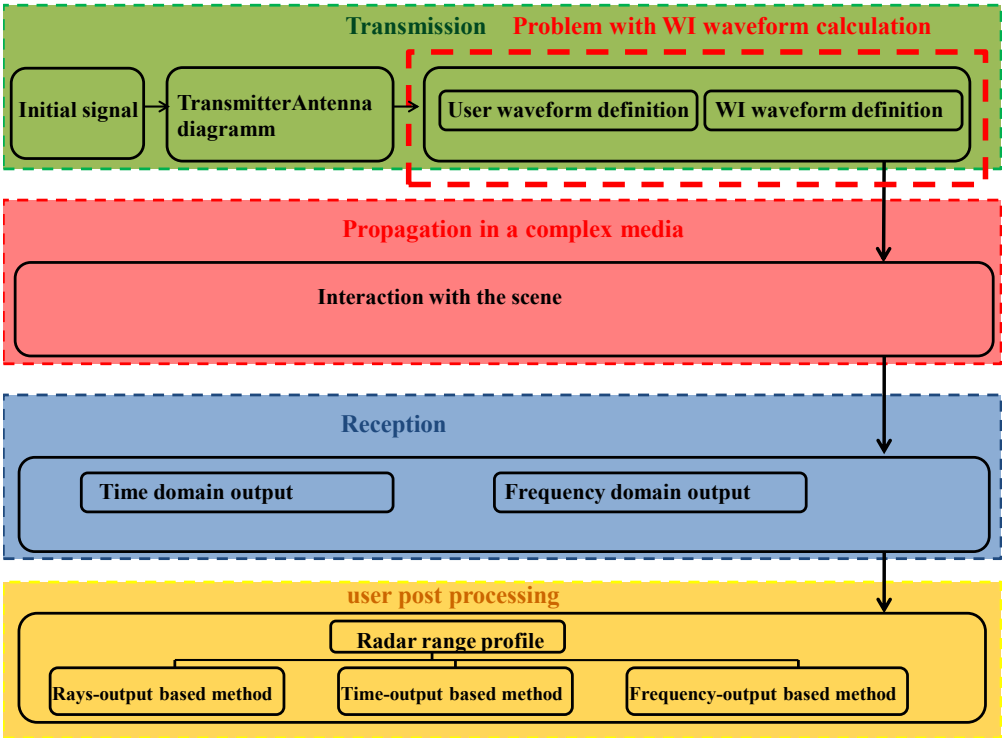

Figure 3.1: Radar acquisition chain in WI.

Waveform definition in the time domain

Let us take the example of the chirp definition in the time domain with a linear modulation in frequency defined in Eq.2.18. The parameters that have to be defined are the amplitude A, the carrier frequency f_0, the total bandwidth Δ_f and the pulse duration T_x. In WI, the user defines:

- T_x: the pulse duration,
- f_i: the initial frequency of the bandwidth,
- f_f: the final frequency of the bandwidth,
- $P_e = A^2$ the power of the emitted signal.

The total bandwidth is defined by $\Delta_f = |f_f - f_i|$ and f_0 is the center frequency of Δ_f.

From these input parameters, WI deduces the following parameters:

- The period of the waveform defined by $T_{per} = \frac{1}{f_f}$,
- The time step $d_t = \frac{T_{per}}{20}$,
- The number of temporal samples is given by this proposed formula:

$$N_t = \left\lfloor \frac{T_x}{d_t} \right\rfloor + 1 + 30 \tag{3.1}$$

The oversampling by a factor of 20 of the time step, as well as the 30 additional time samples are set in WI, so that the user can not modify them. Once the waveform defined in the time domain, WI calculates the waveform in the frequency domain by applying a Fourrier Transform. WI defines a number of frequency samples N_f

as follows:

$$N_f = 2^{N_t} + 16 \tag{3.2}$$

Then, WI calculates the cut-off frequencies to determine for which frequencies range the signal is representative. The carrier frequency is usually calculated as the frequency corresponding to the average energy of the signal (see the frequency denoted f_0 in Fig.3.2 corresponding to the spectrum of the chirp signal linearly modulated in frequency). For WI, this criterion is not applied. It takes as the carrier frequency, the frequency corresponding to the maximum amplitude of the signal energy (see the frequency denoted $f_{0(WI)}$ in Fig.3.2), which is for wide band signals not convenient, as it selects the maximum at the first oscillation of the spectrum. The calculation of the total bandwidth, where the signal is representative, depends on the carrier frequency, so that the surrounding frequencies achieve 99 % of the total energy. Obviously, in WI, as the calculation of the carrier frequency is "shifted" from the usually defined carrier frequency, the resulting bandwidth (denoted $\Delta_{f(WI)}$ in Fig.3.2) is larger than the usually defined one (denoted Δ_f in Fig.3.2). Hence, the obtained signal is different from the initial one we aimed to model.

In summary, performing simulations with a wide band signal using the chirp definition of WI turns out in practice, to carry out calculations with a huge number of points, partly due to an incorrect estimation of the wide band signal parameters.

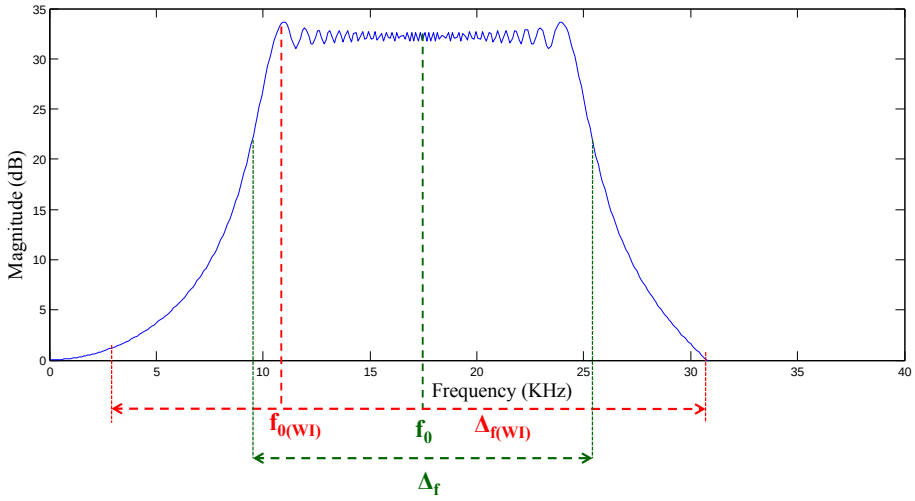

Figure 3.2: Spectrum of the chirp signal linearly modulated in frequency. f_0 and Δ_f are the carrier frequency and the total bandwidth defined with the usual method. $f_{0(WI)}$ and $\Delta_{f(WI)}$ are the carrier frequency and the total bandwidth defined with WI.

Waveform definition in the frequency domain

The user defines the number of frequency samples and the corresponding complex signal of the waveform. However, WI has its own definition to transform this signal in the time domain before generating this waveform in the frequency domain. In fact, WI does not use the user defined parameters to build directly the waveform

in the frequency domain, but, adds un intermediate step to transform the signal in the time domain by an Inverse Fourrier Transform before recalculating it in the frequency domain by Fourrier Transform. To illustrate more in details this operation, we propose in Fig.3.3 an organigramm for an example of a chirp waveform calculation in the frequency domain. The user defined signal is calculated on 801 frequency samples corresponding to a waveform with the following parameters:

$$\begin{cases} f_i = 33 \text{ GHz} \\ f_f = 37 \text{ GHz} \\ f_0 = 35 \text{ GHz} \\ T_x = 10^{-8} s \end{cases} \tag{3.3}$$

WI applies an an Inverse Fourrier Transform to obtain a time domain signal. The number of calculated time samples is $N_t = 4095$. Then, a Fourrier Transform is applied to obtain the new calculated signal in the frequency domain. The obtained parameters corresponding to the new calculated signal are:

$$\begin{cases} N_f = N_t = 4095 \\ f_i = 32,5 \text{ GHz} \\ f_f = 39,4 \text{ GHz} \\ f_0 = 31,76 \text{ GHz} \end{cases} \tag{3.4}$$

As we can notice, the final generated signal in the frequency domain is obtained using a different carrier frequency and bandwidth. Hence, the resulting signal is different from the initial one defined by the user.

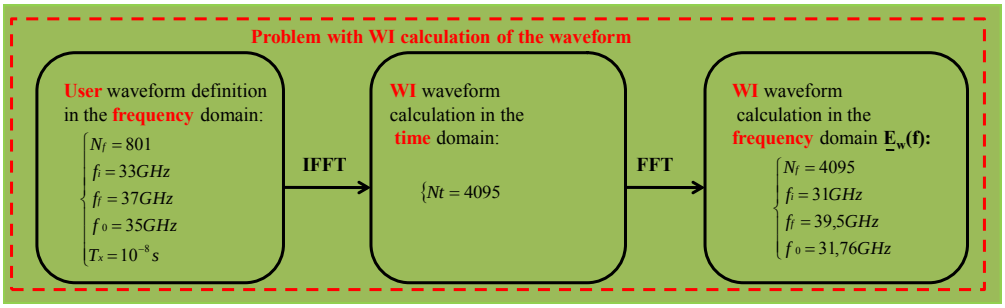

Figure 3.3: Organigramm presenting an example of the final waveform parameters calculated by WI from a user defined signal in the frequency domain.

3.2.3.2 Difficulty 2: Range profile extraction

To extract the range profile, we propose three methods differing from the outputs used in the calculation.

Time-output based method

The output is the complex received electric field $\underline{E}(t)$. The range profile is obtained by plotting the magnitude of $\underline{E}(t)$ expressed by 20 $log_{10}(|\underline{E}(t)|)$ according to the distance $d = c \times t$ where c is the speed of the light.

Rays-output based method

With WI, we have access to the complex electric field $\underline{E}_k$ associated to each ray k, whose path length is d_k. The power P_k associated to each of these rays is also available. To each distance d_k is associated the corresponding time $t_k = \frac{d_k}{c}$. Depending on the used parameters ($\underline{E}_k$ or P_k) to calculate the radar range profile, we will apply this formula:

$$\begin{cases} \mathcal{F}^{-1}(\underline{E}(f)) \\ \underline{E}(f_i) = \sum_{k=1}^{N_R} \frac{|}{\underline{E}_k|} N_R \exp(-j2\pi t_k f_i) \end{cases} \tag{3.5}$$

where N_R the number of rays going back to the radar and N_f is the number of frequency samples. This calculation implicitly assumes that the amplitude associated to each ray is constant regardless of the frequency within the used band of the signal.

In the following, we will present the methods used to calculate $|\underline{E}_k|$ from the available outputs.

- Method using the power of each ray
  In order to extract the radar range profile, we can calculate the amplitude $|\underline{E}_k|$ by applying the square root of the power P_k corresponding to each ray. We use the following formula in WI's user guide:

$$P_k = \frac{\lambda^2 \beta}{8\pi\eta_0} |\underline{E}_{\theta_k} \underline{g}_{\theta_k} + \underline{E}_{\phi_k} \underline{g}_{\phi_k}|^2 \tag{3.6}$$

  Where:
  - $\underline{E}_{\theta_k}$, $\underline{E}_{\phi_k}$ are the complex theta and phi components of the electric field of the k^{th} ray at the receiver point,
  - $\underline{g}_{\theta_k}$, $\underline{g}_{\phi_k}$ are the complex theta and phi components of the receiving antenna gain.

  The factor $\frac{\lambda^2\beta}{8\pi\eta_0}$ comes from the consideration of the gain of the receiving antenna. Supposing for example that we aim to calculate the power received by an antenna of gain G from an electric field defined as $\overrightarrow{\underline{E}} = \overrightarrow{\underline{E}_0} \cos wt$, thus the following formula can be applied:

$$\overrightarrow{\underline{P}} = | < \overrightarrow{\underline{S}} > |A \tag{3.7}$$

  where:
  - A is the antenna effective area such as:

$$A = \frac{\lambda^2 G}{4\pi} \tag{3.8}$$

  - $< \overrightarrow{\underline{S}} >$ is the time average Poynting vector defined as:

$$< \overrightarrow{\underline{S}} >= \frac{< \overrightarrow{\underline{E}} \wedge \overrightarrow{\underline{B}} >}{\mu_0} = \frac{< \overrightarrow{\underline{E}^2} >}{c\mu_0} \overrightarrow{u} = \frac{{\underline{E}_0}^2}{2c\mu_0} \overrightarrow{u} = \frac{{\underline{E}_0}^2}{2\eta_0} \overrightarrow{u} \tag{3.9}$$

    where $\overrightarrow{u}$ is the the direction of propagation of the wave.

Hence:

$$P = |\overrightarrow{\underline{P}}| = \frac{\lambda^2}{8\pi\eta_0} G {E_0}^2 \tag{3.10}$$

The β factor is added to take into account the dispersive effects of the waveform. The way it is determined is not indicated. Therefore, referring to Eq.3.10 (by replacing E_0 by $|\underline{E}_k|$ and P by P_k), the amplitude of the complex electric field $|\underline{E}_k|$ associated to each ray k of power P_k will be:

$$|\underline{E}_k| = \sqrt{\frac{P_k}{\frac{\lambda^2 \beta G}{8\pi\eta_0}}} = \sqrt{\frac{8\pi\eta_0}{\lambda^2\beta G}}\sqrt{P_k} \tag{3.11}$$

To extract the range profile, the formula in Eq.3.5 is applied with a new definition of $|E_k|$:

$$\begin{cases} \mathcal{F}^{-1}(\underline{E}(f)) \\ \underline{E}(f_i) = \sum_{k=1}^{N_R} \sqrt{\frac{8\pi\eta_0}{\lambda^2\beta G}} \frac{\sqrt{P_k}}{N_R} \exp(-j2\pi t_k f_i) \end{cases} \tag{3.12}$$

- Method using the amplitude of each ray
  We have to point out a problem encountered with WI in the way it calculates the amplitude of $\underline{E}_k$. Indeed, considering the complex components $\underline{E}_{\theta_k}$ and $\underline{E}_{\Phi_k}$ in the orthonormal coordinate system ($\overrightarrow{e_\theta}$,$\overrightarrow{e_\Phi}$), then $\overrightarrow{E_k}$, the electric field at the receiver point, can be defined as:

$$\overrightarrow{\underline{E}_k} = |\underline{E}_{\theta_k}| e^{j\varphi_{\theta_k}} \overrightarrow{e_\theta} + |\underline{E}_{\Phi_k}| e^{j\varphi_{\Phi_k}} \overrightarrow{e_\Phi} \tag{3.13}$$

Thus:

$$\begin{aligned} |\overrightarrow{\underline{E}_k}|^2 &= (|\underline{E}_{\theta_k}| e^{j\varphi_{\theta_k}} + |\underline{E}_{\Phi_k}| e^{j\varphi_{\Phi_k}})(|\underline{E}_{\theta_k}| e^{j\varphi_{\theta_k}} + |\underline{E}_{\Phi_k}| e^{j\varphi_{\Phi_k}})^* && (3.14)\\ &= (|\underline{E}_{\theta_k}| e^{j\varphi_{\theta_k}} + |\underline{E}_{\Phi_k}| e^{j\varphi_{\Phi_k}})(|\underline{E}_{\theta_k}| e^{-j\varphi_{\theta_k}} + |\underline{E}_{\Phi_k}| e^{-j\varphi_{\Phi_k}}) && (3.15)\\ &= |\underline{E}_{\theta_k}|^2 + |\underline{E}_{\theta_k}||\underline{E}_{\Phi_k}| e^{j(\varphi_{\theta_k} - \varphi_{\Phi_k})} + |\underline{E}_{\Phi_k}||\underline{E}_{\theta_k}| e^{j(\varphi_{\Phi_k} - \varphi_{\theta_k})} && (3.16)\\ &\quad + |\underline{E}_{\Phi_k}|^2 && (3.17) \end{aligned}$$

If the two components of the electric field $\underline{E}_{\theta_k}$ and $\underline{E}_{\Phi_k}$ are in phase then the Eq.3.17 will be:

$$|\overrightarrow{\underline{E}_k}|^2 = |\underline{E}_{\theta_k}|^2 + |\underline{E}_{\Phi_k}|^2 \tag{3.18}$$

In the outputs generated by WI, we have only access to the the magnitude of the complex components of the electric field ($|\underline{E}_{\theta_k}|$, $|\underline{E}_{\Phi_k}|$), the phase of these components do not exist. This problem has been pointed out to WI developers and they explained that the components of the electric fields are in phase, so that there is no need for the phase information. It is clear in this context that the effects of phase between polarizations is not taken into account in this model. Using the Eq.3.18, the radar range profile is calculated as follows:

$$\begin{cases} \mathcal{F}^{-1}(\underline{E}(f)) \\ \underline{E}(f_i) = \sum_{k=1}^{N_R} \frac{\sqrt{|\underline{E}_{\theta_k}|^2 + |\underline{E}_{\phi_k}|^2}}{N_R} \exp(-j2\pi t_k f_i) \end{cases} \tag{3.19}$$

Frequency-output based method

This method is used in the case when the user defines its own waveform in the frequency domain. For each of the defined frequencies, WI generates three complex outputs $\underline{E}_x(f)$, $\underline{E}_y(f)$ and $\underline{E}_z(f)$. For example, if the user defines a waveform of $N_f = 801$ frequency samples, then 801 samples corresponding to the magnitude and phase of $\underline{E}_x(f)$, $\underline{E}_y(f)$, $\underline{E}_z(f)$ denoted $(|\underline{E}_x(f)|/\varphi_{E_x}, |\underline{E}_y(f)|/\varphi_{E_y}, |\underline{E}_z(f)|/\varphi_{\underline{E}_z})$ are generated as outputs. $\underline{E}_x(f)$, $\underline{E}_y(f)$ and $\underline{E}_z(f)$ are then calculated using this formula:

$$\underline{E}_x(f) = |\underline{E}_x(f)| \exp\left(j\varphi_{\underline{E}_x}\right) \tag{3.20}$$

$\underline{E}_x(f)$, $\underline{E}_y(f)$ and $\underline{E}_z(f)$ are transformed in the spherical coordinates: $\underline{E}_\theta(f)$ corresponds to the polarization V and $\underline{E}_\phi(f)$ to the polarization H. In Fig.3.4, an illustration of the spherical coordinate system in WI. The complex electric field

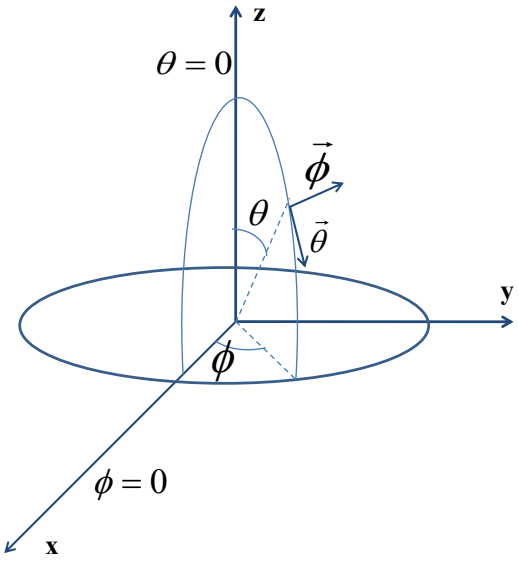

Figure 3.4: The Wireless InSite spherical coordinate system.

components in the spherical domain are deduced from the cartesian complex components using the matrix transform in the following equation:

$$\begin{bmatrix} \underline{E}_r(f) \\ \underline{E}_\theta(f) \\ \underline{E}_\phi(f) \end{bmatrix} = \begin{bmatrix} \sin(\theta_A)\cos(\phi_A) & \sin(\theta_A)\sin(\phi_A) & \cos(\theta_A) \\ \cos(\theta_A)\cos(\phi_A) & \cos(\theta_A)\sin(\phi_A) & -\sin(\theta_A) \\ -\sin(\phi_A) & \cos(\phi_A) & 0 \end{bmatrix} \times \begin{bmatrix} \underline{E}_x(f) \\ \underline{E}_y(f) \\ \underline{E}_z(f) \end{bmatrix} \tag{3.21}$$

where (θ_A, ϕ_A) is the direction from which the ray arrives at the receiver.

The following step is an operation of adaptive filtering that consists in multiplying the theta component of the received electric field in the frequency domain $\underline{E}_\theta(f)$ by the conjugate spectrum of the defined waveform denoted by $\underline{E}_2^{WI^*}(f)$. The range profile is calculated using this formula:

$$\mathcal{F}^{-1}(\underline{E}(f)\underline{E}_2^{WI^*}(f)) \tag{3.22}$$

In this calculation, it is still the power level contained in the frequency description of the waveform that we don't control yet. In Fig.3.5, the organigramm illustrating

the radar acquisition chain in WI when using a frequency-output based method to extract the radar range profile.

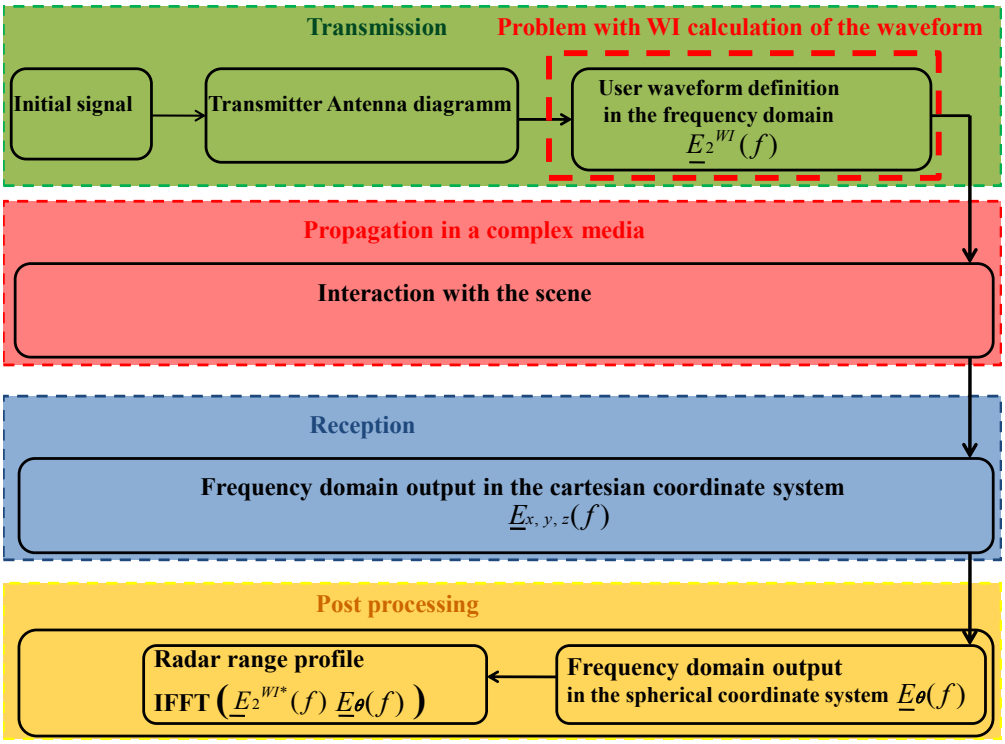

Figure 3.5: Radar acquisition chain in WI when using a frequency-output based method to extract the radar range profile. The waveform is recalculated in the frequency domain based on the user defined waveform to obtain $\underline{E}_2^{WI^*}(f)$ (The dashed red rectangle corresponds to the sub-organigramm in Fig.3.3).

Radiometric calibration

To understand the influence of each parameter of simulation on the power levels of the different outputs, we conducted several tests on a target (4-in-1 corner reflector), changing various input parameters, such as the transmitted power, the antenna gain, etc..

We recall the radar equation from which the RCS σ of the target can be calculated at long distance, for the monostatic case:

$$P_R = \frac{P_E G_E G_R \lambda^2}{(4\pi)^3 R^4} \sigma \tag{3.23}$$

where:

- P_E, P_R are the emitted and received power respectively,
- G_E, G_R are the antenna gains of the transmitter and receiver respectively,
- λ is the wavelength,
- R is the distance between the antenna and the target.

In Fig.3.6, an example of the parameters used to calculate the RCS of a trihedral corner reflector for the monostatic case. To obtain the maximum value of RCS,

the trihedral is oriented so that its symmetry axe corresponds to the antenna beam direction.

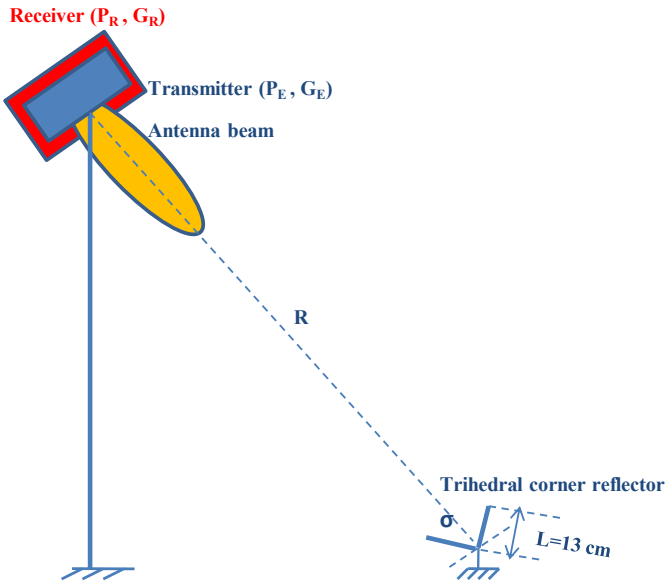

Figure 3.6: Parameters used to calculate the RCS σ of a trihedral corner reflector in the monostatic case. The transmitter antenna of emitted power and gain (P_E, G_E) is located at the same position as the receiver antenna of received power and gain (P_R, G_R). The target (a trihedral corner reflector of $L = 13$ cm) is located at a distance R from the antennas.

The general conclusion is that there are still a large number of uncertainties concerning this EM software to be considered as a reliable EM tool. In particular, we have listed the problems below:

- The calculation time is too long for wide band waveform specially when the target is at a long distance from the antenna. This can be due to the problem we encountered with WI in the way it calculates the waveform. For example, if we consider the corner reflector of $L = 13$ cm of Fig.3.6 located at a distance $R = 15$ m of the antenna for a frequencies band [6,18]GHz, then the calculation time is 130 min,
- The influence of the distance on the received power calculation is not fully understood. We know that the power P_k intercepted by a target located at a distance R_k of the radar is:

$$P_k = \frac{P_E G}{4\pi R_k^2}\sigma \tag{3.24}$$

Supposing that two identical targets are located at a distance R_k and R_j from the antenna (see Fig.3.7). Using the formula in Eq.3.24, the difference between the intercepted powers of the two targets is:

$$P_k - P_j = \frac{1}{R_k^2} - \frac{1}{R_j^2} \tag{3.25}$$

Thus, we can conclude that the variation of power is proportional to $\frac{1}{R^2}$,

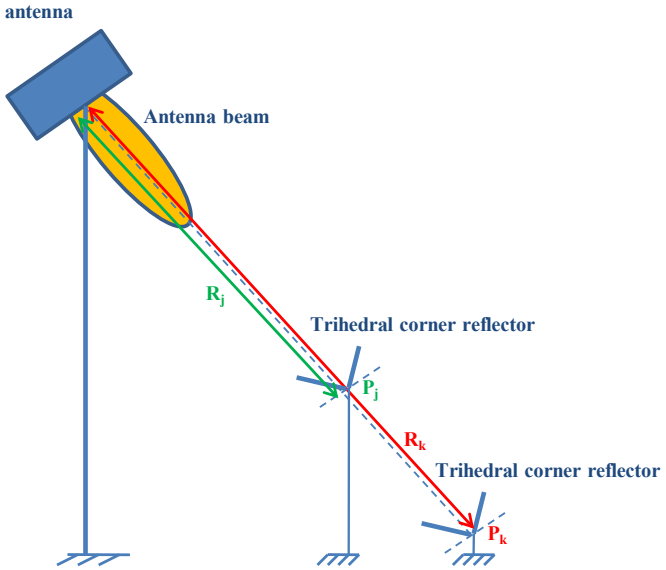

Figure 3.7: The difference between the intercepted power P_k and P_j of the two trihedral corners reflectors located respectively at a distance R_k and R_j from the antenna is equal to $\frac{1}{R_k^2} - \frac{1}{R_j^2}$.

where R is the distance between the radar and the point where the power is measured. To test if this difference is verified using WI, we simulated the scene configuration of Fig.3.8 where the transmitter is fixed and we moved the receiver at different positions 1, 2 , 3 and 4 to collect the measured powers at these positions. Then, we extracted the received power using WI outputs. The difference in Eq.3.25 is verified for the position 1 and 2, however, this difference is not respected between the point 3 and 4.

- The RCS calculation of typical targets is not validated. In fact, the influence of the antenna gains outside the main lobe is not mastered to perform this calculation. To calculate the RCS, the target must be far enough to not take into account the local variations of the incident rays comparing to the main lobe. One approach to overcome this problem was to consider an antenna beam with a uniform illumination. The next step was to simulate the configuration of Fig.3.6 for a trihedral corner reflector located at a distance R =20 m from the antenna at the frequency of 35 GHz. The trihedral was oriented so that its symmetry axis corresponds to the incidence direction to obtain a maximum value of the RCS. According to the formula in Eq.2.13:

$$\sigma_{max}^{trihedral} = \frac{4\pi L^4}{3\lambda^2} = 16.17m^2 \tag{3.26}$$

  Nevertheless, this value was not validated with the calculated outputs of WI.
- The absolute power level of the complex electric field according to the frequency $\underline{E}(f)$ (output calculated by WI) is not controlled yet. Indeed, we still do not know at the moment, how the power of the waveform is managed by WI.

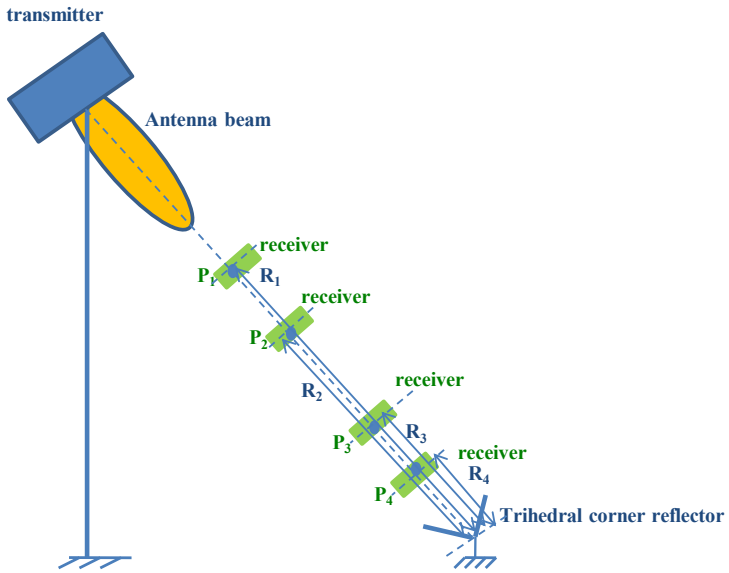

Figure 3.8: Configuration used in WI to verify the influence of the distance on the received power calculation. The transmitter (blue box) is fixed and the receiver (green box) is translated at the different positions 1 to 4 to extract the powers $P_{1,..4}$.

For all these reasons, as the amplitude has not been validated for simple canonical structures, we did not investigated additional tests on our object of interest (the urban canyon). WI was rejected due to all the problems listed before.

3.3 MOCEM

3.3.1 General description

MOCEM is a SAR image simulator that can produce high resolution SAR images from CAD models (VRML, 3DS..) taking into account basic material descriptions [Cochin 2008]. MOCEM covers many aspects of the SAR imagery including polarimetry and interferometry. SAR images are typically produced in a few minutes, using a 2D SAR radar transfer function that takes into account the main parameters of the SAR image quality.

Scene modelling
MOCEM uses a polygon intersection algorithm to get all visible parts of the scene that can be observed from the radar. A recursive computation is done to seek illuminated facets that the radar can see after one, two or three reflections. Only dihedral or trihedral effects are considered. Double or triple reflections that are not coming from this topology are eliminated.

Validity domain
As MOCEM is basically based on Geometric Optics Method (described in Sec.3.4),

it has some limitations. Considering the global RCS, results are very good in far field. For different kind of objects and targets, MOCEM images have been compared to ISAR and SAR measurements and RCS computations. It appears that MOCEM provides satisfying results, even if the amplitude levels that strongly depend on the material parameters are locally a couple dB different from the real ones [Cochin 2008].

3.3.2 Radar acquisition chain

In Fig.3.9, the radar acquisition chain for MOCEM. The two specificities of this chain should be noticed:

- For the emission block, the simulations are preformed with a planar incident wave with a constant amplitude (no waveform definition),
- As MOCEM produces directly SAR images as outputs, the radar range profile corresponds to a range line of the image.

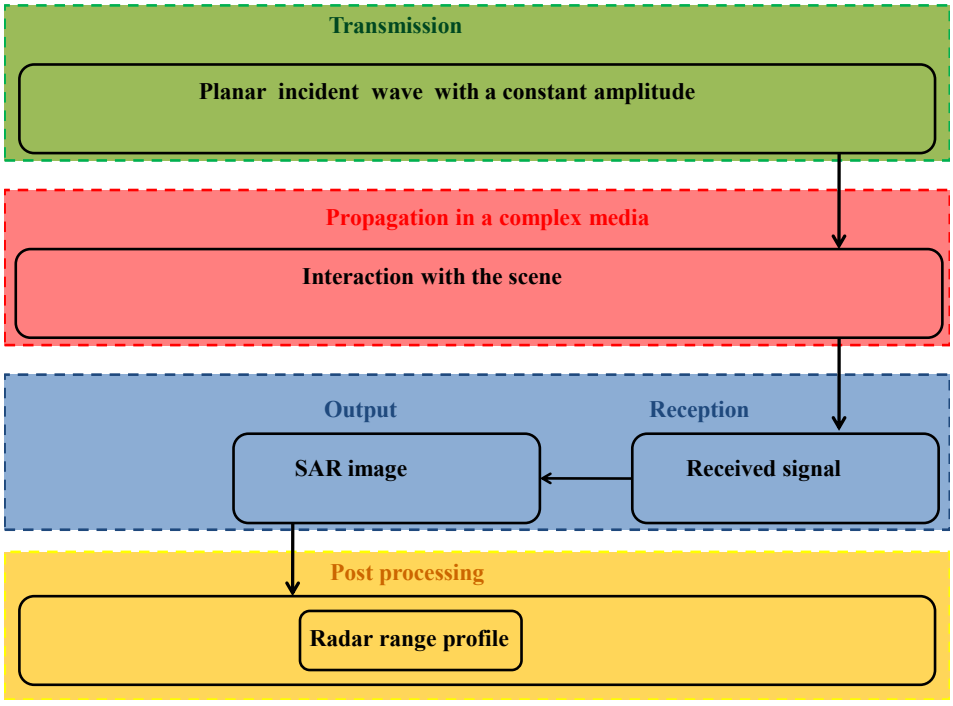

Figure 3.9: MOCEM radar acquisition chain.

3.3.3 Tests with MOCEM

MOCEM was used to interpret the second set of indoor data (data of the anechoic chamber BABI of ONERA, see Sec.2.3). It can be used to analyze these data using different d/λ ratios, even for a ratio tending to the real one. Indeed, MOCEM is able to perform simulations at high frequencies (up to 45 GHz) for the canyon configuration of the indoor environment. MOCEM has validated the radiometric response of a trihedral corner reflector with respect to the following conditions:

- The symmetry axe of the trihedral and the incidence direction must correspond in order to compare to the theoretical maximum value of RCS,

- The pixel size must be small comparing to the trihedral size,
- The far field case.

In fact, we simulated the maximum value of RCS for the trihedral corner reflector of Fig.3.10 where $L = 13$ cm and the frequency $F = 35$ GHz. The symmetry axe is obtained for $\theta = 54.73°$. Using the Eq.3.26, the maximum value of the RCS of a trihedral corner is 16.17 m^2. The maximum value of RCS obtained using MOCEM is 16.07 m^2.

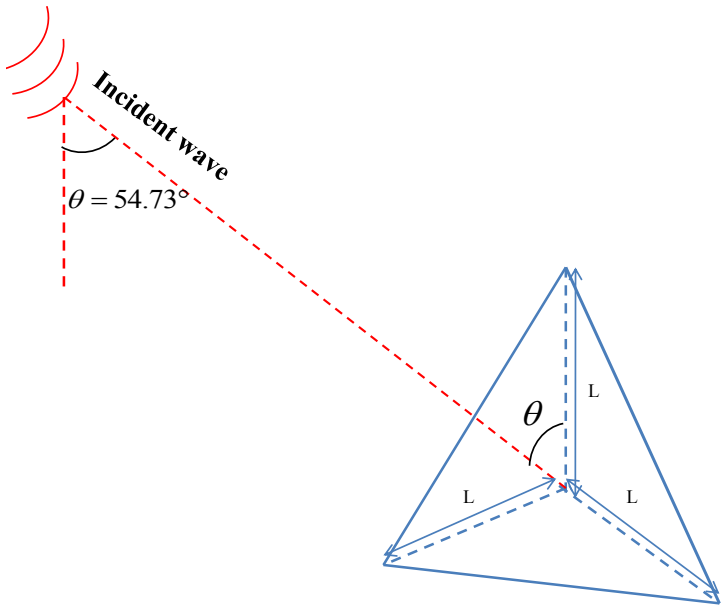

Figure 3.10: Trihedral corner reflector configuration used in MOCEM to validate the RCS. The symmetry axe corresponds to the incidence angle $\theta = 54.73°$ to obtain the maximum value of RCS. In this case, considering $L = 13$ cm and the simulating frequency F=35 GHz, the maximum RCS value is $\sigma_{max} = 16.17m^2$.

Difficulties of MOCEM application in our context

The main drawbacks to the use of MOCEM in this context are:

- The limit in terms of the number of interactions. Indeed, MOCEM simulates only:
  - The dihedral effect + 1 reflection on the wall (3 number of bounces),
  - The trihedral effect + 1 reflection on the wall (4 number of bounces),
  - The specular reflection on a surface + 1 reflection on the wall (2 number of bounces).

  Some simulations using MOCEM have been performed on the canyon configuration of the anechoic chamber BABI with an included parallelepiped target by multiplying the dimensions by a factor 60 to obtain a d/λ ratio equal to:

$$r_{sim} = 60 \times r_{ac_2} = 60 \times 4 = 240 \tag{3.27}$$

  The expected mechanisms corresponding to this new r_{sim} are illustrated in Fig.3.11. These mechanisms are:

– The dihedral corner reflector effect corresponding to the detection of wall 1,
– The dihedral corner reflector effect corresponding to the detection of the right side of the target (4 number of bounces),
– The dihedral corner reflector effect corresponding to the detection of the left side of the target (6 number of bounces).

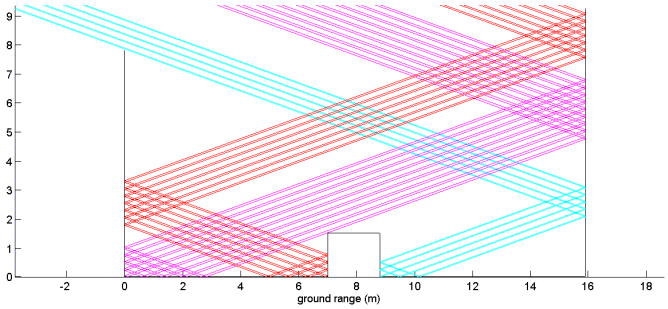

Figure 3.11: Geometric mechanisms corresponding to the canyon configuration of the anechoic chamber BABI when the d/λ ratio is equal to r_{sim}. Number of bounces associated to the blue ray (4), purple ray (4) and red ray (6).

Nevertheless, MOCEM simulates only the mechanism of detection by the right side as illustrated in Fig.3.12. The mechanism of detection by the left side involves a dihedral effect with two refections on the wall, so that it is not taken into account by MOCEM.

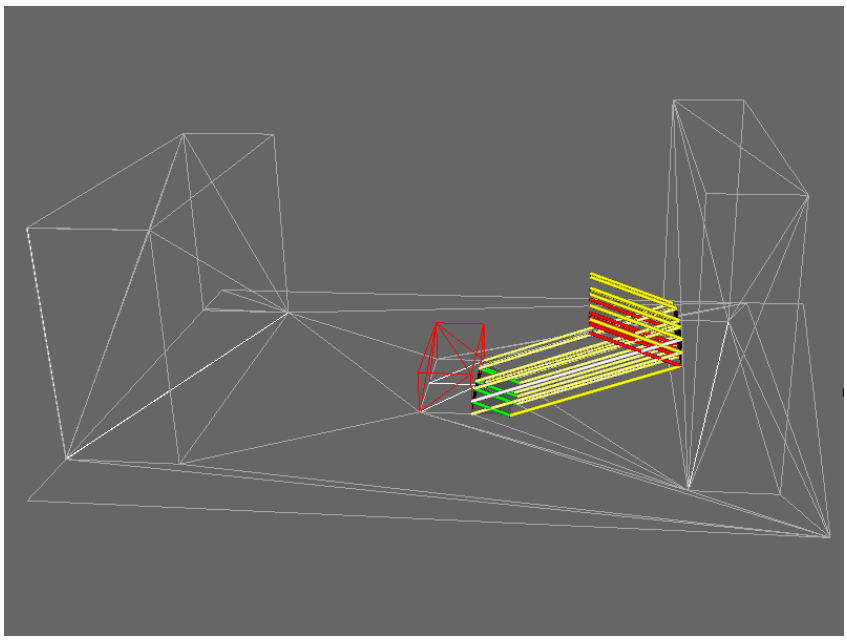

Figure 3.12: Dihedral effect on the right side of the target simulated by MOCEM.

- The materials must be completed by the user. The metal case is taken into account, but for the dielectric materials, the user has to introduce σ^0 (defined in Eq.2.2) curve according to the polarization for each material [Cochin 2008].

3.4 FEKO

3.4.1 General description

FEKO is an EM commercial tool used for EM field analysis of 3D structures. FEKO simulations are based on exact EM methods to provide solutions to Maxwell equations as well as approximated methods. In Tab.3.1 a summary of the different implemented EM methods in FEKO, the different applications and the capabilities of this EM software (see [fek] for further details).

Table 3.1: FEKO: EM methods, applications and capabilities. Table extracted from [fek].

Solution Methods	Applications	Special Features
• Method of Moments (MoM), • Finite Element Method (FEM), • Physical Optics (PO), • Geometrical Optics (GO), • Uniform Theory of Diffraction (UTD).	• 3D Antenna design • 3D RF components (Waveguide) • Scattering analysis (RCS)	• Hybridisation between EM methods (MoM with FEM, PO, GO and UTD), • Parallel processing, • Optimisation, • Time domain analysis, • Low frequency analysis, • GPU acceleration.

3.4.1.1 EM methods used in FEKO

The extremely wide range of EM problems has led to the development of many different CEM (computational electromagnetics) algorithms, each with its own benefits and limitations. These algorithms are typically classified as so called "exact" or "low frequency" and "approximated" or "high frequency" methods and further sub-classified into time or frequency-domain methods.

- The low frequency methods: these methods are so-named because they solve Maxwell's equations with no implicit approximations and are typically limited to problems of small electrical size due to the limitations of computation time and system memory,
- The high frequency methods: these methods concern EM problems of large size. Common examples of large problems are those of radar cross section prediction and calculation of an antenna's radiation pattern. Many approximations have been made to the equations of radiation and scattering to make these problems tractable. Most of these treat the fields in the asymptotic or high frequency limit and employ ray optics and edge diffraction. Thus, the name of high frequency methods.

MoM: Method of Moments

The MoM [Gibson 2007] is a full wave solution of Maxwell's integral equations in the frequency domain: it is a low frequency method used to solve EM boundary or volume integral equations in the frequency domain. Because the electromagnetic sources are the quantities of interest, the MoM is very useful in solving radiation and scattering problems. It is named also BEM method (Boundary Element Method) for solving linear partial differential equations which have been formulated as integral equations (i.e. in boundary integral form). It can be applied in many areas of engineering and science including fluid mechanics, acoustics, electromagnetics, fracture mechanics, and plasticity.

Advantages

Because it requires calculating only boundary values, rather than values throughout the space, MoM is significantly more efficient in terms of computational resources for problems with a small surface/volume ratio. When using field based solution techniques (Finite Element Method [Jin 2002], Finite Difference Time Domain [Kunz 1993]), the discretisation of the field through the free space introduces a very small error as a wave propagates through the mesh. For very large meshes, these errors could increase and hence, the accuracy of the results is reduced. The error can be reduced by using a finer discretisation, but this requires more computer resources. An advantage of the MoM is that it is a "source method" meaning that only the structure in question is discretised, not the whole free space which means that the propagation distance does not degrade the accuracy of the results.

Disadvantages

Full-wave techniques such as MoM generally suffer from poor scalability. This limits the electrical size of the problems that can be solved on typical computers. Conceptually, it works by constructing a "mesh" over the modeled surface. However, for many problems, MoM is significantly less efficient than volume-discretization methods (Finite Element Method, Finite Difference Method [Rübenkönig 2006], Finite Volume Method [Eymard 2000]). Boundary element formulations typically give rise to fully populated matrices. This means that the storage requirements and computational time will tend to grow according to the square of the problem size. Supposing that N is the size of the problem. The memory requirements for MoM is proportional to N^2, whereas that of the MLFMM (Multilevel Fast Multipole Method [fek]) is $Nlog(N)$. We notice that for a large N, there is a huge difference in terms of memory and computational time. Asymptotic high frequency techniques (PO, GO and the UTD) offer a solution to the scalability hurdles in such problems.

MoM implementation in FEKO

The MoM is applicable to problems involving currents on metallic and dielectric structures and radiation in free space. The structures are electrically small and are typically made of metals, although special extensions allow the inclusion of dielectrics and also layered dielectrics ([fek]).

GO: Geometric Optics

Geometrical Optics [Keller 1962], or ray optics, describes light propagation in terms of "rays". It is a high frequency method often used to determine the distribution

of light intensity, polarization, and phase throughout space. This is accomplished by assigning a field value to each ray and letting the total field at a point be the sum of the fields on all the rays through that point. The phase of the field on a ray is assumed to be proportional to the optical length of the ray from some reference point where the phase is zero. The amplitude is assumed to vary in accordance with the principle of conservation of energy in a narrow tube of rays. The direction of the field, when it is a vector, is given by a unit vector perpendicular to the ray. This vector slides parallel to itself along the ray in a homogeneous medium, and rotates around the ray in a specific way as it slides along it in an inhomogeneous medium.

Advantages

GO is a ray-based technique that models objects based on optical propagation, reflection and refraction theory [Pedrotti 2012]. GO (ray launching) is well suited to the solution of large structure scattering problems, since the "shooting and bouncing rays" approach is very efficient for an arbitrary number of multiple reflections.

Disadvantages

- GO ignores the wave effects: interference, diffraction and polarization effects,
- When the wavelength is very small compared with the size of structures with which the light interacts, new EM phenomena different from reflection and refraction appear, therefore, GO can not be applied.

GO implementation in FEKO

FEKO integrates the GO method with the current-based MoM, by launching rays from each radiating MoM element ([fek]). The ray-interactions with metallic and dielectric structures are then modelled using Huygens sources placed on each ray-contact point (reflected, refracted and transmitted rays) on the material boundaries.

PO: Physical Optics

Physical optics (PO) ([Balanis 1989]) is a method for approximating the high-frequency surface currents, allowing a boundary integration to be performed to obtain the fields. The PO and the MOM are used to solve the same integral equation, though the MOM calculates the surface currents directly instead of approximating them. PO is an intermediate method between geometric optics, which ignores wave effects, and full wave electromagnetism, which is a precise theory. The word "physical" means that it is more physical than geometric or ray optics and not that it is an exact physical theory. This approximation consists of using ray optics to estimate the current on a surface and then integrating that current over the surface to calculate the transmitted or scattered field.

Advantages

PO models the interference and the polarization effects for which the ray approximation of geometric optics is not valid [Pedrotti 2008].

Disadvantages

PO requires an additional method to compute the contribution due to the diffraction phenomena such as the PTD (Physical Theory of Diffrac-

tion [Ufimtsev 1971]) which is applied in joint to the PO formulation [Gutiérrez-Meana 2011].

PO implementation in FEKO

FEKO hybridises the current based accurate MoM with PO by modifying the interaction matrix, to ensure accuracy ([fek]). Nevertheless, PO may require a large mesh for extremely large problems, while run-time grows exponentially with multiple reflections.

UTD: Uniform Theory of Diffraction

The Uniform Theory of Diffraction (UTD), a high frequency method incorporates diffraction into the ray theory of light ([Kouyoumjian 1974], [Keller 1962]). The UTD treats an infinite wedge as a secondary source of diffracted waves that in turn, can be reflected and diffracted before reaching the receiver. Diffracted waves are produced by incident rays which hit edges, corners, or vertices of boundary surfaces. For a given point source and point receiver location, the diffraction of a wave over an infinite wedge is represented by a single ray whose contribution to the wave field is attenuated by a complex valued diffraction coefficient. The ray follows the path satisfying Fermat's principle: if the propagation medium is homogeneous, the ray follows the shortest path from the source to the receiver, stabbing the diffracting edges (see Fig.3.13). Diffraction coefficients are determined for each diffracting object-source combination. These coefficients are then used to calculate the field strength and phase for each direction away from the diffracting point. These fields are then added to the incident fields and reflected fields to obtain a total solution.

Advantages

UTD takes into account an important EM effect neglected with PO and GO which is the diffraction. UTD studies the diffraction on edges, corners or vertices of boundary surface.

Disadvantages

As for the case of MoM, this approximated EM method is a time and resources consuming method when the structures are large.

UTD implementation in FEKO

As for PO, FEKO hybridises MoM with UTD by modifying the interaction matrix. Frequency does not influence the memory resources required for UTD treatment of a structure as only points of reflection from surfaces and diffraction from edges or corners are considered without meshing the structure. Multiple reflections, edge and corner diffraction, double diffraction and creeping waves (cylinders) are taken into account ([fek]).

In Tab.3.2, a summary of the different EM methods implemented in FEKO used in our simulations with their advantages, drawbacks and their specific usage in FEKO.

3.4.2 Radar acquisition chain

In Fig.3.14, the radar acquisition chain for FEKO. One characteristic of this chain should be noticed: as for MOCEM, the simulations are preformed with a planar incident wave with a constant amplitude set to 1.

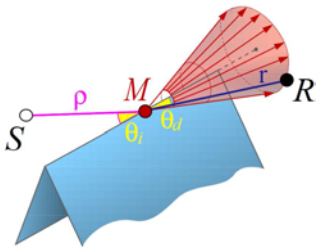

Figure 3.13: According to the UTD, an incoming ray ρ gives rise to a cone of diffracted rays, where the aperture angle θ_d of the cone is equal to the angle θ_i between the incident ray and the edge (the axis of the cone is the edge). For a given receiver location, a single ray describes the diffracted field [Tsingos 2001].

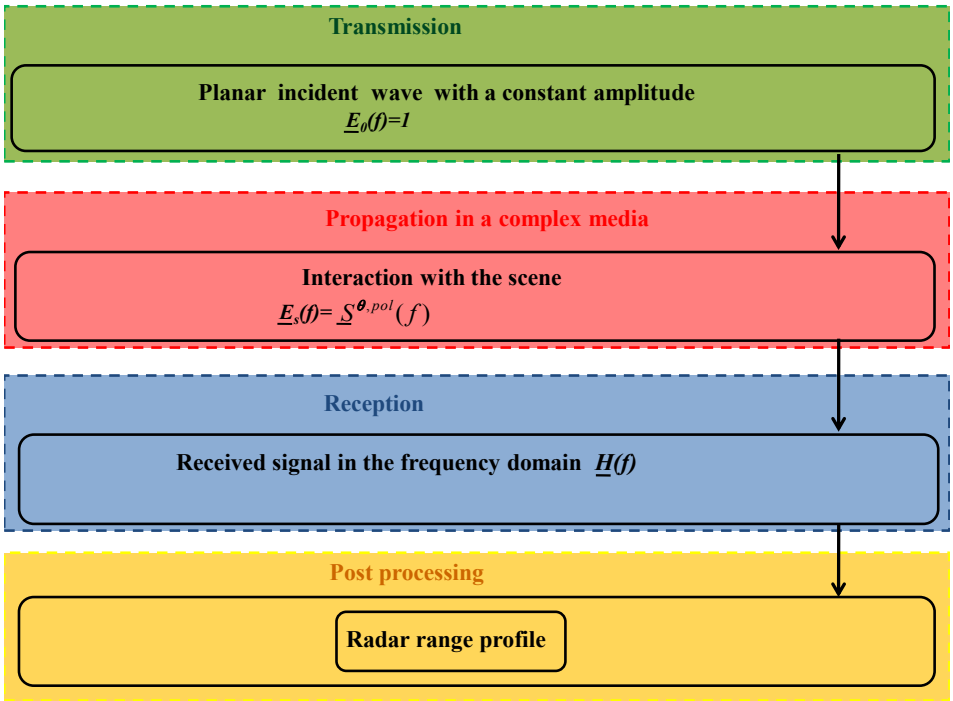

Figure 3.14: FEKO radar acquisition chain.

3.4.3 Tests with FEKO

Different tests have been performed using FEKO with the different EM methods listed before (MoM, PO, GO and UTD) for the canyon configuration of the anechoic chamber BABI described in Sec.2.3. The different tests concerned:

- An empty canyon,
- A canyon with an included parallelepiped target.

A good agreement between the simulation results using FEKO with the different EM methods and the experimental data has been found. The next chapter will concern the analysis of the experimental indoor measurements.

Table 3.2: Table summarizing the advantages and disadvantages of the EM methods: MoM, GO, PO and UTD and their use in FEKO.

	EM method	Advantages	Disadvantages	Usage in FEKO
Low Frequency	MoM	• Efficient for problem with a small surface/volume ratio, • Accurate comparing to field based solution techniques (FEM, FDTD).	• Poor scalability, • Memory consumption, • Increasing time computation.	Current-based method for small structures made of metal and dielectrics.
High Frequency	GO	• Simple method to study geometric mechanisms, • Low memory consumption, • Low time computation.	• Failure to account optical effects such as polarization and interference.	Ray-based method for metallic and dielectric structures that are very large.
	PO	• Study interference and polarization effects.	• Failure to account the fields diffracted by edges, • Run-time growing exponentially with multiple reflections.	Current-based method for very large metallic and dielectric structures.
	UTD	• Study diffraction on edges, corners, or vertices of boundary surface.	• Computer resources and time consuming method.	Ray-based method dedicated to electrically extremely large structures.

3.5 CST

3.5.1 General description

CST MicroWave Studio (CST MWS) is an EM commercial tool based on EM methods that provide solutions to the Maxwell's equations in both time and frequency domains thanks to the different solvers implemented on it [cst]. For the simulations we performed using CST, we used a time domain solver which is the finite domain time difference method (FDTD). The FDTD method models the propagation of an incident EM wave into a volume of space containing the structure of interest [Chu 1989]. The advantages of FDTD are its simplicity and its flexibility. By formulating the computational procedure locally and time-explicitly, the complete interaction between the incident wave and the geometry can be analyzed portion by portion at any given time. The localization of the procedure allows the analysis to be performed without having to find the simultaneous solution to the entire problem. One weakness of the FDTD method is that it requires a full discretization of the electric and magnetic fields throughout the entire volume domain [Gedney 2011] which can be time and computer resources consuming.

Advantages and drawbacks
CST is a very fast simulation tool comparing to FEKO. However, as it is based on volume discretization methods to calculate the electric filed, therefore, when the structures become large, the time running simulation increases drastically and can exceed the time running simulation for FEKO when using the MoM method.

3.5.2 Radar acquisition chain

In Fig.3.15, the radar acquisition chain for CST.

3.5.3 Tests with CST

The same tests as for FEKO have been performed using CST for the canyon configuration of the anechoic chamber BABI described in Sec.2.3. The different tests concerned:

- An empty canyon,
- A canyon with an included parallelepiped target.

As for FEKO, a good agreement between the simulation results and the experimental data has been ensured using CST. The simulations results will be presented in the chapter 5.

3.6 Conclusion

This chapter was an overview of the different EM tools tested in order to find the most reliable EM tool that correctly simulates the EM phenomenology of propagation inside a controlled environment where the d/λ ratio is different from the real one. The objective is to select a validated tool both in terms of phase and amplitude in order to use it to investigate about the scattering for a canyon configuration where the d/λ ratio tends to the real one. After that, based on the simulation

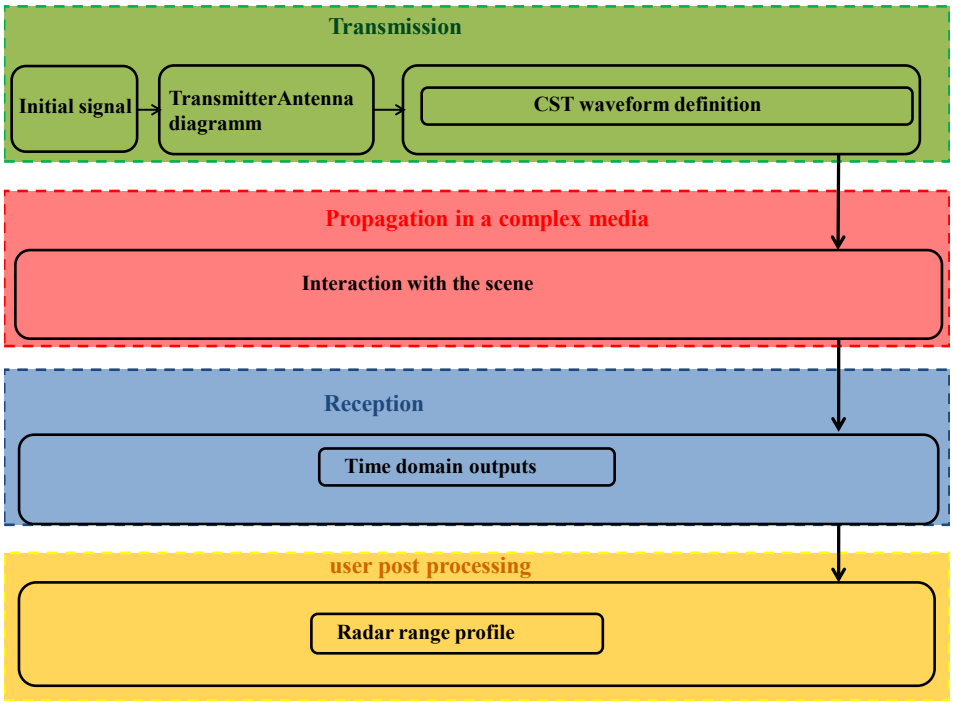

Figure 3.15: CST radar acquisition chain.

results, we can develop our in-house EM tool dedicated to NLOS targets detection for real case canyon configurations. The approach to validate a commercial EM tool is to compare its simulation results with the experimental data. Two EM tools have been rejected and two others have been validated (FEKO and CST).

In the next chapter, we will give a detailed presentation of the indoor data that we used to first analyze the EM phenomenology of propagation inside a canyon for the case of a controlled environment and in a second step for the benchmarking of the used EM tools that allowed to select FEKO and CST, as reliable EM tools.

Chapter 4

Detailed presentation of the new measurements

Contents

4.1 Introduction

As mentioned in the second chapter of the thesis where we presented the data at our disposal, we indicated that the new measurements that we used to perform our study of the EM phenomenology of propagation inside the urban canyon will be described more in details in this current chapter. In fact, this chapter has a twofold objectives: the first objective is to present in details the measurement setup in order to better analyze the experimental outputs. The second objective is to provide a first analysis of the EM scattering inside a controlled urban canyon configuration where the d/λ ratio is very low comparing to the real one. This analysis has been performed using the experimental data as well as a theoretical study. This will allow to better understand the simulation results of the validated EM tools presented in the next chapter.

This chapter is organized as follows: we give at first a description of the measurements setup in the anechoic chamber. Then, in the third section, we present

a first analysis of the experimental results. In the following section, we present a complete analysis of the EM effects observed in the output data of the anechoic chamber using the results of a theoretical study. We end up this chapter by a conclusion.

4.2 Measurement setup presentation

In this section, a full description of the measurement setup is given. We start by introducing the indoor environment where the experiment has been led. Then, we give a two aspects description of the experiment. The first aspect deals with the geometric configuration of the scene under study and the second aspect is a description of the radar parameters. We present also the output data and how these data have been exploited for our EM analysis as well as the d/λ ratio corresponding to the canyon configuration in the anechoic chamber.

4.2.1 Anechoic chamber BABI of ONERA

BABI is an indoor coherent bistatic RCS measurement facility in ONERA. The frequency range of operation can extend from 600 MHz to 40 GHz. It allows to transmit and receive coherent continuous wave (CW) signals in the horizontal and vertical polarizations by using two bipolarized wideband horn antennas (EM Systems model A610) and an HP 8510 network analyzer system. The transmitting and receiving antennas carried on trolleys can move on a circular rail of radius 5.5 m placed at a height of 2.5 m. These trolleys are pulled by engines which assure a reproducibility of location of antennas better than 10^{-2} degree. The target (for our case it consists of the scaled canyon) is mounted on a turning polyfoam column. This configuration is shown schematically in Fig.4.1. As we consider monostatic case, the two antennas are placed near each other and the polyfoam column height is chosen so that the incidence angle is equal to 70°. This is illustrated in Fig.4.2.

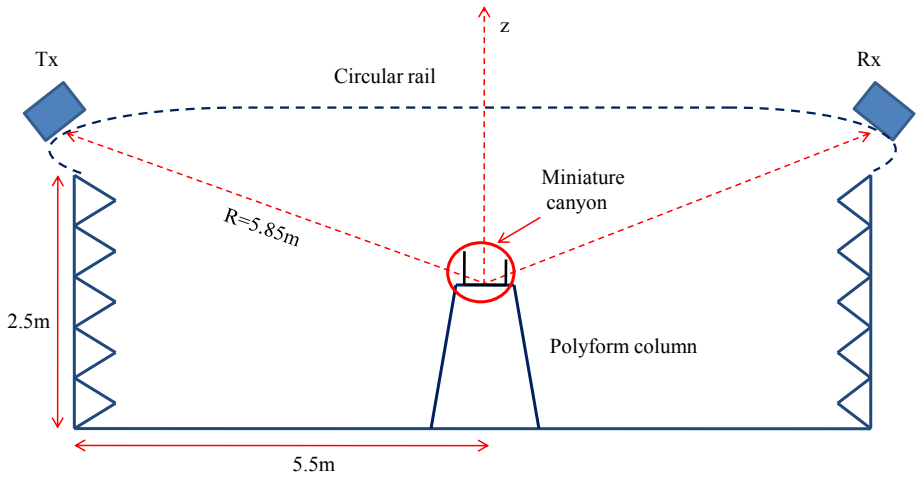

Figure 4.1: Azimuthal bistatic configuration. Tx and Rx are the transmitting and receiving antennas, respectively. R is a constant distance between the center of the polyform column and the antennas.

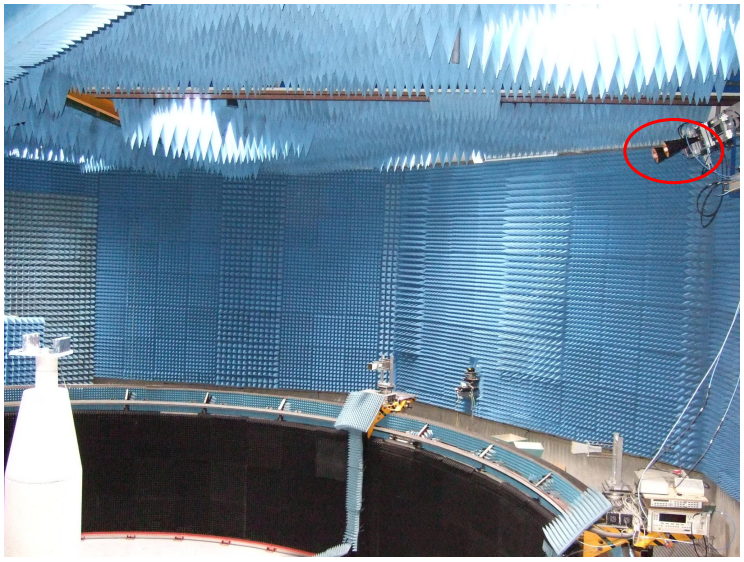

Figure 4.2: Configuration of the anechoic chamber BABI to ensure the monostatic case for the experiment. The two antennas in the red circle are located near each others.

4.2.2 Geometric description of the scene under study

4.2.2.1 First configuration: empty canyon

Our work is a preliminary one in the context of the EM phenomenology of propagation inside the urban canyon. Thus, we imposed some constraints to our object of interest (the urban canyon) to ensure the simplest case to study. The constraints on the canyon under study are:

- PEC (Perfect Electric Conductor) case: By this EM constraint, we decide to study a simple and complete case. In fact, considering the PEC case, all the expected responses of the scatterers can be detected and studied since there is no loss in the amplitude due to the material properties,
- Canyon perpendicular to the propagation plan: The canyon is oriented perpendicularly to the propagation plan. This orientation has been chosen as it ensures a maximum of multipath propagation mechanisms. With this orientation, the propagation in the transverse direction is avoided and consequently the loss of some mechanisms. The propagation plan is the plan containing $\overrightarrow{n}$, defined as the vector normal to the ground and $\overrightarrow{k_i}$ the vector of the incident wave as illustrated in Fig.4.5.

The two walls of the canyon are modeled by two boxes separated by a horizontal plate. To reproduce the PEC case, the two walls and the plate separating them are covered by aluminium (see Fig.4.3). The dimensions of the canyon are illustrated in Fig.4.4 and Fig.4.5. These dimensions have been chosen to ensure the case of far field.

4.2.2.2 Second configuration: canyon with an included target

Two different targets have been included inside the canyon:

- A toy modelling a car (see Fig.4.6),

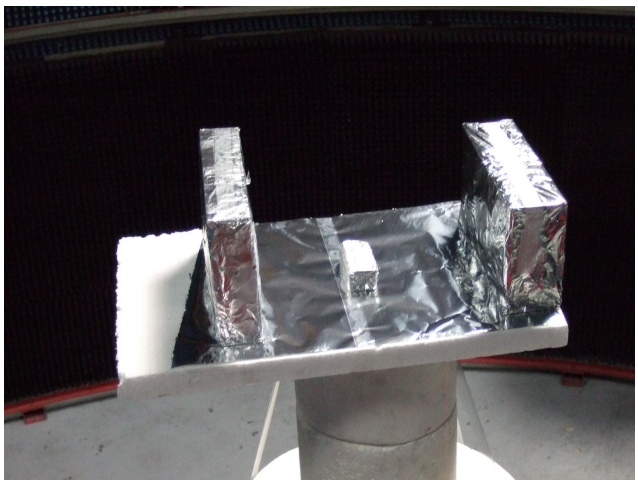

Figure 4.3: The used scaled canyon for the experiment with an included parallelepiped target.

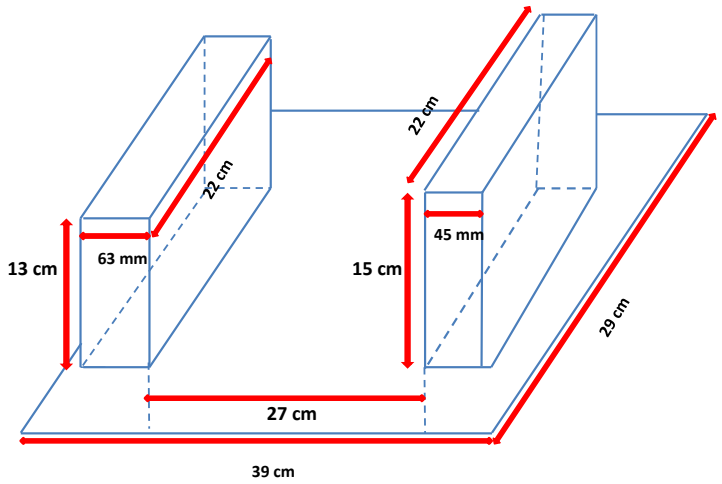

Figure 4.4: 3D description of the scaled canyon used in the anechoic chamber.

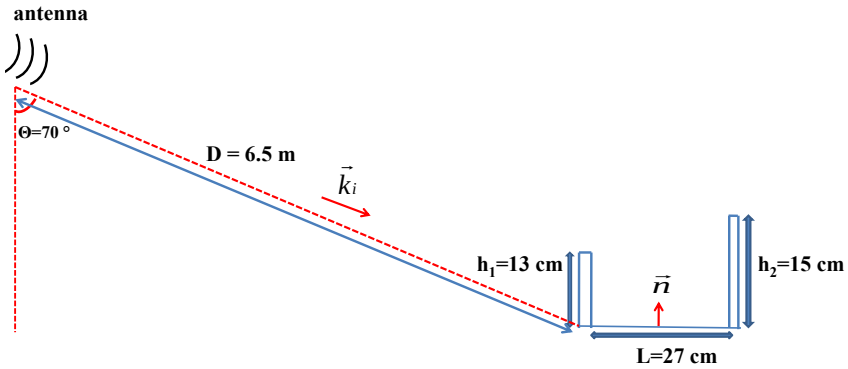

Figure 4.5: 2D description of the canyon. h_1 and h_2 are the height of the two walls. L is the distance separating them. θ is the incidence angle. $\overrightarrow{n}$ is the vector normal to the ground and $\overrightarrow{k_i}$ is the vector of the incident wave.

Table 4.1: Dimensions of the parallelepiped target.

height (cm)	length (cm)	thickness (cm)
2.5	7	3

- A parallelepiped target covered with aluminium (see Fig.4.3), its dimensions are presented in Tab.4.1.

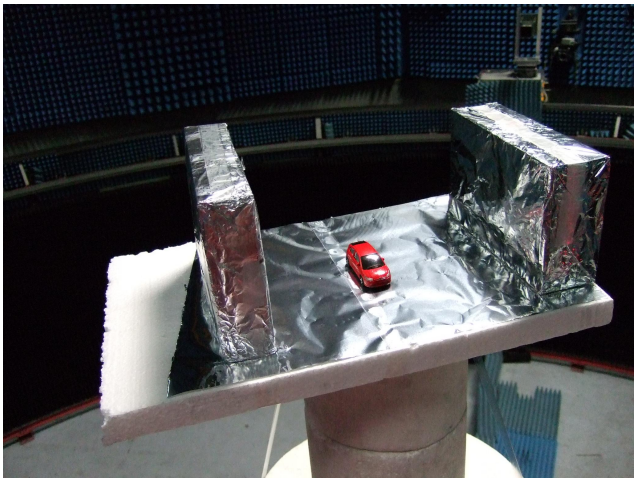

Figure 4.6: A toy modelling a car is included inside the scaled canyon.

In the following, we will present only the results of a canyon with the PEC parallelepiped target, because for the case of an included toy target, the corresponding response is so low (due to the material properties of the toy) that we can not study it. The parallelepiped is located at a distance of d_1= 16 cm from the first wall as shown in Fig.4.7.

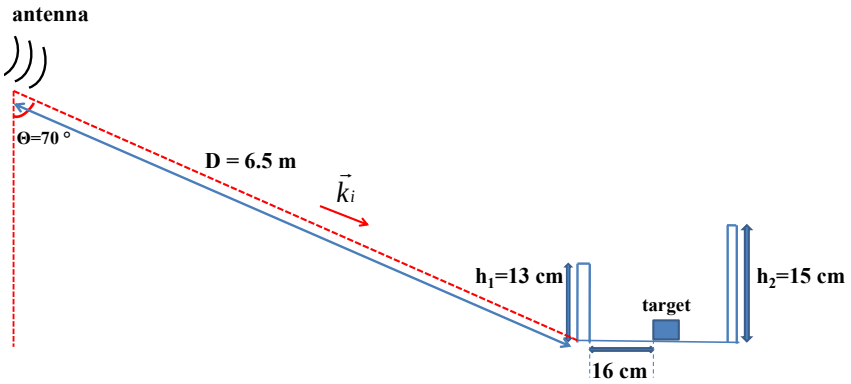

Figure 4.7: 2D description of the canyon with an included parallelepiped target at a distance of d_1= 16 cm from the first wall.

4.2.3 Radar parameters

4.2.3.1 Frequency band, range resolution

We used a chirp with a center frequency of 12 GHz and a bandwidth between 6 GHz and 18 GHz. We chose this carrier frequency because we wanted to achieve the best resolution meaning that we needed the widest frequency band. In BABI, this was only possible at 12 GHz. The corresponding range resolution is:

$$\delta_r = c/2B = 1,25cm \tag{4.1}$$

where c corresponds to the light speed and B is the total bandwidth.

4.2.3.2 Frequency step, total range

The experimental frequency step denoted δ_f is set to 15 MHz allowing thus a total range distance Δ_r of 20 m calculated as follows:

$$\Delta_r = \frac{c}{\delta_f} = 20m \tag{4.2}$$

4.2.4 Far field condition

To over come the difficulties due to the near field (in particular the angular variation in incidence causing multiple reflections), we have chosen to work in the case of far field. In this case, the far field condition will concern the canyon with no multipath propagation inside so that its dimension will not increase with the multipath propagation effects. The far field case is fulfilled when the following condition is true:

$$\begin{cases} D \geq D_1 \\ D_1 = 2\dfrac{d^2}{\lambda} \end{cases} \tag{4.3}$$

Where:

- D is the distance between the antenna and the object (the canyon). For our case, D =6.5 m as shown in Fig.4.5,
- d is the typical dimension of the object. For our case, it can be the dimension of the antenna, h_1 or h_2,
- λ is the radar wavelength corresponding to the center frequency of 12 GHz.

We have to ensure that:

- The antenna is in far field of the canyon. Considering a dimension d equal to the height of the second wall of the canyon (d = 15 cm), D_1 is equal to 1.8 m and thus the far field condition in Eq.4.3 is true.
- The canyon is in far field of the antenna. Considering d approximately equal to the dimension of the used antenna in the anechoic chamber ($d \simeq$ 10 cm), D_1 is equal to 0.8 m which validates the far field condition in Eq.4.3 also.

4.2.5 Anechoic chamber data outputs

In the following, we will present the methodology of the measurements of the RCS in the anechoic chamber BABI.

4.2.5.1 Methodology of measurement of RCS in BABI

The outputs of the anechoic chamber BABI is actually a complex reflection coefficient of the target denoted $\underline{H}(f_j, \theta_k)$ such as the squared amplitude corresponds to a measure of the target RCS:

$$RCS(f_j, \theta_k) = |H(f_j, \theta_k)|^2 \tag{4.4}$$

where $\underline{H}(f_j, \theta_k)$ is calculated as follows:

$$\underline{H}(f_j, \theta_k) = \frac{[A_1 e^{\Phi_1} - A_2 e^{\Phi_2}](f_j, \theta_k)]}{[A_3 e^{\Phi_3} - A_2 e^{\Phi_2}](f_j, \theta_0)]} B e^{\Phi_0}(f_j, \theta_0) \tag{4.5}$$

where

- $A_1 e^{\Phi_1}$ is the measurement of the target and the clutter response,
- $A_2 e^{\Phi_2}$ is the measurement of the clutter response,
- $A_3 e^{\Phi_3}$ is the measurement of the calibration target and the clutter response,
- $B e^{\Phi_0}$ is the theoretical calibration target response.

f_j and θ_k correspond to the incident frequency and to the direction of the incident signal, respectively. This variation in frequencies and incidence directions allows to form the final SAR image. In real case, the angular variation in incidence between the target and the sensor is usually ensured by the motion of the sensor. For these anechoic chamber measurements, as the antenna is fixed, the angular variation will be ensured by a motion of the target. Indeed, the plate located on the top of the polyform column where the scaled canyon is can rotate. The angular variation for the experiment is set between $-8.5°$ and $11.5°$ with an angular step Δ_θ of $0.5°$, thus, the total number of angular samples is 41. The angle corresponding to a perpendicular position of the canyon according to the propagation plan is $\theta_{18} = 0°$. $\widehat{\theta}$ is the vector of the incident directions defined as:

$$\begin{cases} \widehat{\theta} = (\theta_1, .., \theta_{41}) \\ \theta_1 = -8.5° \\ \theta_{41} = 11.5° \\ \theta_{18} = 0° \\ \Delta_\theta = 0.5° \end{cases} \tag{4.6}$$

We consider a total bandwidth of 12 GHz with a frequency step of 15 MHz, then, the total number of the frequency samples is 801. $\widehat{f}$ is the vector of the used frequencies defined as:

$$\begin{cases} \widehat{f} = (f_1, .., f_{801}) \\ f_1 = 6 \text{ GHz} \\ f_{801} = 18 \text{ GHz} \\ \delta_f = 15 \text{ MHz} \end{cases} \tag{4.7}$$

The outputs of this experiment will be of two types:

- a complex matrix $\underline{H}$ of size 801 × 41 defined as:

$$\underline{H} = \begin{bmatrix} \underline{H}(f_1, \theta_1) & \cdots & \underline{H}(f_1, \theta_{41}) \\ \vdots & \ddots & \vdots \\ \underline{H}(f_{801}, \theta_{41}) & \cdots & \underline{H}(f_{801}, \theta_{41}) \end{bmatrix} \tag{4.8}$$

  The elements of $\underline{H}$ correspond to the complex reflection coefficients $\underline{H}(f_j, \theta_k)$ defined in Eq.4.5. This matrix is measured for the co polarization Hh and Vv and for the cross polarization Hv and Vh. $\underline{H}$ can be used to generate the SAR image.
- the complex reflection coefficients corresponding to the orientation of the canyon which is perpendicular to the propagation plan, meaning for the angle $\theta_{18} = 0°$. These complex reflection coefficients will be used to calculate the radar range profile by applying the formula in Eq.3.5 where:

$$\begin{cases} \mathcal{F}^{-1}(\underline{E}(f)) \\ \underline{E}(f_i) = \underline{H}(:, \theta_{18}) \end{cases} \tag{4.9}$$

Fig.4.8 illustrates the process of calculating the experimental radar range profile from the outputs of the anechoic chamber.

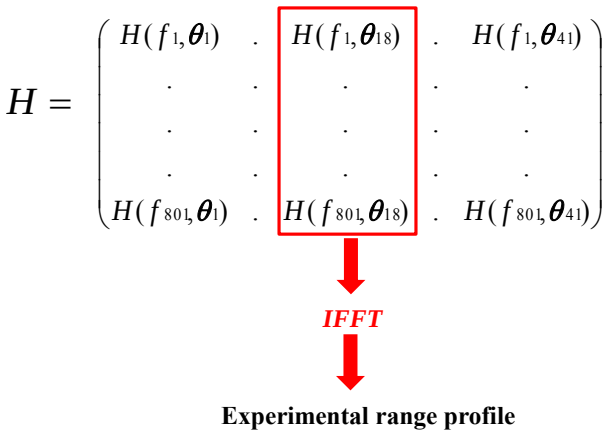

Figure 4.8: Process of calculating the radar range profile from the complex reflection coefficients $H(f_j, \theta_k)$ corresponding the experiment described in Sec.4.2.

The full method to calculate the radar range profile by applying an Inverse Fourrier Transform to $\underline{E}(f_i)$ is explained in details in Appendix.A (where $\underline{E}(f_i) = H_o(k_{xj})$).

4.2.6 Ratio d/λ in the anechoic chamber

The problem we face for the measurements is that the obtained ratio between the dimensions of the scaled canyon and the operating wavelength ($r_{ac_2} = 4$) is different from the real one ($r_{rc} = 166,66$) (see Sec.2.3). Unless a very high operating frequency which is technically not achievable, the real ratio can never be ensured in the anechoic chamber. To conclude, we can say that trying to model a realistic

configuration in this anechoic chamber will never be possible, and this will probably affect its EM signature.

4.3 Analysis of the anechoic chamber data

In this section, we analyze the anechoic chamber data corresponding to the experiment described in the previous section. We keep the same canyon configuration as well as the same radar parameters. The approach is to calculate a radar range profile and then to analyze the different peaks in terms of phase and amplitude in order to know more about the different mechanisms occurring inside the canyon of the anechoic chamber.

4.3.1 Radar range profile description

We present in Fig.4.9, the experimental range profile obtained for the empty canyon described in Fig.4.5 for the Vv polarization. As we can notice, the range profile contains a multitude of peaks that correspond to different mechanisms inside the canyon. In the next, we will identify the geometric mechanism leading to each peak, using the phase information.

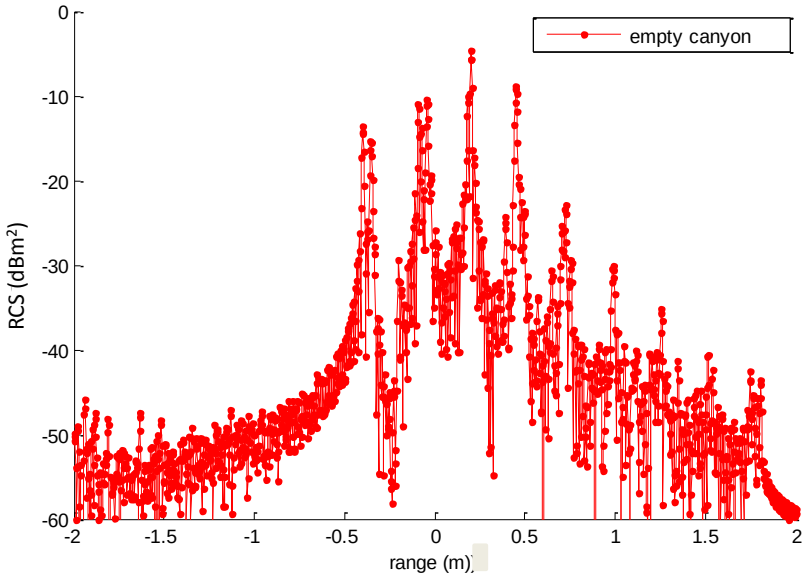

Figure 4.9: Experimental range profile obtained for the canyon of Fig.4.5 (Vv polarization).

4.3.2 Identification of the geometric mechanism leading to each peak

Using the canyon configuration and the phase of each peak, we have identified by a geometric distance calculation the mechanisms corresponding to the five first peaks as illustrated in Fig.4.10. To do so, we have reported the range profile of Fig.4.9 but for a restricted range from -1 m to 1 m in order to better differentiate between

the two first double peaks. We have assigned to each peak a color and we have used the same color to illustrate the geometric mechanism leading to this peak in Fig.4.11. As we can see, we have validated using a geometric calculation, the phase

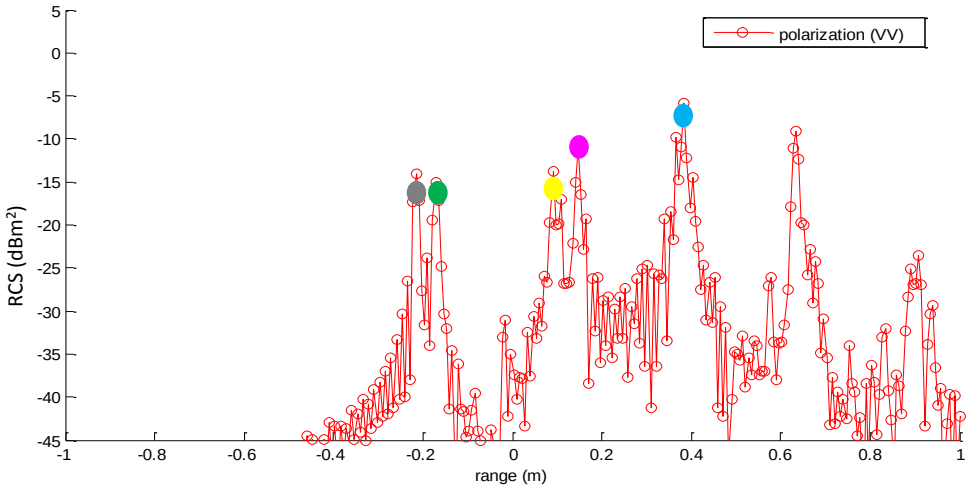

Figure 4.10: Experimental range profile of Fig.4.9 for a distance ranged between -1m and 1m. Colored circles have been added to identify the geometric mechanisms corresponding to each peak.

of five peaks (the amplitude is not validated yet). Indeed, the first two double peaks correspond to a backscattering mechanism on the top and the bottom of the first wall. Similarly, the next two peaks correspond also to a backscattering mechanism on the top and the bottom of the second wall. The fifth peak correspond to the dihedral effect on the first wall. It is illustrated by the ongoing continuous line from the corner of wall 1 (blue line in Fig.4.11). Nevertheless, in reality, it models the dihedral effect of a group of incident rays as illustrated in Fig.4.12. These rays, colored in red, correspond to a caustic which can be defined as a group of rays having the same distance as a central ray: the ongoing ray from the corner (colored in black). For all the figures, every dihedral effect will be illustrated with one ray (the central ray of the corresponding caustic) that represents all the rays of the corresponding caustic.

These five identified peaks are expected if we consider a small angular variation in incidence. However, the experimental range profile contains others peaks, approximatively spaced by a distance x_L defined in Eq.4.10, that are probably due to other mechanisms.

$$x_L = L \sin \theta \tag{4.10}$$

L and θ are illustrated in Fig.4.5.

x_L is the difference in range between two peaks of two geometric mechanisms defining two dihedral effects with a difference of two bounces between the rays of each corresponding caustic. This is explained in Fig.4.13 where there are two caustics defining the dihedral effect of the first wall and the second wall. The rays of

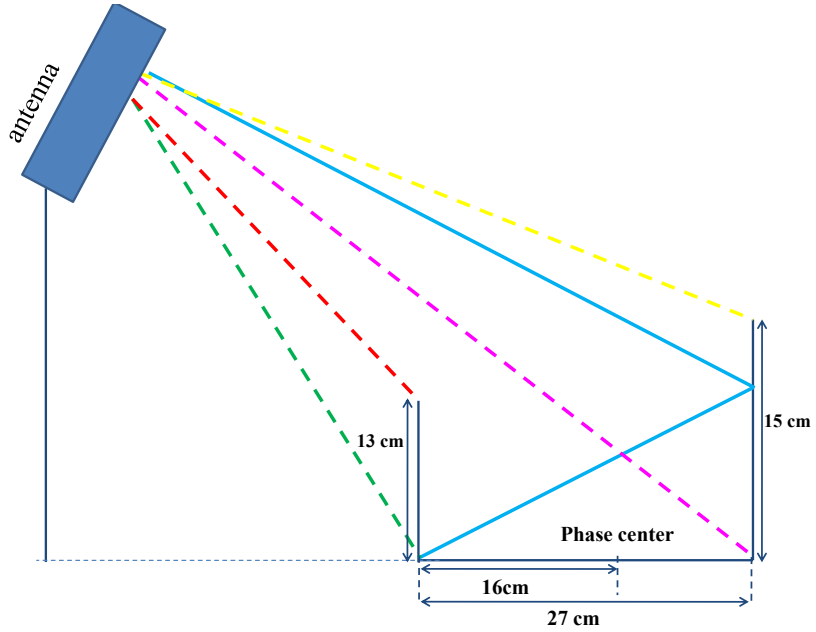

Figure 4.11: Identification of the different mechanisms leading to the five first peaks in the range profile.

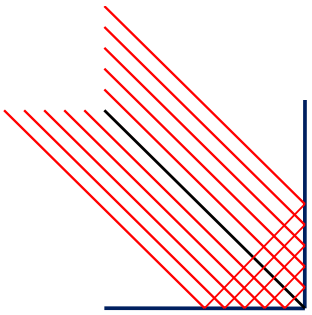

Figure 4.12: The dihedral effect is defined by a caustic which is a group of rays (illustrated in red color) having the same distance as a central ray (illustrated in black color).

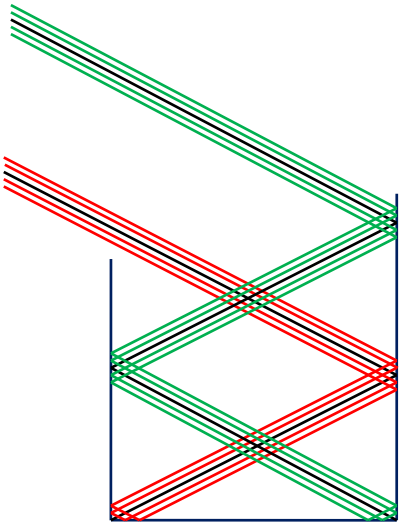

Figure 4.13: The dihedral effect of wall 1 and 2 are due to the red and green caustics, respectively. The peaks of these two geometric mechanisms will be separated by a distance $x_L = L \sin\theta$.

the red caustic make four number of bounces, whereas the rays of the green caustic make six number of bounces. The peaks of these two geometric mechanisms will be separated by a distance of x_L (defined in Eq.4.10) in the range profile. The next step is to identify the origin of the additional peaks in the range profile of Fig.4.9.

4.4 Origin of the additional effects

In this section, an EM theoretical analysis is proposed to help understanding the origin of the peaks in the experimental range profile. The approach is to study the scattering on the walls of the canyon. Thus, the EM response of the plate (modelling the wall) at the frequency and incidence angle of the anechoic chamber is investigated. The goal is to provide an explanation to the existence of these additional peaks on the experimental range profile.

4.4.1 Response of a metallic plate at the frequency of the anechoic chamber

The existence of many peaks in the experimental range profile supposes the existence of many geometric mechanisms that can be due to an angular variation in incidence. Once we have ensured the case of far field, this angular variation in incidence can not exist since the antenna pattern is assimilated to a narrow beam. This leads us to think about a possible angular variation in diffusion for the rays arriving on the wall of the canyon. For this reason, we have studied the EM response of a plate having the same dimensions as the second wall of the canyon at the center frequency of the anechoic chamber (12 GHz) for the considered incidence angle of the experiment. We can conclude (as shown in Fig.4.14) that this plate will scatter in a lobe of 13° around the specular reflection direction (110°). This angular variation in diffusion may explain the origin of the additional peaks in the experimental range profile.

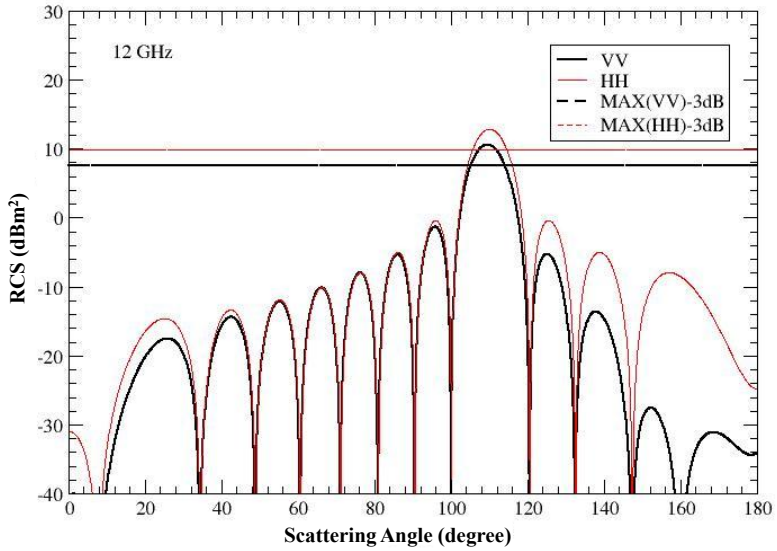

Figure 4.14: Scattering by a PEC plate of dimensions 15 cm × 22 cm at the frequency of 12 GHz and an incidence angle of 70°.

4.4.2 Response of a metallic plate at a higher frequency

If we consider higher frequencies, in order to tend to the real d/λ ratio, the main scattering lobe will be narrower as illustrated in Fig.4.15 (less that 1°). The larger is the lobe, the more mechanisms are expected, as it introduces new scattering directions. Hence, more peaks are expected in the measured range profile in the anechoic chamber than in reality.

4.4.3 Identification of the geometric mechanisms inside the canyon

4.4.3.1 Case of an empty canyon

We propose in Fig.4.16 an illustration of the plate diffusion (modelling the second wall of the canyon) at the frequency of the anechoic chamber and for a higher frequency. In Fig.4.16(a), as d/λ ratio is not the real one, the reflection will be in a large lobe inducing thus an angular variation in diffusion. Consequently, additional geometric mechanisms appear and cause additional peaks. Fig.4.17 illustrates the angular variation in diffusion that leads to additional mechanisms (illustrated in black, brown and purple color). These geometric mechanisms correspond to the dihedral effects of wall 1 and wall 2 with different number of bounces for the incident rays. Fig.4.18 shows the associated peaks corresponding to these identified mechanisms. Indeed, these peaks are not equally spaced by a distance x_L (Eq.4.10). This is due to the angular variation in diffusion. In fact, at every reflection of the incident rays on the walls or on the ground, there is a multitude of reflected directions and hence different reflection angles. Therefore, the initial incident angle is not preserved when the rays propagate inside the canyon. This provides an expla-

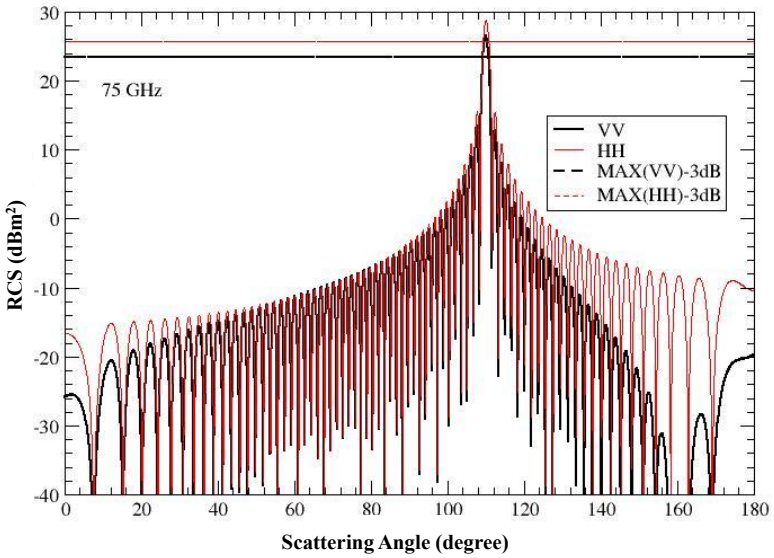

Figure 4.15: Scattering by a PEC plate of dimensions 15 cm × 22 cm at the frequency of 78 GHz and an incidence angle of 70°.

nation to the fact that the peaks are not equally spaced because the incident angle changes after the penetration of the rays inside the canyon.

In Fig.4.16(b), the reflection is in a narrow lobe so the number of mechanisms is expected to be reduced and thus the number of peaks in the range profile. In order to verify this assumption, the approach will be to simulate the configuration of the canyon at higher frequency (not achievable in the anechoic chamber) using a validated EM tool, ensuring thus a d/λ ratio tending to the real one. The corresponding simulation results will be presented in the next chapter.

4.4.3.2 Case of a canyon with an included parallelepiped target

Fig.4.19 illustrates the experimental range profile corresponding to the canyon configuration with an included parallelepiped target of Fig.4.7. If we consider a diffusion in a narrow beam, the target will be detected by its left side (the mechanism of detection is illustrated in continuous red line in Fig.4.20). The corresponding peak on the range profile will be separated from the first peak of the canyon by a distance x_{d1} defined as:

$$x_{d1} = d_1 \times \sin(70^\circ) = 16 \times \sin(70^\circ) = 15.03cm \tag{4.11}$$

However, in the range profile, this peak is located at a distance of 14.3 cm from the first wall (the peak identified with red circle in Fig.4.19). This is explained by the angular variation in diffusion. In addition, it has a low amplitude which makes the detection difficult referring only to the range profile. However, in the corresponding SAR image, the effects of the presence of the target are more distinguishable. This

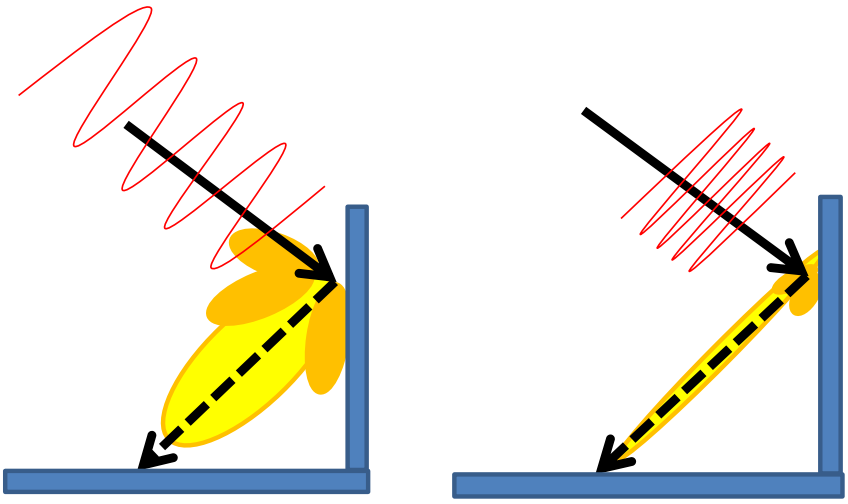

(a) Scattering of a plate in a large lobe of diffusion for a low d/λ ratio.

(b) Scattering of a plate in a narrow lobe of diffusion for a d/λ ratio tending to the real case.

Figure 4.16: Illustration of the scattering of PEC plate having the same dimension as the second wall of the canyon at the frequency of 12 GHz (Left) and at the frequency of 78 GHz (Right).

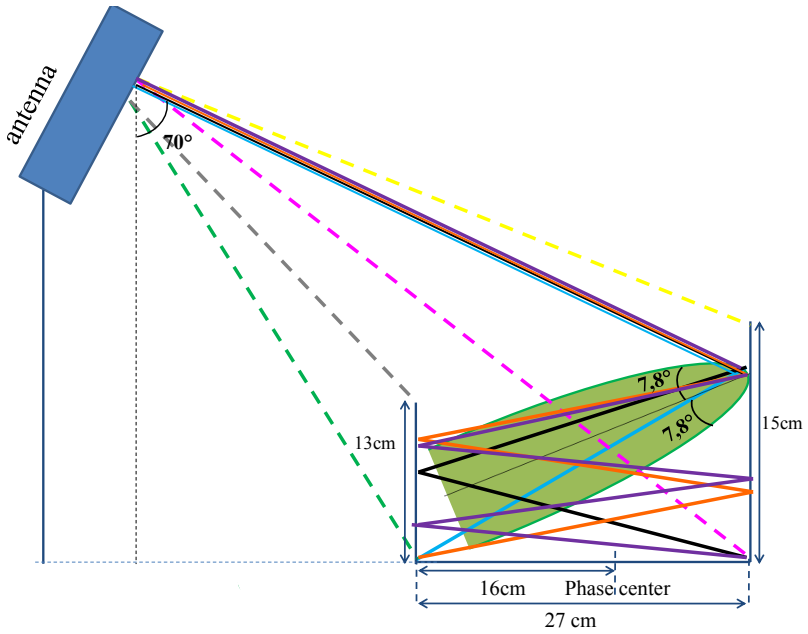

Figure 4.17: The angular variation in diffusion is the explanation of the origin of the additional geometric mechanisms (illustrated in black, orange and purple color).

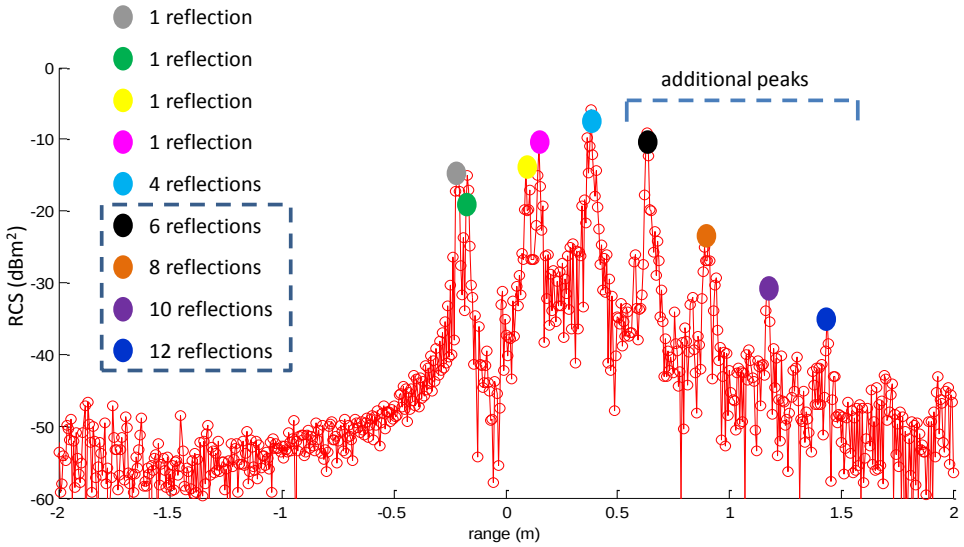

Figure 4.18: Experimental range profile of Fig.4.9 with colored circles on the peaks that identify the corresponding geometric mechanism illustrated in Fig.4.17. Each geometric mechanism is defined by a caustic and the number of bounces of the rays corresponding to each caustic is indicated.

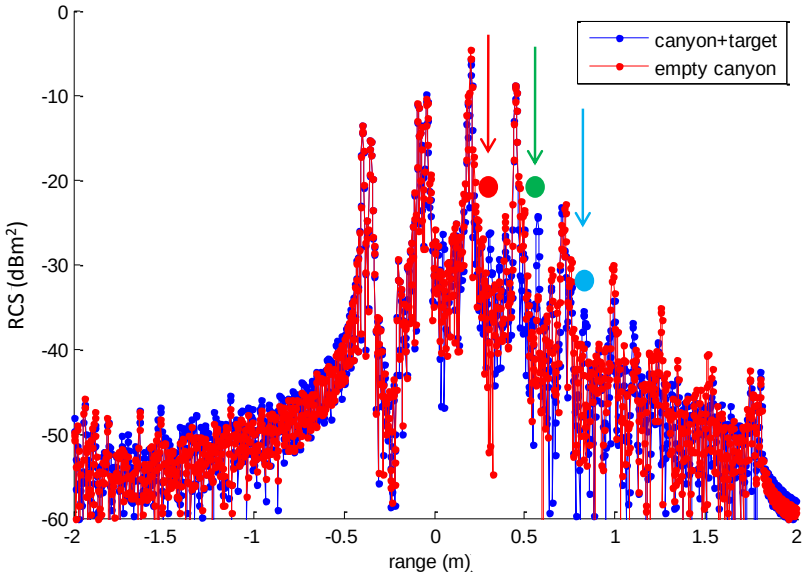

Figure 4.19: Experimental range profile corresponding to a canyon configuration with an included parallelepiped target (Vv polarization).

is illustrated in Fig.4.21 where the SAR image of the canyon with the included parallelepiped target is reported. As we can see, the target in the SAR image is detectable by three responses:

- The first response at a range position of 0.24 m (in red circle),
- The second response at a range position of 0.51 m (in green circle),
- The third response at a range position of 0.75 m (in blue circle).

These responses correspond to the peaks identified in Fig.4.19. We notice that the peaks identified with green and blue circles have a very low amplitude so that they are difficult to distinguish in the range profile due the angular variation in diffusion that induces mechanisms with big number of interactions and hence an important loss in the amplitude for the associated peak.

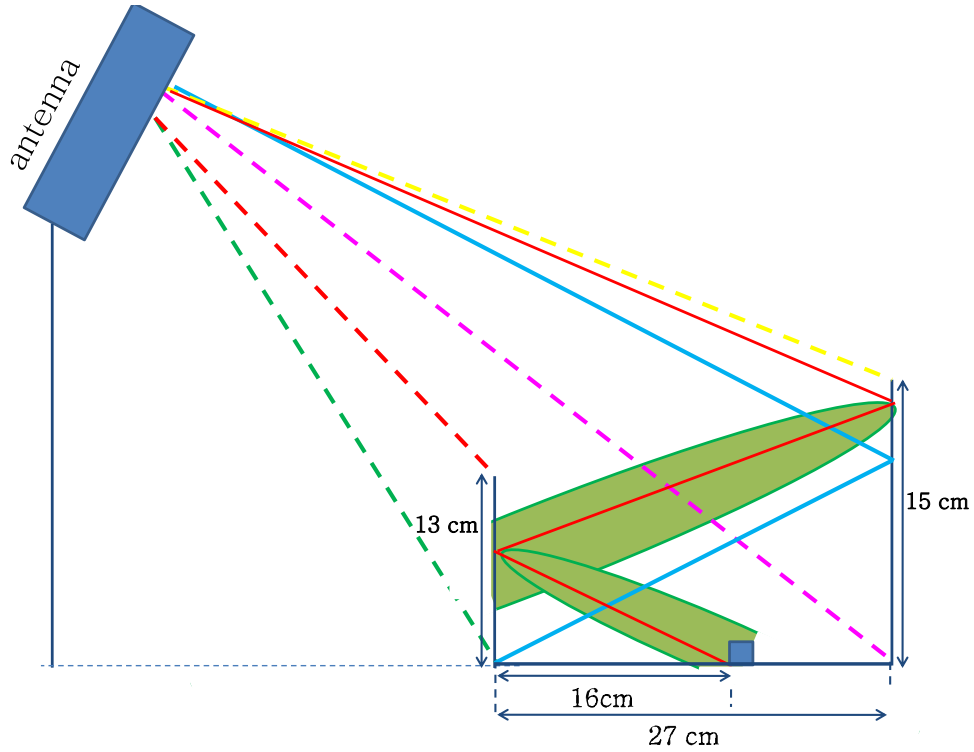

Figure 4.20: Canyon configuration with the parallelepiped target located at a distance of 16 cm from the first wall.

4.5 Conclusion

In this chapter, we gave a detailed presentation of the measurement setup of the experiment we conducted in the anechoic chamber, as well as the experimental results obtained. With a theoretical study, we provided an explanation of some aspects of the EM behaviour inside a controlled environment where the d/λ ratio is very low comparing to the real one. This EM behaviour has been investigated through the analysis of the experimental range profiles for the case of an empty canyon and for the case of a canyon with an included target. This chapter will help to understand the results of the different simulations we performed using the EM validated tools (FEKO and CST) in the next chapter.

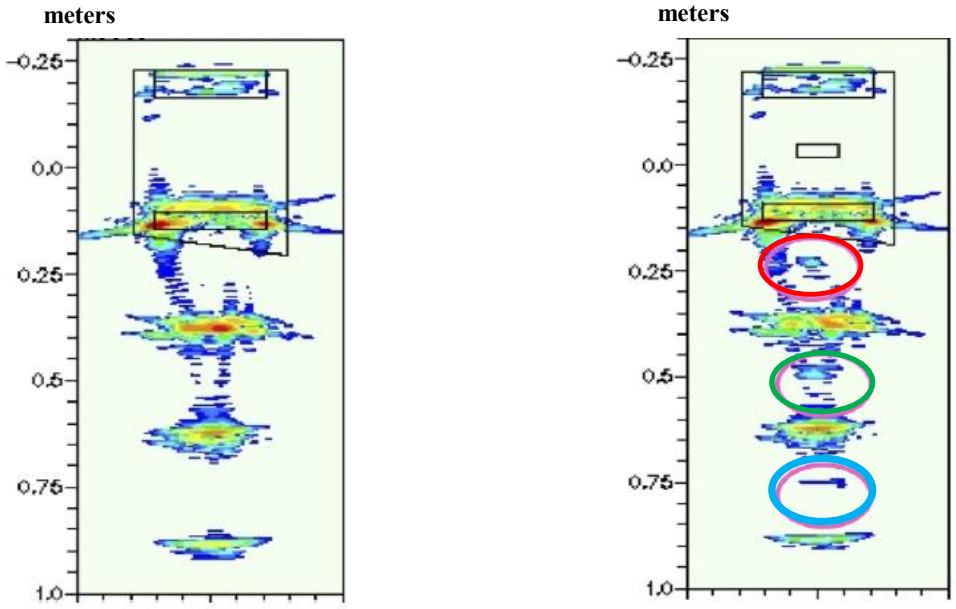

Empty canyon **Canyon+target**

Figure 4.21: (Left) SAR image of an empty canyon. (Right) SAR image of the canyon with an included parallelepiped target: the responses of the target are illustrated with red, green and blue circles.

Chapter 5

Simulations and comparisons using FEKO and CST

Contents

5.1 Introduction

The present chapter has three objectives. The first objective is to present the results of validation of FEKO and CST and the second objective is to perform additional simulations using FEKO in order to gain knowledge about the influence of the scene geometry on the canyon range signature. The third objective is to perform simulations at higher frequency (d/λ ratio tending to the real one) with the validated EM tool to investigate about the propagation in real case configuration, which will help to develop our EM in-house tool. The results of validation of the two EM tools will be presented through comparison between the simulated range profiles and the experimental range profiles of the anechoic chamber data. These data have been described in details in the previous chapter. Then, FEKO has been used to perform simulations on different canyon geometries (tilted canyon and distorted canyon) to study the influence of the geometry of the scene on the EM scattering effects happening inside the canyon. A polarimetric study is also performed to investigate these effects. This study is clearly not comprehensive, however, this constitutes a preliminary investigation on the EM behaviour of a more realistic canyon. Indeed,

we expect that in reality the walls are not perfectly parallel between them and with respect to the sensor trajectory. In addition, in the real life, the walls are not always PEC, but this effect will be addressed in the last chapter of this thesis.

Finally, as our goal is to build an in-house EM tool dedicated to NLOS target detection inside real urban canyons, we performed simulations at higher frequency ensuring thus a d/λ ratio tending to the real one.

This chapter is organized as follows: the first two sections are devoted to present the validation results of FEKO and CST. Then, the next section is dedicated to study the influence of the canyon geometry of the EM mechanisms happening inside it, and finally, the last section concerns the study of the multipath propagation inside a canyon configuration with a d/λ ratio tending to the real one.

5.2 Validation of FEKO

5.2.1 Scene and radar parameters in FEKO

5.2.1.1 Scene parameters in FEKO

Two canyon configurations have been tested with FEKO differing from the number of used meshes:

- The first configuration is the same as in the anechoic chamber. It is illustrated in Fig.5.1. This canyon configuration will be called the "exact" canyon configuration,
- The second configuration is a simplified canyon in the sense where the number of meshes has been greatly reduced. In fact, the width of the walls is suppressed, as well as the extra part of the ground (Fig.5.2). This canyon configuration will be called the "simplified" canyon configuration. This second configuration has been used essentially to reduce the calculation time of the simulations. This will be explained more in details later.

For all the simulations, the phase center is located on the bottom of wall 2.

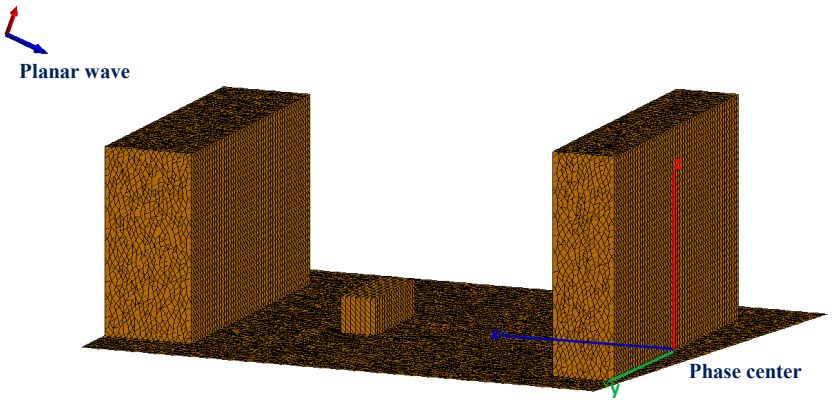

Figure 5.1: 3D canyon configuration used in FEKO simulations corresponding to the "exact" canyon configuration. The phase center is located on the bottom of wall 2.

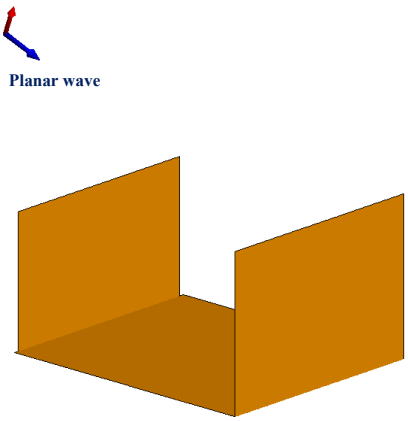

Figure 5.2: 3D canyon configuration used in FEKO simulations corresponding to the "simplified" canyon configuration.

5.2.1.2 Radar parameters in FEKO

As mentioned in the radar acquisition chain in Fig.3.14, the incident wave in FEKO is modeled with a planar wave of a constant amplitude. FEKO is able to perform simulations for all the polarizations. Two frequency steps have been used differing on the canyon configuration used in the simulations ("exact" or "simplified"). In Tab.5.1, a summary of the radar and scene parameters corresponding to each of the used canyon configuration.

Table 5.1: The differences between the "Exact" and "Simplified" canyon configurations used in FEKO.

	Number of meshes	Frequency bandwidth	Incidence angle	Frequency step	Total range
"exact" canyon configuration	92277	[6-18] GHz	70°	15 MHz	20 m
"simplified" canyon configuration	16580	[6-18] GHz	70°	25 MHz	12 m

5.2.2 Case of an empty canyon

5.2.2.1 Simulations on "exact" configurations

Simulations using MoM

In Fig.5.3, a FEKO simulation using the exact method EM method MoM applied to the "exact" canyon configuration at Vv polarization. As we can notice, there is a good agreement between the simulated and experimental range profiles in terms of range and also the amplitude corresponds as well. The first and the second double peaks agree with the simulation results for the phase as well as for the amplitude. These two double peaks observed for the response of wall 1 and wall 2 correspond actually to the contribution of the top and the bottom of each plate. This will be further explained in Subsec.5.4.1. For the others peaks, the position

in the range corresponds, but, there are some differences in amplitude specially for the peaks due to the interactions inside the canyon. This can be explained by some experimental parameters that are neglected in the simulations (in particular the roughness of the foil paper is not taken into account, the parallelism has not been checked accurately). However, this comparison is sufficiently good to state that FEKO is a reliable tool able to correctly simulate the EM scattering for the anechoic chamber canyon configuration where the d/λ ratio is not respected. We should notice that the MoM is really a time consuming method since the simulations on an "Exact" canyon configuration took 20 days (full polarization).

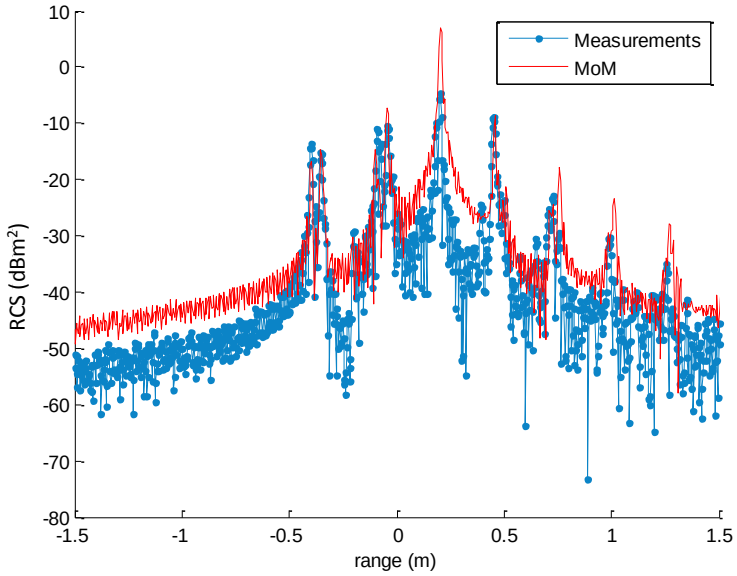

Figure 5.3: Simulated range profile using MoM on the "exact" canyon configuration and experimental range profile in Vv polarization.

5.2.2.2 Simulations on "simplified" configurations

Simulations using MoM

As the MoM provides accurate results, we decided to use it to simulate a "simplified" canyon configuration in order to compare if there is a difference between the simulated range profiles using the MoM on an "exact" canyon configuration and on a "simplified" canyon configuration. As we can see in Fig.5.4, there is no important differences between the two range profiles (except for the first two peaks because the thickness of the walls is now null), noticing that the MoM applied on a "simplified" canyon configuration is really less time consuming (6 hours). In the following, we will present the results of simulation performed on "simplified" canyon configurations, but using approximated methods.

Simulations using PO

In order to speed up the calculation time, we have simulated using PO applied the "simplified" canyon configuration. Three simulations have been performed, differing

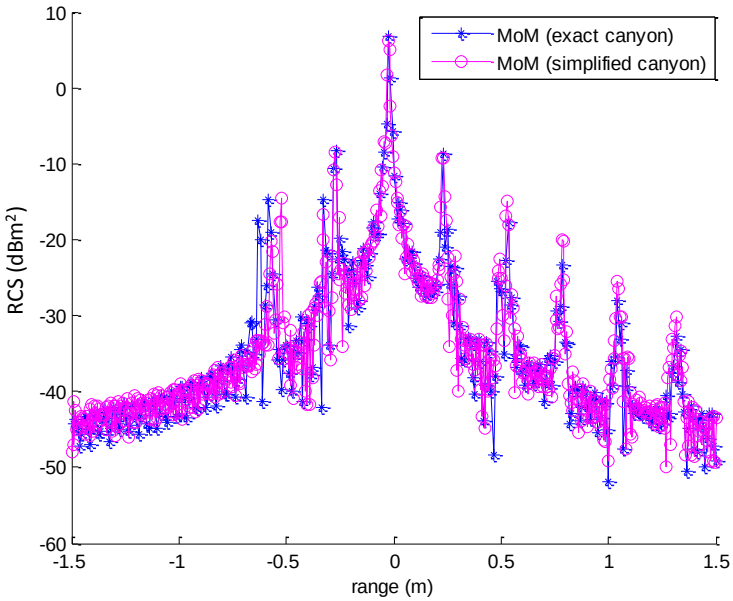

Figure 5.4: Comparison between two range profiles simulated with FEKO. The blue curve is obtained using MoM on an "exact" canyon configuration and the pink curve is obtained using MoM on a "simplified" canyon configuration.

on the number of reflections used to estimate the EM scattered fields. The results are illustrated in Fig.B.11. The first simulation is using PO without indicating the number of optic rays or "reflections" (the default is 1) to estimate the scattered field on the surface, the second one is carried out by setting the number of optic rays to 4 and the last one by setting the number of reflections to 12.

- For the first simulation, the expected peaks are the two double peaks on the two walls of the canyon,
- For the second simulation, the peak of the dihedral effect on the wall 1 is expected to appear on the simulated range profile as it corresponds to a geometric mechanism with 4 number of reflections of the incident rays (the peak identified with clear blue circle in Fig.4.18 whose corresponding mechanism is illustrated in blue color in Fig.4.17),
- For the third simulation, when considering 12 reflections, more peaks are expected to appear (see Fig.4.18), but not all the peaks simulated with MoM.

This is validated with the simulation results as illustrated in Fig.B.11. We notice that there is a good agreement between the range profile using MoM and the range profile using PO with 12 reflections, when the peaks are simulated. Surprisingly, PO with 4 reflections is more time consuming than the MoM, probably because this latter method has been dramatically optimized, on the contrary of PO. In the case of PO simulations with more than 1 reflection, shadow effects have to be calculated in order to determine precisely the illuminated surfaces. This could explain the huge time difference between simulations with 1 reflection (less than 1 min) and 4 reflections (13h).

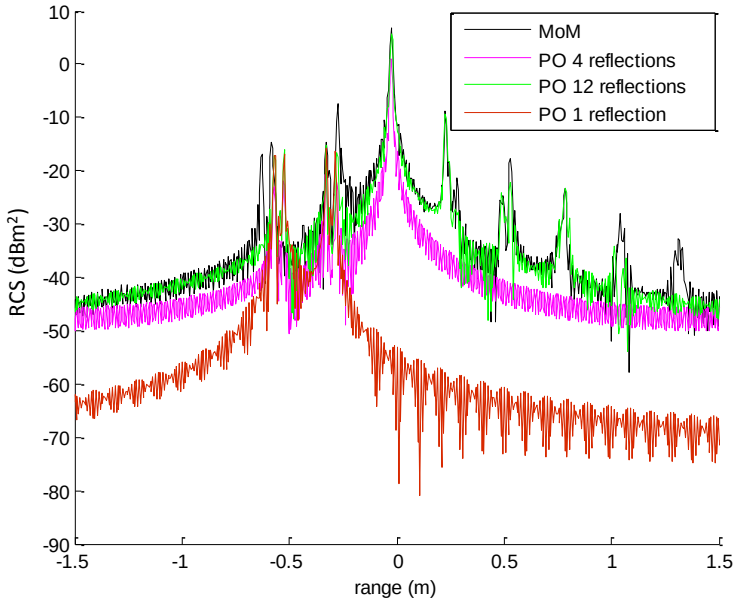

Figure 5.5: Simulations results using MoM and PO with 1, 4 and 12 reflections.

Simulations using GO

As the GO is a ray tracing based method, it considers that the diffusion is in a narrow lobe (assimilated to a ray). No angular variation in diffusion is taken into account. Hence, the only possible mechanisms are the the mechanisms induced by a small angular variation in incidence which are the backscattering on the two walls and the dihedral effect of wall 1 with 4 number of reflections. These mechanisms are illustrated in Fig.4.11. Setting a number of reflections greater than 4 does not change the simulation results (see Fig.5.6). Indeed, the range profiles for GO using 5 number of reflections is the same as for GO using 10 reflections. GO is not able to simulate the effects observed in the anechoic chamber.

Finally, the MoM applied to a "simplified" canyon configuration seems to be the more relevant method to simulate the effects occurring inside the canyon in the anechoic chamber.

Simulations using UTD

As the UTD can be considered as an extension of the GO since it is a ray tracing method allowing the calculation of a new effect which is the diffraction, we have simulated a range profile with UTD and we compared to a range profile with GO (5 reflections) in order to determine if there are diffraction effects. As illustrated in Fig.5.7, there is no difference between the two range profiles. So, we can conclude that for this case of the canyon in the anechoic chamber BABI, there are no diffraction effects.

5.2.3 Case of a canyon with an included target

Since the MoM takes into account all the EM multipath propagation effects inside an empty canyon, we will check now if the MoM can correctly simulate the case

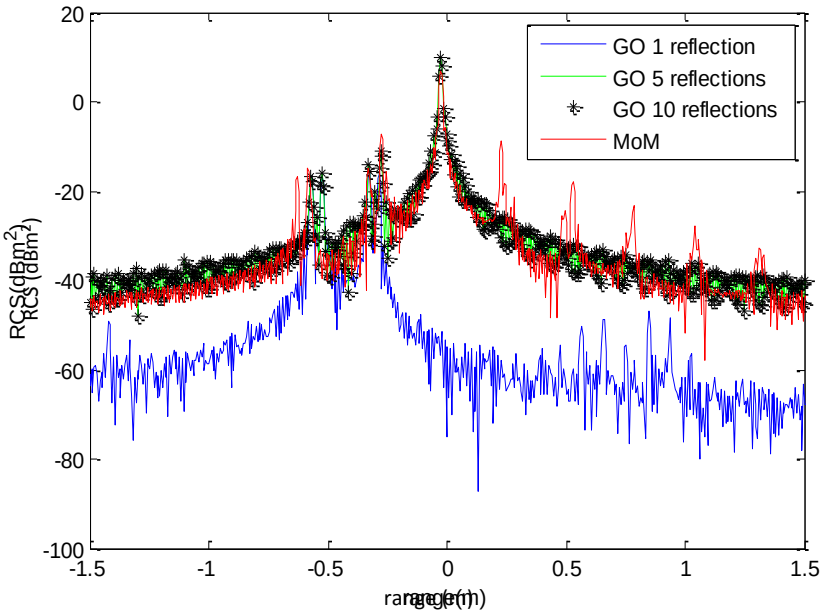

Figure 5.6: Simulations results using GO with 1, 5 and 10 reflections.

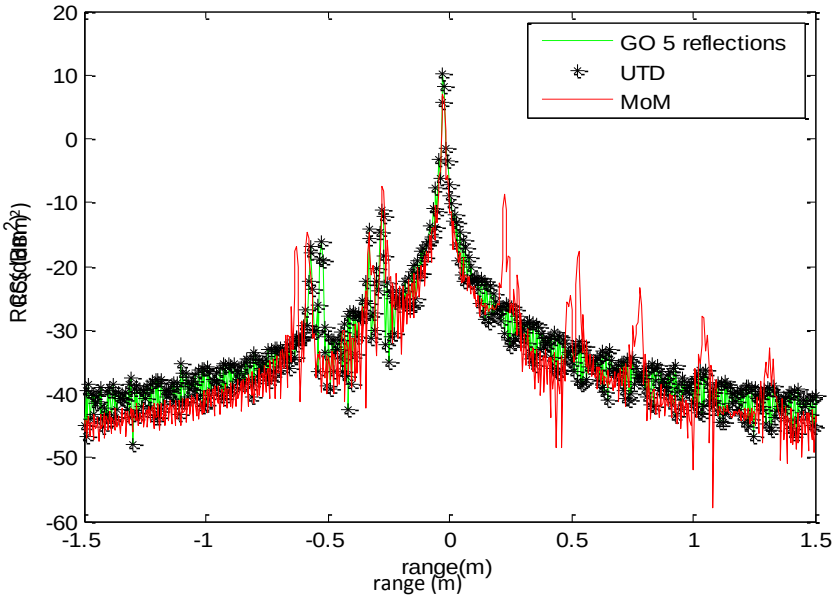

Figure 5.7: Simulations results using UTD, GO with 5 reflections and MoM.

of a canyon with an included target corresponding to the scene of Fig.4.7. Fig.5.8 presents a comparison between the simulated range profile using MoM for an empty canyon and for a canyon with an included target. As we can notice, MoM simulates the three responses of the target identified in the experimental range profile of Fig.4.19. The peaks of the responses are illustrated in red, green and blue circles. We notice that the amplitude of the peaks of the target is more important for the simulations than for the measurements since for the simulations, no roughness effects are taken into account as well as the antenna pattern that may cause a loss of the amplitude.

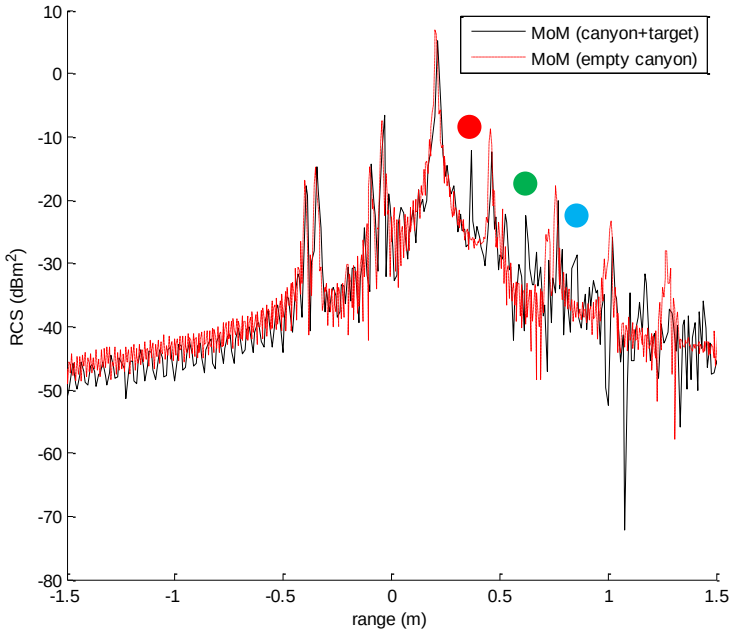

Figure 5.8: Simulated range profiles using MoM for an empty canyon and for a canyon with an included parallelepiped target. The responses of the target are illustrated with red, green and blue circles.

5.3 Validation of CST

In this section, we will present the results of simulations of the validated tool CST on an empty canyon configuration and on a canyon with an included target.

5.3.1 Case of an empty canyon

Fig.5.9 presents a comparison between an experimental range profile and a range profile simulated with CST and FEKO (MoM) for an empty canyon configuration (the "exact" canyon configuration). As we can notice, there is a good agreement in terms of phase and amplitude of the different peaks between the experimental data, the EM method of reference (MoM) and CST. The form of the range profile using MoM is different from the form of the range profile using CST for two reasons:

- The outputs of MoM are in the frequency domain, therefore, an Inverse Fourrier Transform is applied to obtain the signal in the time domain in order to calculate the radar range profile. This is not the case of CST since the outputs are generated directly in the time domain,
- CST applies a convolution with the initial signal to calculate the radar range profile.

We can conclude that CST is a reliable EM tool. In addition, the calculation time of the simulations is significantly less than FEKO. Nevertheless, as mentioned in Sec.3.5, CST is based on the FDTD method that requires a full discretization of the electric and magnetic fields throughout the entire volume domain which can be time and computer resources consuming for the case where the considered structures become large.

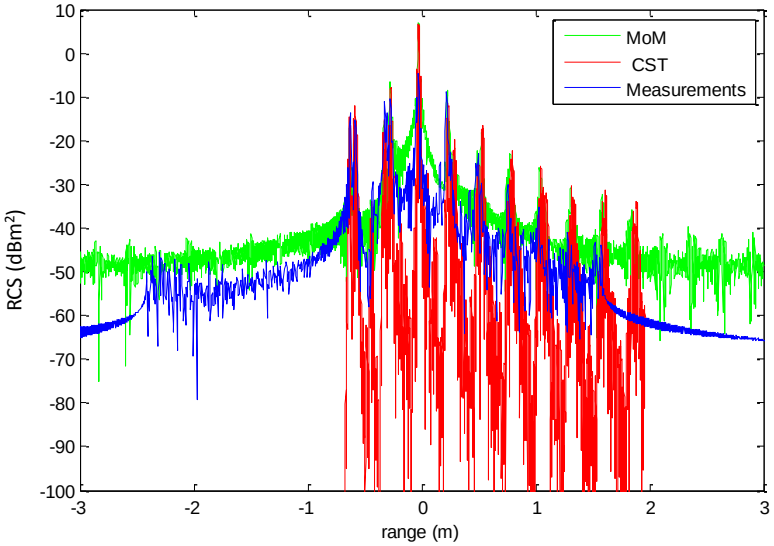

Figure 5.9: Comparison between an experimental range profile and simulated range profiles using MoM and CST.

5.3.2 Case of a canyon with an included target

In Fig.5.10, a comparison between two simulated range profiles by CST for the case of an empty canyon (Fig.5.10(a)) and for the case of a canyon with an included target (Fig.5.10(b)) for Vv and Hh polarizations. The responses of the co-polarized channel have not been represented since they have a very low value (-200 dB). As we can see, a range profile for an empty canyon has a periodic appearance (a periodicity of the peaks), however, when including the target, this periodicity is no more preserved. We can conclude that the presence of the target breaks the periodicity of the peaks in the range profile calculated for an empty canyon.

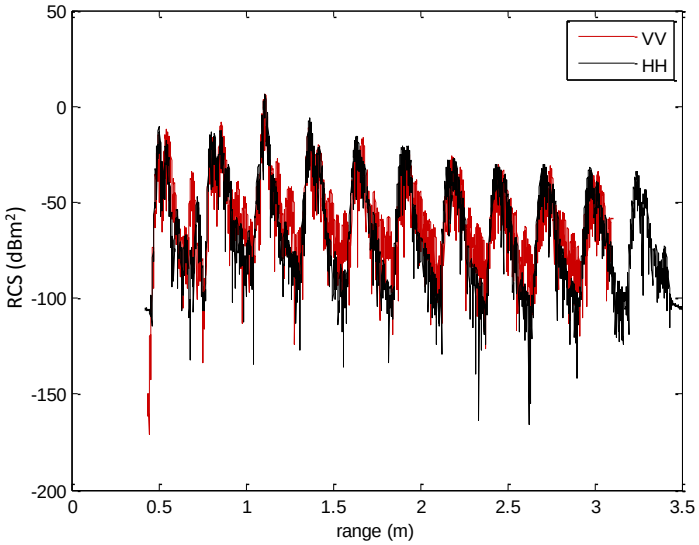

(a) CST range profile simulation for an empty canyon.

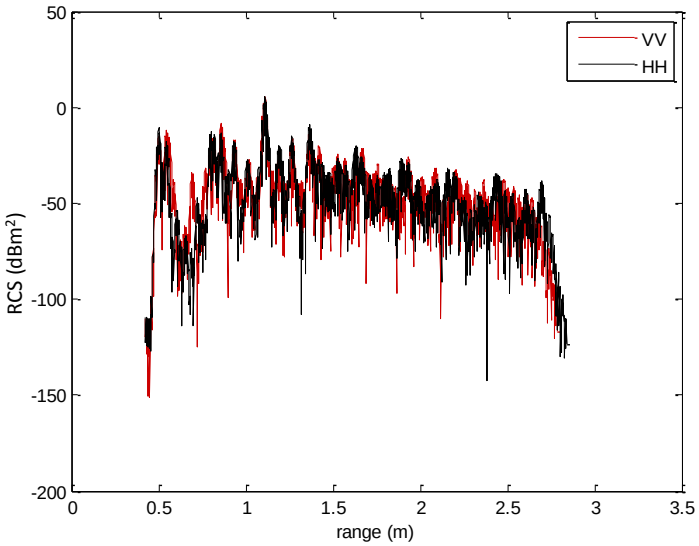

(b) CST range profile simulation for a canyon with an included target.

Figure 5.10: CST simulations for a canyon configuration with and without target.

5.4 Effects of the geometry of the canyon on the range profile

In this section, the goal is to perform additional FEKO simulations in order to investigate what happens in a non perfectly symmetric case. With the use of polarimetry, we expect to gain additional knowledge about the influence of the geometry of the canyon on the EM mechanisms occurring inside it. Two types of simulations have been performed:

- Simulations on a tilted canyon,
- Simulations on a distorted canyon.

The polarimetric information has been investigated using Pauli decomposition [Zhang 2008] assuming that:

- The decomposition concerns pure targets,
- The system is assumed to be reciprocal,
- The scattering matrix is rearranged to highlight the surface, the double, and the volume scattering.

For the simulations, combinations of the polarimetric channels have been done to highlight some EM effects. In fact, in FSA (Forward Scattering Alignment) system [Ulaby 1990] :

- The sum of co-polarization channels is related to single or odd bounce scattering (the surface scattering),
- The difference of co-polarization channels is related to double or even bounce scattering,
- The cross-polarization is related to the volume scattering.

5.4.1 Simulations on a "well oriented" canyon: the canyon of reference

In Fig.5.11, we present the simulations results using MoM on a "simplified" canyon structure for all the polarizations at the frequency of the anechoic chamber, meaning for a low d/λ ratio. As we have already noticed, there is a multitude of peaks which are approximatively spaced by x_L (defined in Eq.4.10). As for the explanation concerning the measurements results (see Subsec.4.4.3), the position of the peaks are different from the expected ones (by the theoretical calculation) due to the angular variation in diffusion. The cross polarization channels contain a very low information (-70 dB) due to the symmetry of the canyon under study. In Fig.5.12, we performed simulations using the Pauli decomposition to confirm the predicted mechanisms occurring inside the canyon in terms of bounces of the incident rays.

- The orange curve related to the sum of the co polarization channels indicates the double or even bounces scattering mechanisms,
- The black curve related to the difference of the co polarization channels indicates the single or odd bounces scattering mechanisms,
- The green curve related to the cross polarization channels indicates the volume scattering effect.

When analyzing the different range profiles, we noticed that:

- For the first double peaks related to the backscattering on the top and the bottom of the first wall, the single bounce response is dominant, the difference

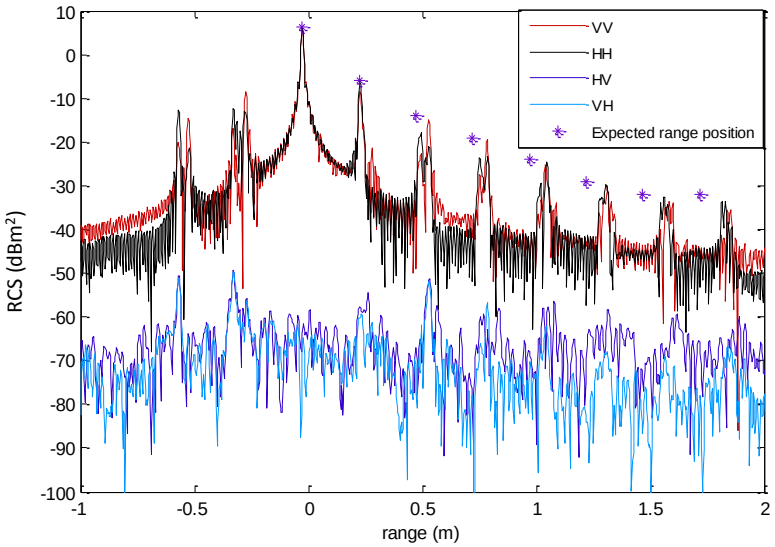

Figure 5.11: Simulated range profiles using MoM for all the polarization channels. The expected range positions by the theoretical calculation are illustrated in purple color.

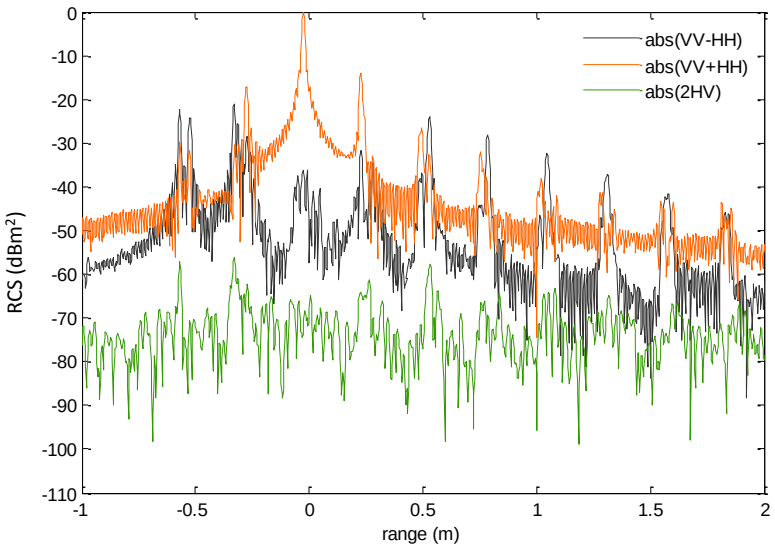

Figure 5.12: Simulated range profiles using MoM according to the Pauli decomposition.

in range between these two peaks has been verified as it corresponds to the the difference in path length denoted d_L in Fig.5.13 and defined as:

$$d_L = h_1 \times \cos\theta \tag{5.1}$$

θ is the incidence angle and h_1 is the height of the first wall.

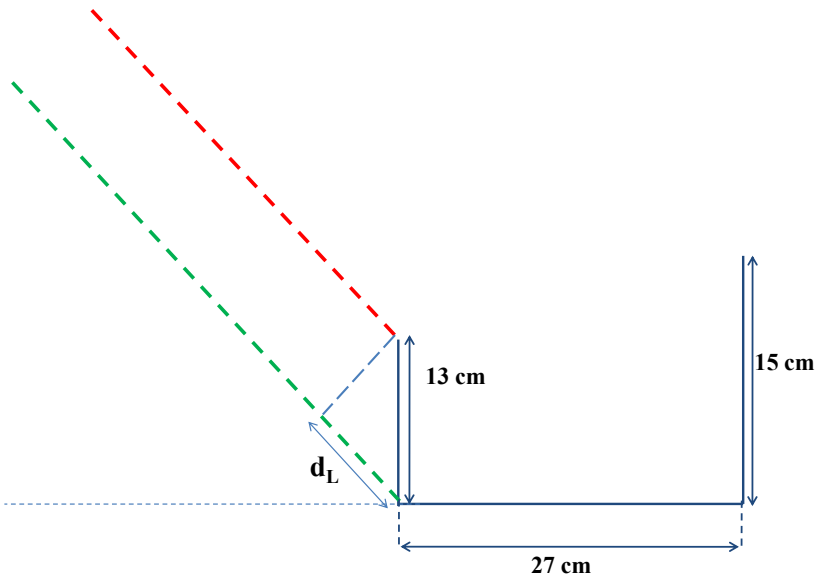

Figure 5.13: The difference in path length between the two mechanisms of backscattering on the top and the bottom of the first wall.

- For the following double peaks related to the backscattering on the top and the bottom of the second wall, the single bounce response is dominant for the first peak. However, the double bounce response is dominant for the second peak (see the mechanism illustrated with pink dashed line in Fig.5.14). This is due to the angular variation in diffusion that induces a dihedral effect (a double bounce mechanism) on the bottom of wall 2,
- For the peaks related to multipath propagation inside the canyon, the corresponding double bounce response dominates. However, as the number of interaction increases, the angular variation in diffusion becomes more significant. The parity of bounces changes and new mechanisms of odd number of bounces appear.

5.4.2 Simulations on a "tilted" canyon

Since in realistic configurations, the canyons are not always parallel to the flight direction, in addition, the trajectory of the sensor can not be always parallel to the each of the canyons composing an urban scene, we decided to study the impact of a disoriented canyon on the different mechanisms happening inside. To investigate these effects, We studied the effects of a "tilted" canyon on the mechanisms occurring inside it using the polarimetric information. In Fig.5.15, we present the MoM simulations according to the Pauli decomposition for:

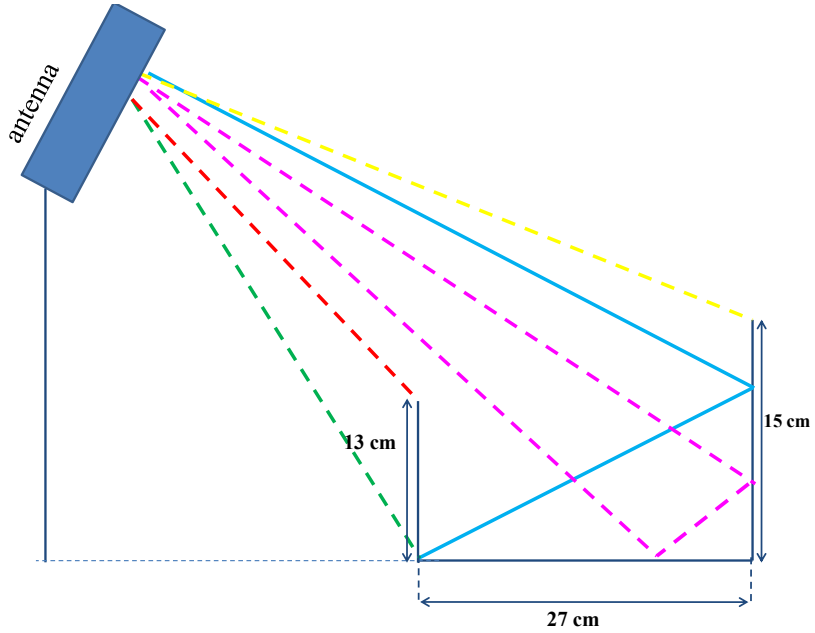

Figure 5.14: Double bounce effect on the bottom of wall 2 illustrated with dashed pink line.

- A "simplified" canyon configuration which is oriented perpendicularly to the propagation plan (named canyon of reference) (Fig.5.15(a)),
- A "simplified" canyon configuration tilted by 5.2° (Fig.5.15(b)),
- A "simplified" canyon configuration tilted by 37° (Fig.5.15(c)).

As we can notice, the more disoriented the canyon is, the more the cross polarization responses increase and hence the amplitudes of the different polarimetric mechanisms tend to be the same. In addition, the periodicity of the peaks that existed in a well-oriented canyon disappears and the different responses on the range profile become difficult to distinguish. This typically lead to a high entropy [Cloude 1996] on the contrary of what is usually observed in urban areas. Therefore, for a classification problem, due to a change on the geometry of the urban structures, the urban areas can be classified as vegetation which decreases the accuracy of the classification.

5.4.3 Simulations on a "distorted" canyon

In some urban areas, some canyons can have walls that are not be parallel between them. To investigate about the effect of such distorted geometry on the effects happening inside the canyon, we performed some simulations on a canyon with no parallel walls as illustrated in Fig.5.16. In Fig.5.17, we present the MoM simulation results according to the Pauli decomposition for:

- A "simplified" canyon configuration which is oriented perpendicularly to the propagation plan (named canyon of reference) (Fig.5.17(a)),
- A "simplified" canyon configuration where the wall 2 is not parallel to the wall 1 (see Fig.5.16), the corresponding range profile is illustrated in Fig.5.17(b).

As for the case of a tilted canyon, the entropy increases inside distorted canyons as the cross polarization responses increases and on the other hand, the response of

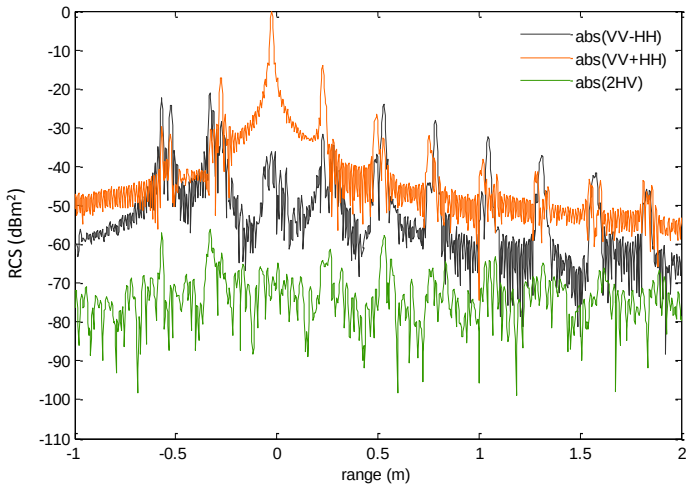

(a) Canyon of reference.

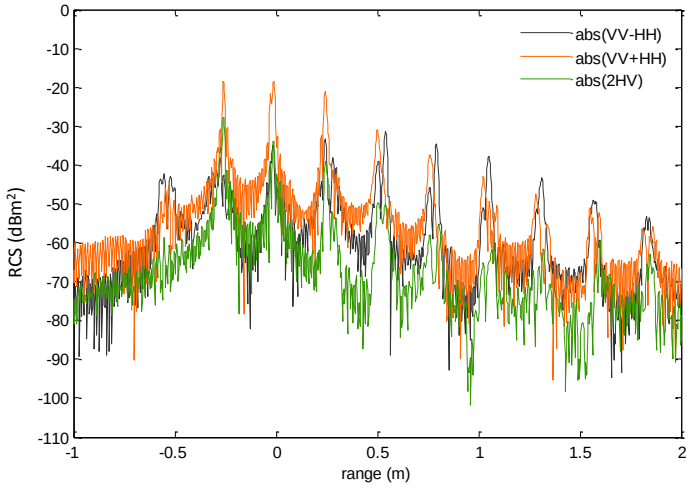

(b) "Tilted" canyon of 5.2°.

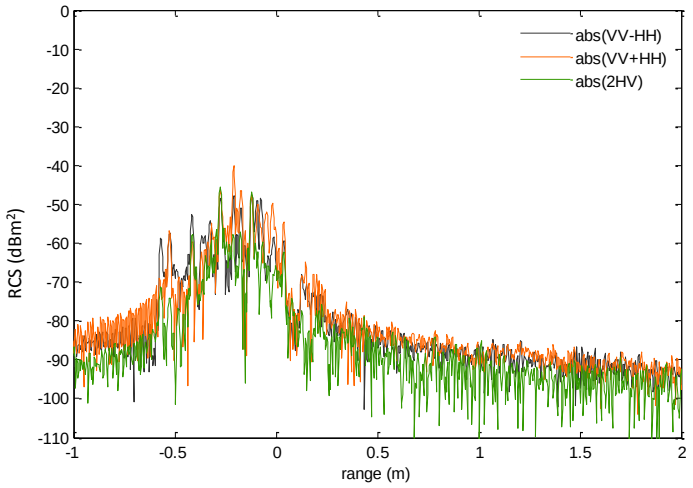

(c) "Tilted" canyon of 37°.

Figure 5.15: Effects of the disorientation of the canyon on the polarimetric signature.

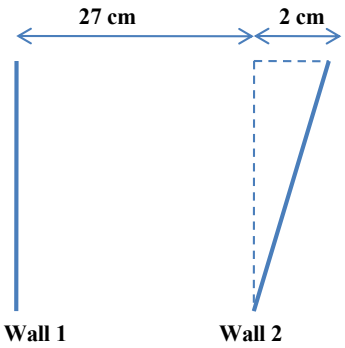

Figure 5.16: Distorted canyon used for the simulations: Wall 2 not parallel to wall 1.

the mechanisms with an odd and even number of bounces decreases.

5.5 Effects of a very high frequency (d/λ ratio tending to the real one)

Since our main objective is investigate about the EM effects in real case configurations, we have to ensure a d/λ ratio that tends to the real one. Therefore, an increase of the frequency is required for the simulations on the canyon configuration. Referring to the scattering by a PEC plate of dimensions 15 cm $\times$ 22 cm at the frequency of 78 GHz and an incidence angle of 70° in Fig.4.15, we can expect that the diffusion at higher frequency will be in a narrow lobe so that all the mechanisms due to the angular variation of diffusion will disappear. We present in Fig.5.18, the simulation results of the MoM and GO on a "simplified" canyon structure at the frequency of 78 GHz. As expected by the theoretical results, the number of peaks decreases because only the geometric mechanisms illustrated in Fig.4.11 exist. The MoM and GO agree in terms of phase and amplitude noticing that the GO is faster that the MoM in terms of simulation time. From this simulation, we can conclude that:

- In real case configurations, the diffusion is in a narrow lobe, so an EM method based on ray launching will be efficient to model the EM scattering,
- GO, as it is a ray based method, provides a satisfying trade-off between the calculation time and the accuracy of the results. Thus it can be used to study the EM phenomenology of propagation for real case urban scenes.

Current simulations are performed to investigate about the detection of the parallelepiped target using GO and CST at the frequency of 78 GHz.

5.6 Conclusion

In this chapter, we presented the results of validation of FEKO with an exact EM method (MoM) and approximated EM methods (GO, PO and UTD), as well as the results of validation of CST, using the anechoic chamber data. FEKO has been

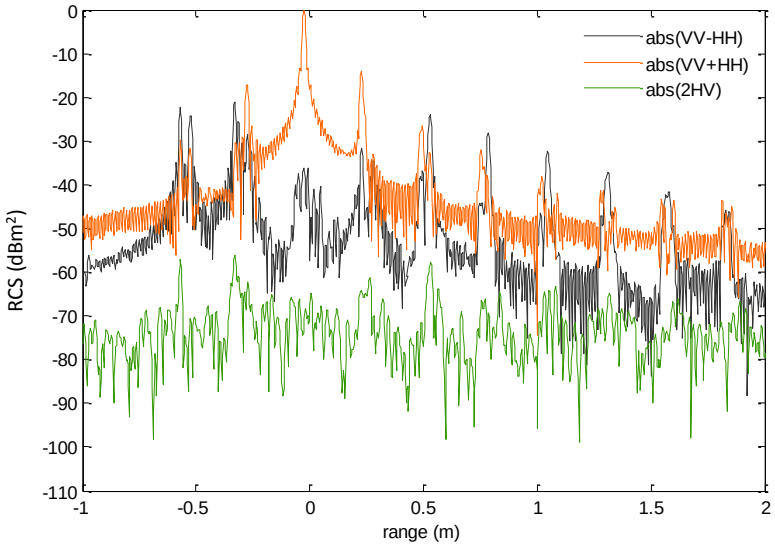

(a) Canyon of reference.

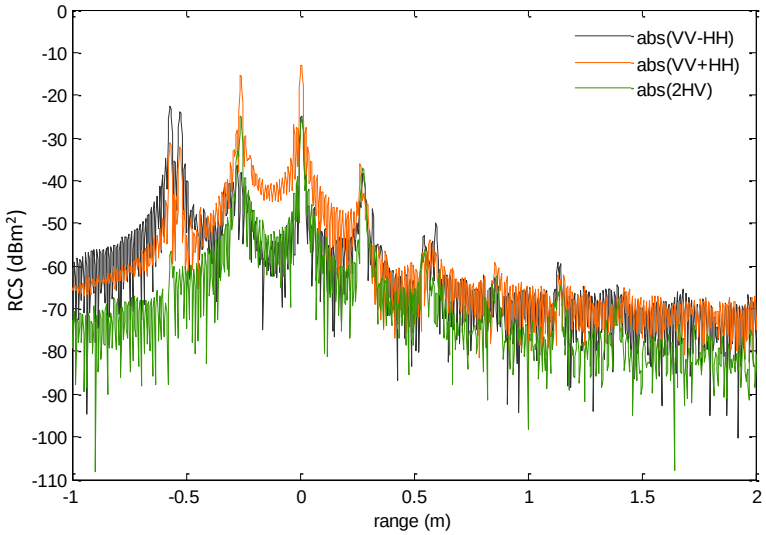

(b) Wall 2 not parallel to Wall 1.

Figure 5.17: Effects of a distorted canyon on the polarimetric signature.

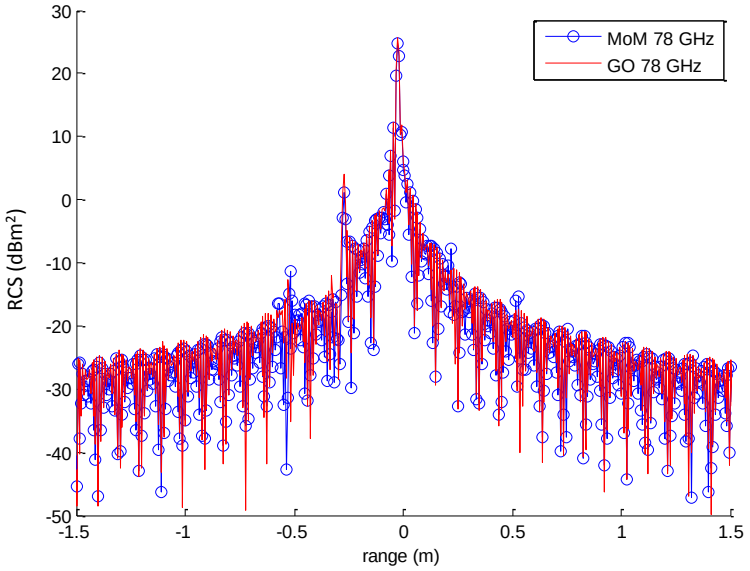

Figure 5.18: Simulated range profiles using MoM and GO at the frequency of 78 GHz on a "simplified" canyon structure .

used on a "simplified" canyon configuration to avoid the heavy time calculation specially for high frequency simulations. We have concluded that the MoM, the method of reference, simulates correctly the scattering effects inside the canyon and that the others approximated methods have no advantages comparing to the MoM whether for the accuracy of the results (GO does not simulate all the effects and PO need a big number of reflections to simulate all the effects and hence a huge time calculation) or for the time simulation (UTD is a time consuming method).

To gain additional knowledge about the influence of the scene geometry on the range signature as in real case, the canyons are not always oriented parallel to the flight direction, we performed simulations on a tilted and distorted canyon. We used Pauli decomposition to use the polarimetric information. We noticed that the entropy increases with a disorientation of the canyon that may lead to a misclassification of the urban areas.

In addition, we performed simulations at higher frequency ensuring a d/λ ratio tending to the real one and the theoretical results concerning the scattering in a narrow lobe for real case configurations have been confirmed. An agreement has been found between MoM and GO noticing that GO is less time consuming than MoM so that we can consider that FEKO with GO is an optimal EM tool to study real case configurations. Based on these simulation results, our EM tool has been developed to investigate NLOS target detection inside real case urban canyons and its validation with FEKO will be presented in the next part.

Summary

The second part of the thesis concerned the presentation of the different EM tools used to investigate about the EM phenomenology of propagation inside a controlled environment where the d/λ ratio is not respected. The first chapter was an overview of the different EM tools that we tested. Two of them have been selected (FEKO and CST) as they have been validated with the measurements and the others have been rejected due to their limitations to model the urban scattering as well as the difficulties we encountered to validate them.

We gave in the second chapter a detailed presentation of the anechoic chamber data as well as the obtained experimental results. With a theoretical study of the response of the plate having the same dimensions as the walls of the canyon at the frequency of the anechoic chamber, we provided an explanation to the unexpected multitude of mechanisms that occurred inside a canyon which is in far field of the antenna. Due to the angular variation in diffusion because of a low d/λ ratio, multitude of peaks approximatively equally spaced have been found on the experimental range profile. The theoretical study showed that this effect can disappear when ensuring a d/λ ratio tending to the real one since the scattering will be in a narrow lobe. As it is technically not possible to investigate this effect on the anechoic chamber, the idea was to perform simulations at high frequency with a validated EM tool. This was investigated in the third chapter where we presented the results of simulation of FEKO and CST on a canyon configuration with and without a target. Moreover, additional simulations have been performed to assess about the impact of the geometry of the canyon on the range signature responses. Simulations have been performed on a distorted canyon and consequently, the periodicity of the peaks that existed in the range profile of a well oriented canyon disappeared, the cross polarization responses increased with the same amplitude as the co-polarization responses which lead to a high entropy. This can mislead to a wrong classification of the urban areas. In addition, simulations at high frequency ensuring a d/λ ratio tending to the real one, showed that the scattering is in a narrow lobe in realistic configurations.

The study of this increase in frequency, led us to validate a simple method, such as the GO, that could perfectly fit to our needs whereas it has been rejected as it failed to correctly reproduce the indoor data. This implied that a simple in-house code could be developed based on very simple EM approximations in order to have a fast tool operating for real d/λ ratios.

Part III

In-house EM code: presentation, results and application

Introduction

The second part of the thesis has been devoted to investigate the EM phenomenology of propagation inside a canyon with an included target in a controlled environment (the anechoic chamber). The main conclusions we have drawn is that the propagation in real case for a PEC canyon will be according to the specular direction with no significant diffusion effect to take into account. This assumption is demonstrated by a theoretical study and confirmed by a validated EM commercial tool (FEKO) based on an exact EM method (MoM) (see chapter 3 of part II).

The use of a validated EM commercial code to investigate NLOS target detection turns out to be really time consuming, even for small urban structures. Thus, the need to develop a fast EM tool based on an approximated EM method to avoid an enormous time running simulation.

Referring to the conclusions concerning the EM phenomenology of propagation in real case configurations, we developed our own EM tool. This tool is dedicated to PEC canyons that are perpendicular to the propagation plan. However, in real case configurations, unless we have a model of the materials composing the scene both in terms of permittivity and roughness, the amplitude can never be validated due to the wide variety of materials and the dependance of the reflection coefficients on the incidence angle and the frequency as already stated in [Hammer 2008]. In urban areas case, such model is unfortunately not available. This partly explains the reason why we have chosen to build a tool dedicated to a general case (PEC case) and to adapt it after by assigning the reflection coefficients of some dielectric materials. The choice of PEC materials enables to validate the amplitude of the responses without an a priori knowledge of the materials composing the scene. The second assumption concerning the orientation of the canyon is established because we restrict ourselves in this preliminary study to the 2D case which is the most favorable configuration to investigate the multipath propagation effects. In fact, based on the analysis performed with FEKO on tilted and distorted canyons, we can state that the geometry of the canyons has a considerable impact of the different mechanisms occurring inside it.

Our EM tool is based on an approximated EM method. This method takes into account only specular reflection mechanism, and assumes that the total scattered electric field depends only on the paths of the rays. The first output of the code is the NLOS detectability areas inside the canyon where a target can be detected. In the state-of-art works that investigated the tracking of target in simple urban scenarios, the potential of multipath propagation has been demonstrated in the frame of detecting moving targets. In the present thesis, this assumption is confirmed by the study of NLOS detectability areas inside a canyon. In fact, we will demonstrate through examples that the NLOS areas illuminated by multipath propagation provide a wide coverage comparing to the areas illuminated by LOS and hence this is an additional proof of the interest of multipath propagation study inside urban canyons.

In addition to the detectability areas, our EM developed code predicts for the case where the target is present, if it can be detected and the corresponding mecha-

nisms of detection. Moreover, this tool calculates the radar range profile, a fast and simple output that is efficient to investigate about the detection of NLOS targets. Actually, when analyzing the radar range profile, we can determine the location of the target, its nature and its orientation. The validation of this EM developed tool has been investigated by a comparison with the simulation results of FEKO and a good agreement was found both in terms of phase and amplitude for the different responses. Our EM tool, even simple, is efficient to rapidly investigate about the detection of NLOS targets with a complete validation. The validation of a commercial EM code as well as the validation of a developed code constitutes the main contribution of this thesis, because we have demonstrated through our study of the current state-of-art, that many sophisticated simulators exist and provide satisfying simulation results of detailed urban scenes, but the validation of the amplitude has not been assessed yet. The first two chapters of this part are dedicated to provide a complete description of our developed EM tool with its different versions. A presentation of the inputs, outputs, the simulation results and the process of validation is given.

A second proof of the efficiency of this simple EM tool is demonstrated through its application to interpret real SAR data of a canyon with targets. In fact, this tool has been used to analyze InSAR image of a more complex canyon including different materials. It helped to distinguish the different features of the image where a radiometric and interferometric study has been performed to provide an explanation of the interferometric signature. We should notice that even if the data of the canyon under study have been acquired with a tilt in azimuth of 9°, the results of our tool, initially developed for a canyon parallel to the flight direction of the sensor, remain valid.

The goal of the InSAR data analysis is to highlight one of the most common effects (named layover) observed in the SAR images of urban areas due to the geometric acquisition of the SAR systems (side looking illumination). This effect has a significant impact on the interferometric signature. Therefore, we performed a complete study of the distribution of the backscattering coefficients as well as the coherence coefficients in the areas of interest (layover areas) delimited by our EM tool. To do so, we proposed formulas that required a knowledge of the reflection coefficients of the materials composing the scene at the used polarization and incidence angle (chapter 8).

Chapter 6

In-house EM code for an empty canyon and for a canyon with an included point target

Contents

6.1 Introduction

In this chapter, the main goal is to present the first two versions of our EM tool dedicated in its first version to the study of multipath propagation inside an empty urban canyon (Urban Canyon V1) and to the detection of NLOS point targets in the realistic case in its second version (Urban Canyon V2). The long term objective is to develop an EM tool that helps in determining rapidly the most relevant radar configurations for future radar campaigns allowing a large percentage of detectability areas. The short term objective is to perform a complete study of the detectability areas for a canyon configuration with an included point target before investigating the case of more complex target (the extended target) that will be presented in the next chapter. The anechoic chamber data that we have at our disposal as well as the EM study we performed gave us useful information concerning the scattering inside the urban canyon for the indoor as well as for the outdoor environment (see the previous part). The main conclusion is that in real case, the diffusion by a PEC canyon is in a narrow lobe, so that considering

only specular reflection mechanism between the walls of the canyon and the ground separating them is a valid assumption. Based on this, we developed a simple EM code that takes into account only specular reflection mechanism to study multipath propagation inside urban canyons. As we are focusing on a very specific geometry (the urban canyon), with a particular goal which is the possible detection of NLOS targets, we do not aim to produce a sophisticated SAR simulator. Our objective is to develop a simple (and consequently fast) EM tool to predict the possible detection of targets in NLOS configurations, and further to localize and identify them. To achieve this goal, the developed EM tool should be able to analyze all the possible canyon configurations (empty canyon and canyon with a target included) and to determine automatically if a return back to the radar is possible. The canyon we performed our studies on is a simple but representative object of an urban area involving a rich multipath propagation environment and that is the reason why we developed our EM code dedicated to it. In addition, we assumed that it is PEC, as for the moment we decided to consider the most simple and general case (no loss in the case of PEC so that all the predicted responses of the geometric mechanisms exist). We assumed also that it is perpendicular to the propagation plan, to restrict this preliminary study to a 2D problem before moving to 3D problem (future works). The first output of our developed EM code is the NLOS detectability areas. These detectability areas include the areas where the point target can be detected whatever its orientation (the NLOS detectability areas by specular reflection mechanism) and the areas where the point target can be detected provided it is well oriented (the NLOS detectability areas by backscattering mechanism). The second output is the canyon range signature evaluated by the radar range profile. The simulation and analysis of the range profiles provide useful information concerning the detection of NLOS targets inside the urban canyon. In fact, a deep analysis of the range profiles gives information about the possible location of the target, its directivity and its orientation. In addition, the phenomenology we derived from our simple EM tool is sufficient to obtain a good correspondence between the calculated range profile using our code and the simulated range profiles using the EM commercial tool (FEKO) we selected to study real case configurations. In fact, the validation of the results of our code has concerned the phase as well as the amplitude of the different retrieved peaks in the range profile. Even if our tool is strictly dedicated to urban canyons, it shows accurate results to investigate the NLOS point target detection inside this simple urban structure. The results of the second version of our EM tool (Urban Canyon V2) will be used later to interpret InSAR data for a canyon with two types of target included inside it (target scattering from one side that can be modelled as a point target and an extended target). This chapter is organized as follows: in the first section, we give a general description of our developed EM code. Then, the results of simulation of this code on different canyon configurations are presented. The simulation results concern the determination of NLOS detectability areas and the radar range signature for an empty canyon (Sec.6.3) and for a canyon with a point target (Sec.6.4). We pointed out the interest of the study concerning the NLOS detectability areas in the field of target detection through examples. Finally, some conclusions are drawn.

6.2 Presentation of the developed in-house code

The developed geometric code is a ray-tracing based code that simulates for a succession of canyons, all the rays that are able to go back to the receiver and calculates the corresponding radar range profile.

6.2.1 Inputs

As mentioned before, the input of the code consists of the description of N_c successive different canyons configurations defined by:

- The height of the two walls of each canyon,
- The width of the two walls of each canyon,
- The distance separating the walls of each canyon,
- The incidence angle (θ).

The canyons under study consist of PEC vertical walls separated by PEC horizontal surfaces representing the ground. Our analysis is based on the interpretation of distance profiles in a viewing direction belonging to a plane perpendicular to the wall surface. So for the moment the problem amounts to a 2D problem. Diffraction and diffusion outside the specular direction are neglected for all plates, hence only geometric mechanisms are taken into consideration. In Fig.6.1, an example of simulation of our code on a succession of three canyons ($N_c = 3$). They are delimited by dashed rectangles of different colors. However, as we aim to validate the results

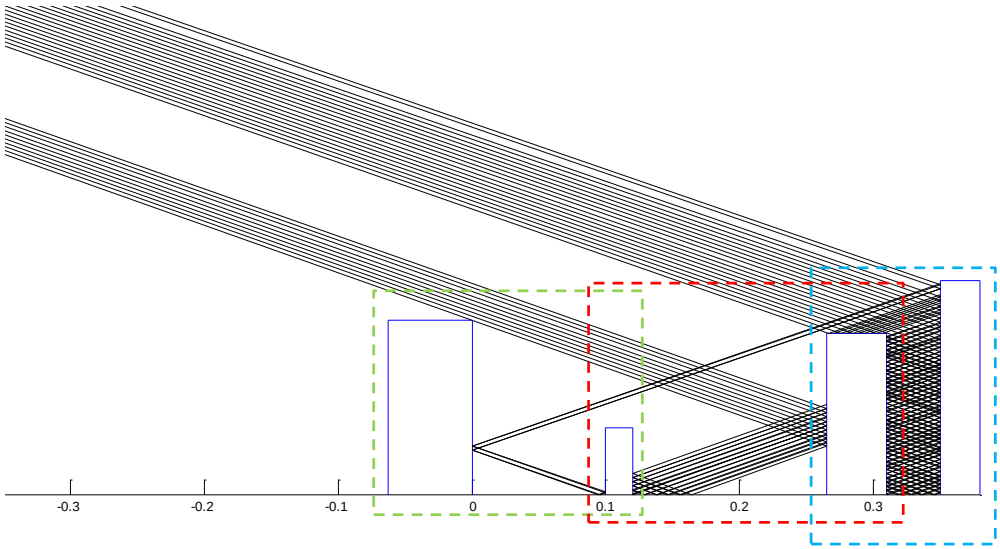

Figure 6.1: Visualisation of the simulated rays using our in-house EM code for a succession of three canyons ($N_c = 3$). They are delimited by green, red and blue dashed rectangles.

of our developed code with the simulation results of the selected EM code FEKO that has been tested on a single canyon, then, all the coming results will concern just one canyon to allow the validation.

6.2.2 Outputs

The outputs of our developed in-house code are:

- A visualisation of the incident rays that are able to return back to the receiver. This visualisation will help to determine the NLOS detectability areas,
- An evaluation of the range signature with an automatic calculation of the radar range profile.

In Fig.6.2, we give an example of a simulated radar range profile corresponding to the scene of Fig.6.1.

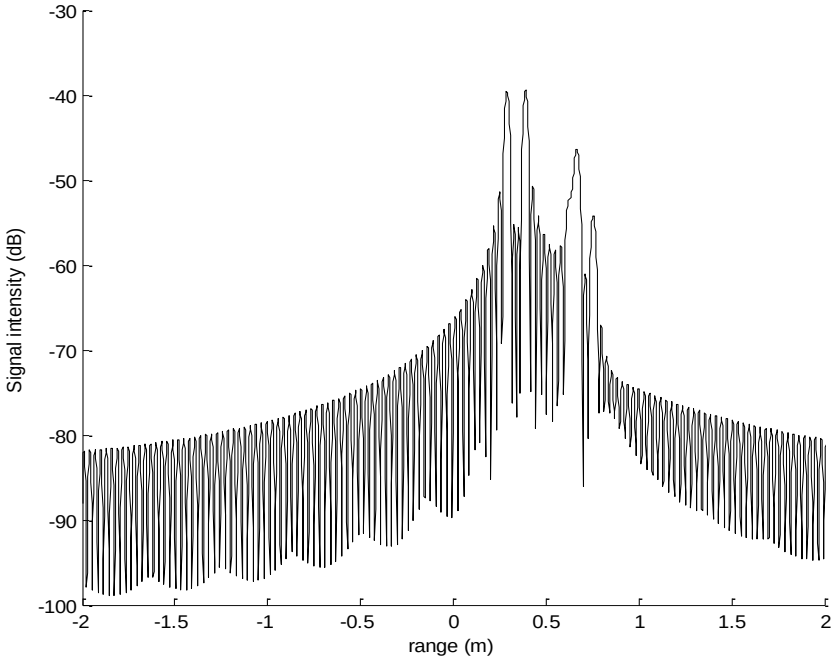

Figure 6.2: Radar range profile corresponding to the three canyons configurations described in Fig.6.1.

6.2.2.1 Output 1: NLOS detectability areas

The first output of this code is a visualisation of all the rays penetrating inside a canyon, making several specular bounces and going back to the antenna. An example of simulation on a single canyon is illustrated in Fig.6.3. The widths of the walls are not taken into account when simulating the incident rays since the rays of interest are those penetrating in the internal part of the canyon. However, we should notice that for a succession of canyons, the width of the different walls could impact the final outputs. The code simulates all the rays of the beam ranged in the angular aperture defined by the antenna and the two walls of the canyon. The number of rays N_R (fixed by the user) is obtained by sampling this beam. Since the antenna is located far from the canyon to ensure the far field case, the incident beam will contain parallel rays.

6.2.2.2 Output 2: Radar Range Profile

The second output of our code is the range signature of the canyon under study. This signature is determined via the range profile that means the squared amplitude of the radar return as a function of slant range. To be able to simulate such range profiles, we have made the following assumptions:

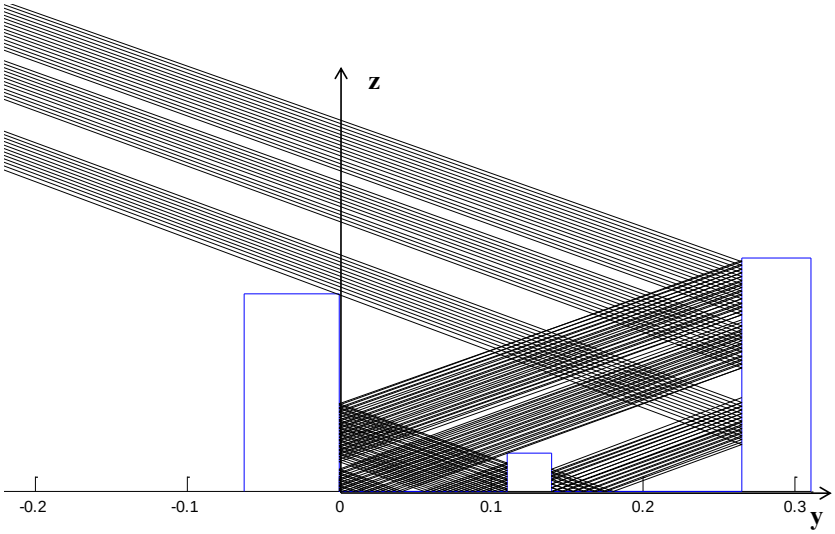

Figure 6.3: Visualisation of the simulated rays using the developed geometric code for a canyon with the presence of a parallelepiped target. The simulated rays are the rays able to return back to the receiver.

- The rays carry all the same amplitude over a frequency bandwidth,
- As we consider PEC case, the amplitude of the electric field corresponding to each ray will be proportional to the path of the ray R_i.

Considering N_R rays whose traveled path is given by $R_i, i = [1, N_R]$, then the total complex electric field $\underline{E}$ obtained for the frequency f_i is written as:

$$\underline{E}(f_i) = \frac{A}{N_R} \sum_{i=1}^{N_R} \frac{1}{R_i} \exp\left(-j\frac{2\pi}{c} R_i f_i\right) \tag{6.1}$$

A is the amplitude of the incident electric field which is supposed to be a plane wave. For simplicity in the following, A is set to 1. Then the Inverse Fourier Transform is applied on $\sum_{i=1}^{N_f} E(f_i)$ (where N_f is the number of frequency samples) to obtain the range profile.

$$\begin{cases} \mathcal{F}^{-1}(\underline{E}(f)) \\ \underline{E}(f_i) = \frac{A}{N_R} \sum_{i=1}^{N_R} \frac{1}{R_i} \exp\left(-j\frac{2\pi}{c} R_i f_i\right) \end{cases} \tag{6.2}$$

For all the following simulations using our EM code, the phase center is fixed in the bottom of wall 1 (see Fig.6.3).

6.3 Analysis of an empty urban canyon: Urban Canyon V1

The first step to analyze the response of an empty canyon is to determine the NLOS areas that are illuminated by multipath. Once these areas are determined, we can predict if a NLOS target within the canyon can be detected or not. In this section, we only consider the cases where the incident rays illuminating the NLOS zones can return back to the radar by specular reflection mechanism. These areas are named

the NLOS detectability areas by specular reflection mechanism and represent the first output of our dedicated developed EM code. The first version of the code is named Urban Canyon V1. This code takes as an input any canyon configuration defined by the height of the two walls (h_1, h_2) (the width of the walls will not be considered), the distance separating them (L) and the incidence angle (θ). These parameters are shown in Fig.6.4. The outputs are of two types:

- The NLOS detectability areas by specular reflection mechanism,
- The range signature of any empty canyon which is evaluated via the radar range profile.

In the following, the outputs will be explained more in details and analyzed through different examples. Then, we concluded this section by an illustration of the interest to perform the study of the NLOS detectability areas by specular reflection mechanism in term of target detection comparing the LOS ones.

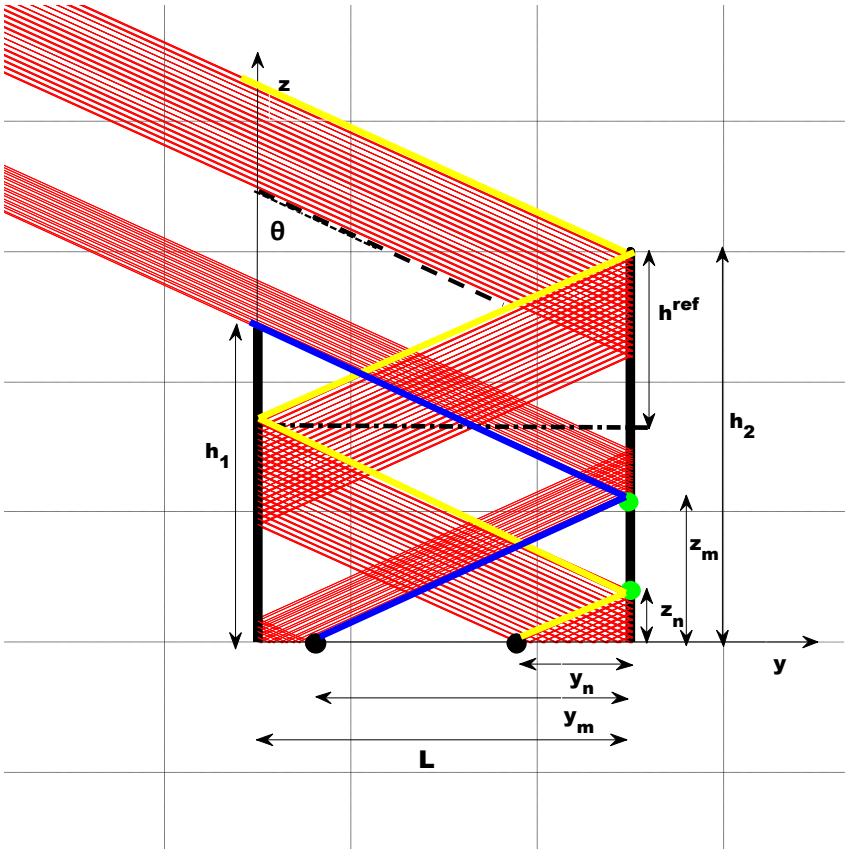

Figure 6.4: Geometric description of an urban canyon in a monostatic configuration: the incidence angle θ, the width L, the height h_1 and h_2 of the walls of the canyon, the penetration depth h^{ref} between two successive bounces, the height of the last bounce for different paths before reaching the ground (z_m, z_n) and quantities defining the illuminated part of the ground (y_m, y_n).

6.3.1 NLOS detectability areas by specular reflection mechanism

Urban Canyon V1 is an EM code that takes as an input any canyon configuration, determines the NLOS detectability areas by specular reflection mechanism and produces the corresponding range profile, as outputs. Still considering the 2D problem

and supposing that the antenna is far away from the canyon, geometric simplifications help to determine these areas literally, by assuming a constant incidence angle all over the canyon. First we have to check that the surface of the second wall is not entirely in the shadow of the first wall for the case where the first wall is higher than the second wall, that means that we have to ensure:

$$h_1 - h_2 \leq h^{\text{ref}} \text{ if } h_1 \geq h_2 \tag{6.3}$$

with:

$$h^{\text{ref}} = \frac{L}{\tan\theta} \tag{6.4}$$

and θ is the incidence angle (see Fig.6.4). Then, to determine the NLOS detectability areas by specular reflection mechanism, we have to consider two different rays:

- The ray that just passes the top of the first wall. It is represented in blue color (Fig.6.4). It penetrates into the canyon with a depth of h^{ref} making M bounces before reaching the ground. M is given by:

$$M = \left\lfloor \frac{h_1}{h^{\text{ref}}} \right\rfloor \tag{6.5}$$

  The elevation of the final impact point of this ray, denoted z_m, is simply given by the fractional part of $\frac{h_1}{h^{\text{ref}}}$. Its final abscissa on the ground, relative to the first wall, is given by $L - y_m$ where $y_m = z_m \tan\theta$.
- The ray that just passes the top of the second wall. It is represented in yellow color (Fig.6.4). The number of impacts along the incident path is defined by N given by:

$$N = 1 + \left\lfloor \frac{h_2}{h^{\text{ref}}} \right\rfloor. \tag{6.6}$$

  The elevation of the final impact point of this ray, noted z_n, is simply given by the fractional part of $\frac{h_2}{h^{\text{ref}}}$. Its final abscissa on the ground, relative to the first wall, is given by $L - y_n$ where $y_n = z_n \tan\theta$.

The condition of penetration of the two limit rays inside the canyon is expressed as follows:

$$|h_1 - h_2| \leq h^{\text{ref}} \tag{6.7}$$

The rays ranged between these two limit rays define an incident beam of parallel rays. The number of rays N_R is obtained by sampling this beam. This is equivalent to the sampling of the part of wall 2 illuminated by this beam. Once the condition in Eq.6.7 allowing the two limit rays penetrating inside the canyon is true, we have to ensure at least a return of one of the two previous considered rays (blue and yellow ray) to the antenna, which corresponds to the conditions expressed in Eq.6.8 and in Eq.6.9:

$$h_1 + h_2 \geq (2M + 1)h^{\text{ref}} \tag{6.8}$$

$$h_1 + h_2 \leq (2N - 1)h^{\text{ref}} \tag{6.9}$$

The NLOS detectability areas by specular reflection mechanism are determined according to the parity of M and N. This is shown in the chart of Urban Canyon V1 presented in Fig.6.5.

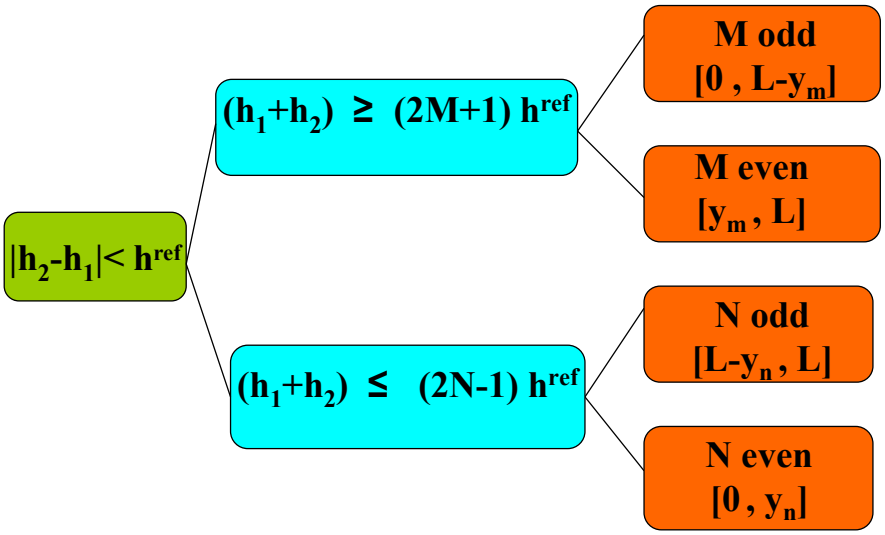

Figure 6.5: Algorithm for **Urban Canyon V1**: the condition to respect for the two limit rays to penetrate inside the canyon is recalled in the green box. The condition to go back to the radar (in the blue box) depends on the ongoing ray: either it just passes the top of the first wall (inequation with M), or the top of the second wall (inequation with N). Finally, the orange boxes contain the illuminated segments, depending on the ongoing ray and on the parity of bounces.

6.3.2 Canyon Range Signature

The second output of Urban Canyon V1 consists of calculating the range signature of any empty canyon. The range profile of an empty canyon may contain up to two peaks. We illustrate the three cases by some examples of range profile. Fig.6.7 and Fig.6.8 illustrate two examples of the simulated range profiles for an empty canyon using Urban Canyon V1. For these range profiles, the frequency band is equal to 500 MHz, leading to a range resolution of 30 cm. The central frequency is 35 GHz, the frequency step is 15 MHz and N_R=50.

- **0 peak:** none of the conditions in Eq.6.8 and Eq.6.9 is fulfilled,
- **1 peak:** one of the conditions is fulfilled. Depending on the parity of M (or N), either wall 1 or wall 2 is detected. We present in Fig.6.6 a canyon configuration corresponding to the case where M is odd ($M = 3$, $N = 4$). For instance, as M is odd and referring to the algorithm of Fig.6.5, the NLOS detectability area is $[0, L - y_m]$, hence, wall 1 is detected as the rays contributing to the dihedral effect of wall 1 belong to this area. Fig.6.7 illustrates the corresponding range profile.

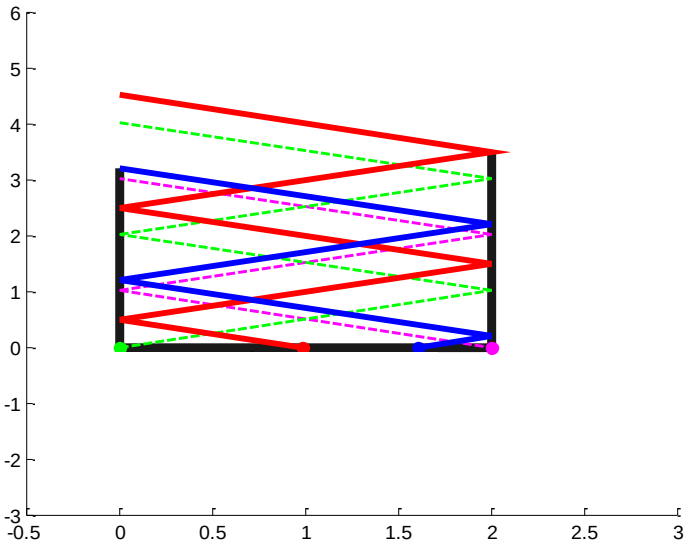

Figure 6.6: Example of a canyon configuration corresponding to the case where M is odd ($M = 3$, $N = 4$). Canyon parameters: $\theta = 63.4°$, $h_1 = 3.2m$, $h_2 = 3.5m$, $L = 2m$.

- **2 peaks:** both of the conditions are fulfilled. The two walls are detected and in the range profile, their corresponding peaks are separated by a distance of $L \sin\theta$ as we can see in Fig.6.8.

6.3.3 Percentage of detectability areas

Since in a NLOS detectability area with specular reflection mechanism, there is always a return of the incident rays to the antenna, hence, a target present in this area is always detected. Moreover, the NLOS areas are large comparing to the LOS ones. This is illustrated in Fig.B.13 where the percentage of NLOS detectability areas by

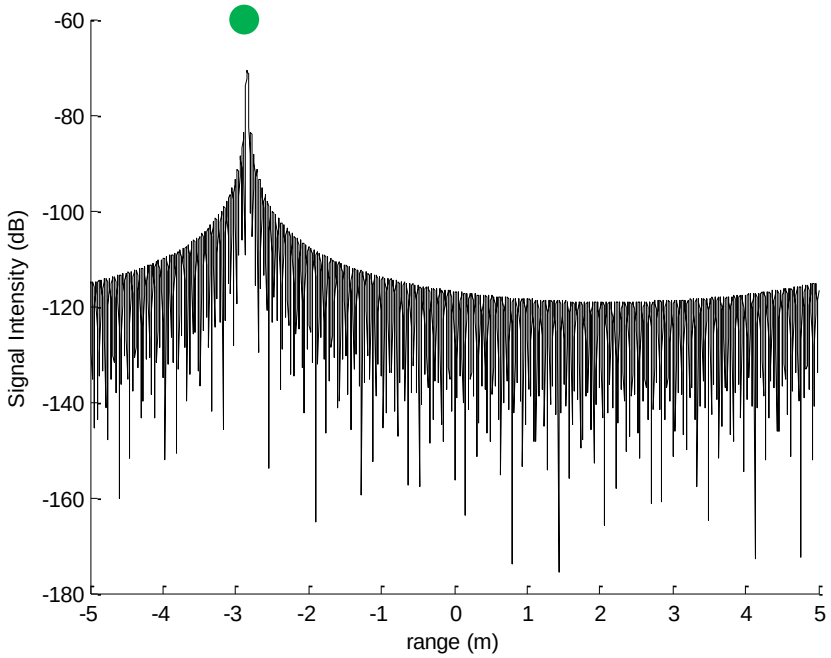

Figure 6.7: Range profile for the canyon configuration of Fig.6.6. The green dot refers to the peak of wall 1.

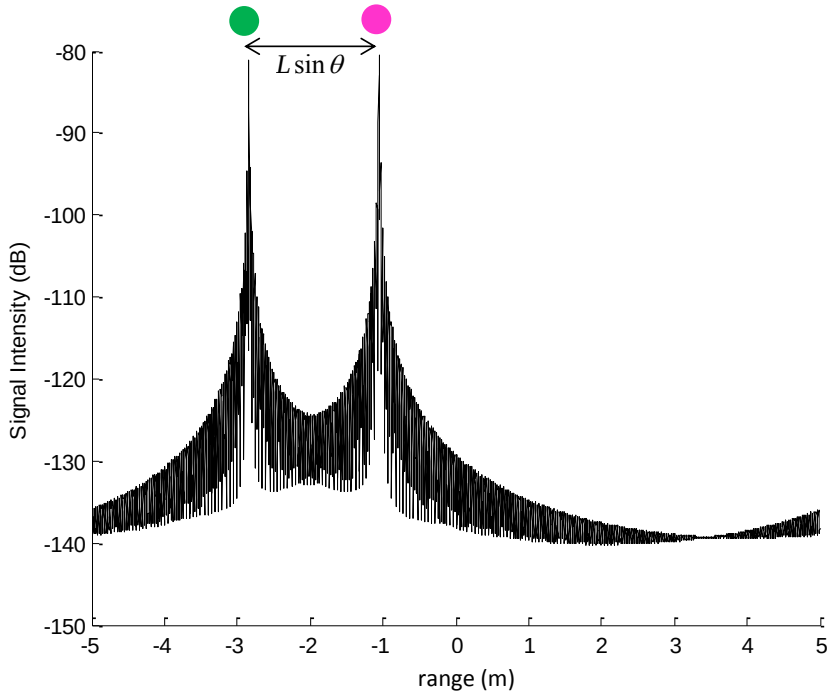

Figure 6.8: Range profile for a canyon configuration where both of the two walls are detected. The green dot of the first peak refers to the dihedral effect of wall 1 whereas the pink dot of the second wall refers to the dihedral effect of wall 2.

specular reflection mechanism for the canyon of Fig.6.6 is presented according to the incidence angle. The ratio between the size of the NLOS detectability area and the width of the canyon allows to derive this percentage. We notice that in this canyon configuration, no LOS areas exist. As we can see, the NLOS detectability areas vary according to the incidence angle. For this example, the percentage of NLOS detectability areas is always more than 30% and may reach 65% for $\theta = 64.5°$ whereas no LOS detectability area exists. Therefore, there is a clear interest in studying their location to determine if a target can be detected or not.

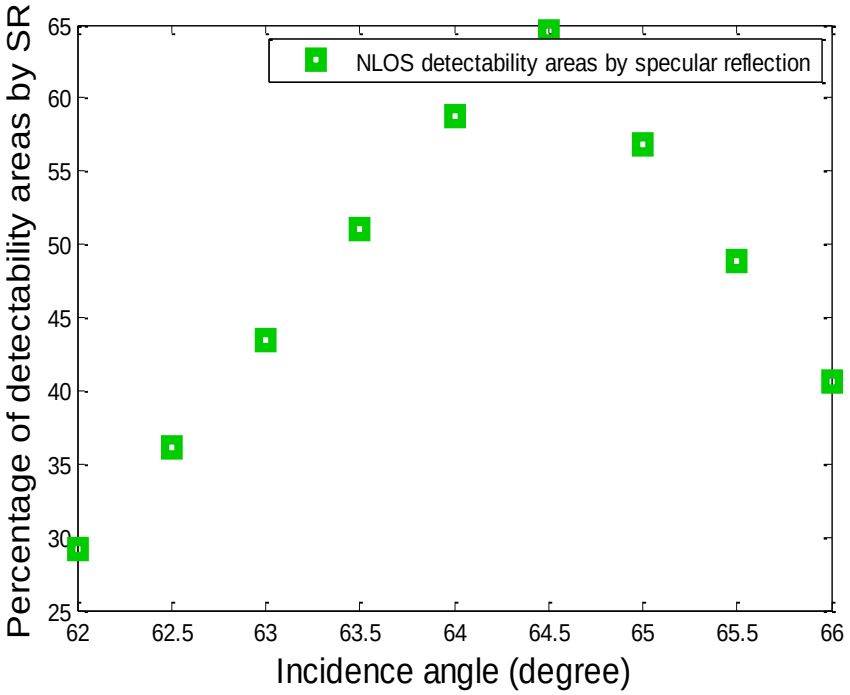

Figure 6.9: Percentage of NLOS detectability areas by specular reflection mechanism for the canyon configuration of Fig.6.6 according to the incidence angle.

In this section, the first developed EM code named Urban Canyon V1 has been presented with its proposed outputs. The range signature of an empty canyon has been investigated through the analysis of the corresponding radar range profile. Even if the radar range profile is a simple output that performs the response of the canyon according to a unique and specific direction, it is well adapted to our urban object of study as it provides useful information concerning the different mechanisms occurring. Moreover, we have pointed out the interest to study NLOS detectability areas comparing to the LOS ones to allow target detection. However, in the case where the target is located outside these areas, is this detection still possible?

6.4 Analysis of a canyon with an included point target: Urban Canyon V2

As for the previous section, we still investigate the NLOS areas of the canyon that are illuminated by multipath, but with a canonical target inside. Indeed,

this target can create a new mechanism of detection due to its scattering property. In the specific case of vehicle detection, two main mechanisms have to be taken into consideration: the specular reflection mechanism by the roof and the backscattering mechanism by the two sides of the vehicle. For this reason, we have developed a second EM code named Urban Canyon V2 that integrates these two additional backscattering mechanisms of detection and determines hence (as output) the NLOS detectability areas by backscattering mechanism. We assume that the target responsible for the backscattering mechanism is a point target, that can be seen either by its left side, right side or both. Similarly to Urban Canyon V1, the second output of this code is the range signature of the canyon with a point target. Several cases have been investigated with different types of targets, orientation and location through the analysis of the corresponding radar range profile.

6.4.1 NLOS detectability areas with backscattering mechanisms

Urban Canyon V2 is an extension of the first code as it includes an additional mechanism of detection: the backscattering mechanism. The first output is the NLOS detectability areas by backscattering mechanism. In fact, these areas can be defined as the zones where a potential point target can be detected. Due to its scattering proprieties, the incident rays arriving on the point target can be backscattered to the radar by the same path, allowing thus its detection. To help the reasoning that identifies the NLOS detectability areas via backscattering mechanism, two additional fictitious rays are considered. The first is the ray that would impact the bottom of the first wall (in green color in Fig.6.10) and the second is the ray impacting the bottom of the second wall (in purple color in Fig.6.10). They are fictitious because they do not necessarily penetrate inside the canyon. Their position relative to both blue and red rays depends on the parity of M and N. This parity directly conditions the position of the illuminated areas. We can demonstrate that the con-

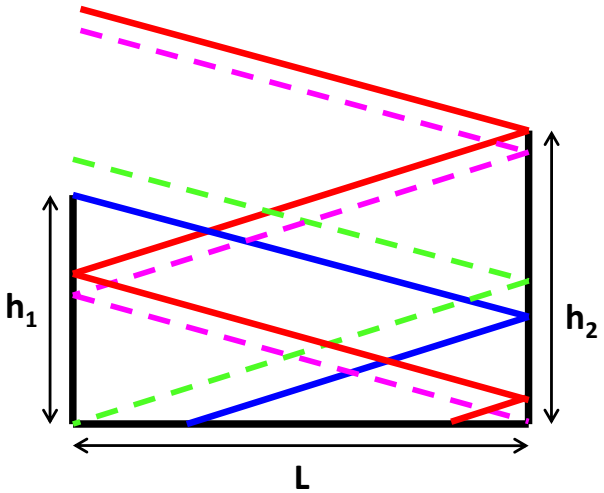

Figure 6.10: Representation of the four canonical rays: the red ray arriving on the top of the second wall, the blue ray arriving on the top of the first wall, the dashed green ray reaching the bottom of the first wall and the dashed pink ray reaching the bottom of the second wall.

dition in Eq.6.3 restricts the difference between N and M (defined respectively in

Eq.(6.6) and (6.5)). Thus, the only possible cases are $N = M$, $N = M + 1$ and $N = M + 2$. Every case is studied according to the parity of M and N which implies six different cases of parity represented in the algorithm Urban Canyon V2 (See Fig.6.14). Urban Canyon V2 identifies according to any canyon configuration the NLOS detectability part of the canyon illuminated by backscattering mechanism and the corresponding range profile. Without giving here all detailed demonstration of Urban Canyon V2, let us have a look on the different cases:

6.4.1.1 $N = M$

There is one illuminated area with an odd or even number of bounces. This area is denoted either z_{odd} or z_{even}. Fig.6.11 is an illustration of the case $M = N = 2$: there is one illuminated area issued from incident rays penetrating inside the canyon and making two bounces on the walls before reaching the ground. This area is represented by the blue horizontal bar. The number of bounces is recalled inside. In this zone, a return back to the radar is possible via backscattering. As there is at most only one NLOS detectability area by backscattering mechanism and no target allowing a return to the antenna, no possible response is expected in the range profile except of the noise.

6.4.1.2 $N = M + 1$

There are two NLOS detectability areas by backscattering mechanism. Fig.6.12 illustrates the case where $N = 4$, $M = 3$: there are one illuminated area with four bounces and one illuminated area with three bounces. We note the presence of one crossing area between these areas of different parity of bounces. In this crossing area, the point target can be viewed by two directions of illumination and thus can induce another possible mechanism: the specular mechanism. These crossing areas correspond exactly to the NLOS detectability areas by specular mechanism, identified in the previous sections. These areas are illustrated using green box. The areas where only one backscattering mechanism exists are illustrated using a yellow box. For the specific case of $N = M + 1$, there is only one crossing area, so that wall 1 or wall 2 will be detected depending on the parity of M (or N).

6.4.1.3 $N = M + 2$

There are three NLOS detectability areas by backscattering mechanisms and two crossing areas. The Fig.6.13 illustrates the case where $N = 5$, $M = 3$: this corresponds to three illuminated areas: the first with five bounces, the second with four bounces and the third with three bounces. As it exists two crossing areas located near the walls, the two walls will be detected.

Urban Canyon V2 applied to an empty canyon determines at first the NLOS detectability areas by backscattering mechanism and consequently (if they exist) the NLOS detectability areas by specular reflection mechanism. We notice that the detectability areas with backscattering mechanism are more important than the ones illuminated by specular reflection mechanism. Indeed, for the case $N = M$, no return is possible by specular reflection mechanism, but we can define a NLOS detectability area by backscattering mechanism. In the case $N = M + 2$, the whole

canyon is detectable by backscattering mechanisms which is not the case for the specular reflection mechanisms.

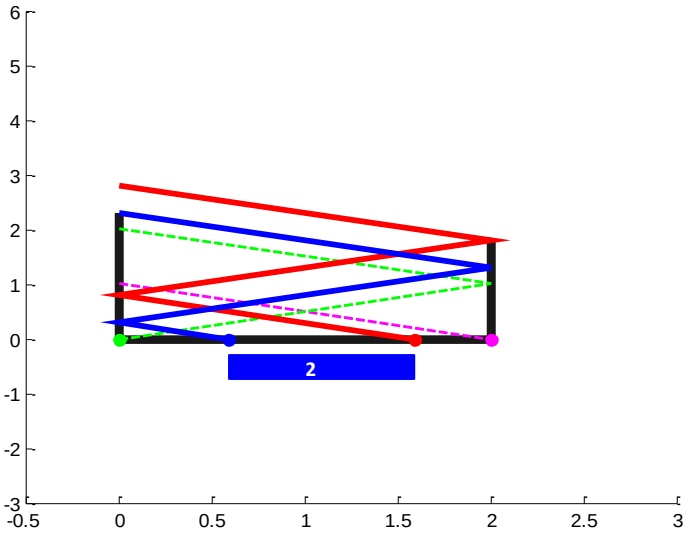

Figure 6.11: Determination of the NLOS detectability area by backscattering mechanism for the case where $M = 2$ and $N = 2$ (canyon configuration: $\theta = 63.4°$, $h_1 = 2.3m$, $h_2 = 1.8m$, $L = 2m$). The blue bar represents the illuminated area and the number inside refers to the number of bounces of the incident rays arriving on this zone.

In the following, we will study the impact of a point target located in these NLOS detectability areas. The point target is an ideal target that backscatters either by its left or right side. In the real case, a target may be oriented and therefore, the backscattering will exist only for one side. In the following, we consider different types of target (4-in-1, dihedral..) and study the range profile according to their position within the canyon. We will focus on two cases: the case where the target is located in a NLOS detectability area by specular reflection mechanism and the case where the target is located in a NLOS detectability area by backscattering mechanism.

6.4.2 Canyon Range Signature

6.4.2.1 Target Position 1

We consider the canyon configuration corresponding to Fig.6.13 where we notice the presence of two NLOS detectability areas by specular reflection mechanism. The first one is between [0,0.41] m and the second one is between [1.61,2] m. We include a point target in the first considered area at a distance d_1 =0.38 m from the first wall in order to study the canyon signature. We choose at first two point targets scattering by one side: the dihedral corner and the trihedral corner as illustrated in Fig.6.15. Hence, the range profile will contain one additional peak (with respect to the empty canyon) due to the target regardless of its orientation. This peak will be separated from the peak of the first wall by a distance of $d_1 \sin\theta$ (see Fig.6.16).

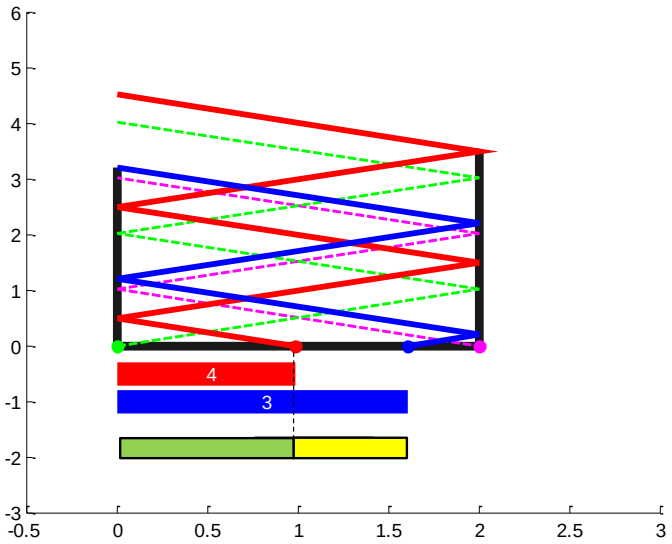

Figure 6.12: Determination of the NLOS detectability areas by specular reflection mechanism and by backscattering mechanism for the case $M = 3$ and $N = 4$ (canyon configuration: $\theta = 63.4°$, $h_1 = 3.2m$, $h_2 = 3.5m$, $L = 2m$). The red bar indicates the area illuminated by incident rays making four bounces before reaching this zone. Similarly, the blue bar presents the area illuminated by the incident rays arriving on this zone after three bounces. The green area corresponds to the NLOS detectability area by specular reflection mechanism. It is the intersection between the red and the blue zones, presenting different parities for the number of bounces. The yellow area represents the area where only one backscattering mechanism exists.

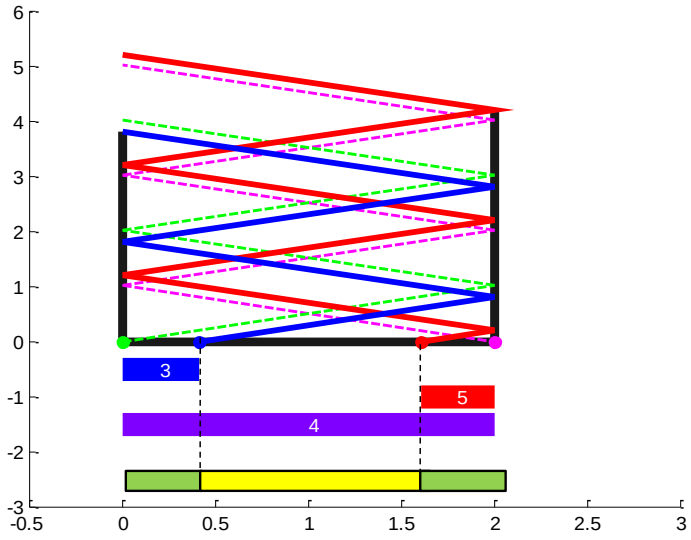

Figure 6.13: Determination of the NLOS detectability areas by specular reflection mechanism and by backscattering mechanism for the case $M = 3$ and $N = 5$ (canyon configuration:$(\theta = 63.4°, h_1 = 3.8m, h_2 = 4.2m, L = 2m)$).

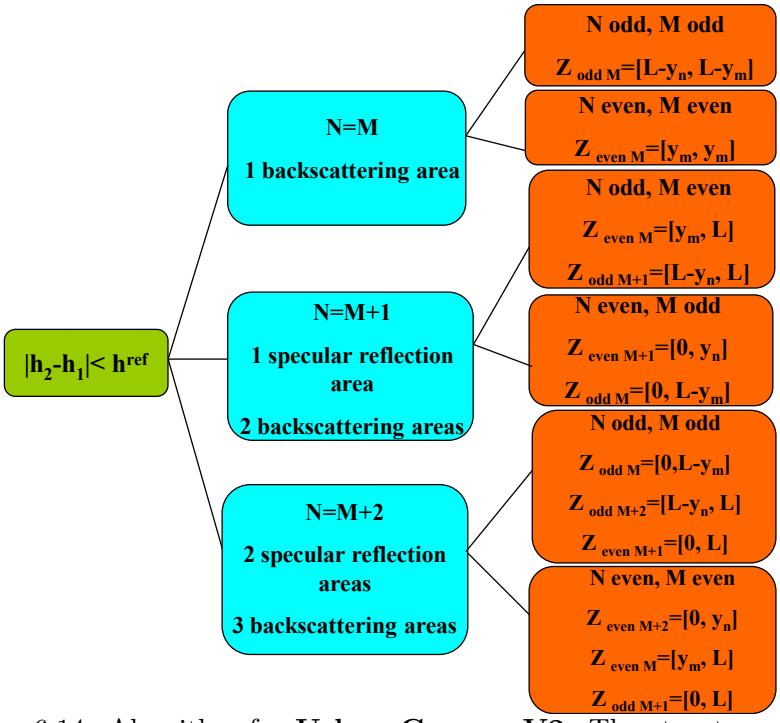

Figure 6.14: Algorithm for **Urban Canyon V2**. The structure of this algorithm and the ongoing and outgoing conditions are similar as the ones presented for **Urban Canyon V1**. However, in the particular case of backscattering mechanism, three different cases have to be considered: $N = M$, $N = M + 1$, $N = M + 2$.

Then, if we choose point targets scattering by both of the two sides such as the 4-in-1 corner reflector (see Fig.6.15), two additional peaks due to the target appear on the range profile which are symmetric and separated from the peak of the first wall by a distance of $d_1 \sin\theta$. The second peak of the target is separated from the peak of the second wall by a distance of $d_2 \sin\theta$ (see Fig.**??**). As a conclusion, we can say that the response of a point target in a NLOS detectability area by specular reflection mechanism will depend on its nature (detectable by one or two peaks).

6.4.2.2 Target Position 2

We focus now on the configuration of Fig.6.12 where there is a NLOS detectability area by only one backscattering mechanism between [0.98,1.61] m (yellow area in Fig.6.17). To study the effect of the presence of the target in this area, different point targets are included at the distance of d_1 =1.5 m. As the incident rays arrive in this area with an odd number of bounces (three), the target will be detected by its right side. If we choose a 4-in-1 corner reflector, it is always detected. As regards the dihedral corner and the trihedral corner, they can be detected provided they are well oriented. Concerning the canyon response, the range profile corresponding to the canyon configuration with the 4-in-1 corner reflector, or with one of the well oriented targets will contain two peaks: one peak due to wall 1 and one additional peak due to the target. These two peaks will be separated by a distance of $d_1 \sin\theta$ as we can see in Fig.6.18. Hence, the detection of the target in NLOS detectability area by backscattering mechanism depends on its nature but also on its orientation.

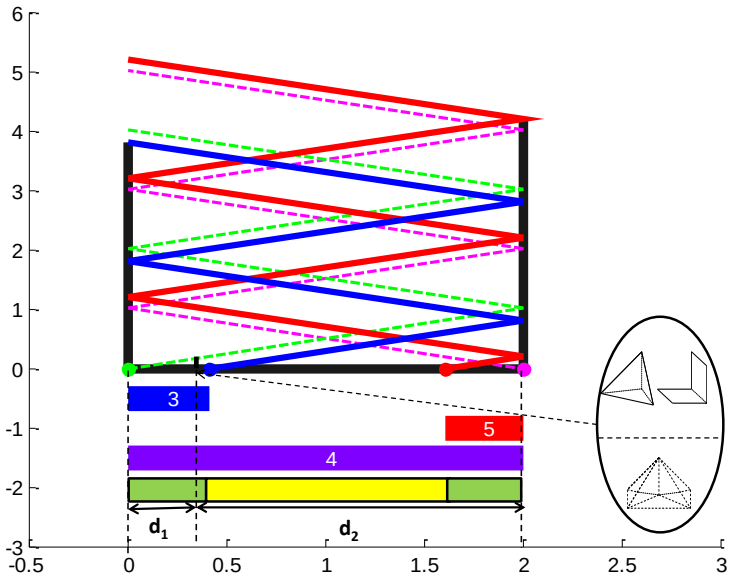

Figure 6.15: Example of point target located in the specular reflection area (green area) at a distance d_1 =0.38 m from the first wall. The target may be seen by one side (the dihedral and the trihedral corner reflector) or by two sides (the 4-in-1 corner reflector).

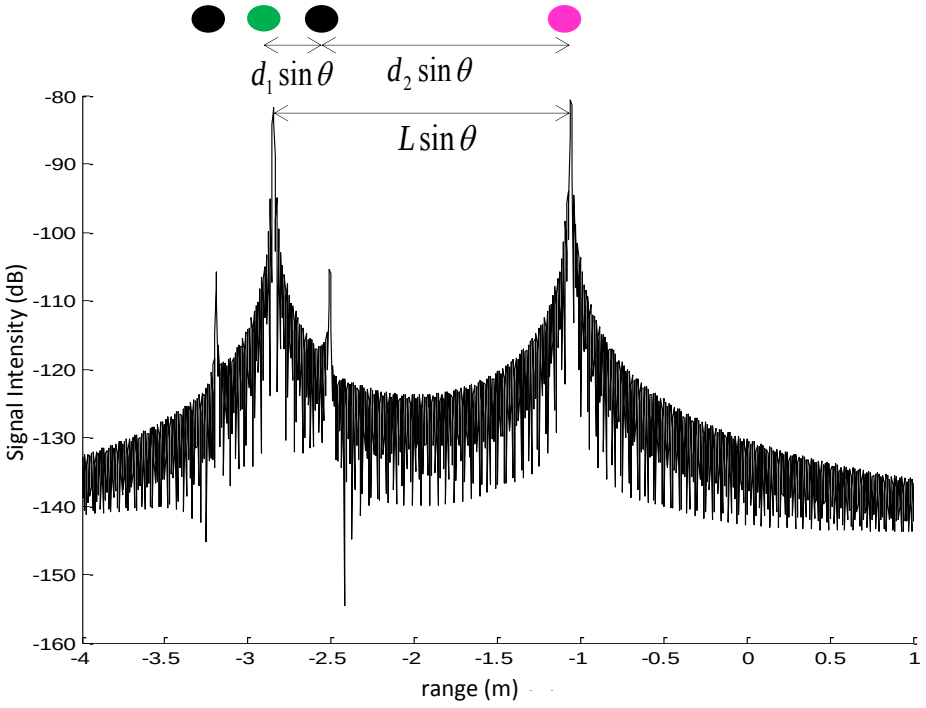

Figure 6.16: Range profile corresponding to the canyon configuration of Fig.6.15 when including a 4-in-1 corner reflector in the specular reflection area. The black dot corresponds to the peak of the target.

We have seen in this section that a point target located inside a canyon implies

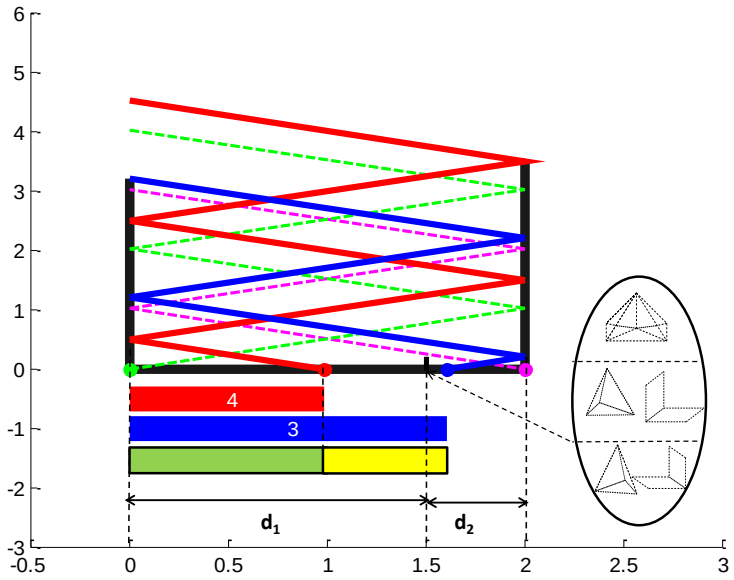

Figure 6.17: Example of a point target located in the backscattering area (yellow part). This target may be seen by one side (4-in-1 corner reflector, a well oriented dihedral or trihedral corner reflector) or may be not detected (not well oriented directional target).

a new mechanism of scattering (the backscattering mechanism) and hence expands the detectability zone. The target present in a NLOS detectability area by specular reflection mechanism is always detected, however, outside this area, the detection can be possible provided it is well oriented. Depending on the position of the target inside the canyon, the mechanisms of scattering allowing the detection vary from the specular reflection to the backscattering from the right or from the left. Therefore, depending on the mechanism of scattering induced by the target, we can determine if it is directive or not and its orientation. Concerning the response of the canyon with an included target, we expect to have up to 4 peaks: 2 peaks due to the walls and two peaks due to the target. All these information provided by the study of the NLOS detectability zones are a real potential in the area of target detection since when analyzing the range profile, we are able to predict the position of the target, its nature and its orientation. This offers the possibility to analyze more precisely the nature of the target thanks to its multiple responses.

6.4.3 Percentage of detectability areas

The detectability areas by backscattering mechanism provides a better coverage than the areas detectable by specular reflection mechanism, thus, the interest of their study since the probability of target detection increases. We present in Fig.6.19 a comparison between the percentage of NLOS detectability areas by specular reflection mechanism and by backscattering mechanism for the canyon illustrated in Fig.6.6 according to the incidence angle. We notice that the NLOS detectability

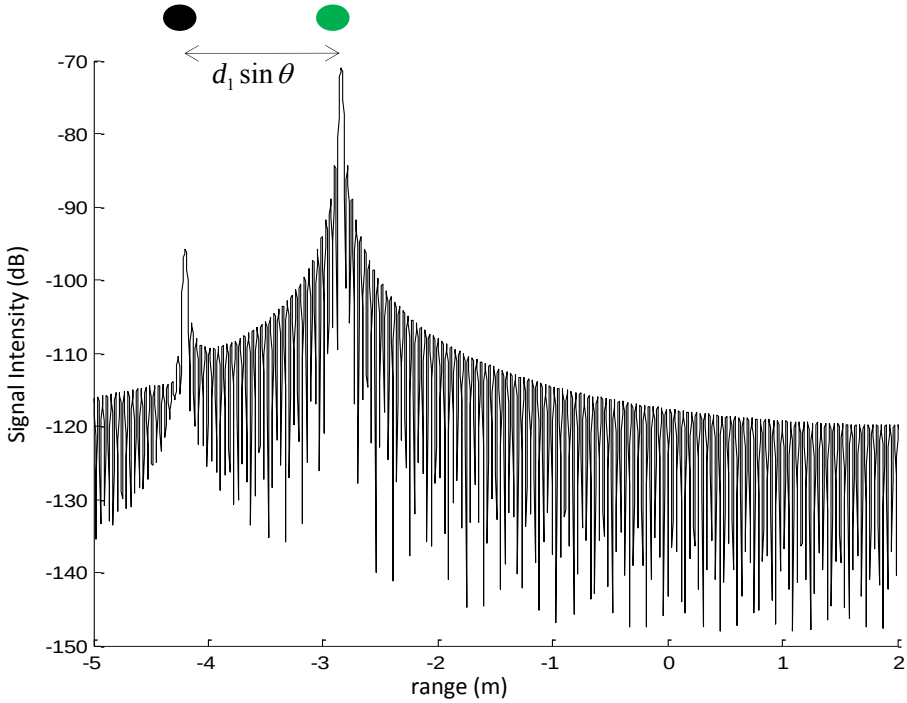

Figure 6.18: Range profile corresponding to the case of Fig.6.17 when including a 4-in-1 corner reflector or a well oriented target in the backscattering area. The black dot corresponds to the peak of the target.

areas by backscattering mechanism provides a better coverage, always superior to 65%.

However, it exists some point targets (the horizontal plate) present in a NLOS detectability area by backscattering mechanism that can be detected provided their thickness is sufficient. This is illustrated in the left part of Fig.6.20 where the horizontal plate of negligible thickness can never be detected. The blue rays illustrate the incident rays that can come into the canyon and return back to the radar. If we consider the same target with a thickness (see the right part), new mechanisms are created as the incident rays are intercepted. These new rays that can go back to the sensor are represented in pink color. The detection is then possible. As a consequence, it is now necessary to take into account the size of the target if we want to be able to predict accurately the NLOS detectability areas and the range profiles. The next chapter is devoted to the study of the detection of an extended target (most common targets in real case configurations). We can already expect that the detectability percentage will increase since due to the dimensions of the target, all the previous studied mechanisms can exist together. For this reason, we have developed Urban Canyon V3 to study the detectability of a NLOS extended target.

6.5 Conclusion

In this chapter, our ultimate goal was to present the first two versions of our simple and fast EM simulation tool for NLOS target detection inside urban canyons. This

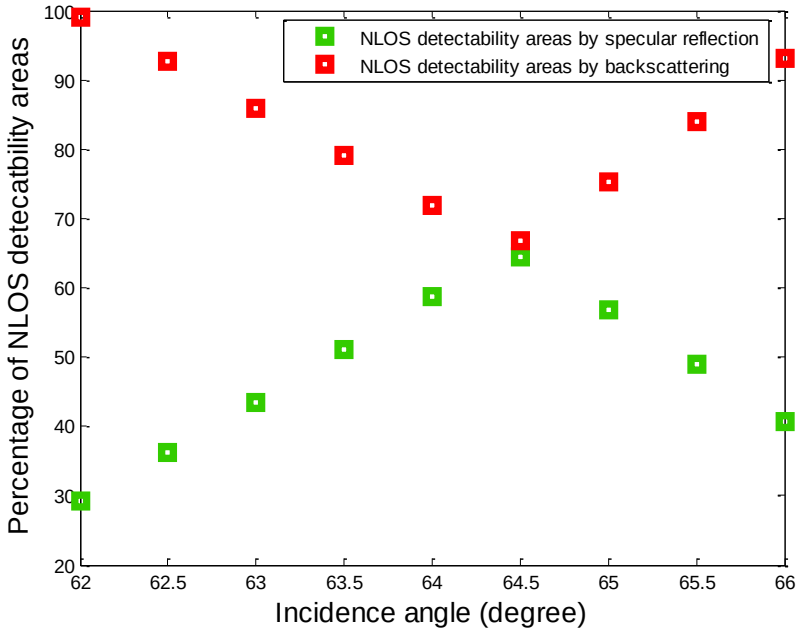

Figure 6.19: Percentage of NLOS detectability areas by backscattering mechanism and by specular reflection mechanism according to the incidence angle for the canyon of Fig.6.6.

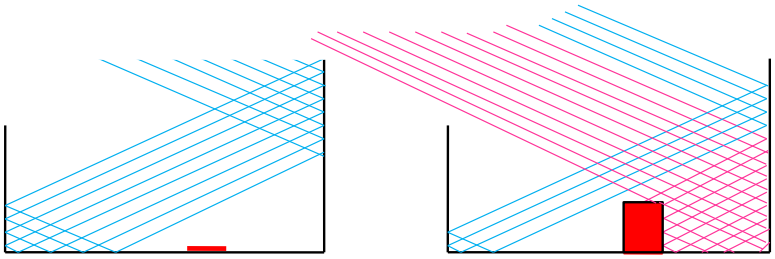

Figure 6.20: (Left) Example of a non detectable target (horizontal plate), represented by a red segment, lying in the shadow area. (Right) If a thickness is assigned to the horizontal plate, its detection would be possible.

EM tool is dedicated to PEC canyons as we decided to consider the most simple and complete case. In fact, for this case, the simulated mechanisms are the specular reflection mechanisms. The first approach was to investigate the NLOS detectability areas with specular reflection mechanism where any target can be detected. Urban Canyon V1 is the first developed algorithm that determines for any canyon configuration these areas. We have evaluated the importance of these NLOS detectability areas by specular reflection mechanism comparing to the LOS ones. Thus, the interest of their study since the percentage of targets detection is increased. Then, considering that in real case configuration, there are always targets located inside the canyon, we decided to study at first the response of a canyon with simple targets (point targets) before moving to more complex targets (the extended targets). Therefore, we have established a second algorithm named Urban Canyon V2 that determines the NLOS areas where a point target due to its scattering property can induce a new mechanism of detection: the backscattering mechanism. The second conclusion is that considering this additional mechanism, the percentage of target detection increases comparing to the detection with specular reflection mechanism. Furthermore, when analyzing the canyon response, we are able to extract additional information concerning the nature of the target and its orientation. Since in real life case, the targets are more complex, a third algorithm named Urban Canyon V3 was developed to study the detection of an extended target (the parallelepiped). This algorithm will be presented in the next chapter.

Chapter 7

In-house EM code for a canyon with an extended target

Contents

7.1 Introduction

This chapter describes the last version of our developed EM tool dedicated to the detection of NLOS extended targets inside urban canyons. This tool is more appropriate to study real case configurations as in real cases, the number of extended targets (car, truck..) exceeds the number of point targets. The corresponding developed code is named Urban Canyon V3 and constitutes a global code since it includes the study of empty canyons, canyons with point targets and canyons with extended targets. For this EM tool, we keep the same conditions as for the last two versions (PEC canyon perpendicular to the propagation plan) and we assume also that the target is PEC and oriented in parallel of the walls. The outputs are the NLOS detectability areas as well as a radar range profile where it is possible to distinguish the responses of the target from the response of the canyon. Using Urban Canyon V3, we can predict for any canyon configuration with the presence of an extended target, if the target can be detected by its right side, left side or

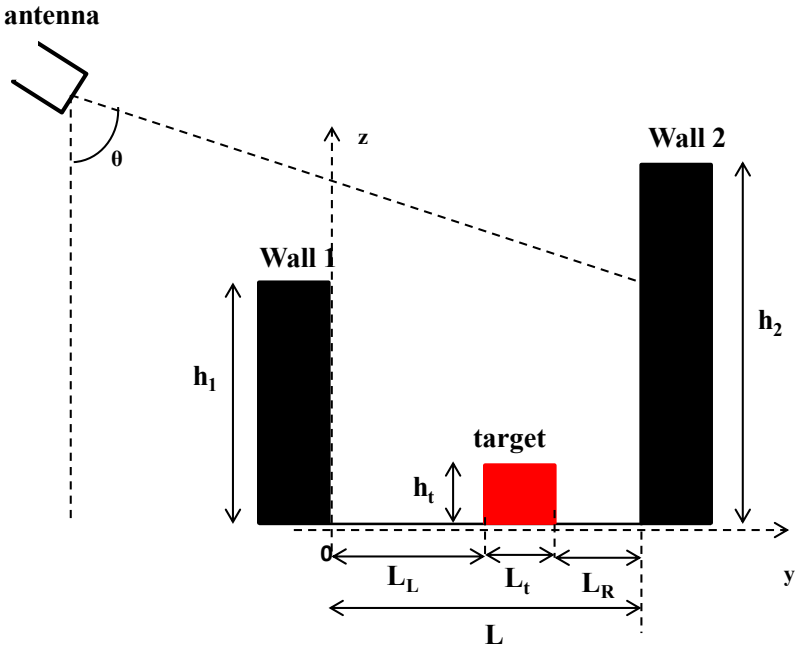

Figure 7.1: Reference scene: urban canyon with a parallelepiped target.

roof and the corresponding range signature. The general approach of establishing this algorithm is to study into two parts the response of the canyon when including an extended target inside it. The first part will deal with the detection of the two walls with the presence of a parallelepiped target (Sec.7.3). The second part will be devoted to the study of the cases where a parallelepiped target can be illuminated and detected (sec.7.4). The last section presents the results of validation of Urban Canyon V3 using FEKO (sec.7.5). We end up this chapter by a conclusion.

7.2 Reference scene

To restrict the study of extended targets, we consider here a parallelepiped target, characterized in the incidence plane by both its width L_t and its height h_t (see Fig.7.1). This target is located inside a canyon defined as previously by the heights h_1 and h_2 of its two walls and the distance L separating them. Actually, the target defines two sub-canyons: the one located on the left of the target and referred to as "left canyon", the other one called "right canyon" is at the right of the target. The width of the left canyon is L_L and the one of the right is L_R, so that $L_L+L_R+L_t = L$. As before, we still only consider the geometrical specular mechanisms associated to a perfectly conducting case. In the following, we will present the first part of Urban Canyon V3 related to the walls detection and the second part related to the detection of the extended target.

7.3 Walls detection

Results concerning the walls detection for an empty canyon have been presented in Sec.6.3 where the three possible cases (no wall detected, one wall detected, both

of the two walls detected) have been presented with their corresponding canyon signatures. We deal now with the walls detection when including an extended target inside the canyon.

7.3.1 Example

To explain our approach, we choose the case illustrated in Fig.7.2 corresponding to the detection of the first wall. This canyon configuration corresponds to the case $N = M + 1$ where M is odd ($M = 1$). Two zones are defined using two limit rays. The first limit ray is the incoming ray that hits the corner of the first wall (illustrated in red) and the second limit ray is the ray arriving on the top of the second wall (in green color). The detection of the first wall is possible provided that one of these two limit rays exists. The intersection of these two limit rays defines two zones called zone A and zone B. Depending on the target position inside the canyon and on its height, we can predict if the first wall is detected and the corresponding range profile. If the target is in zone A with a height $h_t < h'_L(M)$ ($h'_L(M)$ is illustrated in the left part of Fig.7.2), then, the green limit ray exists allowing thus the detection of the first wall. If the target is in zone B with a height $h_t < h''_R$ (see right part of Fig.7.2), then the detection of the first wall is possible via the second limit ray (in red color) even if the height of the target prevents the green limit ray to go back to the receiver. Therefore, we can conclude that depending on the case, the position of the target and its height, wall 1, wall 2 or both of them can be detected. We will present now the two cases ($N = M + 1$, $N = M + 2$) with different parities of N and M, the corresponding limit rays used to define the zones, the zones in which to study the target detection and the conditions about the target's height to allow the detection of the walls.

7.3.2 General case: N=M+1 (M odd)

This case corresponds to the detection of wall 1 since M is odd (M and N are defined in Eq.6.5 and Eq.6.6 respectively). The two first limit rays used to define the zones of target detection are illustrated in green and red color (see Fig.7.3.a). First, we have to ensure the condition of existence of the green limit ray expressed in Eq.6.9. The two defined zones are:

- Zone A: $[0, (h_2 \tan\theta - ML)/2]$,
- Zone B: $[(h_2 \tan\theta - ML)/2, L]$.

If the target is in zone A, then the detection of wall 1 is possible only if:

$$\begin{cases} h_t < h'_L(M) & (7.1) \\ h'_{L,R}(M) = h_2 - Mh^{\text{ref}} - h'^{\,\text{ref}}_{L,R} & (7.2) \\ h'^{\,\text{ref}}_{L,R} = L_t/\tan\theta + h^{\text{ref}}_{L,R} & (7.3) \\ h^{\text{ref}}_{L,R} = L_{L,R}/\tan\theta & (7.4) \end{cases}$$

where h^{ref} is defined in Eq.6.4.

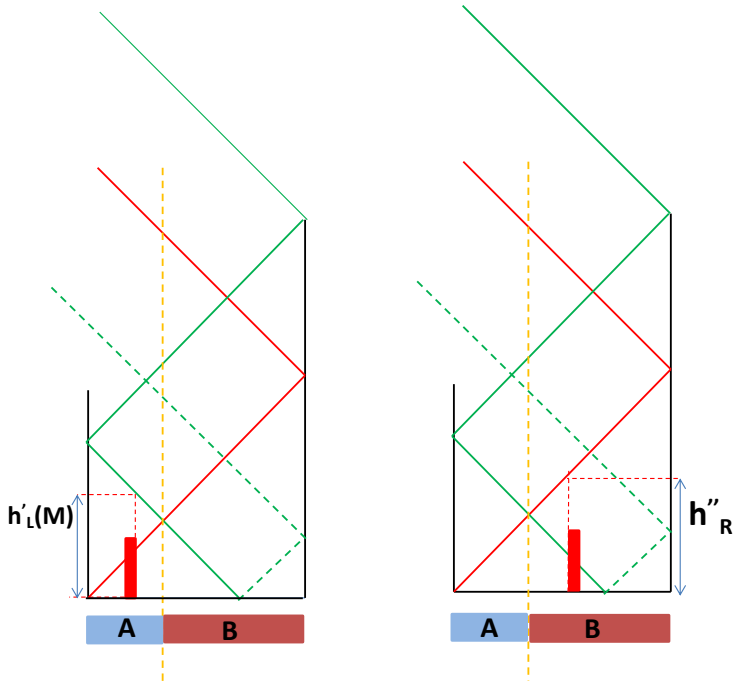

Figure 7.2: Detection of the first wall when including an extended target inside the canyon. Left Figure: target located in Zone A is detected provided its height is inferior to $h'_L(M)$. Right Figure: target located in Zone B is detected provided its height is inferior to h''_R.

If the target is in zone B, then the detection of wall 1 is possible only if:

$$\begin{cases} h_t < h''_R & (7.5) \\ h''_{L,R} = h^{\text{ref}} - h'^{\,\text{ref}}_{L,R} & (7.6) \end{cases}$$

We define c'_1, the condition of detection of the first wall via the green or red limit rays, as:

$$c'_1 = (h_t < h'_L(M)) \;||\; (h_t < h''_R) \tag{7.7}$$

where || refers to the logical 'OR'.

If c'_1 is false, two other limit rays are defined and are illustrated in red and pink color in Fig.7.3.a. The pink limit ray exists provided the condition in Eq.6.8 is true. Their intersection defines two zones:

- Zone A': $[0, ((1+M)\,L - h_1 \tan\theta)\,/2]$,
- Zone B': $[((1+M)\,L - h_1 \tan\theta)\,/2, L]$.

If the target is in zone A', then the detection of wall 1 is possible only if:

$$\begin{cases} h_t < h'''_L(M) & (7.8) \\ h'''_{L,R}(M) = h^{\text{ref}}(1+M) - h_1 - h'^{\,\text{ref}}_{L,R} & (7.9) \end{cases}$$

If the target is in zone B', then the detection of wall 1 is possible only if:

$$h_t < h''_R \tag{7.10}$$

We define $c_1^{''}$, the condition of detection of the first wall via the red or pink limit rays, as:

$$c_1^{''} = (h_t < h_L^{'''}(M)) \,||\, (h_t < h_R^{''}) \tag{7.11}$$

Wherever the position of the target, the peak of wall 1 denoted P_{w1} will be at the position:

$$P_{w1} = (M+1)\, L \sin\theta \tag{7.12}$$

7.3.3 General case: N=M+1 (M even)

As seen previously, this case corresponds to the detection of the second wall. The two limit rays used to define the zones of detection are illustrated in green and black color (see Fig.7.3.b). The green limit ray exists provided the condition in Eq.6.9 is true. The intersection of the two limit rays defines two zones:

- Zone C: $[0, L - (h_2 \tan\theta - ML)/2]$,
- Zone D: $[L - (h_2 \tan\theta - ML)/2, L]$.

If the target is in zone C, then, the detection of wall 2 is possible only if:

$$h_t < h_L^{''} \tag{7.13}$$

If the target is in zone D, then, the detection of wall 2 is possible only if:

$$h_t < h_R^{'}(M) \tag{7.14}$$

We define $c_2^{'}$, the condition of detection of the second wall via the green or black limit rays, as:

$$c_2^{'} = (h_t < h_L^{''}) \,||\, (h_t < h_R^{'}(M)) \tag{7.15}$$

If $c_2^{'}$ is false, two other limit rays are defined and are illustrated in black and pink color in Fig.7.3.b. The pink limit ray exists provided the condition in Eq.6.8 is true. Their intersection defines two zones:

- Zone C': $[0, (h_1 \tan\theta + L(1-M))/2]$,
- Zone D': $[(h_1 \tan\theta + L(1-M))/2, L]$.

If the target is in zone C', then, the detection of wall 2 is possible only if:

$$h_t < h_L^{''} \tag{7.16}$$

If the target is in zone D', then, the detection of wall 2 is possible only if:

$$h_t < h_R^{'''}(M) \tag{7.17}$$

We define $c_2^{''}$, the condition of detection of the second wall via the black or pink limit rays, as:

$$c_2^{''} = (h_t < h_L^{''}) \,||\, (h_t < h_R^{'''}(M)) \tag{7.18}$$

On the range profile, the peak of wall 2 will be at the position denoted $P_{w2} = P_{w1}$.

7.3.4 General case: N=M+2 (M even)

For this case, both walls can be detected (see Fig.7.3.c and Fig.7.3.d). The limit rays responsible for the detection of the first wall are the red and green rays. The green limit ray exists provided the condition in Eq.6.9 is true. Their intersection defines two zones:

- Zone E: $[0, (h_2 \tan\theta - (M+1)\,L)\,/2]$,
- Zone F: $[(h_2 \tan\theta - (M+1)\,L)\,/2, L]$.

If the target is in zone E, then, the detection of wall 1 is possible only if:

$$h_t < h'_L(M+1) \tag{7.19}$$

If the target is in zone F, then, the detection of wall 1 is possible only if:

$$h_t < h''_R \tag{7.20}$$

We define c'_3, the condition of detection of the first wall via the green or red limit rays, as:

$$c'_3 = (h_t < h'_L(M+1)) \;||\; (h_t < h''_R) \tag{7.21}$$

On the range profile, the peak of wall 1 will be at the position:

$$P_{w1} = (M+2)\,L\sin\theta \tag{7.22}$$

The limit rays responsible for the detection of wall 2 are the ray arriving on the top of the first wall and the ongoing ray via the corner of the second wall (see the pink and black rays in Fig.7.3.d). The pink limit ray exists provided the condition in Eq.6.8 is true. These two limit rays define two zones:

- Zone G: $[0, (h_1 \tan\theta + (1-M)\,L)\,/2]$,
- Zone H: $[(h_1 \tan\theta + (1-M)\,L)\,/2, L]$.

If the target is in zone G, then, the detection of wall 2 is possible only if:

$$h_t < h''_L \tag{7.23}$$

If the target is in zone H, then, the detection of wall 2 is possible only if:

$$h_t < h'''_R(M) \tag{7.24}$$

We define c'_4, the condition of detection of the second wall via the pink or black limit rays, as:

$$c'_4 = (h_t < h''_L) \;||\; (h_t < h'''_R(M)) \tag{7.25}$$

On the range profile, the peak of wall 2 will be at the position:

$$P_{w2} = (M+1)\,L\sin\theta \tag{7.26}$$

7.3.5 General case: N=M+2 (M odd)

This case is illustrated in Fig.7.3.e and in Fig.7.3.f. The limit rays responsible for the detection of wall 1 are illustrated in pink and red color (see Fig.7.3.e). The pink

limit ray exists provided the condition in Eq.6.8 is true. Their intersection defines two zones:

- Zone I: $[0, (-h_1 \tan\theta + (M+1)\, L)\, /2]$,
- Zone J: $[(-h_1 \tan\theta + (M+1)\, L)\, /2, L]$.

If the target is in zone I, then, the detection of wall 1 is possible only if:

$$h_t < h_L^{'''}(M) \tag{7.27}$$

If the target is in zone J, then, the detection of wall 1 is possible only if:

$$h_t < h_R^{''} \tag{7.28}$$

We define $c_5^{'}$, the condition of detection of the first wall via the pink or red limit rays, as:

$$c_5^{'} = (h_t < h_L^{'''}(M)) \;||\; (h_t < h_R^{''}) \tag{7.29}$$

The peak of the first wall will be at the position P_{w1} defined as:

$$P_{w1} = (M+1)\, L \sin\theta \tag{7.30}$$

The limit rays responsible for the detection of the second wall are illustrated in green and black color (see Fig.7.3.f). The green limit ray exists provided the condition in Eq.6.9 is true. Their intersection defines two zones:

- Zone K: $[0, (-h_2 \tan\theta + (M+3)\, L)\, /2]$,
- Zone L: $[(-h_2 \tan\theta + (M+3)\, L)\, /2, L]$.

If the target is in zone K, then, the detection of wall 2 is possible only if:

$$h_t < h_L^{''} \tag{7.31}$$

If the target is in zone L, then, the detection of wall 2 is possible only if:

$$h_t < h_R^{'}(M+1) \tag{7.32}$$

We define $c_6^{'}$, the condition of detection of the second wall via the green or black limit rays, as:

$$c_6^{'} = (h_t < h_L^{''}) \;||\; (h_t < h_R^{'}(M+1)) \tag{7.33}$$

The peak of the second wall will be at the position P_{w2} defined as:

$$P_{w2} = (M+2)\, L \sin\theta \tag{7.34}$$

The different cases of parity and the conditions relative to the detection of the walls when including an extended target inside the canyon are summarized in the Fig.7.9 (see the green box relative to walls detection) and in Tab.7.1. In the following section, we will study the possible detection of a parallelepiped target inside the canyon and the different responses caused by the presence of this extended target on the range profiles.

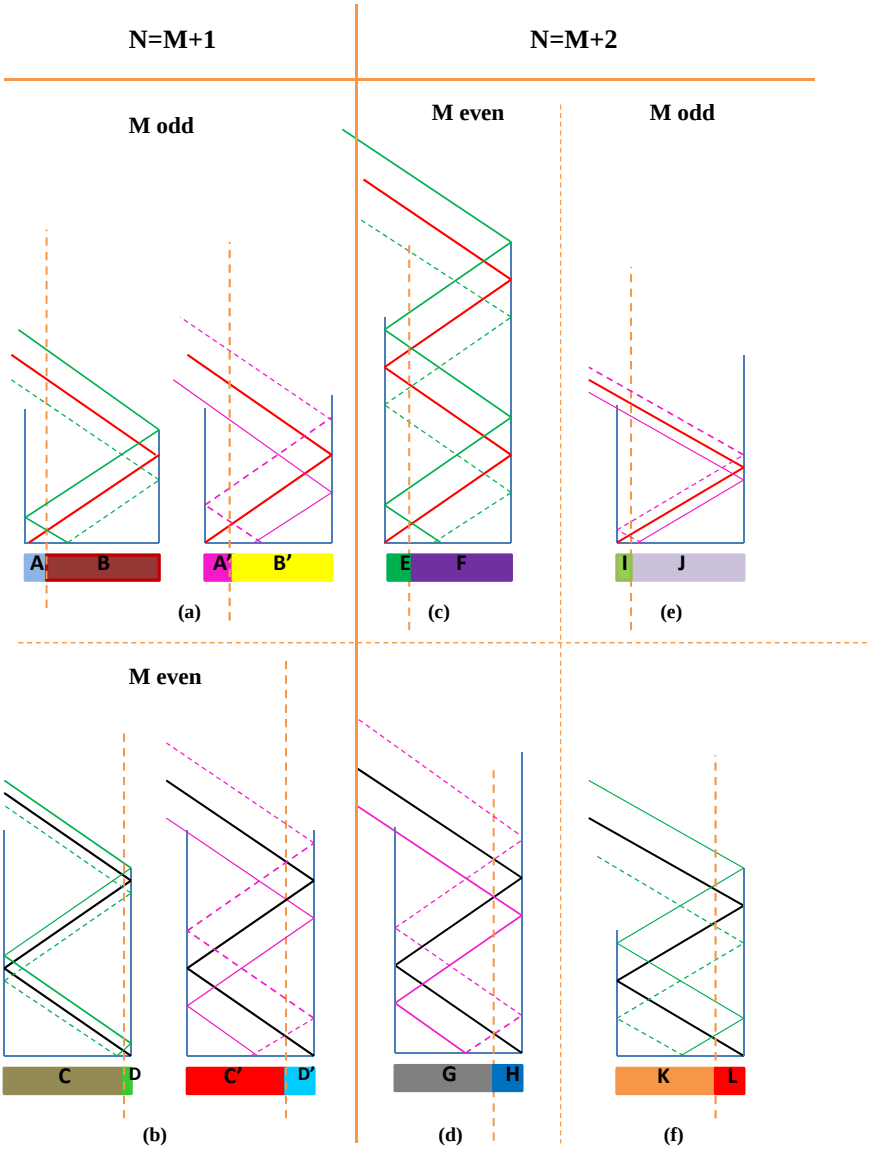

Figure 7.3: Detection of the two walls according to the cases $N = M + 1$ and $N = M + 2$.

Table 7.1: Table summarizing the different cases relative to the detection of wall 1 or wall 2 alone.

	Case N=M+1					**Case N=M+2**				
	Location of the target	**Condition on target height**	**Definition**	**Wall detected**	**Peak position**	**Location of the target**	**Condition on target height**	**Definitions**	**Wall detected**	**Peak position**
M odd	Zone A	$h_t < h'_L(M)$	$h'_L(M)$ in Eq.7.2	Wall 1	P_{w1} in Eq.7.12	Zone K	$h_t < h''_L$	$h'_R(M+1)$ in Eq.7.2	Wall 2	P_{w2} in Eq.7.34
	Zone B	$h_t < h''_R$	h''_R in Eq.7.6			Zone L	$h_t < h'_R(M+1)$			
	Zone A'	$h_t < h'''_L(M)$	$h'''_L(M)$ in Eq.7.9			Zone I	$h_t < h'''_L(M)$	$h'''_L(M)$ in Eq.7.9	Wall 1	P_{w1} in Eq.7.30
	Zone B'	$h_t < h''_R$				Zone J	$h_t < h''_R$			
M even	zone C	$h_t < h''_L$	h''_L in Eq.7.6	Wall 2	$P_{w2} = P_{w1}$	Zone E	$h_t < h'_L(M+1)$	h''_R in Eq.7.6	Wall 1	P_{w1} in Eq.7.22
	Zone D	$h_t < h'_R(M)$	$h'_R(M)$ in Eq.7.2			Zone F	$h_t < h''_R$			
	Zone C'	$h_t < h''_L$	$h'''_R(M)$ in Eq.7.9			Zone G	$h_t < h''_L$	$h'''_R(M)$ in Eq.7.9	Wall 2	P_{w2} in Eq.7.26
	Zone D'	$h_t < h'''_R(M)$				Zone H	$h_t < h'''_R(M)$			

7.4 Study of the response of the parallelepiped target

In the first part of this section, we study the cases where the target can be viewed by its right side. With an analogical study, we present in a second part, the cases where the target can be viewed by its left side. The last part is devoted to the study of the target detection by its roof. In all cases, we have to ensure at first that the penetration condition in Eq.6.3 is true. We have to determine then which part(s) of the target is (are) illuminated. For this purpose, we introduce the following parameter K, calculated as follows:

$$K = \left\lfloor \frac{h_2 - h_t}{h^{\text{ref}}} \right\rfloor \tag{7.35}$$

Depending on the parity of K and provided that some additional conditions are respected, the right or the left side of the target can be illuminated.

7.4.1 Which sub-canyon is illuminated ?

In the case where K **is even**, the left side of the target can be illuminated if c_1 or c_2 is true.

$$\begin{cases} c_1 : h_2 - \left(K h^{\text{ref}} + h_R^{'\text{ref}} \right) \geq h_t & (7.36) \\ c_2 : h_1 - \left(K h^{\text{ref}} + h_L^{\text{ref}} \right) < h_t & (7.37) \end{cases}$$

where $h_R^{'\text{ref}}$, h^{ref} and h_L^{ref} are defined in Eq.7.3, Eq.6.4 and Eq.7.4, respectively.

The right side of the target can be illuminated if c_3 or c_4 is true.

$$\begin{cases} c_3 : h_1 - \left((K+1)\, h^{\text{ref}} + h_R^{\text{ref}} \right) < h_t & (7.38) \\ c_4 : h_2 - \left(K h^{\text{ref}} + h_R^{\text{ref}} \right) \leq h_t & (7.39) \end{cases}$$

where h_R^{ref} is defiend in Eq.7.4.

In the case where K **is odd**, the left side of the target can be illuminated if c_5 or c_6 is true.

$$\begin{cases} c_5 : h_2 - \left(K h^{\text{ref}} + h_L^{\text{ref}} \right) \leq h_t & (7.40) \\ c_6 : h_1 - \left((K+1)\, h^{\text{ref}} + h_L^{\text{ref}} \right) < h_t & (7.41) \end{cases}$$

The right side of the target can be illuminated if c_7 or c_8 is true.

$$\begin{cases} c_7 : h_1 - \left(K h^{\text{ref}} + h_R^{\text{ref}} \right) > h_t & (7.42) \\ c_8 : h_2 - \left(K h^{\text{ref}} + h_L^{'\text{ref}} \right) > h_t & (7.43) \end{cases}$$

The logigramm in Fig.7.9 summarizes these results concerning the target detection by its right side and left side considering the canyon configuration (h_1, h_2, L, θ) with the target dimension and position (h_t, L_t, L_R/L_L) (see the orange box relative to the target detection).

Our goal is now to characterize the range profile associated to the scene under study. To do this, we have to answer to the following questions:

- Is there any peak? How many?,
- What are their positions?,
- What is the origin of these peaks? Do they imply walls only or also the sides of the target, or/and the roof of the target?.

In the following, we focus on the case where the right side of the target is illuminated.

7.4.2 Analysis of the right sub-canyon

We have started by identifying the possible cases where the right side of a parallelepiped target can be illuminated. We propose to first have a look to a general case where the incident rays have several big reflections (between the first wall and the second wall) and several small reflections between the target and the second wall (see Fig.7.4(a)). We define a **limit ray** composed by an ongoing sub-ray (illustrated with a continuous red line) and an outgoing sub-ray (dashed red line). In Fig.7.5 (left), we have colored in orange all the rays ranged between the two sub-rays of the limit ray. These rays specify a **caustic** which is responsible for the dihedral effect in the left side of the target. All the rays of the caustic contribute to the same peak on the range profile. We have now to determine if the limit ray can go back to the radar to ensure the detection. This leads us to consider four cases that are illustrated in Figs. 7.4(a), 7.4(b), 7.4(c), and 7.4(d).

7.4.2.1 Case 1 of a target viewed by its right side

In the **first case** illustrated in Fig.7.4(a), the limit ray denoted LR_R^1 is the ray arriving on the top of the second wall making several big and small reflections before returning to the radar. This limit ray exists if both the ongoing and outgoing sub-rays exist. The number of big reflections between the two walls, denoted Q_1, and the number of small reflections between the second wall and the target, denoted M_R, are given by:

$$Q_1 = \left\lfloor \frac{h_2 - h_t}{h^{\text{ref}}} \right\rfloor \tag{7.44}$$

$$M_R = \left\lfloor \frac{h_t}{h_R^{\text{ref}}} \right\rfloor \tag{7.45}$$

h^{ref} and h_R^{ref} are defined in Eq.6.4 and Eq.7.4 respectively.

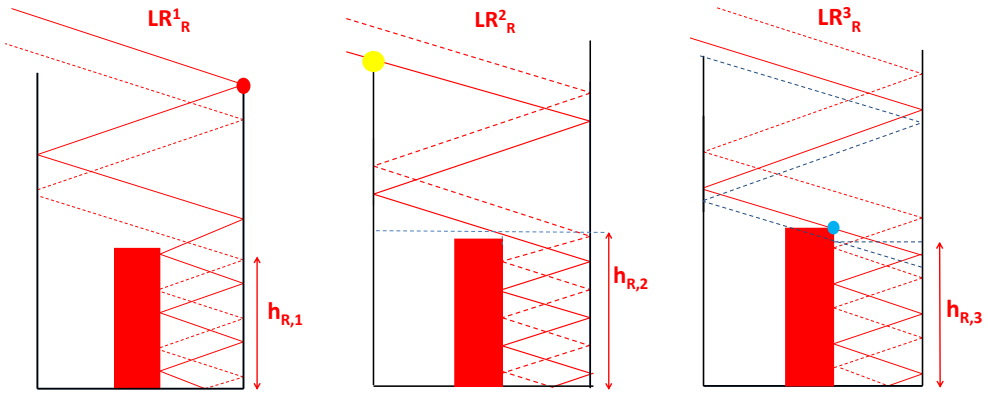

(a) Case 1: the red dot delimits the first limit ray arriving on the top of the second wall.

(b) Case 2: the yellow dot delimits the second limit ray arriving on the top of the first wall.

(c) Case 3: the blue dot delimits the third limit ray (the ongoing ray via the right corner of the target's roof).

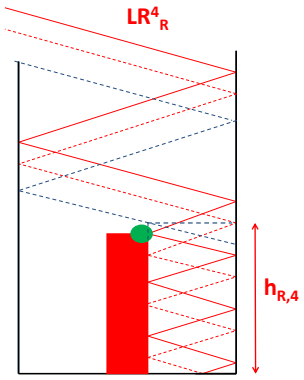

(d) Case 4: the green dot delimits the fourth limit ray.

Figure 7.4: Detection of the right side of the extended target using four different limit rays.

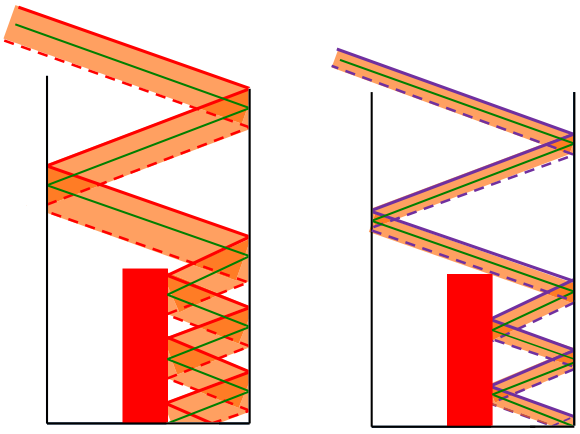

Figure 7.5: We call caustic all the rays ranged between the two sub-rays of the limit ray. All these rays have the same distance, that is equal to the distance of the central ray (in green). The caustics have been colored in orange. (Left) The first caustic defined by the red limit ray is responsible for the detection of the bottom of the target. (Right) The second caustic defined by purple limit ray is responsible for the detection of the second wall.

In Tab.7.2 are presented, according to the parity of Q_1 and M_R, the four cases of study. For each case, we specify:

- the two conditions ensuring the existence of the ongoing sub-ray denoted C_{onR1_1} and C_{onR1_2} ("C" for condition, "on" for ongoing sub-ray, "R" for right sub-canyon, "1" for case 1). They are expressed in Eq.7.46 and Eq.7.47:

$$\begin{cases} C_{onR1_1}(Q) = (h_2 - Qh^{\text{ref}} - h_R^{\text{ref}}) \leq h_t & (7.46) \\ C_{onR1_2}(Q) = (h_2 - Qh^{\text{ref}} - h_L^{\text{'ref}}) \geq h_t & (7.47) \end{cases}$$

  where $h_L^{\text{'ref}}$ is defined Eq.7.3.
- the condition ensuring the existence of the outgoing sub-ray denoted C_{outR1} and expressed in Eq.7.48:

$$C_{outR1}(M_R, Q) = (2M_R h_R^{\text{ref}} - h_2 + (2Q_+1)h^{\text{ref}}) \geq h_1 \quad (7.48)$$

- P_{R1} and P_{R2}: the position of the two peaks associated to the second wall and to the target depending on $P(M_R, Q)$ defined in Eq.7.49:

$$P(M_R, Q) = (M_R L_R + QL)\sin\theta \quad (7.49)$$

- the condition of existence of the second peak denoted C_{R1} defined in Eq.7.50:

$$C_{R1}(M_R, Q) = (M_R h_R^{\text{ref}} + Qh^{\text{ref}}) \geq h_1 \quad (7.50)$$

- the conditions denoted C_{1_1} and C_{1_2} defining the possible sub-cases are expressed in Eq.7.51 and Eq.7.52. $\overline{C_{1_1}}$ and $\overline{C_{1_2}}$ refer to the case where these

conditions are false:

$$\begin{cases} C_{1_1}(M_R, Q) = ((1 + 2M_R)h_R^{\text{ref}} - h_2 + Qh^{\text{ref}}) \leq h_t & (7.51) \\ C_{1_2}(Q) = mod(\left\lfloor \dfrac{h_2 - Qh^{\text{ref}} - h_R^{\text{ref}}}{h_R^{\text{ref}}} \right\rfloor, 2) = 0 & (7.52) \end{cases}$$

Existence of one or two peaks

According to the four cases defined by the parity of M_R and Q_1, the range profile will contain at least one peak ensured by the limit ray. However, a second peak may exist if C_{R1} is true.

Definition of the corresponding caustics

For the first case, we have assigned to each of the two possible responses the corresponding caustic defined by its limit ray. The caustic defined by the red limit ray is responsible for the detection of right side of the target whereas the caustic defined by the purple limit ray is responsible for the detection of the second wall (see Fig.7.5).

Position of the peaks

The range profile will contain at most two peaks:

- If two peaks exist, they will be at the position P_{R1} and P_{R2},
- If only one peak exists, it will be at P_{R1}.

Origin of the peaks

In order to determine the origin of the peaks on the range profile (due to wall 2 or to the target), we have to consider both the parity of M_R and Q_1. For this case, the peak of wall 2 will be always at P_{R2} provided the condition C_{R1} is true, whereas the peak of the target will be in P_{R1}. In the following, to avoid redundancy and to present the results concisely, the peak of the target will be written in red color whereas the peak of the wall will be written in blue color.

7.4.2.2 Case 2 of a target viewed by its right side

LR_R^1 may not exist. However, the detection of the right side is still possible if we consider another limit ray. Thus, we move to case 2 defining a new limit ray. This limit ray is the ongoing ray via the top of the first wall. This limit ray is denoted LR_R^2 and is illustrated in Fig.7.4(b). The number of big reflections between the two walls is now denoted Q_2 defined as:

$$Q_2 = \left\lfloor \frac{h_1 - h_t}{h^{\text{ref}}} \right\rfloor \quad (7.53)$$

where h^{ref} is defined in Eq.6.4.

In Tab.7.3 are presented, according to the parity of Q_2 and M_R (defined in Eq.7.45), the four cases of study. For each case, we specify:

- The two conditions ensuring the existence of the ongoing sub-ray denoted C_{onR2_1} and C_{onR2_2}. They are expressed in Eq.7.54 and Eq.7.55:

$$\begin{cases} C_{onR2_1}(Q) = (h_1 - Qh^{\text{ref}} - h_R^{\text{ref}}) \leq h_t & (7.54) \\ C_{onR2_2}(Q) = (h_1 - Qh^{\text{ref}} - h_L^{\text{'ref}}) \geq h_t & (7.55) \end{cases}$$

where: h_R^{ref} , $h_L^{'\text{ref}}$ are defined in Eq.7.4 and Eq.7.3, respectively,

- The condition ensuring the existence of the outgoing sub-ray denoted C_{outR2} and expressed in Eq.7.56:

$$C_{outR2}(M_R, Q) = (2M_R h_R^{\text{ref}} - h_1 + (2Q-1)h^{\text{ref}}) \leq h_2 \tag{7.56}$$

where M_R is defined in Eq.7.45,

- P_{R3} and P_{R4}: the position of the two peaks associated to the second wall and to the target depending on $P(M_R, Q)$ defined in Eq.7.49,
- The condition of existence of the second peak denoted C_{R2} defined in Eq.7.57:

$$C_{R2}(M_R, Q) = (M_R h_R^{\text{ref}} + Q h^{\text{ref}}) \leq h_2 \tag{7.57}$$

- The conditions denoted C_{2_1}, C_{2_2} and C_{2_3} defining the possible sub-cases are expressed in Eq.7.58, Eq.7.59 and Eq.7.60:

$$\begin{cases} C_{2_1}(M_R, Q) = ((1+2M_R)h_R^{\text{ref}} - h_1 + Q h^{\text{ref}}) \leq h_t & (7.58) \\ C_{2_2} = \dfrac{h_t}{h_R^{\text{ref}}} \in \mathbb{N} & (7.59) \\ C_{2_3}(Q) = mod(\left\lfloor \dfrac{h_1 - (Q+1)h^{\text{ref}} - h_R^{\text{ref}}}{h_R^{\text{ref}}} \right\rfloor, 2) = 0 & (7.60) \end{cases}$$

Existence of one or two peaks

According to the four cases defined by the parity of M_R and Q_2, the range profile will contain at least one peak. However, a second peak may appear if C_{R2} is true,

Position of the peaks

The range profile will contain at most two peaks:

- If two peaks exist, they will be at the position P_{R3} and P_{R4},
- If only one peak exists, it will be at P_{R3}.

Origin of the peaks

The origin of the peaks on the range profile (due to wall 2 or to the target) is indicated in Tab.7.3. The peak of the target is written with red color whereas the peak of the wall is written with blue color.

7.4.2.3 Case 3 of a target viewed by its right side

If the detection of the right side is impossible via LR_R^2, we can consider a third limit ray (denoted LR_R^3) corresponding to the ongoing ray via the right corner of the target's roof (see Fig.7.4(c)).

In Tab.7.4 are presented, according to the parity of Q_2 (defined in Eq.7.53) and M_R (defined in Eq.7.45), the four cases of study. For each case, we specify:

- The two conditions ensuring the existence of the ongoing sub-ray denoted C_{onR3_1} and C_{onR3_2}. They are expressed in Eq.7.61 and Eq.7.62.

$$\begin{cases} C_{onR3_1}(Q) = (h_t + h_L^{'\text{ref}} + Q h^{\text{ref}}) \leq h_2 & (7.61) \\ C_{onR3_2}(Q) = (h_t + h_L^{'\text{ref}} + Q h^{\text{ref}}) \geq h_1 & (7.62) \end{cases}$$

where h^{ref} and $h_L^{'\text{ref}}$ are defined in Eq.6.4 and Eq.7.3,

- The two conditions ensuring the existence of the outgoing sub-ray denoted C_{outR3_1} and C_{outR3_2}. They are expressed in Eq.7.63 and Eq.7.64:

$$\begin{cases} C_{outR3_1}(Q) = ((1+2M_R)h_R^{\text{ref}} - h_t + Qh^{\text{ref}}) \leq h_2 & (7.63) \\ C_{outR3_2}(Q) = ((1+2M_R)h_R^{\text{ref}} - h_t + Qh^{\text{ref}}) \geq h_1 & (7.64) \end{cases}$$

where h_R^{ref} is defined in Eq.7.4.

- P_{R5} and P_{R6}: the position of the two peaks associated to the second wall and to the target depending on $P(M_R, Q)$ defined in Eq.7.49,
- The condition of existence of the second peak denoted C_{R3} defined in Eq.7.65:

$$C_{R3}(M_R, Q) = (M_R h_R^{\text{ref}} + Qh^{\text{ref}}) \leq h_2 \quad (7.65)$$

- The condition denoted C_{3_1} defining the possible sub-case is expressed in Eq.7.66:

$$C_{3_1}(Q) = (h_t + h_R^{\text{ref}} + Qh^{\text{ref}}) \geq h_1 \quad (7.66)$$

Existence of one or two peaks

According to the two cases defined by the parity of Q_2, the range profile will contain at least one peak. However, a second peak may exist if C_{R3} is true.

Position of the peaks

The range profile will contain at most two peaks:

- If two peaks exist, they will be at the position P_{R5} and P_{R6},
- If only one peak exists, it will be at P_{R5}.

Origin of the peaks

The origin of the peaks on the range profile (due to wall 2 or to the target) is indicated in Tab.7.4. The peak of the target is written with red color whereas the peak of the wall is written with blue color.

7.4.2.4 Case 4 of a target viewed by its right side

The previous limit ray can not exist. (For example, the first wall obstructs the ongoing sub-ray of LR_R^3 as it is now higher.) So, we move to the last case defined by the limit ray LR_R^4 illustrated in Fig.7.4(d).

In Tab.7.5 are presented, according to the parity of Q_2 (defined in Eq.7.53) and M_R (defined in Eq.7.45), the four cases of study. For each case, we specify:

- The two conditions ensuring the existence of the ongoing sub-ray denoted C_{onR4_1} and C_{onR4_2}. They are expressed in Eq.7.67 and Eq.7.68:

$$\begin{cases} C_{onR4_1}(Q) = (h_t + h_R^{\text{ref}} + Qh^{\text{ref}}) \leq h_2 & (7.67) \\ C_{onR4_2}(Q) = (h_t + h_R^{\text{ref}} + Qh^{\text{ref}}) \geq h_1 & (7.68) \end{cases}$$

where h^{ref} and h_R^{ref} are defined in Eq.6.4 and Eq.7.4,

- The condition ensuring the existence of the outgoing sub-ray denoted C_{outR4} and expressed in Eq.7.69:

$$C_{outR4} = ((1+2M_R)h_R^{\text{ref}} - h_t + Qh^{\text{ref}}) \geq h_1 \quad (7.69)$$

- P_{R7} and P_{R8}: the position of the two peaks associated to the second wall and to the target depending on $P(M_R, Q)$ defined in Eq.7.49,
- The conditions of existence of the second peak denoted C_{R4_1} and C_{R4_2} defined in Eq.7.70 and Eq.7.71:

$$\begin{cases} C_{R4_1}(M_R, Q) = (M_R h_R^{\text{ref}} + Q h^{\text{ref}}) \geq h_1 & (7.70) \\ C_{R4_2}(M_R, Q) = (M_R h_R^{\text{ref}} + Q h^{\text{ref}}) \leq h_2 & (7.71) \end{cases}$$

Existence of one or two peaks

According to the two cases defined by the parity of Q_2, the range profile will contain at least one peak. However, a second peak may exist if C_{R4_1} or C_{R4_2} is true,

Position of the peaks

The range profile will contain at most two peaks:

- If two peaks exist, they will be at the position P_{R7} and P_{R8},
- If only one peak exists, it will be at P_{R7}.

Origin of the peaks

The origin of the peaks on the range profile (due to wall 2 or to the target) is indicated in Tab.7.5. The peak of the target is written with red color whereas the peak of the wall is written with blue color.

Fig.7.10 presents a summary of the four cases relative to the target detection by its right side is given. The conditions of existence of the limit rays as well as the position of peaks are presented in a logigramm.

Table 7.2: Table summarizing the conditions of existence of LR_R^1, the number and position of the peaks in the range profile.

Q_1 / M_R	odd	even
odd	$\mathbf{C_{1_1}(M_R, Q_1 + 1)}$ $C_{onR1_1}(Q_1 + 1)$ & $C_{onR1_2}(Q_1)$ $C_{outR1}(M_R + 1, Q_1)$ $P_{R1} = P(M_R, Q_1 + 2)$ $P_{R2} = P(M_R + 1, Q_1)$ if $C_{R1}(M_R + 1, Q_1)$	$\mathbf{C_{1_2}(Q_1)}$ $C_{onR1_1}(Q_1)$ & $C_{onR1_2}(Q_1 - 1)$ $C_{outR1}(M_R, Q_1)$ $P_{R1} = P(M_R, Q_1 + 1)$ $P_{R2} = P(M_R + 1, Q_1 - 1)$ if $C_{R1}(M_R + 1, Q_1 - 1)$
	$\overline{\mathbf{C_{1_1}(M_R, Q_1 + 1)}}$ $C_{onR1_1}(Q_1 + 1)$ & $C_{onR1_2}(Q_1)$ $C_{outR1}(M_R, Q_1 + 1)$ $P_{R1} = P(M_R, Q_1 + 2)$ $P_{R2} = P(M_R + 1, Q_1)$ if $C_{R1}(M_R + 1, Q_1)$	$\overline{\mathbf{C_{1_2}(Q_1)}}$ $C_{onR1_1}(Q_1)$ & $C_{onR1_2}(Q_1 - 1)$ $C_{outR1}(M_R + 1, Q_1)$ $P_{R1} = P(M_R + 1, Q_1 + 1)$ $P_{R2} = P(M_R, Q_1 + 1)$ if $C_{R1}(M_R, Q_1 + 1)$
even	$C_{onR1_1}(Q_1 + 1)$ & $C_{onR1_2}(Q_1)$ $C_{outR1}(M_R, Q_1)$ $P_{R1} = P(M_R + 1, Q_1)$ $P_{R2} = P(M_R, Q_1)$ if $C_{R1}(M_R, Q_1)$	$C_{onR1_1}(Q_1)$ & $C_{onR1_2}(Q_1 - 1)$ $C_{outR1}(M_R + 1, Q_1)$ $P_{R1} = P(M_R + 1, Q_1 + 1)$ $P_{R2} = P(M_R, Q_1 + 1)$ if $C_{R1}(M_R, Q_1 + 1)$

Table 7.3: Table summarizing the conditions of existence of LR_R^2, the number and position of the peaks in the range profile.

M_R \ Q_2	odd	even
odd	$\mathbf{C_{2_1}(M_R, Q_2)}$ $C_{onR2_1}(Q_2-1)$ &$C_{onR2_2}(Q_2)$ $C_{outR2}(M_R+1, Q_2)$ $P_{R3} = P(M_R+1, Q_2)$ $P_{R4} = P(M_R, Q_2+2)$ if $C_{R2}(M_R, Q_2+1)$	$C_{onR2_1}(Q_2)$ & $C_{onR2_2}(Q_2+1)$ $C_{outR2}(M_R, Q_2+1)$ $P_{R3} = P(M_R, Q_2+1)$ $P_{R4} = P(M_R+1, Q_2+1)$ if $C_{R2}(M_R+1, Q_2)$
	$\overline{\mathbf{C_{2_1}(M_R, Q_2)}}$ $C_{onR2_1}(Q_2-1)$ & $C_{onR2_2}(Q_2)$ $C_{outR2}(M_R, Q_2+1)$ $P_{R3} = P(M_R-1, Q_2+2)$ $P_{R4} = P(M_R, Q_2+2)$ if $C_{R2}(M_R, Q_2+1)$	
even	$\mathbf{C_{2_2}}$ $C_{onR2_1}(Q_2-1)$ & $C_{onR2_2}(Q_2)$ $C_{outR2}(M_R, Q_2)$ $P_{R3} = P(M_R, Q_2)$ $P_{R4} = P(M_R+1, Q_2)$ if $C_{R2}(M_R+1, Q_2-1)$	$\mathbf{C_{2_3}(Q_2)}$ $C_{onR2_1}(Q_2)$ & $C_{onR2_2}(Q_2+1)$ $C_{outR2}(M_R, Q_2+1)$ $P_{R3} = P(M_R, Q_2+1)$ $P_{R4} = P(M_R+1, Q_2+1)$ if $C_{R2}(M_R+1, Q_2)$
	$\overline{\mathbf{C_{2_2}}}$ $C_{onR2_1}(Q_2-1)$ & $C_{onR2_2}(Q_2)$ $C_{outR2}(M_R+1, Q_2)$ $P_{R3} = P(M_R+1, Q_2)$ $P_{R4} = P(M_R, Q_2+2)$ if $C_{R2}(M_R, Q_2+1)$	$\overline{\mathbf{C_{2_3}(Q_2)}}$ $C_{onR2_1}(Q_2)$ & $C_{onR2_2}(Q_2+1)$ $C_{outR2}(M_R+1, Q_2+1)$ $P_{R3} = P(M_R+1, Q_2+1)$ $P_{R4} = P(M_R, Q_2+3)$ if $C_{R2}(M_R, Q_2+2)$

Table 7.4: Table summarizing the conditions of existence of LR_R^3, the number and position of the peaks in the range profile.

Q_2 / M_R	odd	even
odd	$\mathbf{C_{3_1}(Q_2)}$ $C_{onR3_1}(Q_2)$ $C_{outR3_2}(Q_2)$ $P_{R5} = P(M_R+1, Q_2)$ $P_{R6} = P(M_R, Q_2+2)$ if $C_{R3}(M_R, Q_2+1)$ $\overline{\mathbf{C_{3_1}(Q_2)}}$ $C_{onR3_1}(Q_2)$ $C_{outR3_1}(Q_2+1)$ $P_{R5} = P(M_R, Q_2+2)$ $P_{R6} = P(M_R+1, Q_2+2)$ if $C_{R3}(M_R+1, Q_2+1)$	$C_{onR3_1}(Q_2-1)$ & $C_{onR3_2}(Q_2)$ $C_{outR3_1}(Q_2)$ $P_{R5} = P(M_R, Q_2+1)$ $P_{R6} = P(M_R+1, Q_2+1)$ if $C_{R3}(M_R+1, Q_2)$
even	$\mathbf{C_{3_1}(Q_2)}$ $C_{onR3_1}(Q_2)$ $C_{outR3_2}(Q_2)$ $P_{R5} = P(M_R+1, Q_2)$ $P_{R6} = P(M_R, Q_2+2)$ if $C_{R3}(M_R, Q_2+1)$ $\overline{\mathbf{C_{3_1}(Q_2)}}$ $C_{onR3_1}(Q_2)$ $C_{outR3_1}(Q_2+1)$ $P_{R5} = P(M_R, Q_2+2)$ $P_{R6} = P(M_R+1, Q_2+2)$ if $C_{R3}(M_R+1, Q_2+1)$	$C_{onR3_1}(Q_2-1)$ & $C_{onR3_2}(Q_2)$ $C_{outR3_1}(Q_2)$ $P_{R5} = P(M_R, Q_2+1)$ $P_{R6} = P(M_R+1, Q_2+1)$ if $C_{R3}(M_R+1, Q_2)$

Table 7.5: Table summarizing the conditions of existence of LR_R^4, the number and position of the peaks in the range profile.

Q_2 / M_R	odd	even
odd	$C_{onR4_1}(Q_2-1)$ & $C_{onR4_2}(Q_2)$ $C_{outR4}(Q_2)$ $P_{R7} = P(M_R+1, Q_2)$ $P_{R8} = P(M_R, Q_2+2)$ if $C_{R4_2}(M_R, Q_2+1)$	$C_{onR4_1}(Q_2)$ $P_{R7} = P(M_R+1, Q_2+1)$ $P_{R8} = P(M_R, Q_2+1)$ if $C_{R4_1}(M_R, Q_2+1)$
even	$C_{onR4_1}(Q_2-1)$ & $C_{onR4_2}(Q_2)$ $C_{outR4}(Q_2)$ $P_{R7} = P(M_R+1, Q_2)$ $P_{R8} = P(M_R, Q_2+2)$ if $C_{R4_2}(M_R, Q_2+1)$	$C_{onR4_1}(Q_2)$ $P_{R7} = P(M_R+1, Q_2+1)$ $P_{R8} = P(M_R, Q_2+1)$ if $C_{R4_1}(M_R, Q_2+1)$

7.4.3 Analysis of the left sub-canyon

The approach is the same as in the case of target right side detection since it is symmetric. Hence, we will present the four different cases relative to the detection of the target by its left side. For each case, we will present the corresponding limit ray and we will analyze the range profile.

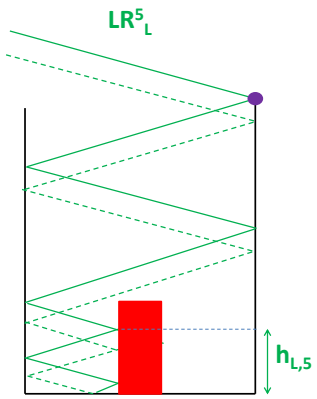

(a) Case 5: the purple dot delimits the first limit ray arriving on the top of the second wall.

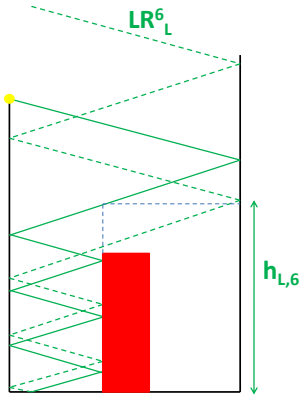

(b) Case 6: the yellow dot delimits the second limit ray arriving on the top of the first wall.

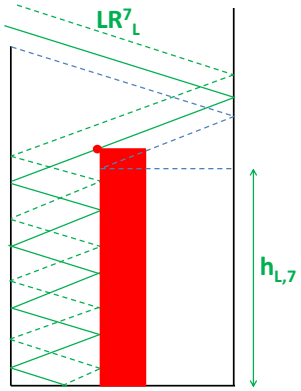

(c) Case 7: the red dot delimits the third limit ray (the ongoing ray via the left side of the target).

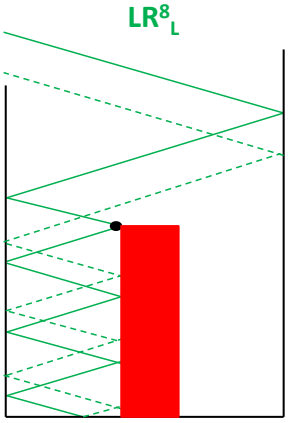

(d) Case 8: the black dot delimits the fourth limit ray.

Figure 7.6: Target's left side detection using the limit rays.

7.4.3.1 Case 5 of a target viewed by its left side

The limit ray of case 5 denoted LR_L^5 is the ray arriving on the top of the second wall as illustrated in Fig.7.6(a) (L because we are in the left sub-canyon and 5 as we consider case 5). This limit ray exists if both the ongoing and outgoing sub-rays exist. The number of small reflections between the second wall and the target (now denoted N_L) is calculated as follows:

$$N_L = \left\lfloor \frac{h_t}{h_L^{\text{ref}}} \right\rfloor \tag{7.72}$$

where h_L^{ref} is defined in Eq.7.4.

In Tab.7.6 are presented, according to the parity of Q_1 (defined in Eq.7.44) and N_L, the four cases of study. For each case, we specify:

- The two conditions ensuring the existence of the ongoing sub-ray denoted C_{onL5_1} and C_{onL5_2}. They are expressed in Eq.7.73 and Eq.7.74:

$$\begin{cases} C_{onL5_1}(Q) = (h_2 - Qh^{\text{ref}} - h_L^{\text{ref}}) \leq h_t & (7.73) \\ C_{onL5_2}(Q) = (h_2 - Qh^{\text{ref}} - h_R^{'\text{ref}}) \geq h_t & (7.74) \end{cases}$$

  where h^{ref}, h_L^{ref} and $h_R^{'\text{ref}}$ are defined in Eq.6.4, Eq.7.4 and Eq.7.3, respectively,
- The condition ensuring the existence of the outgoing sub-ray denoted C_{outL5} is expressed in Eq.7.75:

$$C_{outL5}(N_L, Q) = (2N_L h_L^{\text{ref}} - h_2 + (2Q+1)h^{\text{ref}}) \geq h_1 \quad (7.75)$$

- P_{L1} and P_{L2}: the positions of the two peaks associated to the first wall and to the target depending on $P(N_L, Q)$ defined in Eq.7.76:

$$P(N_L, Q) = (N_L L_L + QL)\sin\theta \quad (7.76)$$

- The conditions of existence of the second peak denoted C_{L5} defined in Eq.7.77:

$$C_{L5}(N_L, Q) = (N_L h_L^{\text{ref}} + Qh^{\text{ref}}) \geq h_1 \quad (7.77)$$

- The conditions denoted C_{5_1} and C_{5_2} defining the possible sub-cases are expressed in Eq.7.78 and Eq.7.79:

$$\begin{cases} C_{5_1}(N_L, Q) = ((1+2N_L)h_L^{\text{ref}} - h_2 + Qh^{\text{ref}}) \leq h_t & (7.78) \\ C_{5_2}(Q) = mod(\left\lfloor \dfrac{h_2 - Qh^{\text{ref}} - h_L^{\text{ref}}}{h_L^{\text{ref}}} \right\rfloor, 2) = 0 & (7.79) \end{cases}$$

Existence of one or two peaks

According to the four cases defined by the parity of N_L and Q_1, the range profile will contain at least one peak. However, a second peak may exist if C_{L5} is true.

Position of the peaks

The range profile will contain at most two peaks:

- If two peaks exist, they will be at the position P_{L1} and P_{L2},
- If only one peak exists, it will be at P_{L1}.

Origin of the peaks

In order to determine the origin of the peaks on the range profile (due to wall 1 or to the target), we have to consider both the parity of N_L and Q_1. For this case, the peak of wall 1 (written with blue color in Tab.7.6) will be always at P_{L2} provided the condition C_{L5} is true, whereas the peak of the target (written with red color) will be at P_{L1}.

7.4.3.2 Case 6 of a target viewed by its left side

The limit ray of case 6 denoted LR_L^6 is the ongoing ray via the top of the first wall as illustrated in Fig.7.6(b).

In Tab.7.7 are presented, according to the parity of Q_2 (defined in Eq.7.53) and N_L (defined in Eq.7.72), the four cases of study. For each case, we specify:

- The two conditions ensuring the existence of the ongoing sub-ray denoted C_{onL6_1} and C_{onL6_2}. They are expressed in Eq.7.80 and Eq.7.81:

$$\begin{cases} C_{onL6_1}(Q) = (h_1 - Qh^{\text{ref}} - h_L^{\text{ref}}) \leq h_t & (7.80) \\ C_{onL6_2}(Q) = (h_1 - Qh^{\text{ref}} - h_R^{'\text{ref}}) \geq h_t & (7.81) \end{cases}$$

  where h^{ref}, h_L^{ref} and $h_R^{'\text{ref}}$ are defined in Eq.6.4, Eq.7.4 and Eq.7.3, respectively,
- The condition ensuring the existence of the outgoing sub-ray denoted C_{outL6} is expressed in Eq.7.82:

$$C_{outL6}(N_L, Q) = (2N_L h_L^{\text{ref}} - h_1 + (2Q-1)h^{\text{ref}}) \leq h_2 \quad (7.82)$$

- P_{L3} and P_{L4}: the positions of the two peaks associated to the first wall and to the target depending on $P(N_L, Q)$ defined in Eq.7.76,
- The condition of existence of the second peak denoted C_{L6} defined in Eq.7.83:

$$C_{L6}(N_L, Q) = (N_L h_L^{\text{ref}} + Qh^{\text{ref}}) \leq h_2 \quad (7.83)$$

  ,
- The conditions denoted C_{6_1}, C_{6_2} and C_{6_3} defining the possible sub-cases are expressed in Eq.7.84, Eq.7.85 and Eq.7.86:

$$\begin{cases} C_{6_1}(N_L, Q) = ((1+2N_L)h_L^{\text{ref}} + Qh^{\text{ref}} - h_1) \leq h_t & (7.84) \\ C_{6_2} = \dfrac{h_t}{h_L^{\text{ref}}} \in \mathbb{N} & (7.85) \\ C_{6_3}(Q) = mod(\left\lfloor \dfrac{h_1 - (Q+1)h^{\text{ref}} - h_L^{\text{ref}}}{h_L^{\text{ref}}} \right\rfloor, 2) = 0 & (7.86) \end{cases}$$

  where Q_2 is defined in Eq.7.53.

Existence of one or two peaks

According to the four cases defined by the parity of N_L and Q_2, the range profile will contain at least one peak. However, a second peak may exist if C_{L6} is true.

Position of the peaks

The range profile will contain at most two peaks:

- If two peaks exist, they will be at the position P_{L3} and P_{L4},
- If only one peak exists, it will be at P_{L3}.

Origin of the peaks

In order to determine the origin of the peaks on the range profile (due to wall 1 or to the target), we have to consider both the parity of N_L and Q_2. The origin of the peaks on the range profile is indicated in Tab.7.7. The peak of the target is written with red color whereas the peak of the wall is written

with blue color.

7.4.3.3 Case 7 of a target viewed by its left side

The limit ray of case 7 denoted LR_L^7 is the ongoing ray via the left corner of the target's roof as illustrated in Fig.7.6(c).

In Tab.7.8 are presented, according to the parity of Q_2 (defined in Eq.7.53) and N_L (defined in Eq.7.72), the four cases of study. For each case, we specify:

- The two conditions ensuring the existence of the ongoing sub-ray denoted C_{onL7_1} and C_{onL7_2}. They are expressed in Eq.7.87 and Eq.7.88:

$$\begin{cases} C_{onL7_1}(Q) = (h_t + h_R^{'\text{ref}} + Qh^{\text{ref}}) \leq h_2 & (7.87) \\ C_{onL7_2}(Q) = (h_t + h_R^{'\text{ref}} + Qh^{\text{ref}}) \geq h_1 & (7.88) \end{cases}$$

  where h^{ref} and $h_R^{'\text{ref}}$ are defined in Eq.6.4 and Eq.7.3, respectively,
- The conditions ensuring the existence of the outgoing sub-ray denoted C_{outL7_1} and C_{outL7_2} are expressed in Eq.7.89 and Eq.7.90:

$$\begin{cases} C_{outL7_1}(Q) = ((1+2N_L)h_L^{\text{ref}} - h_t + Qh^{\text{ref}}) \leq h_2 & (7.89) \\ C_{outL7_2}(Q) = ((1+2N_L)h_L^{\text{ref}} - h_t + Qh^{\text{ref}}) \geq h_1 & (7.90) \end{cases}$$

  where h_L^{ref} is defined in Eq.7.4.
- P_{L5} and P_{L6}: the positions of the two peaks associated to the first wall and to the target depending on $P(N_L, Q)$ defined in Eq.7.76,
- The conditions of existence of the second peak denoted C_{L7} defined in Eq.7.91:

$$C_{L7}(N_L, Q) = (N_L h_L^{\text{ref}} + Qh^{\text{ref}}) \leq h_2 \quad (7.91)$$

- The condition denoted C_{7_1} defining the possible sub-cases is expressed in Eq.7.92:

$$C_{7_1}(Q) = (h_t + h_L^{\text{ref}} + Qh^{\text{ref}}) \geq h_1 \quad (7.92)$$

Existence of one or two peaks

According to the two cases defined by the parity of Q_2, the range profile will contain at least one peak. However, a second peak may exist if C_{L7} is true.

Position of the peaks

The range profile will contain at most two peaks:

- If two peaks exist, they will be at the positions P_{L5} and P_{L6},
- If only one peak exists, it will be at P_{L5}.

Origin of the peaks

In order to determine the origin of the peaks on the range profile (due to wall 1 or to the target), we have to consider both the parity of N_L and Q_2. The origin of the peaks on the range profile is indicated in Tab.7.8. The peak of the target is written with red color whereas the peak of the wall is written with blue color.

7.4.3.4 Case 8 of a target viewed by its left side

The limit ray of case 8 denoted LR_L^8 is illustrated in Fig.7.6(d).

In Tab.7.9 are presented, according to the parity of Q_2 (defined in Eq.7.53) and N_L (defined in Eq.7.72), the four cases of study. For each case, we specify:

- The two conditions ensuring the existence of the ongoing sub-ray denoted C_{onL8_1} and C_{onL8_2}. They are expressed in Eq.7.93 and Eq.7.94:

$$\begin{cases} C_{onL8_1}(Q) = (h_t + h_L^{\text{ref}} + Qh^{\text{ref}}) \leq h_2 & (7.93) \\ C_{onL8_2}(Q) = (h_t + h_L^{\text{ref}} + Qh^{\text{ref}}) \geq h_1 & (7.94) \end{cases}$$

  where h^{ref} and h_L^{ref} are defined in Eq.6.4 and Eq.7.4,
- The condition ensuring the existence of the outgoing sub-ray denoted C_{outL8} is expressed in Eq.7.95:

$$C_{outL8}(Q) = ((1 + 2N_L)h_L^{\text{ref}} - h_t + Qh^{\text{ref}}) \geq h_1 \quad (7.95)$$

- P_{L7} and P_{L8}: the positions of the two peaks associated to the first wall and to the target depending on $P(N_L, Q)$ defined in Eq.7.76,
- The conditions of existence of the second peak denoted C_{L8_1} and C_{L8_1} defined in Eq.7.96 and Eq.7.97:

$$\begin{cases} C_{L8_1}(N_L, Q) = (N_L h_L^{\text{ref}} + Qh^{\text{ref}}) \geq h_1 & (7.96) \\ C_{L8_2}(N_L, Q) = (N_L h_L^{\text{ref}} + Qh^{\text{ref}}) \leq h_2 & (7.97) \end{cases}$$

Existence of one or two peaks

According to the two cases defined by the parity of Q_2, the range profile will contain at least one peak. However, a second peak may exist if C_{L8_1} or C_{L8_2} are true.

Position of the peaks

The range profile will contain at most two peaks:

- If two peaks exist, they will be at the position P_{L7} and P_{L8},
- If only one peak exists, it will be at P_{L7}.

Origin of the peaks

In order to determine the origin of the peaks on the range profile (due to wall 1 or to the target), we have to consider both the parity of N_L and Q_2. The origin of the peaks on the range profile is indicated in Tab.7.9. The peak of the target is written with red color whereas the peak of the wall is written with blue color.

In Fig.7.11 a summary of the four cases relative to the target detection by its left side. The conditions of existence of the limit rays as well as the position of peaks are presented in a logigramm.

Table 7.6: Table summarizing the conditions of existence of LR_L^5, the number and position of the peaks in the range profile.

Q_1 / N_L	odd	even
odd	$\mathbf{C_{5_2}(Q_1)}$ $C_{onL5_1}(Q_1)$ & $C_{onL5_2}(Q_1-1)$ $C_{outL5}(N_L, Q_1)$ $P_{L1} = P(N_L, Q_1+1)$ $P_{L2} = P(N_L+1, Q_1-1)$ if $C_{L5}(N_L+1, Q_1-1)$	$\mathbf{C_{5_1}(N_L, Q_1+1)}$ $C_{onL5_1}(Q_1+1)$ & $C_{onL5_2}(Q_1)$ $C_{outL5}(N_L+1, Q_1)$ $P_{L1} = P(N_L, Q_1+2)$ $P_{L2} = P(N_L+1, Q_1)$ if $C_{L5}(N_L+1, Q_1)$
	$\overline{\mathbf{C_{5_2}(Q_1)}}$ $C_{onL5_1}(Q_1)$ & $C_{onL5_2}(Q_1-1)$ $C_{outL5}(N_L+1, Q_1)$ $P_{L1} = P(N_L+1, Q_1+1)$ $P_{L2} = P(N_L, Q_1+1)$ if $C_{L5}(N_L, Q_1+1)$	$\overline{\mathbf{C_{5_1}(N_L, Q_1+1)}}$ $C_{onL5_1}(Q_1+1)$ & $C_{onL5_2}(Q_1)$ $C_{outL5}(N_L, Q_1+1)$ $P_{L1} = P(N_L, Q_1+2)$ $P_{L2} = P(N_L+1, Q_1)$ if $C_{L5}(N_L+1, Q_1)$
even	$C_{onL5_1}(Q_1)$ & $C_{onL5_2}(Q_1-1)$ $C_{outL5}(N_L+1, Q_1)$ $P_{L1} = P(N_L+1, Q_1+1)$ $P_{L2} = P(N_L, Q_1+1)$ if $C_{L5}(N_L, Q_1+1)$	$C_{onL5_1}(Q_1+1)$ & $C_{onL5_2}(Q_1)$ $C_{outL5}(N_L, Q_1)$ $P_{L1} = P(N_L+1, Q_1)$ $P_{L2} = P(N_L, Q_1)$ if $C_{L5}(N_L, Q_1)$

Table 7.7: Table summarizing the conditions of existence of LR_L^6, the number and position of the peaks in the range profile.

Q_2 / N_L	odd	even
odd	$C_{onL6_1}(Q_2)$ & $C_{onL6_2}(Q_2+1)$ $C_{outL6}(N_L, Q_2+1)$ $P_{L3} = P(N_L, Q_2+1)$ $P_{L4} = P(N_L+1, Q_2+1)$ if $C_{L6}(N_L+1, Q_2)$	$\mathbf{C_{6_2}}$ $C_{onL6_1}(Q_2-1)$ & $C_{onL6_2}(Q_2)$ $C_{outL6}(N_L, Q_2)$ $P_{L3} = P(N_L, Q_2)$ $P_{L4} = P(N_L+1, Q_2)$ if $C_{L6}(N_L+1, Q_2-1)$
		$\overline{\mathbf{C_{6_2}}}$ $C_{onL6_1}(Q_2-1)$ & $C_{onL6_2}(Q_2)$ $C_{outL6}(N_L+1, Q_2)$ $P_{L3} = P(N_L+1, Q_2)$ $P_{L4} = P(N_L, Q_2+2)$ if $C_{L6}(N_L, Q_2+1)$
even	$\mathbf{C_{6_3}(Q_2)}$ $C_{onL6_1}(Q_2)$ & $C_{onL6_2}(Q_2+1)$ $C_{outL6}(N_L, Q_2+1)$ $P_{L3} = P(N_L, Q_2+1)$ $P_{L4} = P(N_L+1, Q_2+1)$ if $C_{L6}(N_L+1, Q_2)$	$\mathbf{C_{6_1}(N_L, Q_2)}$ $C_{onL6_1}(Q_2-1)$ & $C_{onL6_2}(Q_2)$ $C_{outL6}(N_L+1, Q_2)$ $P_{L3} = P(N_L+1, Q_2)$ $P_{L4} = P(N_L, Q_2+2)$ if $C_{L6}(N_L, Q_2+1)$
	$\overline{\mathbf{C_{6_3}(Q_2)}}$ $C_{onL6_1}(Q_2)$ & $C_{onL6_2}(Q_2+1)$ $C_{outL6}(N_L+1, Q_2+1)$ $P_{L3} = P(N_L+1, Q_2+1)$ $P_{L4} = P(N_L, Q_2+3)$ if $C_{L6}(N_L, Q_2+2)$	$\overline{\mathbf{C_{6_1}(N_L, Q_2)}}$ $C_{onL6_1}(Q_2-1)$ & $C_{onL6_2}(Q_2)$ $C_{outL6}(N_L, Q_2+1)$ $P_{L3} = P(N_L-1, Q_2+2)$ $P_{L4} = P(N_L, Q_2+2)$ if $C_{L6}(N_L, Q_2+1)$

Table 7.8: Table summarizing the conditions of existence of LR_L^7, the number and position of the peaks in the range profile.

N_L \ Q_2	odd	even
odd	$C_{onL7_1}(Q_2-1)$ & $C_{onL7_2}(Q_2)$ $C_{outL7_1}(Q_2)$ $P_{L5} = P(N_L, Q_2+1)$ $P_{L6} = P(N_L+1, Q_2+1)$ if $C_{L7}(N_L+1, Q_2)$	$C_{7_1}(Q_2)$ $C_{onL7_1}(Q_2)$ $C_{outL7_2}(Q_2)$ $P_{L5} = P(N_L+1, Q_2)$ $P_{L6} = P(N_L, Q_2+2)$ if $C_{L7}(N_L, Q_2+1)$
		$\overline{C_{7_1}(Q_2)}$ $C_{onL7_1}(Q_2)$ $C_{outL7_2}(Q_2+1)$ $P_{L5} = P(N_L, Q_2+2)$ $P_{L6} = P(N_L+1, Q_2+2)$ if $C_{L7}(N_L+1, Q_2+1)$
even	$C_{onL7_1}(Q_2-1)$ & $C_{onL7_2}(Q_2)$ $C_{outL7_1}(Q_2)$ $P_{L5} = P(N_L, Q_2+1)$ $P_{L6} = P(N_L+1, Q_2+1)$ if $C_{L7}(N_L+1, Q_2)$	$C_{7_1}(Q_2)$ $C_{onL7_1}(Q_2)$ $C_{outL7_2}(Q_2)$ $P_{L5} = P(N_L+1, Q_2)$ $P_{L6} = P(N_L, Q_2+2)$ if $C_{L7}(N_L, Q_2+1)$
		$\overline{C_{7_1}(Q_2)}$ $C_{onL7_1}(Q_2)$ $C_{outL7_2}(Q_2+1)$ $P_{L5} = P(N_L, Q_2+2)$ $P_{L6} = P(N_L+1, Q_2+2)$ if $C_{L7}(N_L+1, Q_2+1)$

Table 7.9: Table summarizing the conditions of existence of LR_L^8, the number and position of the peaks in the range profile.

N_L \ Q_2	odd	even
odd	$C_{onL8_1}(Q_2)$ $P_{L7} = P(N_L+1, Q_2+1)$ $P_{L8} = P(N_L, Q_2+1)$ if $C_{L8_1}(N_L, Q_2+1)$	$C_{onL8_1}(Q_2-1)$ & $C_{onL8_2}(Q_2)$ $C_{outL8}(Q_2)$ $P_{L7} = P(N_L+1, Q_2)$ $P_{L8} = P(N_L, Q_2+2)$ if $C_{L8_2}(N_L, Q_2+1)$
even	$C_{onL8_1}(Q_2)$ $P_{L7} = P(N_L+1, Q_2+1)$ $P_{L8} = P(N_L, Q_2+1)$ if $C_{L8_1}(N_L, Q_2+1)$	$C_{onL8_1}(Q_2-1)$ & $C_{onL8_2}(Q_2)$ $C_{outL8}(Q_2)$ $P_{L7} = P(N_L+1, Q_2)$ $P_{L8} = P(N_L, Q_2+2)$ if $C_{L8_2}(N_L, Q_2+1)$

7.4.4 Analysis of the parallelepiped target detection by its roof

The approach we propose to study the detection of the target by its roof is to consider that the detection is possible only if the incident rays on the roof can have a specular reflection and return to the receiver. In other words, if the roof is located in a NLOS detectability area by specular reflection mechanism of a specific canyon, it can be detected. To establish if the roof of the target is detected, we first have to define a new canyon. Then, we can apply the results of **Urban Canyon V1** to determine the NLOS detectability areas by specular reflection mechanism. This new canyon is represented in Fig.7.7. The height of the walls are now $h_1 - h_t$ and $h_2 - h_t$, whereas the width of the canyon remains the same. As for **Urban Canyon V1**, we define:

$$m = \left\lfloor \frac{h_1 - h_t}{h^{\text{ref}}} \right\rfloor \tag{7.98}$$

$$n = \left\lfloor \frac{h_2 - h_t}{h^{\text{ref}}} \right\rfloor + 1 \tag{7.99}$$

The logigramm in Fig.7.8 determines according to the cases $n = m+1$, $n = m+2$, the parity of m and n as well as the position of the target inside the canyon:

- If the roof is detected,
- If the response of the roof is represented by one or two peaks,
- The positions of the peaks on the range profile.

Let $P_{\text{rf}_{i,i=\{1,2\}}}$ be the position of the peaks due to the roof in the range profile, where:

$$\begin{cases} P_{\text{rf}_1} = (m+1)\, L \sin\theta & (7.100) \\ P_{\text{rf}_2} = (m+2)\, L \sin\theta & (7.101) \end{cases}$$

The phase center is located on the bottom of wall 1 as illustrated in Fig.7.7. $Z_{odd,m,m+1,m+2}$ and $Z_{even,m,m+1,m+2}$ are defined in Fig.6.14, by analogy.

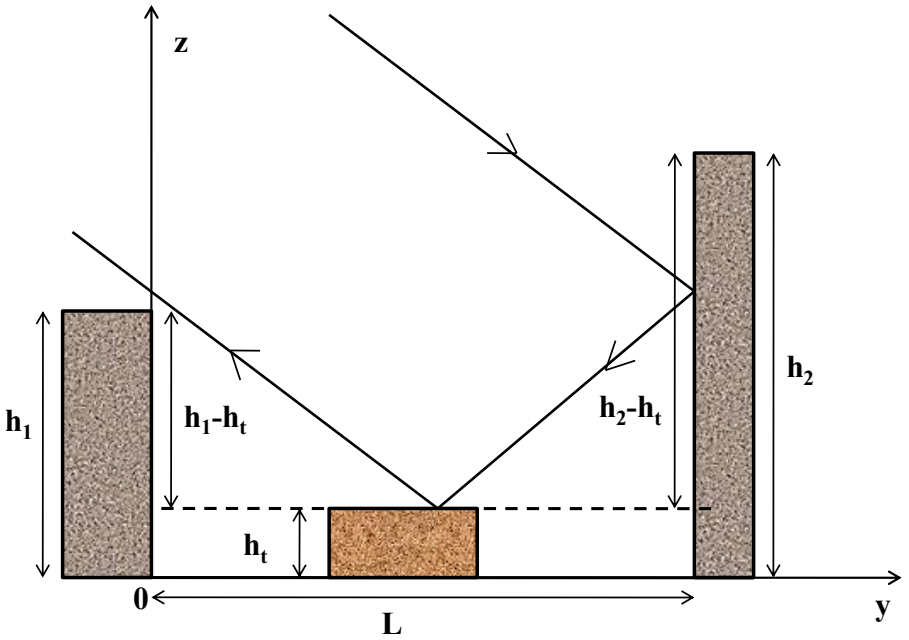

Figure 7.7: Target detection via the roof.

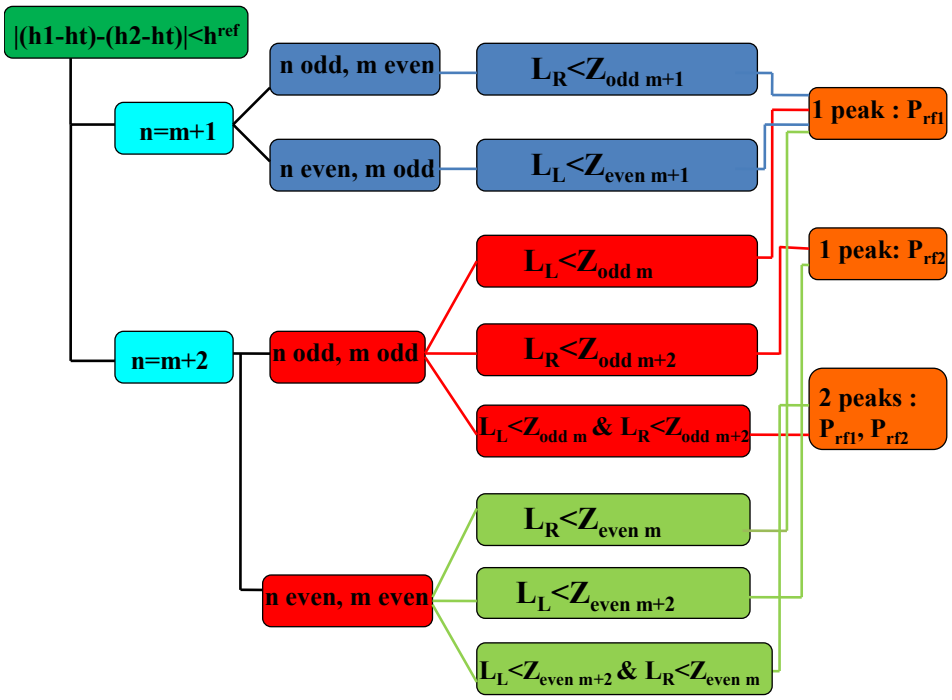

Figure 7.8: Logigramm describing the cases where a target can be detected by its roof.

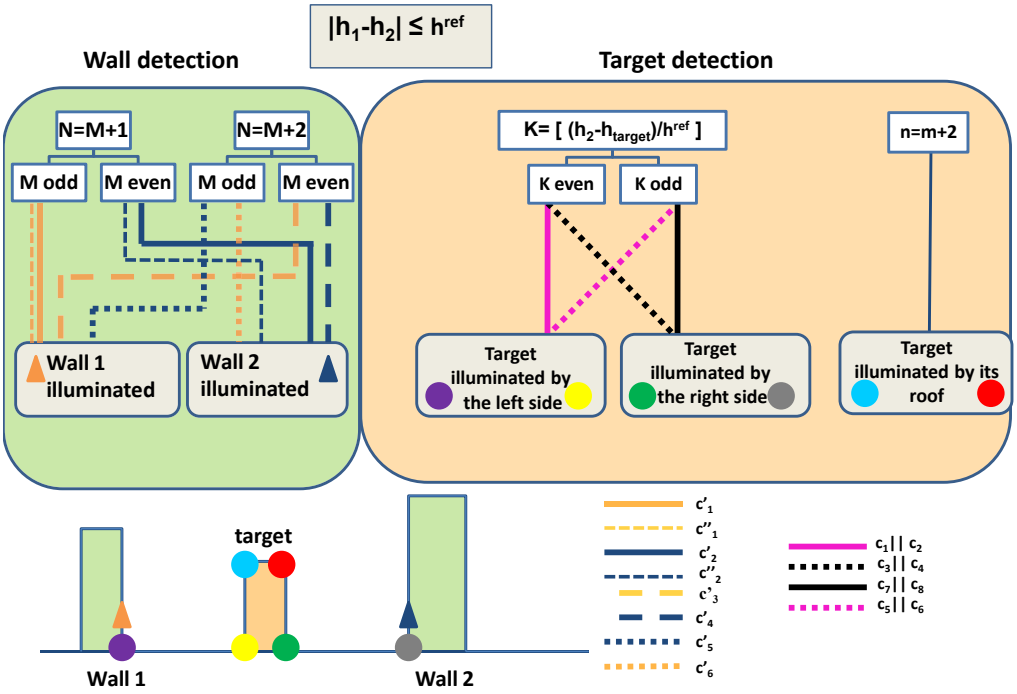

Figure 7.9: Logigramm describing the different cases where the walls of the canyon and the parallelepiped target can be detected.

7.4.5 Percentage of detectability areas

The detectability percentage of an extended target has increased comparing to the point target since the extended target can be detected via multiple responses. Indeed, for the case of a canyon with a parallelepiped target, the range profile can contain up to 8 peaks:

- 2 peaks due to the dihedral effects of the walls with no interactions with the target (see the orange and blue triangles in Fig.7.9 referring to the two geometric mechanisms leading to these two peaks),
- 2 peaks due to the dihedral effects of the walls with interactions with the target (see the purple and gray circles in Fig.7.9 referring to the two geometric mechanisms leading to these two peaks),
- 2 peaks due the dihedral effects on the left side and right side of the target (see the yellow and green circles in Fig.7.9 referring to the two geometric mechanisms leading to these two peaks),
- 2 peaks due to two specular reflection mechanisms on the roof of the target (see the blue and red circles in Fig.7.9 referring to the two geometric mechanisms leading to these two peaks).

Hence, we can conclude that, even if in real case, we expect the presence of less than the six theoretical responses of the target in the range profile (due to the possible loss in the amplitude of the peaks caused by the urban materials), there will be still enough peaks to conclude about the eventual presence of the NLOS target inside the canyon.

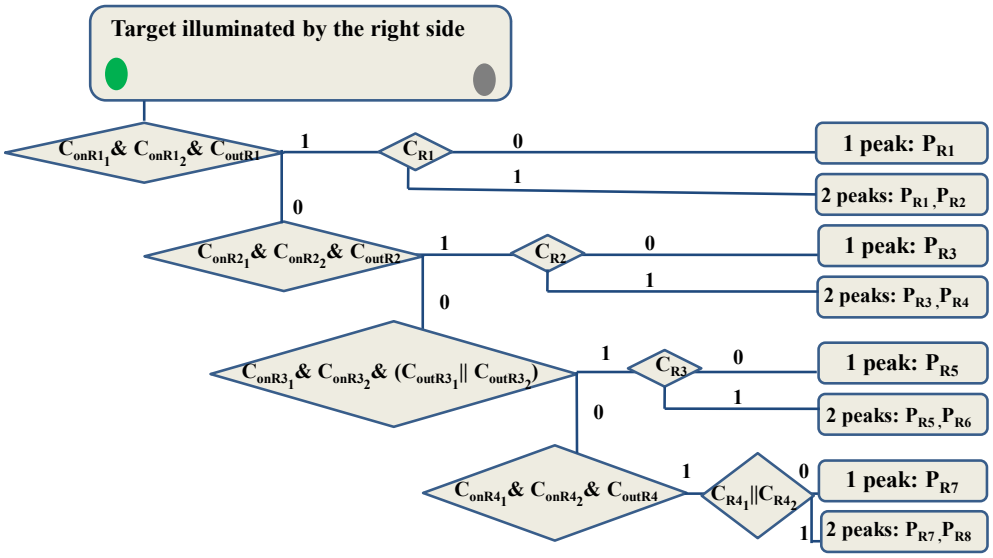

Figure 7.10: Logigramm describing the cases where a target can be detected by its right side.

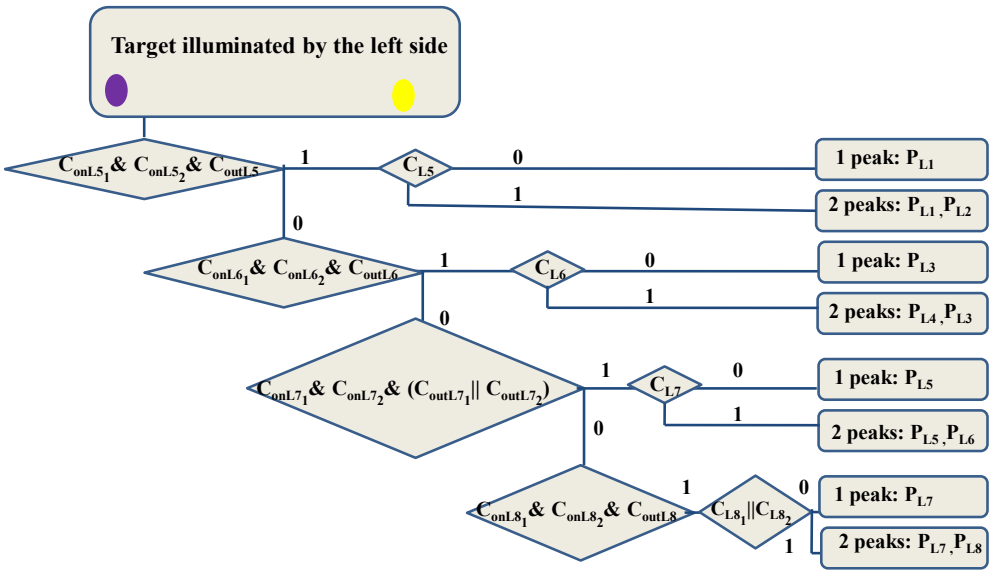

Figure 7.11: Logigramm describing the cases where a target can be detected by its left side.

7.5 Validation of Urban Canyon V3 using FEKO

Urban Canyon V3 can not be validated directly with FEKO since FEKO is a 3D tool and Urban Canyon V3 is a 2D tool. However, we can propose a formula to validate Urban Canyon V3 by assigning a scattering matrix S instead of a reflection coefficient R (R=1 as we consider PEC case) to calculate the RCS σ. We define:

- $\underline{E}^i_{ucv3}$ and $\underline{E}^s_{ucv3}$ the complex incident and scattered electric fields calculated with Urban Canyon V3, respectively,
- $\underline{E}^i_{feko}$ and $\underline{E}^s_{feko}$ the complex incident and scattered electric fields calculated with FEKO, respectively.

Assuming that $\underline{E}^i_{ucv3} = \underline{E}^i_{feko}$, we can write:

$$\begin{cases} \underline{E}^s_{ucv3} = R \times \underline{E}^i_{ucv3} = 1 \times \underline{E}^i_{ucv3} \\ \underline{\hat{E^s}}_{feko} = \hat{S} \times \underline{E}^i_{feko} = \hat{S} \times \underline{E}^s_{ucv3} \end{cases} \tag{7.102}$$

Therefore:

$$\hat{\sigma_{feko}}^{qp} = 20Log_{10}(\hat{S^{qp}}) + \sigma_{ucv3} \tag{7.103}$$

Where $\hat{S^{qp}}$ is the component of $\hat{S}$ at the qp polarization. Referring to this previous equation, the validation of Urban Canyon V3 will concern the evaluation of the σ_{feko} by a comparison with the value calculated with this equation and the value calculated by FEKO. To present an example of validation of Urban Canyon V3, we choose the case of the canyon configuration of the anechoic chamber described in Sec.4.2. In Fig.7.12, we represent the visualisation of the simulated rays that are able to go back to the receiver on this canyon configuration using Urban Canyon V3.

With FEKO, we simulated this canyon configuration at the frequency of 78 GHz, to ensure a d/λ ratio tending to the real one using GO and MoM. This range profile is illustrated in Fig.7.13. As we can notice, $\sigma_{feko} \simeq 23$ dB.

As noticed in Fig.7.12, there are two mechanisms occurring inside the canyon configuration:

- a first mechanism scattered by the plate P_1 of dimension a and b
- a second mechanism scattered by the plate P_2 of dimensions a_1 and b.

The resulting scattered field at the polarization qp (in this case, Vv polarization is considered since the simulations of FEKO have been performed at this polarization) can be expressed by:

$$\underline{\hat{E^s}}_{feko}^{qp} = \hat{S_1^{qp}}\underline{E}^i_{feko} + \hat{S_2^{qp}}\underline{E}^i_{feko} \tag{7.104}$$

$$= \underline{E}^i_{feko}(\hat{S_1^{qp}} + \hat{S_2^{qp}}) \tag{7.105}$$

$$= \underline{E}^s_{ucv3}(\hat{S_1^{qp}} + \hat{S_2^{qp}}) \tag{7.106}$$

Where $\hat{S_i^{qp}}$ is the component of the plate scattering matrix at the polarization qp. It is defined according to [Ulaby 1990] as:

$$\hat{S_i^{qp}} = \frac{a \times b}{\lambda} \sin\theta \tag{7.107}$$

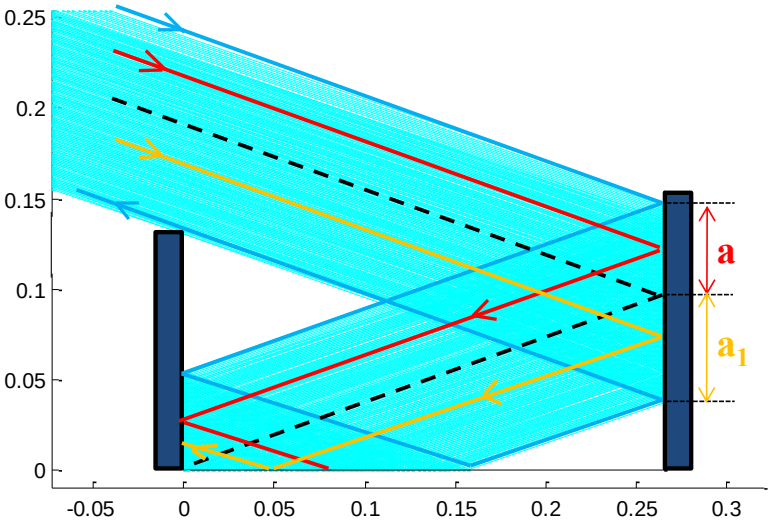

Figure 7.12: 2D visualisation of the incident rays the can go back to the receiver using Urban Canyon V3 for the canyon configuration of the anechoic chamber described in Fig.4.5.

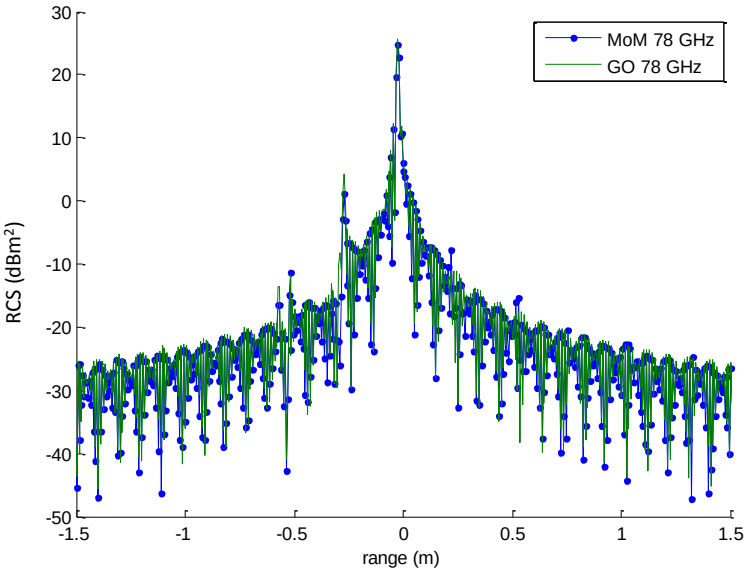

Figure 7.13: Two simulated range profiles with FEKO using MoM and GO for the canyon configuration of Fig.4.5 at the frequency of 78 GHz.

where a and b are the dimensions of the plate, λ is the wavelength and θ is the incidence angle. Hence:

$$\sigma_{feko}^{\hat{qp}} = 20log_{10}(S_1^{\hat{qp}} + S_2^{\hat{qp}}) + \sigma_{ucv3} \tag{7.108}$$

$$= 20log_{10}(\frac{(a+a_1)b\sin\theta}{\lambda}) + \sigma_{ucv3} \tag{7.109}$$

a and a_1 are illustrated in Fig.7.12 and are equal to the width of the incident beam defining the two mechanisms on wall 2, such as:

$$\begin{cases} a = 6cm \\ a_1 = 5.4cm \\ b = 22cm \end{cases} \tag{7.110}$$

λ is the wavelength corresponding to the frequency of 78 GHz and $\theta = 70°$. b corresponds to the length of the walls of the canyon. As noticed in Fig.7.14, $\sigma_{ucv3} = 10.64dBm^2$. Therefore according to Eq.7.109, we obtain:

$$\sigma_{feko}^{\hat{qp}} = 26.73dBm^2 \tag{7.111}$$

In Fig.7.15, we have illustrated the range profile simulated with FEKO and the range profile obtained using the Eq.7.109. We notice that there is a difference of 3 dB between the estimated and the simulated range profile. This is due to the fact that we did some approximations on the estimation of the scattering matrices as well as we did not took into account all the 3D effects considered by FEKO. Nevertheless, the results of validation are quite reasonable. This constitutes a first step to extend our 2D EM tool to a 3D EM tool.

7.6 Conclusion

This chapter was dedicated to present the last and complete version of our developed EM code (Urban Canyon V3) for the detection of NLOS extended targets inside an urban canyon. The first conclusion is that the detectability percentage has increased comparing to the case of the empty canyon and to the case of a canyon with an included point target since the extended target can be detected via multiple responses (up to 6 responses). It is then obvious that the study of NLOS areas inside the canyon and the corresponding scattering mechanism is interesting in the field of target detection inside urban scenes since the percentage of detection may be drastically increased when considering extended targets. In addition, we have validated our EM developed code with a reliable EM commercial code (FEKO) that we selected after a bechmarking of different commercial EM codes. Indeed, the comparison between the simulation results of our code and the simulation results with FEKO shows that there is an agreement in terms of phase and amplitude, even if we have managed the calculation to allow the comparison between our 2D tool and the simulation results of a 3D EM tool. Thus, we can conclude that even if our EM tool is simple in terms of EM considerations (PEC case with no material

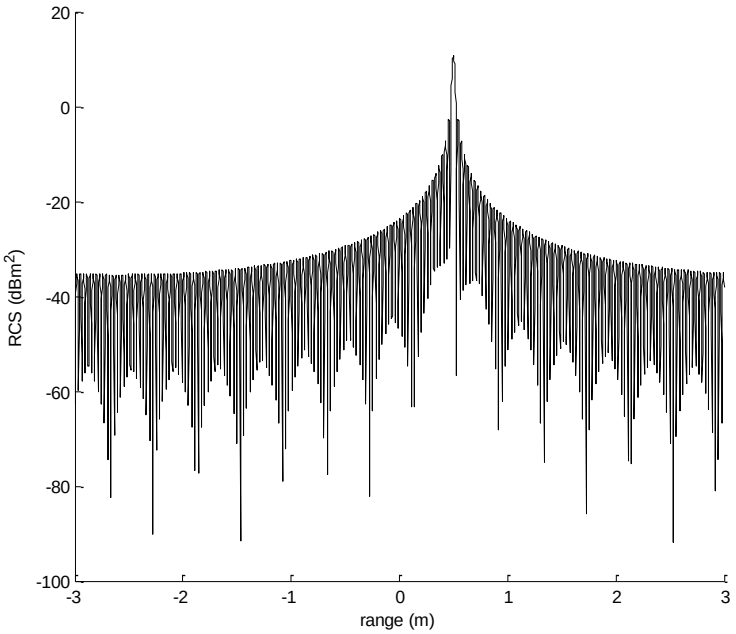

Figure 7.14: Range profile simulated with Urban Canyon V3 corresponding to the canyon configuration of Fig.4.5.

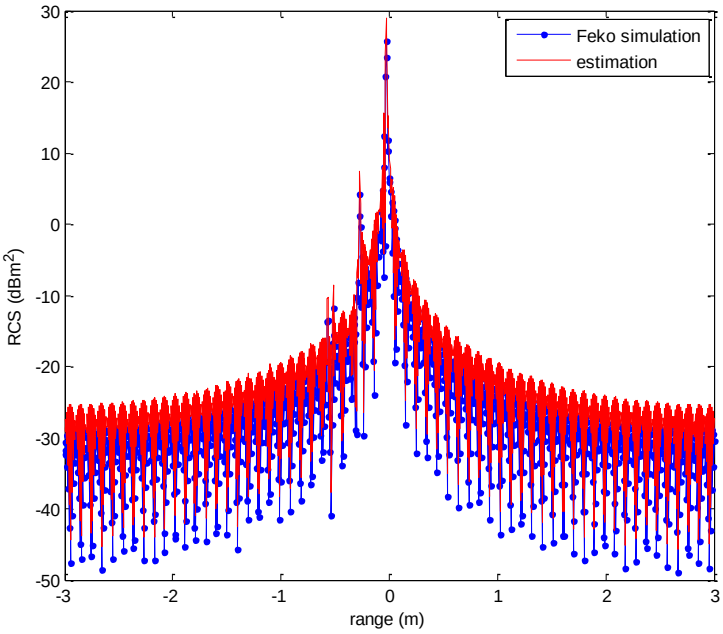

Figure 7.15: Simulated and estimated range profile corresponding to the canyon configuration of Fig.4.5.

properties), complexity of the scene it simulates (urban canyon perpendicular to the propagation plan, 2D considerations) and resulting outputs (range profile), it is a validated tool that shows promising results concerning the detectability of NLOS targets inside urban canyons. In the next chapter, we will use the results of the developed EM code to interpret real SAR data. We will provide a complete analysis of an InSAR image of a scene containing a complex canyon with different materials and different types of targets in NLOS configurations.

Chapter 8

On the use of the in-house EM code to analyze InSAR data

Contents

8.1 Introduction

In the specific frame of InSAR data analysis of urban areas, we propose in this chapter to provide a complete interpretation of a radiometric and interferometric SAR image of a real urban scene containing a canyon with simple and complex targets located inside it. The main objective is to interpret real InSAR data of a canyon with all the possible effects occurring inside, using our EM developed code (Urban Canyon V3). The use of this code on real data constitutes a second validation (the first one has been investigated in the previous chapter). The long-term goal of this analysis is to obtain 3D reconstruction of urban environments thanks to interferometric SAR images. Approaches for a 3D building reconstruction from SAR and

InSAR data have been proposed for rural areas ([Botler 2001]) and industrial plants ([Soergel 2001]) and achieved good results. The situation is more difficult in inner city areas where high buildings are often located in close proximity to each other and can induce effects that burden the interpretation of the data and make the 3D building reconstruction difficult to perform ([Stilla 2003]). These effects such as layover, occlusion by radar shadow, and multipath signal propagation are the consequences of the oblique scene illumination ([Soergel 2003]). Furthermore, specular reflection and multi-bounces scattering can result in very strong signals which superimpose the backscatter of large parts of their neighborhood. Another typical problem due to the urban scene geometry is the mixture of signal contributions of different objects with the same distance to the sensor.

In the SAR field, some well-known techniques for building recognition and height estimation have been proposed. When only a single SAR image is available, classical measure-based methods, using layover [Tupin 2003] or shadow length [Bennett 2003], have been applied for height retrieval. More recently, in the case where the buildings characteristics are available, new statistical [Le Moigne 2007], electromagnetic ([Franceschetti 2002], [Guida 2010]) or simulation-based approaches performing buildings segmentation before the reconstruction ([Brunner 2010], [Sportouche 2009]), have proved to provide satisfying results for building reconstruction.

In SAR interferometry (InSAR) or radargrammetry, there are methods that aim to produce DSM (Digital Surface Model) and DEM (Digital Elevation Model) and are usually based on the height estimation of classes ([Tison 2007]). Others methods focus on the height estimation of single elements: in ([Guillaso 2005]), a phase-to-height procedure after a polarimetric and interferometric segmentation is proposed. In [Cellier 2007], the approach for single building height estimation is based on separating the phases of two contributions in layover areas. With this model, knowing the resulting phase mixture value and one of the two contributions, it is possible to obtain the second. This model has been validated on the estimation of the interferometric height of isolated buildings.

In this present thesis, our approach is similar to the last method since it is based also on phases separation in layover areas, but takes into account the scattering of a whole scene (two buildings with a road separating them and different targets located inside) and not just a detached building. Indeed, the interactions between the buildings, between the building and the ground and even with the targets are taken into account in our interpretation of the InSAR data specially in the zones where there are a mixture of phases. In addition, our second contribution comparing to the work in [Cellier 2007] is that we extended the study of the case corresponding to a mixture of two mechanisms to the more general case of N mechanisms by a proposed formula. Our approach is based on multipath propagation understanding to better explain the origin of some layover areas observed in the InSAR data. We propose to provide a complete interpretation of the radiometric and interferometric image of an urban canyon using Urban Canyon V3 and an EM scattering study of some materials in the scene. An analysis of the different features extracted as well as the EM mechanisms leading to theses features helps in explaining the resulting interferometric signature specially for the zone of layover.

This chapter is organised as follows: as we aim to interpret High Resolution

(HR) SAR data acquired by an airborne system at Ka-band, it is necessary to introduce in the first section a brief description of the existing SAR systems with the used frequencies bands and resolutions in order to have an idea about their evolution. As these current systems provide (HR) SAR images, it is possible to distinguish small structures details like roof, windows and balconies. However, these HR SAR images are strongly affected by geometric distortion effects due to the combination of the SAR side looking acquisition and heights variation of the urban structures within the scene. Therefore, the second section will be devoted to present the most common effects that hinder the analysis of these images and make their visual interpretation difficult. This study will help in understanding the origin of a common geometric effect that impacted in the interferometric signature of the InSAR data we aim to analyze (the layover effect described later). After this state-of-art study, we present the main objectives of the InSAR data analysis. In the fifth section, a description of the scene under study is given with the associated canyon and the different targets dimensions and positions. The corresponding radiometric and interferometric images are introduced. The following section is devoted to the complete analysis of the radiometric image. It deals with the identification of the of the main features in the image and the associated mechanisms leading to each feature. Then, a formula to calculate the backscattering coefficient in layover areas is proposed and validated. The following section is devoted to the interferometric analysis. The interferometric zones of layovers have been delimited using our EM code. After that, the interferometric coherence of each zone has been analyzed with a proposed formula that has been validated with a statistical study. Finally, we end up this chapter by some conclusions.

8.2 Overview of spaceborne and airborne SAR systems

SAR sensors have been used in many cases for disaster mitigation and damage assessment in the past, especially during or after flooding ([Voigt 2005]) and in the aftermath of earthquakes ([Takeuchi 2000]). One recent example is the Wenchuan Earthquake that hit central China in May 2008. The severe damage of a city caused by landslides triggered by the earthquake was investigated using post-strike images of satellites TerraSAR-X (TSX) and Cosmo-Skymed ([Liao 2009]). Spaceborne systems have the advantage of providing almost global data coverage, but the limitation of being tied to a predefined sequence of orbits, which determine the potential time slots and the aspect of observation (ascending or descending orbit) to gather data of a certain area of interest. On the other hand, airborne sensors are more flexible, but have to be mobilized and transferred to the scene. In Tab.8.1, an overview of some spaceborne and airborne SAR sensors operating at different frequency bands with different resolutions. The use of the frequency band depends on the final application. For example, low frequency SAR systems (L and P bands) allow to investigate the sub-surface down to several meters and ensure the penetration into the vegetation cover. In particular, P-band radar can achieve penetration capabilities that could be used for accurate mapping of sub-surface characteristics such as moisture content or geological structures [Jagdhuber].

Table 8.1: Table extracted from [Berens 2006] presenting some examples of space-borne and airborne SAR systems, the year of launch, the resolution and the frequency band.

	name	year of launch	resolution	frequency band
space borne system	Lacrosse	1988	< 1 m $\times$ 1 m	X
	ERS-1	1991	26 m $\times$ 28 m	C
	J-ERS-1	1992	18 m $\times$ 18 m	L
	RADARSAT	1995	10 m $\times$ 9 m	C
	ENVISAT	2002	25 m $\times$ 25 m	C
	Radarsat II	2005	3 m $\times$ 3 m	C
	SAR-Lupe	2005	< 1 m $\times$ 1 m	X
	TerraSAR-X	2006	< 1 m $\times$ 1 m	X
	IGS-2b	2008	30 cm $\times$ 30 cm	X
airborne system	DOSAR	1989	< 1 m $\times$ 1 m	S,C,X,Ka
	CARABAS-II	1997	3 m $\times$ 3 m	VHF
	PAMIR	2003	10 cm $\times$ 10 cm	X
	Lynx	1999	10 cm $\times$ 10 cm	Ku
	MISAR	2003	0.5 m $\times$ 0.5 m	Ka
	RAMSES	1994	10 cm $\times$ 10 cm	P,L,S,C,X,Ku,Ka,W
	MEMPHIS	1997	20 cm $\times$ 20 cm	Ka,W
	MEMPHIS	1994	1.5 m $\times$ 1.5 m	P,L,S,C,X

8.3 Overview of typical SAR effects

The wide diversity of urban structures that have various sizes, shapes and materials impacts on the corresponding SAR images showing high complexity EM scattering effects. Indeed the EM phenomenology of propagation inside urban areas is characterized by a variety of single and multiple interactions with a wide variation of the corresponding amplitudes. In the second part of the thesis, we have shown that even for a simple canonical structure (the urban canyon) without dielectric properties (PEC case), the indoor EM scattering is rather complex to explain. In addition to the EM effects, SAR images over urban areas are strongly affected by geometric distortion mechanisms due to the side-looking acquisition of the SAR system. These geometric effects burden the analysis of SAR images and make some specific applications like automatic pattern recognition difficult to perform. Therefore, a knowledge about the basic effects related to the geometric acquisition of SAR is needed for interpretation. In the following, we present the most common geometric effects that especially happen in dense urban areas where large parts of the scene can be interfered by these phenomena.

8.3.1 Corner reflector effect

Perpendicular alignment of buildings to the sensor leads to strong signal responses by double-bounce scattering at the dihedral corner reflector between the ground and the building (see Fig.8.1). Since the entire power of the incident rays is mirrored back to the sensor, this reflection leads to a line of dominant scattering in azimuth direction that appears as a bright line in SAR image.

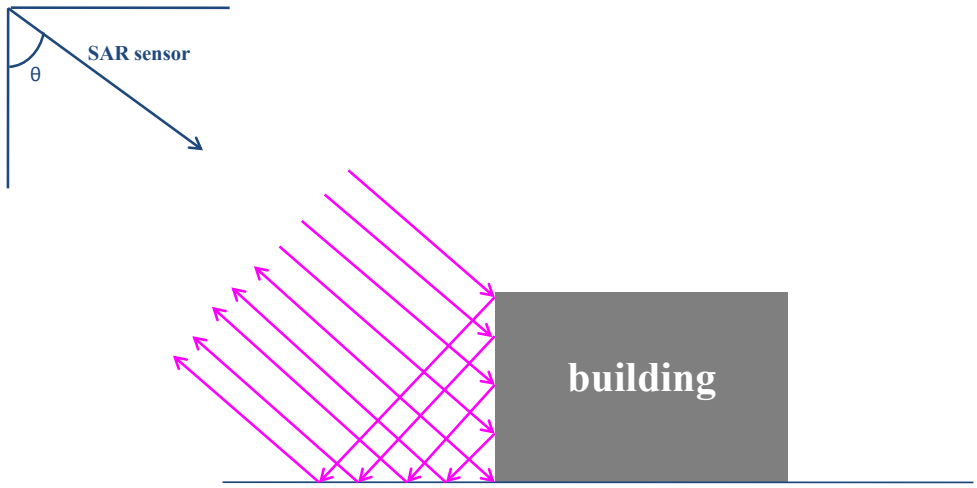

Figure 8.1: Corner reflector effect.

8.3.2 Shadowing effect

Shadow areas are defined as the regions of the scene where there is an obstacle to the electromagnetic wave propagation preventing any signal backscattering to the radar (see Fig.8.2). These regions appear dark in the SAR image, because no signal returns into the related range bins.

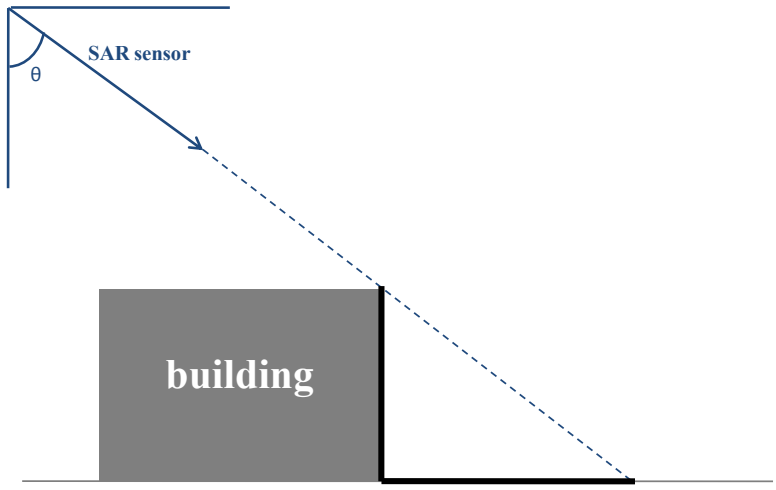

Figure 8.2: Shadowing effect: the dark points are not illuminated with the radar.

8.3.3 Layover effect

Layover occurs always at the regions of the image corresponding to a scene geometry defined by a vertical building wall facing toward the sensor. This scene geometry leads to a mixture of signal contributions from the building and the ground in the SAR image (see Fig.8.3). Because object areas located at different positions have the same distance to the sensor, the backscatter is integrated to the same range cell. In this study, we will investigate the particular effect of layover on the interferometric signature. Fig.8.4 illustrates the impact of the previous effects on the slant image. These effects lead to a geometric distortion in the range direction

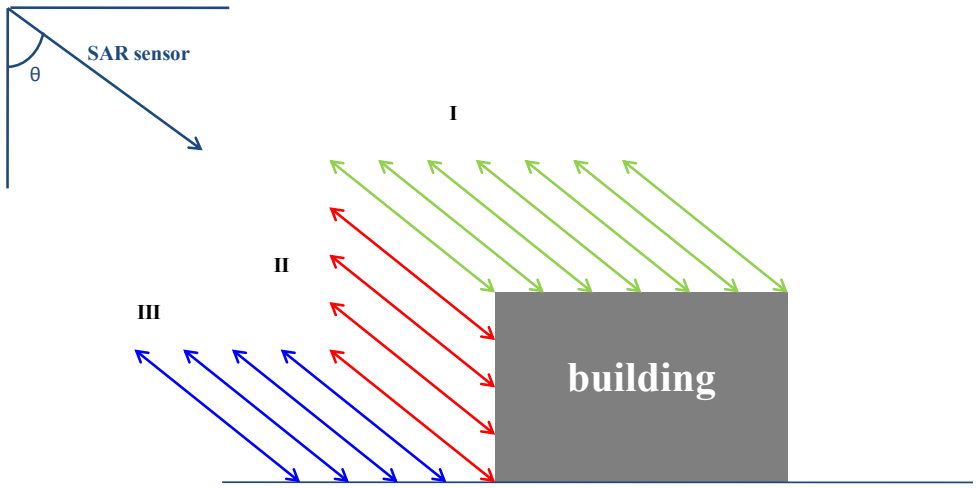

Figure 8.3: Layover area: objects like roof (I), walls (II) and the ground in front of the buildings (III) located at different positions have the same distance to the sensor, the backscatter is integrated to the same range cell (Figure extracted from [Soergel 2003]).

which makes the object recognition and interpretation more difficult. Let's consider the building illustrated in Fig.8.4 with a vertical wall (A-B) and a flat roof (B-C) captured in a side looking manner from point F. In the slant range image I_s, the point A, B and C appear according to their distances to the sensor. Hence, the point A on the corner line of the building appears as A' between B' and C'. The area B'A' corresponds to the layover area.

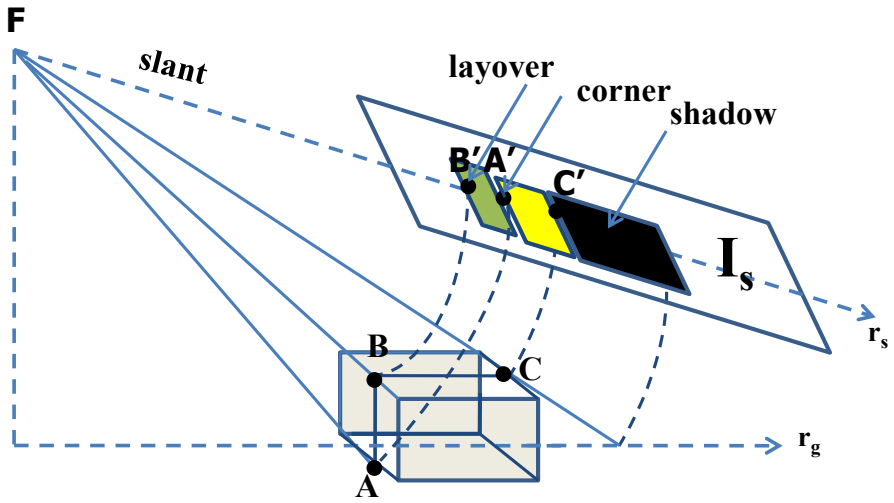

Figure 8.4: Projection of a building into a slant image.

8.4 Objective of the study

We aim to provide a complete analysis of the InSAR data acquired over a canyon in an industrial area (these outdoor measurements will be described later). This analysis will deal with the radiometric and interferometric aspect.

8.4.1 Radiometric analysis

The first analysis of the image concerns the radiometric aspect as it deals with the position and the amplitude of the different scatterers responses. Since the used tool for analysis is the developed EM code (Urban Canyon V3) that does not take into account EM considerations (only PEC case, for the moment), the interpretation of the radiometric image concerns only the detection of the scatterers in terms of distance. We would like to check if our developed code is able to distinguish all the different features on the image. Then, we have also to make sure that the code is able to predict accurately the range responses of the three corner reflectors (modeled as a point target) and to the truck (modeled as a parallelepiped). The other point to focus on is the identification of the layover areas to study further their impact on the interferometric signature. The radiometric study will be used after to analyze the interferometric image.

8.4.2 Interferometric analysis

The second analysis will concern the interferometric aspect as it deals with the prediction of the phase associated to each feature of the interferometric image in order to estimate later its corresponding height. This can concern even the zones where there is a superposition of several mechanisms with different phases. With this interferometric study, we aim to check if we are able with our developed tool to delimit the different interferometric zones having the same interferometric signature. Then, for the case where the interferometric zone contains more than one mechanism, we should be able to predict the resulting interferometric phase of this zone. We have also to provide an explanation to the interferometric phase transition illustrated in the red box in the interferometric image of Fig.8.8.

8.5 Presentation of the data at our disposal

During a measurement campaign dedicated to urban areas, ONERA acquired InSAR data at Ka-band and Vv polarization with a resolution of 30 cm over an industrial area. The first InSAR image contains two buildings with targets located between them as described in Fig.8.5. The first building (denoted building 1 in Fig.8.5) is used as a mask whereas the second building (denoted building 2 in Fig.8.5) is used as a reflector. The experiment consists in illuminating three trihedral corners reflector and a truck facing the second building. The three corner reflectors are oriented so that their corresponding echo is in NLOS of the radar (see the left part of Fig.8.6). For the truck, we expect a NLOS response by the right side and a LOS response by the roof (see the right part of Fig.8.6). The three corner reflectors have been selected through this radar campaign with different size and radar cross sections to analyze attenuation due to indirect path (see Tab.8.2). The results of the attenuation analysis will not be presented as it is not the subject of this study. Table.8.3 contains the dimensions of the truck.

We notice that the wall of the second building is separated into two parts: it is covered by concrete from the ground up to 3m, and then the wall is metallic. Fig.8.7 contains a description of the canyon configuration of the scene under study.

Table 8.2: Size(m) and RCS (dBm^2) of the trihedral corners used in the experiment illustrated in Fig.8.5.

Trihedral corner	Size (m)	RCS (dBm^2)
T_1	0.558	37.4
T_2	0.47	34.4
T_3	0.39	31.4

Table 8.3: Truck dimensions.

length	width	height
5m	2m	2.45m

We present in Fig.8.8 the corresponding radiometric and interferometric images of the scene under study. The next section will be dedicated to the interpretation of these two images.

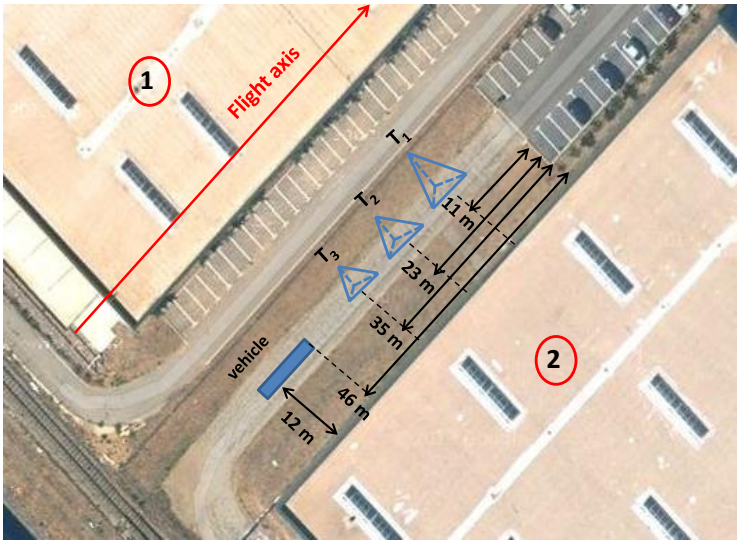

Figure 8.5: Scene under observation: two buildings defining the canyon of study. Three corner reflectors (h_{t1} = 0.55 m, h_{t2} = 0.47 m, h_{t3} = 0.39 m) and a truck (h_t = 2.45 m) are placed in front of the second building.

8.6 Analysis of the radiometric image

8.6.1 Identification of the features of the image

Using Urban Canyon V3 and a geometric distance calculation, we simulated the range profile corresponding to the canyon under study in order to analyze the main features of the radiometric image. This range profile is illustrated in Fig.8.9. The peaks illustrated with continuous line are generated with Urban Canyon V3 whereas the peaks illustrated with dashed lines are added after a geometric distance calculation. These different peaks are delimiting five zones of study that correspond to the interferometric zones to study later in order to explain the interferometric phase transition (see Fig.8.10). Urban Canyon V3 was used to predict the responses of the targets and the response of dihedral effect of the walls. Indeed, the simulated range profile contains:

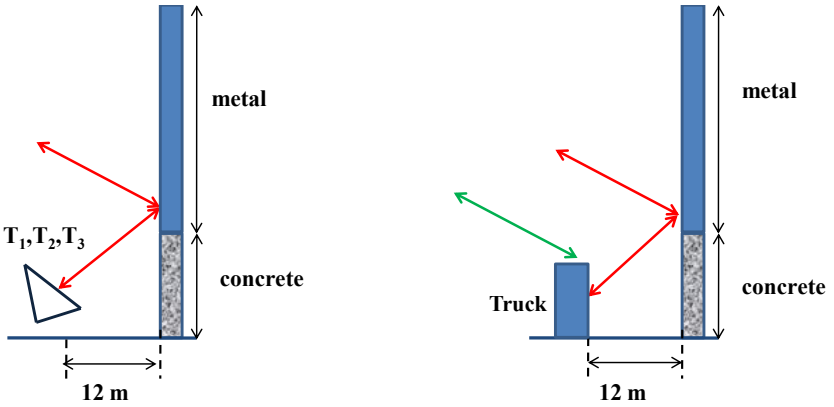

Figure 8.6: The responses of the corner reflectors facing the second building are in NLOS of the radar. The truck is detectable by its right side in NLOS whereas the roof is detectable in LOS. The LOS response is illustrated with green color and the NLOS response is illustrated with red color.

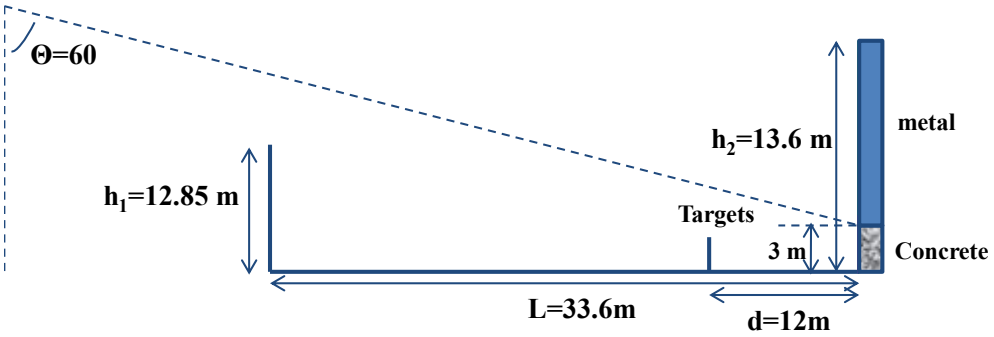

Figure 8.7: Canyon configuration: h_1=12.85 m, h_2=13.6 m and L=33.6 m. Radar parameters: $\theta = 60°$, Frequency = 35 GHz, Vv polarization, total bandwidth =4 GHz. The targets (three corner reflector and the truck) are located at a distance of 12 m from the second building. The wall of the second building is covered by concrete up to 3 m before the metallic part.

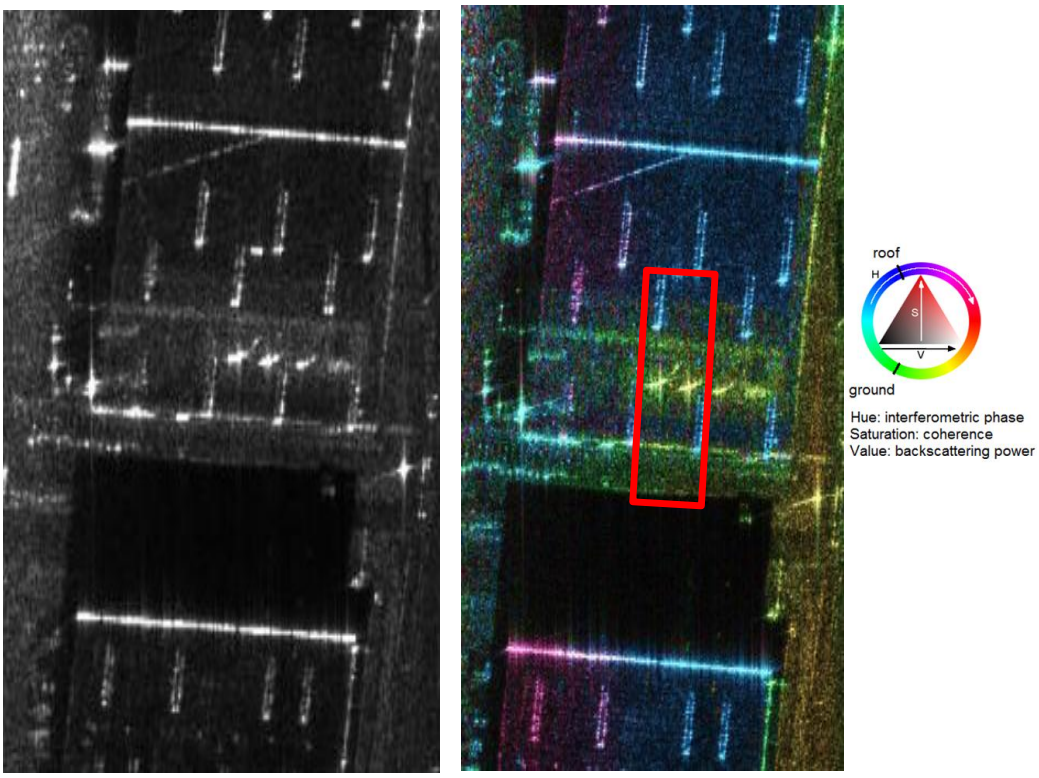

Figure 8.8: (Left) radiometric image corresponding to the scene under study of Fig.8.5. (Right) interferometric image corresponding to the scene under study of Fig.8.5, the green color corresponds to the interferometric phase of the ground, the blue color corresponds to the interferometric phase of the roof, the red box illustrates the interferometric phase transition located on the roof of the second building.

- 1 peak due to the dihedral effect on the bottom of the second building,
- 1 peak due to the NLOS response of the trihedral corners,
- 1 peak due to the NLOS response of the right side of the truck located at the same range as the response of the corner reflectors,
- 1 peak due to the roof of the target.
  For clarity reason, we have reported in Fig.8.12 the area of the radiometric image containing only the responses of the truck. We distinguish the response due to the right side as it is located at the same position as the three corner reflectors. The response due to the roof is not explicit as it is located on the bright line caused by the dihedral effect of the bottom of the second building.

The mechanisms leading to these peaks are illustrated in Fig.8.11 where we have simulated the scene under study using Urban Canyon V3. These responses extracted with our code are not enough to distinguish all the features in the radiometric image. Hence, we have added, using a geometric distance calculation, other peaks corresponding to other main scatterers that are detectable by a backscattering mechanism, such as:

- The end of the shadow area,
- The top of the building 1,
- The top of the building 2,
- The limit of the different zones corresponding the interferometric zones that will be investigated later.

Thus, we can conclude that our EM code can predict the exact position of the different scatterers (simple or complex), but, because of a specific canyon configuration and due to EM considerations, some expected responses can be hidden by others scatterers or difficult to distinguish in the radiometric image due to a low amplitude.

8.6.2 Identifying the mechanisms corresponding to each feature of the image

The second part of this radiometric study deals with the different features distinguished. In fact, five selected zones from the features will be analyzed in terms of scattering mechanisms with equal distances to the radar to determine the final backscattering signature. The approach we followed to select these five zones of study is based on a geometric distance calculation of two possible mechanisms happening inside the scene: the specular reflection mechanism and the backscattering mechanism. We have considered the backscattering mechanism in addition of the specular reflection mechanism since the ground and some materials (on the roof) can induce a backscattering which is not negligible. Then, according to the geometry of the scene and to the different material composing it, we have retrieved five zones of study differing from their width, the nature and the number of mechanisms happening inside them. Let's explain more in details with an illustration in Fig.8.13 of the possible mechanisms that could happen in this canyon depending on the different zones. We propose now to identify the mechanisms according to the zone.

- **In zone 1**, the only possible mechanism is the backscattering from the ground (BG) (illustrated with red line). The corresponding backscattering coefficient

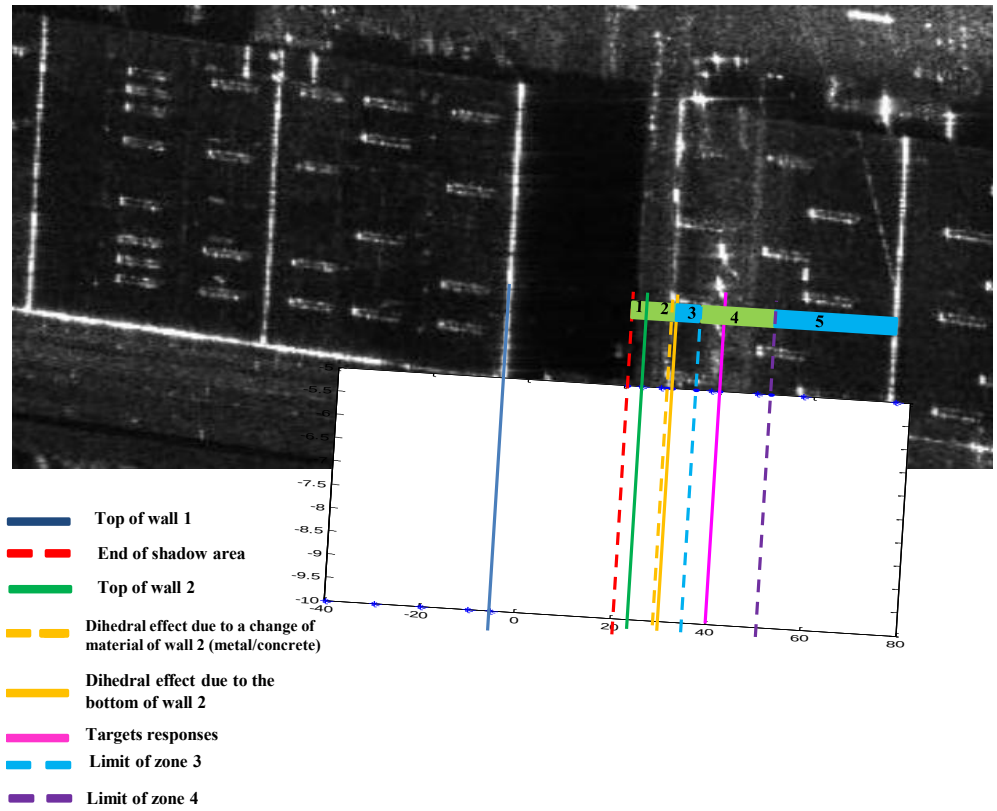

Figure 8.9: Radiometric image corresponding to the scene under study with the associated range profile generated with Urban Canyon V3 and with a geometric distance calculation: 5 zones of study with different number of mechanisms are delimited by the different scatterers responses, the peaks illustrated with continuous lines are generated by Urban Canyon V3 and the peaks illustrated with dashed lines are added using geometric distance calculation of the different mechanisms.

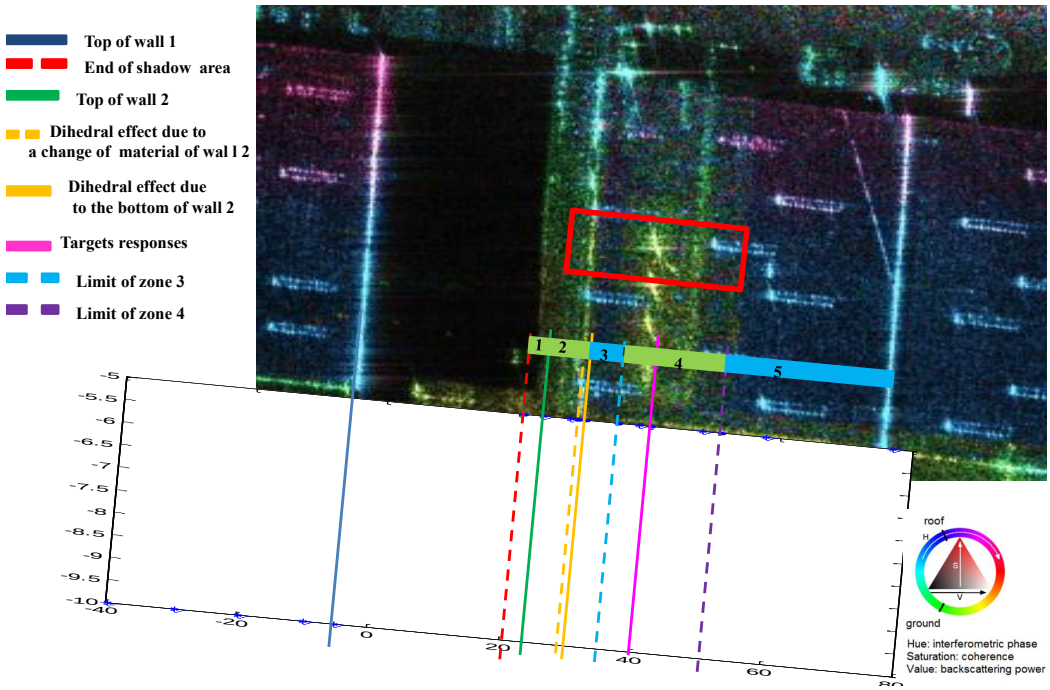

Figure 8.10: Interferometric image corresponding to the scene under study with the associated range profile generated with Urban Canyon V3 and with geometric distance calculation: 5 zones of study with different numbers of mechanisms are delimited by the different scatterers responses, the peaks illustrated with continuous lines are generated by Urban Canyon V3 and the peaks illustrated with dashed lines are added using geometric distance calculation of the different mechanisms. The red box delimits the interferometric phase transition.

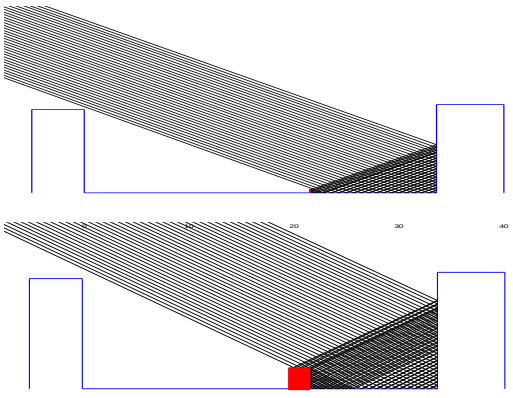

Figure 8.11: Simulation with Urban Canyon V3 of the canyon under study with the presence of the trihedral corner reflector T_1 modeled as a point target scattering by one side (up) and with the presence of the truck (bottom). The trihedral corner is detectable by its right side and the truck is detectable by its right side and its roof.

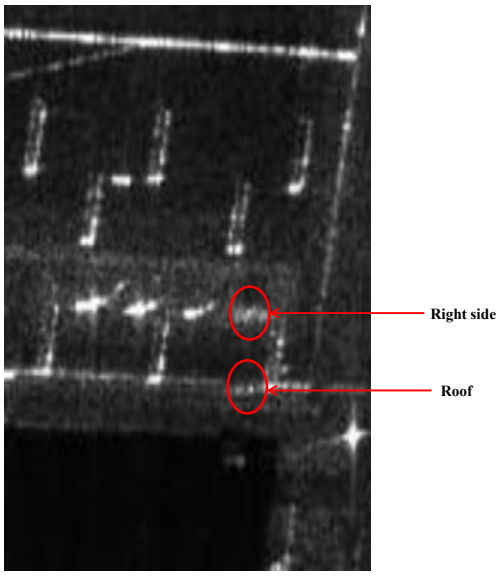

Figure 8.12: Truck detection: two responses predicted by Urban Canyon V3: a response due to the right side located at the same position as the three corner reflectors and a response due to the roof located on the bright line of the bottom of wall 2.

is denoted σ_{gr},

- **In zone 2**, there are two backscattering mechanisms from the ground and from the roof that have the same geometric distance to the radar (green line). Thus, they belong to the same resolution cell,
- **In zone 3**, there are also two mechanisms: the first one is the backscattering from the roof and the second one is composed of two sub-mechanisms: a backscattering from the ground and a reflection on the concrete part of the building (RC) (illustrated with the dashed blue line). The corresponding Fresnel reflection coefficient is denoted R^c_{vv},
- Following the same reasoning for **zone 4**, we distinguish two mechanisms: the first one is the backscattering from the roof and the second one is composed from two sub-mechanisms: a backscattering from the ground and a reflection on the metallic part of the building (RM) (illustrated with the dashed black line). The corresponding Fresnel reflection coefficient is denoted R^m_{vv},
- **In zone 5**, the only possible mechanism is the backscattering from the roof (BR). The corresponding backscattering coefficient is denoted σ_{rf}.

All the mechanisms present in each zone of study are summarized in Tab.8.4. We notice that in zone 2, 3 and 4, more than one mechanism belong to the same resolution cell, so they are defined as layover areas.

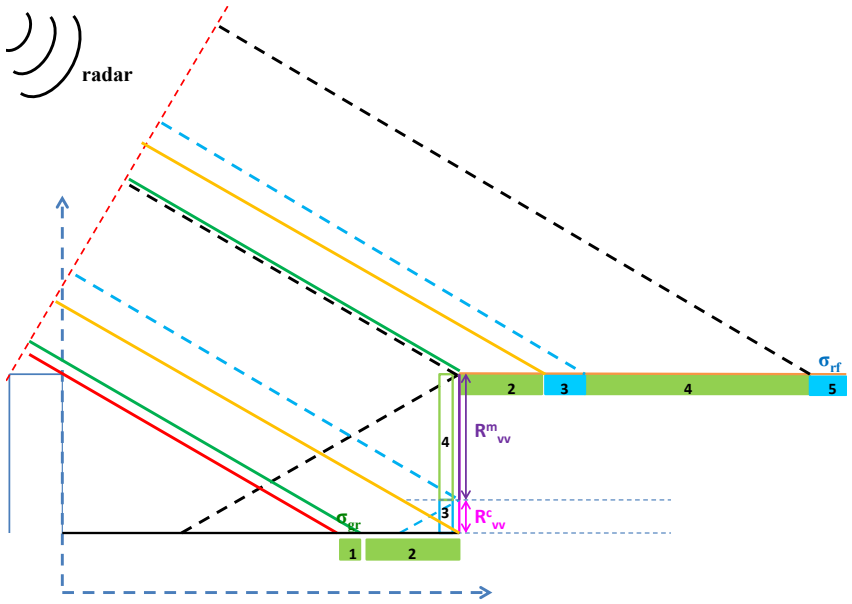

Figure 8.13: Geometric description of the canyon in Fig.8.5 with the different EM mechanisms: backscattering from the ground, backscattering from the roof and reflection on the wall of the second building. The geometric mechanisms illustrated with the same color have the same distance to the radar.

Table 8.4: Table summarizing the mechanisms corresponding to each zone of study and the corresponding backscattering and reflection coefficients.

	zone 1	zone 2	zone 3	zone 4	zone 5
Mechanisms	BG	BG/BR	BG+RC/BR	BG+RM/BR	BR
Backscattering and reflection coefficients	σ_{gr}	σ_{gr}/σ_{rf}	$\sigma_{gr}+R^c_{vv}/\sigma_{rf}$	$\sigma_{gr}+R^m_{vv}/\sigma_{rf}$	σ_{rf}

8.6.3 Analytic expression of the backscattering signature corresponding to each feature of the image

To analyze the resulting radiometric information for a layover area where more than one mechanism exists, our approach is to study the corresponding distribution of the backscattering coefficients. But before, we have to present the general formula to calculate the total backscattering coefficient of a resolution cell containing N mechanisms.

8.6.3.1 Formula for N mechanisms

The total backscattering coefficient for a resolution cell where there is a superposition of N mechanisms is defined as follows:

$$\begin{aligned}\sigma_{tot} &= \lim_{R\to+\infty} \frac{|E^s_{tot}|^2}{|E^i_{tot}|^2}\frac{4\pi R^2}{A_{tot}} \\ &= \lim_{R\to+\infty} \frac{|E^s_1 + E^s_2 + .. + E^s_N|^2}{|E^i_{tot}|^2}\frac{4\pi R^2}{A_{tot}} \\ &= \lim_{R\to+\infty} \frac{(E^s_1 + .. + E^s_N)(E^{s*}_1 + .. + E^{s}_N{}^*)}{|E^i_{tot}|^2}\frac{4\pi R^2}{A_{tot}}\end{aligned} \tag{8.1}$$

With:

- $< >$ is the average over the neighboring pixels,
- E^s_k, E^i_k are respectively the scattered and incident electric field in a resolution cell where only one mechanism k exists,
- E^s_{tot}, E^i_{tot} are respectively the scattered and incident electric field in a resolution cell where N mechanisms exist,
- R is the distance between the radar and the area under study,
- A_k id the area of the resolution cell where we collect the isolated mechanism k
- A_{tot} is the area corresponding to the resolution cell; $A_{tot} = A_k$, as all the cells resolution have the same area.

Given z_k a complex number, we have:

$$\sum_{k=1}^{N} z_k \sum_{k=1}^{N} z^*_k = \sum_{k=1}^{N} |z_k|^2 + 2Re \sum_{k=1}^{N} \left(z_k \sum_{j=k+1}^{N} z^*_j \right) \tag{8.2}$$

with Re indicating the real value. Thus Eq.8.1 can be defined as:

$$\sigma_{tot} = \lim_{R\to+\infty} \frac{4\pi R^2}{A_{tot}|E^i_{tot}|^2} \left\langle \sum_{k=1}^{N} |E^s_k|^2 + 2Re \sum_{k=1}^{N} \left(E^s_k \sum_{j=k+1}^{N} E^{s*}_j \right) \right\rangle \tag{8.3}$$

Knowing that:

$$\frac{|E^i_{tot}|}{A_{tot}} = \frac{|E^i_k|}{A_k} \tag{8.4}$$

Then

$$\sigma_{tot} = \lim_{R\to+\infty} \left\langle \sum_{k=1}^{N} |E_k^s|^2 \frac{4\pi R^2}{A_k |E_k^i|^2} + 2Re \sum_{k=1}^{N} \left(E_k^s \frac{\sqrt{4\pi R^2}}{E_k^i \sqrt{A_k}} \sum_{j=k+1}^{N} E_j^{s*} \frac{\sqrt{4\pi R^2}}{E_j^{i*} \sqrt{A_j}} \right) \right\rangle \tag{8.5}$$

Thus, we can conclude that the total backscattering coefficient for a resolution cell containing N mechanisms can be expressed as:

$$\sigma_{tot} = \left\langle \sum_{k=1}^{N} \sigma_k + 2Re \sum_{k=1}^{N} \left(\alpha_k \sum_{j=k+1}^{N} {\alpha_j}^* \right) \right\rangle \tag{8.6}$$

where σ_k is the backscattering coefficient of the mechanism k and α_k is defined as follows:

$$\alpha_k = \lim_{R\to+\infty} \frac{E_k^s \sqrt{4\pi R^2}}{E_k^i \sqrt{A_k}} \tag{8.7}$$

8.6.3.2 Application to the case $N = 2$ mechanisms

Let R_{vv}^c and R_{vv}^m be the Fresnel reflection coefficients of the concrete and the metal, respectively. Using the Eq.B.3, we are able to write the backscattering coefficient in zone 2, 3 and 4.

For zone 2:

$$\sigma_{tot,2} = \sigma_{rf} + \sigma_{gr} + 2Re \left(\lim_{R\to+\infty} \left(\frac{{E_{rf}^s}^* \sqrt{4\pi R^2}}{{E_{rf}^i}^* \sqrt{A_{rf}}} \frac{E_{gr}^s \sqrt{4\pi R^2}}{E_{gr}^i \sqrt{A_{gr}}} \right) \right) \tag{8.8}$$

For zone 3:

$$\begin{aligned} \sigma_{tot,3} &= \sigma_{rf} + |R_{vv}^c|^2 \sigma_{gr} \\ &\quad + 2Re \left(\lim_{R\to+\infty} \left(\frac{{E_{rf}^s}^* \sqrt{4\pi R^2}}{{E_{rf}^i}^* \sqrt{A_{rf}}} \frac{R_{vv}^c E_{gr}^s \sqrt{4\pi R^2}}{E_{gr}^i \sqrt{A_{gr}}} \right) \right) \end{aligned} \tag{8.9}$$

For zone 4:

$$\begin{aligned} \sigma_{tot,4} &= \sigma_{rf} + |R_{vv}^m|^2 \sigma_{gr} \\ &\quad + 2Re \left(\lim_{R\to+\infty} \left(\frac{{E_{rf}^s}^* \sqrt{4\pi R^2}}{{E_{rf}^i}^* \sqrt{A_{rf}}} \frac{R_{vv}^m E_{gr}^s \sqrt{4\pi R^2}}{E_{gr}^i \sqrt{A_{gr}}} \right) \right) \end{aligned} \tag{8.10}$$

8.6.4 Validation of the analytical expression of the backscattering signature

In order to validate the formula in Eq.B.3, we have proposed a method based on the study of statistical distributions of the backscattering coefficients for each zone of study (zone 1-5). The different steps of the proposed method can be summarized as follows:

1. Select a rectangular area of each zone of study from the radiometric image,
2. Derive the statistical distribution of the backscattering coefficients in each selected area,

3. Simulate the distributions in zone 1 and zone 5 (where only one backscattering mechanism exists) and also in layover areas (zone 2, 3 and 4) using the formulas in Eq.8.8 to Eq.8.10 and compare with the real distributions.

The third step is a validation step of the proposed formula to calculate the resulting backscattering coefficient in layover areas. It is decomposed into sub-steps:

1. Select 1000 random samples of the backscattering coefficients from the rectangular areas selected in zone 1 (ground) and zone 5 (roof) where only one mechanism exists. Since we can not study the distribution of the backscattering coefficients of the roof and ground in zone 2, 3 and 4 independently from the others mechanisms, we assume that their backscattering coefficients distributions in these areas are the same as those in the two areas containing only one backscattering mechanism. Thus, σ_{gr} will be estimated in zone 1 and σ_{rf} in zone 5,
2. Use the formulas in Eq.8.8 to Eq.8.10 to build three vectors of data corresponding the the calculated backscattering coefficients in zone 2, 3 and 4,
3. Compare with the real data distributions in zone 2, 3 and 4.

We have plotted in Fig.B.15, the value of Fresnel reflection coefficients of the concrete in Vv and Hh polarizations (denoted respectively R^c_{vv} and R^c_{hh}) for a relative permittivity ε_r at Ka-band of 2.5+i 0.65 ([Gatesman 2001]) according to different incidence angles (θ). The formula to calculate R^c_{vv} is in Eq.8.11.

$$R^c_{vv} = \frac{\varepsilon_r \cos\theta - \sqrt{\varepsilon_r - \sin^2\theta}}{\varepsilon_r \cos\theta + \sqrt{\varepsilon_r - \sin^2\theta}} \tag{8.11}$$

We notice that at the used incidence angle (60°), the reflection coefficient of the concrete is two low (-15 dB), hence, the value of $|R^c_{vv}|$ is negligible. Eq.8.9 can be written as:

$$\sigma_{tot,3} = \sigma_{rf} \tag{8.12}$$

Similarly, we can assume that $R^m_{vv} = 1$, as the second part of the wall is metallic. Therefore, Eq.8.10 can be simplified and we obtain:

$$\sigma_{tot,4} = \sigma_{tot,2} \tag{8.13}$$

We present in Fig.8.14 and in Fig.8.15 the distribution of the backscattering coefficients in two areas selected in zone 1 (the ground) and in zone 5 (the roof), respectively. As expected, these data follow an exponential distribution [Nicolas 2006]. In zone 2 and 4, the total backscattering coefficient is the sum of two contributions following the exponential distribution and a third term related to the inter correlation between the contribution of the roof and the ground. According to [Nicolas 2006], the sum of two contributions following a gamma distribution of the first order (exponential) will be a gamma distribution of the second order. As unexpected, the simulated distributions of zone 2 (see Fig.8.18(a)) and 4 (see Fig.8.18(a)) follow a gamma distribution of the first order, which leads us to consider that the contribution of the third term is negligible. However, the real data distribution in zone 2 and 4 still follow an exponential distribution. This can be explained by the fact that in real case, the third term, which is supposed to be negligible by the simulations, can add a significant contribution that may change the resulting distribution.

Nevertheless, the means and the variance of the simulated and real data of the distribution in zone 2 and 4 are more or less similar (see Tab.8.5 and Tab.8.6). As expected referring to Eq.8.13, the distribution of the backscattering coefficients in zone 3 follows an exponential distribution both for real data and simulations (see Fig.8.19). In addition, it is approximately the same as the distribution of the backscattering coefficients of the roof (see Fig.8.19 and Fig.8.15 for comparison).

Table 8.5: Mean and variance for the simulated and real data distributions of the backscattering coefficients in zone 2.

	real data	simulations
mean	0.0250	0.03
variance	6.510^{-4}	7.810^{-4}

Table 8.6: Mean and variance for the simulated and real data distributions of the backscattering coefficients in zone 4.

	real data	simulations
mean	0.0253	0.03
variance	6.7710^{-4}	7.810^{-4}

Fig.8.17 summarizes according to each zone of study, the corresponding mechanisms of equal distance to the radar and the resulting backscattering coefficient of the zone.

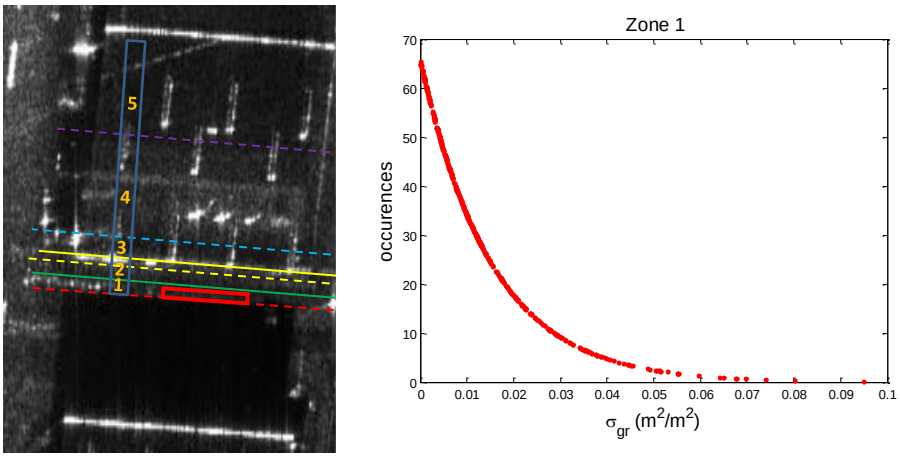

Figure 8.14: Exponential distribution of the backscattering coefficients in the selected area (red box) of zone 1 (the ground).

We have pointed out the effect of the material properties on the distribution of the backscattering coefficients in a resolution cell containing more than one mechanism. A low value of the reflection coefficient of one of the mechanisms make it disappear in favor of others mechanisms that become dominant. Knowing the distribution of the backscattering coefficients in isolated areas where only one mech-

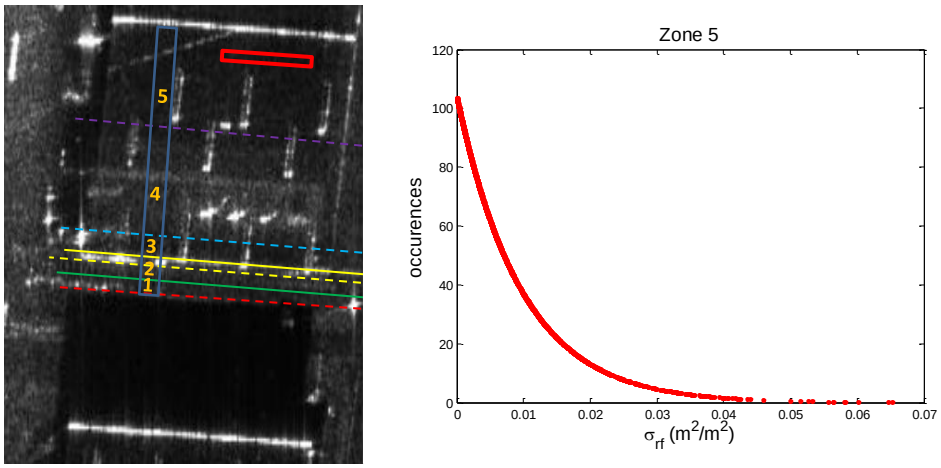

Figure 8.15: Exponential distribution of the backscattering coefficients in the selected area (red box) of zone 5 (the roof).

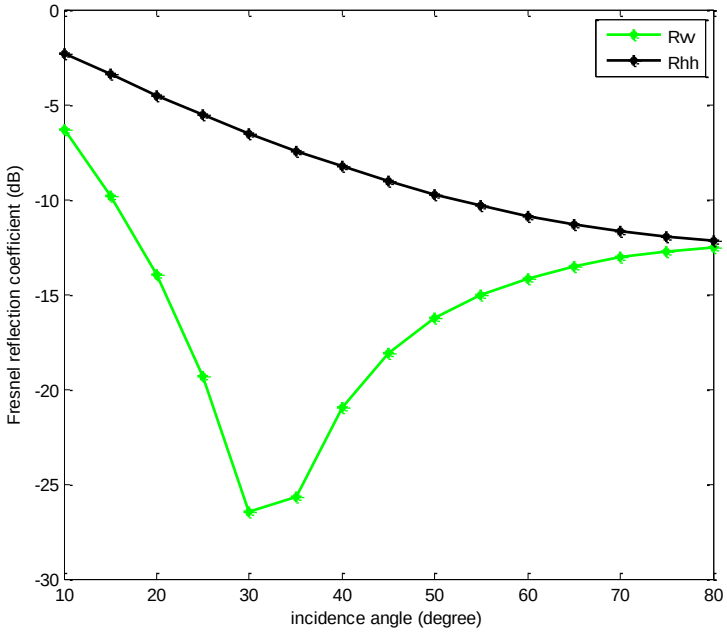

Figure 8.16: Reflection coefficient of the concrete according to the incidence angles for a central frequency of 35 GHz and a permittivity of 2.5+i 0.65 ([Gatesman 2001]).

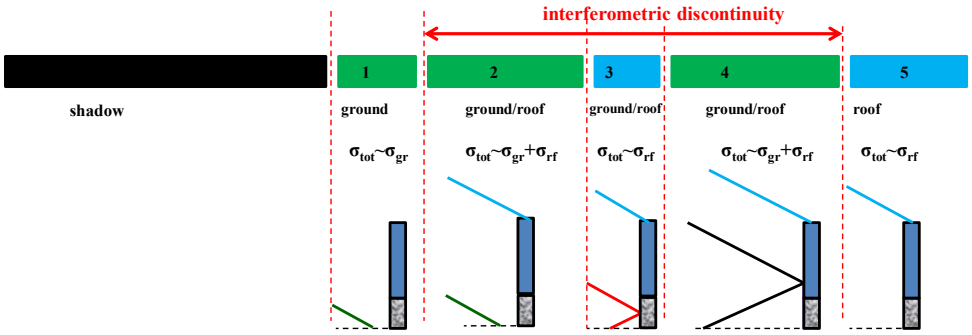

Figure 8.17: Illustration of the different mechanisms having the same distance to the radar according to each zone of study. The value of the total backscattering coefficient of each zone of study is mentioned under the zone. (Green): ground backscattering mechanism. (Blue): roof backscattering mechanism. (Red): ground backscattering mechanism + reflection on the concrete part of the wall. (Black): ground backscattering mechanism + reflection on the metallic part of the wall.

anism exists, we can predict accurately the backscattering coefficients distribution in the layover areas.

We have demonstrated through this radiometric study that we are able using our simple EM code to identify the different features of the image, to assign to each target the corresponding response, to identify for each feature the number of mechanisms happening inside and to predict the resulting backscattering signature of each feature. In the next section, the same work will be done for the interferometric coherence estimation.

8.7 Analysis of the interferometric image

This section is devoted to the analysis of the interferometric image of Fig.8.8. Its consists in predicting the interferometric phase and module associated to each feature even for the features where there are layover areas.

8.7.1 Choice of the interferometric zones to study

We notice that the zones having the same interferometric signature correspond to the zones delimited via Urban Canyon V3 in the radiometric image (see Fig.8.9 and Fig.8.10). We note that the green color is assigned to the ground's phase and the blue color corresponds to the roof's phase.

8.7.2 Analysis of the interferometric coherence of each zone

As the interferometric coherence is expected to be strongly related to the backscattering coefficients of the different mechanisms in a resolution cell, we propose to derive a general analytical formula for the calculation of the interferometric coherence in a resolution cell containing more than a mechanism. Then, we propose to analyze the interferometric phase associated to the five zones which for the study

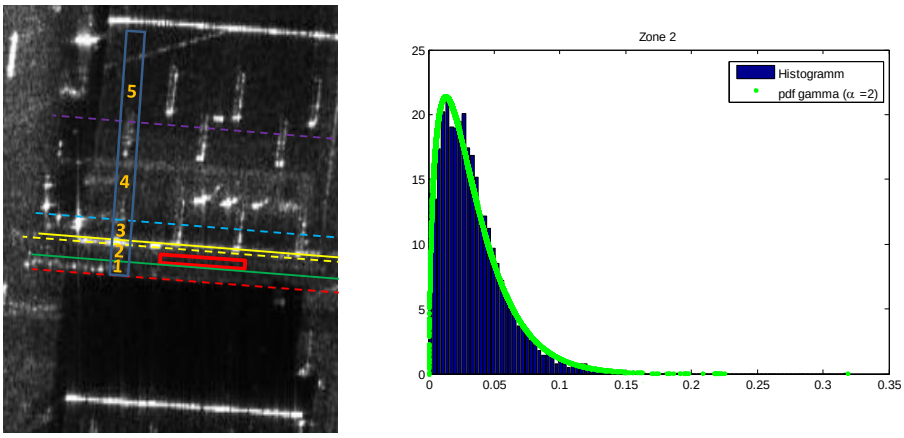

(a) Histogram of the simulated backscattering coefficients in zone 2 with the associated pdf for a gamma distribution of the second order.

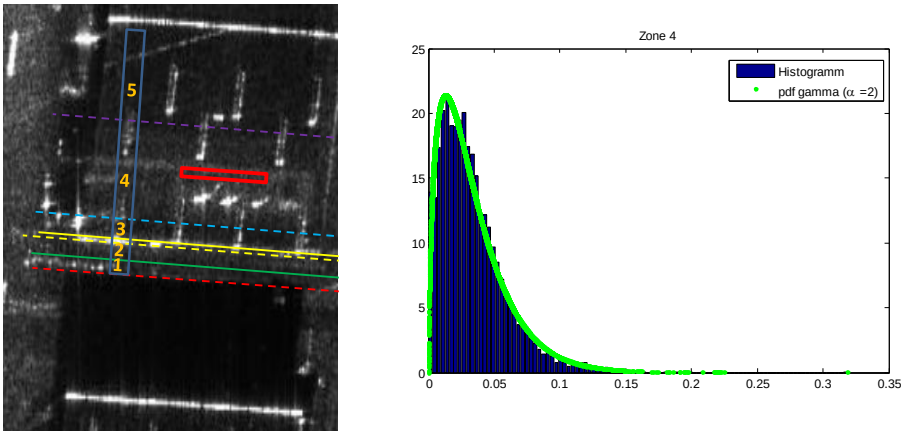

(b) Simulated and real data distributions of the backscattering coefficients in zone 4 with the associated pdf for a gamma distribution of the second order.

Figure 8.18: Histogram of the simulated backscattering coefficients in zone 2 and 4 with the associated pdf for a gamma distribution of the second order illustrated with green color. The real data distributions of each zone are retrieved from the selected red rectangular areas.

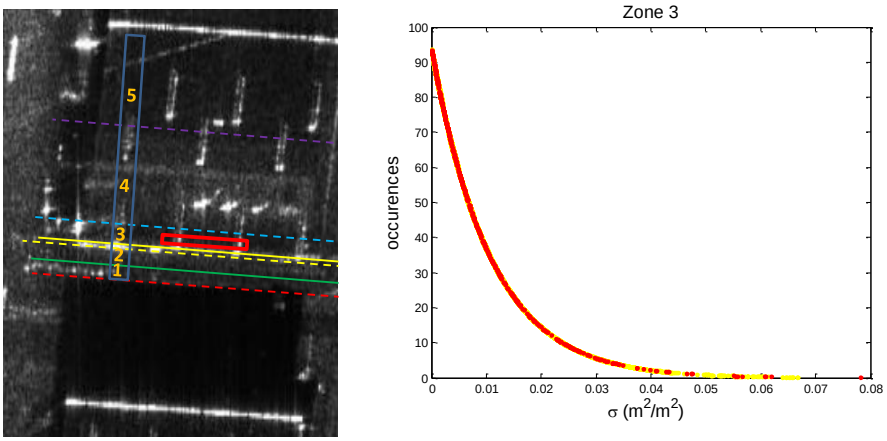

Figure 8.19: Simulated and real data distributions of the backscattering coefficients in zone 3. The simulated distribution is illustrated in yellow color whereas the real distribution is illustrated in red color.

of the backscattering signature is already done. We will provide an explanation to the interferometric phase transition between zone 2, 3 and 4.

8.7.2.1 Formula for N mechanisms

The interferometric coherence for a resolution cell where there is a superposition of N mechanisms is defined as follows:

$$\gamma_{tot} = \frac{< E^s_{tot,1} {E^s_{tot,2}}^* >}{\sqrt{< |E^s_{tot,1}|^2 >< |E^s_{tot,2}|^2 >}} \tag{8.14}$$

Where

$$\begin{aligned} &< E^s_{tot,1} {E^s_{tot,2}}^* >= \\ &< (E^s_{1,1} + .. + E^s_{N,1})({E^s_{1,2}}^* + .. + {E^s_{N,2}}^*) > \end{aligned} \tag{8.15}$$

We note:

- $<>$ is the average over the neighboring pixels,
- $E^s_{tot,1}$, $E^s_{tot,2}$ the electric field scattered by N mechanisms received respectively by antenna 1 or 2 for a resolution cell,
- $E^s_{k,1}$, $E^s_{k,2}$ the scattered electric field of the mechanism k received respectively by antenna 1 or 2 for a resolution cell.

Assuming that the correlation between the scattered electric field of a mechanism k received by antenna 1 and the scattered electric field of another mechanism j received by antenna 2 is negligible:

$$< E^s_{k,1} {E^s_{j,2}}^* >= 0 \; \forall k \neq j \tag{8.16}$$

We obtain

$$< E^s_{tot,1} {E^s_{tot,2}}^* > \simeq \sum_{i=1}^{N} < E^s_{i,1} {E^s_{i,2}}^* > \tag{8.17}$$

Eq.8.14 can then be written as:

$$\begin{aligned}\gamma_{tot} &\simeq \frac{\sum_{i=1}^{N} < E^s_{i,1} {E^s_{i,2}}^* >}{\sqrt{< |E^s_{tot,1}|^2 >< |E^s_{tot,2}|^2 >}} \\ &\simeq \sum_{i=1}^{N} \frac{< E^s_{i,1} {E^s_{i,2}}^* >}{\sqrt{< |E^s_{i,1}|^2 >< |E^s_{i,2}|^2 >}} \frac{\sqrt{< |E^s_{i,1}|^2 >< |E^s_{i,2}|^2 >}}{\sqrt{< |E^s_{tot,1}|^2 >< |E^s_{tot,2}|^2 >}}\end{aligned} \tag{8.18}$$

We set:

$$\frac{\sqrt{< |E^s_{i,1}|^2 >< |E^s_{i,2}|^2 >}}{\sqrt{< |E^s_{tot,1}|^2 >< |E^s_{tot,2}|^2 >}} = \frac{\sqrt{< \sigma_{i,1} >< \sigma_{i,2} >}}{\sqrt{< \sigma_{tot,1} >< \sigma_{tot,2} >}} \tag{8.19}$$

Supposing that the backscattering coefficient of a mechanism i is the same for antenna 1 and antenna 2, we obtain:

$$\begin{aligned}< \sigma_{i,1} > &\simeq < \sigma_{i,2} > \\ < \sigma_{tot,1} > &\simeq < \sigma_{tot,2} >\end{aligned} \tag{8.20}$$

Thus:

$$\frac{\sqrt{< |E^s_{i,1}|^2 >< |E^s_{i,2}|^2 >}}{\sqrt{< |E^s_{tot,1}|^2 >< |E^s_{tot,2}|^2 >}} \simeq \frac{< \sigma_{i,1} >}{< \sigma_{tot,1} >} \tag{8.21}$$

Then, the coherence coefficient for a resolution cell with N mechanisms can be defined as:

$$\gamma_{tot} \simeq \sum_{i=1}^{N} \gamma_i \frac{< \sigma_{i,1} >}{< \sigma_{tot} >} \tag{8.22}$$

We can conclude through the formula in Eq.B.5 that the interferometric phase in a resolution cell is strongly related to the backscattering coefficients of the mechanisms existing inside it. In fact, in a layover area where there are N mechanisms, the dominant mechanism that will define the interferometric phase of the area will be the mechanism with the greatest backscattering coefficient.

8.7.2.2 Application to the case $N = 2$ mechanisms

Using Eq.B.5, we are able to define the interferometric coherence coefficient for zones 2, 3 and 4.
For zone 2:

$$\gamma_{tot,2} \simeq \gamma_{gr} \frac{< \sigma_{gr} >}{< \sigma_{tot} >} + \gamma_{rf} \frac{< \sigma_{rf} >}{< \sigma_{tot} >} \tag{8.23}$$

For zone 3:

$$\gamma_{tot,3} \simeq |R^c_{vv}|^2 \gamma_{gr} \frac{< \sigma_{gr} >}{< \sigma_{tot} >} + \gamma_{rf} \frac{< \sigma_{rf} >}{< \sigma_{tot} >} \tag{8.24}$$

For zone 4:

$$\gamma_{tot,4} \simeq |R^m_{vv}|^2 \gamma_{gr} \frac{< \sigma_{gr} >}{< \sigma_{tot} >} + \gamma_{rf} \frac{< \sigma_{rf} >}{< \sigma_{tot} >} \tag{8.25}$$

As the reflection coefficient of the concrete in zone 3, R^c_{vv} is low and since $R^m_{vv} = 1$, we can rewrite Eq.8.24 and Eq.8.25 as follows:

$$\begin{cases} \gamma_{tot,3} \simeq \gamma_{rf} \dfrac{< \sigma_{rf} >}{< \sigma_{tot} >} & (8.26) \\ \gamma_{tot,4} \simeq \gamma_{gr} \dfrac{< \sigma_{gr} >}{< \sigma_{tot} >} + \gamma_{rf} \dfrac{< \sigma_{rf} >}{< \sigma_{tot} >} \simeq \gamma_{tot,2} & (8.27) \end{cases}$$

Thus, according to Eq.8.26 and Eq.8.27, the expected interferometric phase in zone 3 will be the same as the roof and the expected interferometric phase in zone 4 will be the same as in zone 2, that is a mixture of two interferometric phases (the roof and the ground).

In Fig.8.20, a summary of the predicted interferometric signature according to each zone of study. As we can see, there is a correspondence between the predicted signature and the real one in the interferometric image of Fig.8.10. For zone 2 and 4, where a mixture of the two phases is expected, there is a dominance of the ground interferometric phase. Nevertheless, we have to justify this assumption by a study of the interferometric coherence in each of the five zones of interest. The objective is to find a correspondence between the predicted coherence using Eq.8.26 and Eq.8.27 and the real one to validate the proposed formulas.

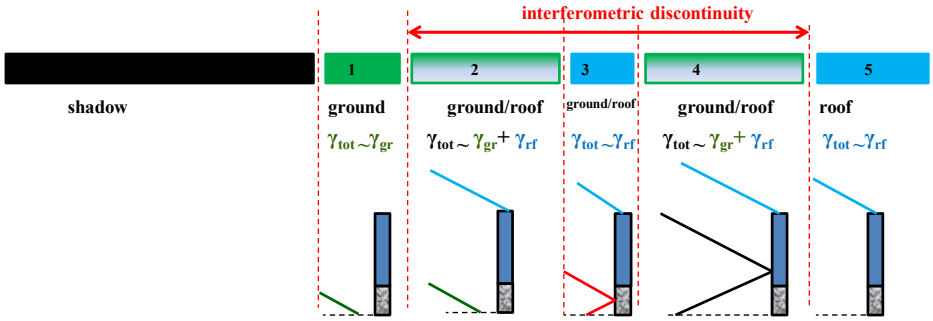

Figure 8.20: Illustration of the different mechanisms having the same distance to the radar according to each zone of study. The value of the predicted interferometric coherence coefficient of each zone of study is mentioned under the zone.

8.7.2.3 Proposed method to determine the interferometric coherence of each feature

To determine the interferometric coherence in each of the five zones of interest, we propose to study of the distributions of the interferometric coherence coefficients. The approach is the same as in the case of the backscattering coefficients. The different steps of the proposed method can be summarized as follows:

1. Select a rectangular area of each zone of study from the coherence image,
2. Derive the statistical distribution of the amplitude and phase of the coherence coefficients in each selected area,
3. Simulate the distributions of the amplitude and phase of the coherence coefficients in zone 1 and zone 5 (where only one backscattering mechanism exists) and also in layover areas (zone 2, 3 and 4) using the formulas in Eq.8.23, Eq.8.26 and Eq.8.27 and compare with the real distributions.

The third step is a validation step of the proposed formula to calculate the resulting coherence coefficient in layover areas. It is decomposed into sub-steps:

1. Select 1000 random samples of the complex coherence coefficients from the rectangular areas selected in zone 1 (ground) and zone 5 (roof) where only one mechanism exists. As for the case of backscattering coefficients calculation, we can not study the distribution of the coherence coefficients of the roof and ground in zone 2, 3 and 4 independently from the others mechanisms, thus, we assume that their distributions in these areas are the same as those in the two areas containing only one mechanism. Thus, γ_{gr} will be estimated in zone 1 and γ_{rf} in zone 5,
2. Use the formulas in Eq.8.23, Eq.8.26 and Eq.8.27 to build three vectors of data corresponding the the calculated coherence coefficients in zone 2, 3 and 4 and derive the corresponding distributions,
3. Compare with the real data distributions in zone 2, 3 and 4.

We present in Fig.8.21 the distribution of the phase and the amplitude of the interferometric coherence for zone 1 (the ground) and zone 5 (the roof). As illustrated, the phase and the amplitude are following a normal distribution.

Fig.8.22 presents the real and simulated distributions of the amplitude and phase of the interferometric coherence in zone 2, 3 and 4. Due to the approximations we have made on the calculation of interferometric coherence (in Eq.8.16 and Eq.8.20), the agreement between the simulated and real data is not so good. Nevertheless, the real and simulated normal distributions converge in terms of mean and variance.

8.7.3 Interpretation of the interferometric phase transition

To provide an interpretation of the interferometric phase associated to each zone, we compared the simulated coherence phase distribution of zone 2, 3 and 4 with the coherence phase distribution of the roof and ground. This is illustrated in Fig.8.23.

- For zone 2, the coherence phase interval is between the roof interval and the ground interval. It is seen on the interferometric image where in this zone, there is a mixture of two colors (the green corresponding to the ground and the blue to the roof). However, the intersection of the phase interval of zone 2 is more important with the ground interval than the roof interval, thus, the predominant color is the green,
- For zone 3, the coherence phase interval corresponds exactly to the roof's interval, thus the associated interferometric phase is the roof one,
- For zone 4, we keep the same reasoning as in zone 2. The coherence phase interval is between the roof interval and the ground interval. As the intersection of the phase interval of zone 2 is more important with the ground interval, thus, the predominant color is the green (ground response).

Hence, by comparing the simulated phase distribution of zone 2, 3 and 4 to the ground or roof, we have provided an explanation to the interferometric phase transition.

We have highlighted the impact of the material properties in the interferometric signature in layover areas. Indeed, with a low value of the reflection coefficient, a mechanism disappears, and the other mechanism becomes dominant, and hence defines the interferometric phase of the resolution cells in the layover areas. This

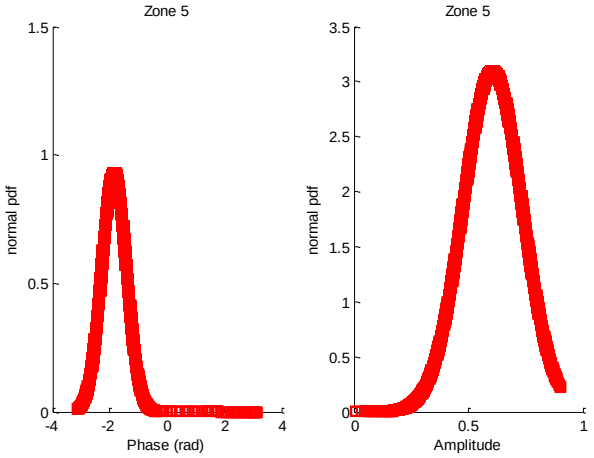

(a) Normal Distribution of the interferometric coherence phase and amplitude in zone 5.

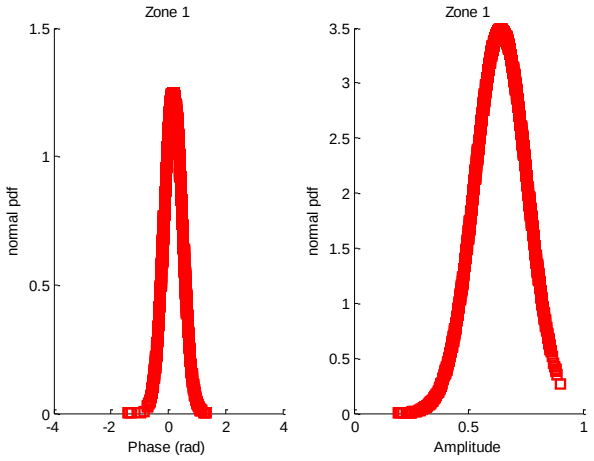

(b) Normal Distribution of the interferometric coherence phase and amplitude in zone 1.

Figure 8.21: Normal Distribution of the coherence phase and amplitude in zone 5 (the roof) and zone 1 (the ground).

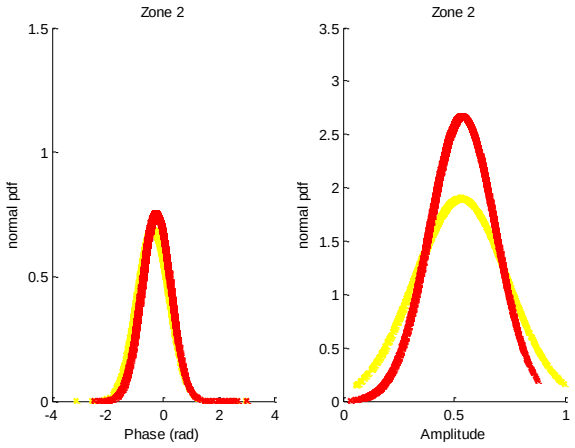

(a) Simulated and real data distributions of the interferometric coherence phase and amplitude in zone 2.

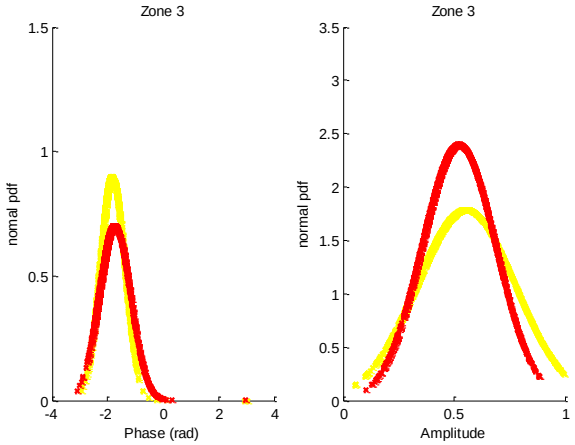

(b) Simulated and real data distributions of the interferometric coherence phase and amplitude in zone 3.

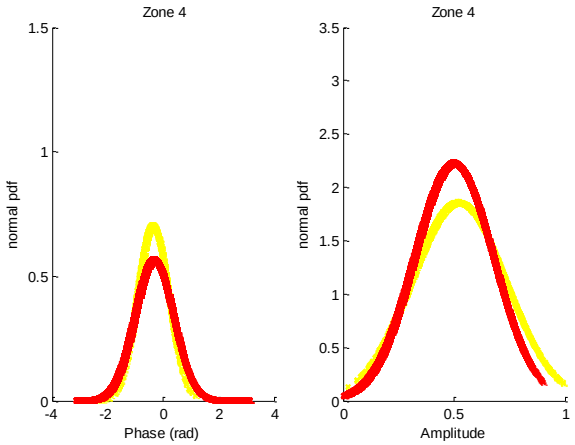

(c) Simulated and real data distributions of the interferometric coherence phase and amplitude in zone 4.

Figure 8.22: Comparison between the simulated and real distributions of the interferometric coherence phase and amplitude in zone 2, 3 and 4. The real data distributions are illustrated with red color and the simulated distributions are illustrated with yellow color.

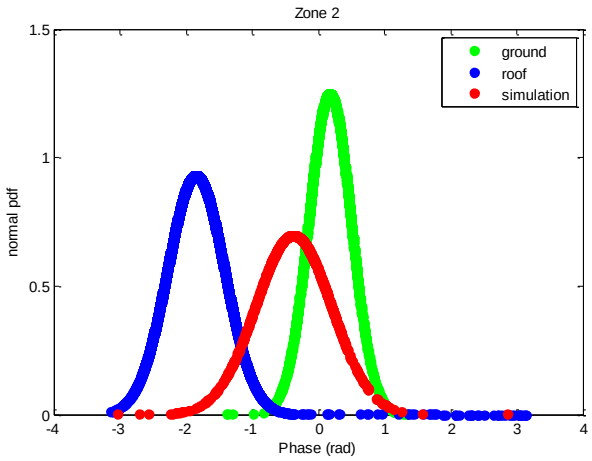

(a) Real phase coherence distribution for the roof and ground and simulated phase coherence distribution for zone 2.

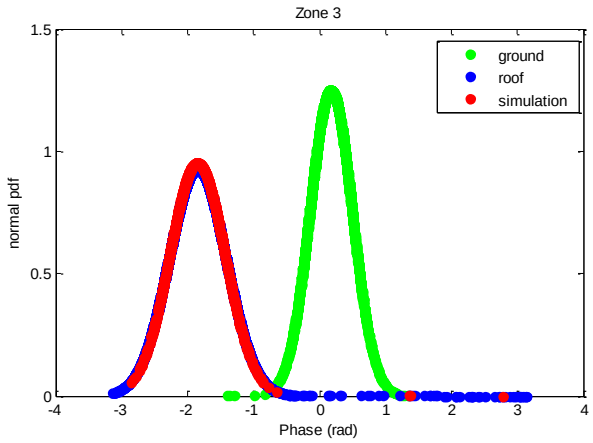

(b) Real phase coherence distribution for the roof and ground and simulated phase coherence distribution for zone 3.

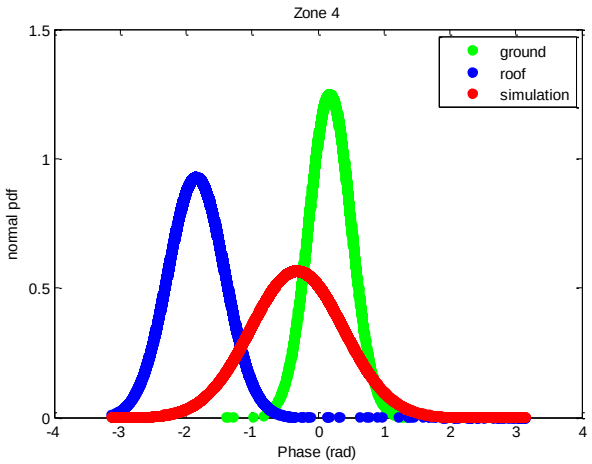

(c) Real phase coherence distribution for the roof and ground and simulated phase coherence distribution for zone 4.

Figure 8.23: Real phase coherence distribution for the roof and ground and simulated phase coherence distribution for zone 2, 3 and 4.

effect is present in zone 3 where a low value of R_{vv}^{c} makes the interferometric contribution of the ground negligible and consequently the resulting interferometric phase is the roof one.

To conclude, we can say that we are able using our developed EM code, the distribution of the backscattering coefficients and the interferometric coherence coefficients in isolated areas where only one mechanism exists, to interpret and predict the interferometric phase associated to a layover area.

8.8 Conclusion

In this chapter, our concern was to provide a complete analysis of the radiometric and interferometric image containing a simple urban scene (an urban canyon) in an industrial area in Salon de Provence (France) acquired in Ka-band with a resolution of 30 cm. This canyon contained two types of targets: three trihedral corner reflectors of different sizes and a truck. The radiometric analysis involved the study of the different mechanisms happening inside the scene as well as the study of the backscattering signature of the different features on the image. The interferometric analysis provided an explanation to the resulting interferometric phase assigned to each feature.

In the perspective to understand the origin of the different responses on the image as well as the different features with the different interferometric signatures, we have used our developed EM tool (Urban Canyon V3) to simulate the canyon configuration of the scene under study with the different included targets. The responses of the targets have been correctly retrieved since there was an agreement between the simulated peaks on the range profile and the different responses in the radiometric image. Indeed, the responses of the trihedral corner reflectors (modelled as a point targets scattering from one side) as well as the responses of a truck (modelled as an extended target) agreed in terms of phase with the real responses extracted from the SAR image. In addition, our EM tool has been used also to delimit the different features of the image to analyze their radiometric and interferometric signatures as they are strongly related. When analyzing the interferometric image, we noticed an interferometric discontinuity in a zone (the roof of the building) where only one interferometric phase is expected. In this zone, different layover areas exist and are the origin of the interferometric phase transition. For this reason, we presented an approach to predict the backscattering and interferometric response in layover areas. A theoretical formula has been proposed to calculate the resulting backscattering coefficient as well as the coherence coefficient for an area where there is a superposition of N mechanisms. This formula has been validated using a statistical study of the different distributions of the backscattering coefficients as well as the phase and amplitude of the coherence coefficients. The first conclusion is that since the interferometric coherence is strongly related to the backscattering coefficient in a resolution cell, the resulting interferometric phase in a layover area will correspond to the phase of the dominant mechanism with the greater backscattering coefficient. At the end of this study, we have provided an explanation to the interferometric phase transition on the roof of the building highlighting thus the effect of the material properties on the interferometric phase

definition. This effect describes the EM behaviour of a material according to the polarization, the incidence angle and to the used frequency. The main conclusion drawn at the end of this study is that our EM code can not provide a complete analysis of the available InSAR data. It can delimit the main features but with no explanation of the corresponding interferometric phase especially for the features where layover areas exist. Therefore, an EM study is required in addition to the proposed theoretical formula to predict the resulting interferometric phase.

Summary

The third part of the thesis was devoted to present our developed EM code dedicated to NLOS targets detection inside urban canyons in real case configurations. Based on the results of the second part concerning the EM phenomenology of propagation inside an urban canyon in real case, we developed a tool dedicated to a specific canyon configuration in order to achieve a specific goal. Indeed, this tool takes into account only specular reflection mechanisms to study multipath propagation inside a PEC canyon which is perpendicular to the propagation plan. The final goal is to investigate the detection of NLOS targets for a general case where all the expected mechanisms are present as no loss in the amplitude is possible due to the EM properties of the dielectrics. This canyon is oriented perpendicularly to the propagation plan to guarantee a configuration favourable to the maximum of multipath propagation mechanisms. Otherwise, some mechanisms may disappear as they will exist on the transverse direction and no return to the sensor is then possible. Three versions of the code have been presented with an increasing level of complexity. The first version has been dedicated to the study of the signature of an empty canyon. The second version investigates the detection of a NLOS point target inside the canyon and the last version, more adapted to real case study, investigates the detection of a NLOS extended target. For each version of this code, the input is the canyon configuration and the outputs are the NLOS detectability areas where a potential target can be detected in addition to a calculated radar range profile that allows an automatic analysis of the different responses. The main conclusion we have drawn is that even if the urban canyon is a simple scene to study, it provides a complex multipath propagation environment. The detection of the target depends strongly on the canyon configuration, on its position in the canyon and its dimensions. We have pointed out also the interest to study the NLOS detectability areas as they provide a wider coverage comparing to the LOS areas. We ended up the first two chapters of this part by presenting the validation results of our EM tool. In fact, the phase as well as the amplitude of the different calculated responses on the range profile have been compared to the simulations results of FEKO and a satisfying agreement has been found. This represents the main contribution of our work comparing to the state-of-art studies investigating the detection of targets in NLOS canyon configuration since we have at our disposal a validated EM tool dedicated to real case target detection.

A proof of the applicability of our tool to analyze InSAR data for a canyon with different types of targets has been presented in the last chapter of this part. This canyon was acquired with a tilt in azimuth of 9 ° and the conclusions remain valid. Indeed, the responses of the targets have been successfully retrieved on the SAR image using a simulated range profile with our EM tool, in addition to the main features that have been delimited. A full radiometric and interferometric study has been conducted to explain the interferometric phase corresponding to each of the extracted features where layover areas exist and may lead to an unexpected interferometric phase. The main conclusion is that our EM tool is not enough to analyze the interferometric data. An EM study is required to analyze the inter-

ferometric signature in layover areas. Our first contribution to separate the phase center comparing to the state-of-art works is the formula we proposed to calculate the coherence coefficient in a zone where there is a superposition of N mechanisms. Our second contribution is that we take into account the mechanisms occurring in the whole scene and not only on an isolated building as in [Cellier 2007], because in urban areas, the interactions happening around a specific zone affect its resulting interferometric signature .

Conclusions and perspectives

The main objective of this present thesis was to investigate about the detection of NLOS target inside a representative urban scene: the urban canyon. Three parts have been proposed to deal with this new topic. The first part was a general introduction to the problematic by presenting the current state of art dealing with the detection of NLOS targets inside urban scenarios via algorithms of detection or EM simulators. The main conclusion drawn at the end of this state-of-art was that there is no existing method or simulator that has been validated in terms of amplitude and therefore no one was adapted to our purpose. The amplitude is crucial to determine whether a target can be detected or not. Based on this ascertainment, we put all the contribution of our work on developing an EM tool dedicated to simple urban structures (PEC urban canyon oriented perpendicular to the propagation plan) but validated in terms of amplitude.

In order to gain knowledge about the EM phenomenology of propagation inside the urban canyons and assess the amplitude parameter, we conducted indoor measurements with ONERA in one of their anechoic chamber measurements. However, it was not possible to respect the ratio d/λ, with the typical dimension of the canyon d and λ the radar wavelength. We decided then to favor the resolution instead. As a consequence, these measurements were not representative of the scattering phenomena in real configurations, but we use them to validate the amplitude and phase produced by the EM tools we selected. The idea was then to consider higher frequencies with these tools to tend to the real d/λ ratio (the second part of the thesis).

The results of this study have been used to develop a fast in-house tool dedicated to the specific goal of NLOS target detection. The development, analysis and validation of this in-house tool are the core subjects of the third part. This tool enabled to fast derive the range profiles in different configurations: with and without target, and considering a point and a parallelepiped target. At last but not at least, this tool helped us to assess the conditions ensuring the detection of NLOS targets. This allowed us to determine what we called the detectability areas, whose size depends on the incidence angle in particular, but also on the dimensions and the positions of the target. In order to illustrate one of the possible benefits of this kind of tool, we finally proposed an analysis of an InSAR image of an urban canyon with different targets, whose responses are in NLOS.

As this work is a preliminary one in the frame of NLOS target detection in urban canyons using a simple EM tool, many perspectives can be considered. For the short-term perspectives, we aim to validate FERMAT[1], an EM simulator developed by both ONERA and OKTALE-SE that has provided satisfying results in modelling the scattering of complex scenes [Mametsa 2002]. This EM tool may fit to our requirements of the EM modelling of the multipath propagation inside urban canyons with a validated amplitude as well as an optimized calculation time. What is more important is that is possible in this case to technically discuss about the approximations implemented in this tool if there is any difficulty. On the con-

[1]FERMAT has been commercialized under the name of SE-RAY-EM [Mametsa 2002].

trary, we could not have access to the details of implementation of the EM methods in Wireless Insite for instance. For this reason, this tool has been rejected as we did not manage to solve the problem induced by the definition of the waveform, despite the numerous discussions we had with some of the point of contacts. At the time of the writing of this thesis, there have been discussions with Henri José Mametsa, who is in charge of FERMAT in ONERA, in order to simulate some of the configurations we tested with FEKO and CST.

The second short-term perspective is to extend our 2D in-house tool to a 3D EM tool to better suit the conditions of real cases where the canyons are not necessarily oriented parallel to the sensor trajectory. In fact, we have evaluated with FEKO the effects of the canyon geometry on the different EM mechanisms occurring inside it. We namely highlighted how a disorientation whether inside the canyon or with respect to the flight direction can increase the entropy leading to a misclassification of the urban areas. Even if our reference case (a canyon oriented perpendicular to the propagation plan) allowed to study a complex multipath propagation, since all the expected effects are present, this does not constitutes a representative case of the reality. Therefore, the need to take into account the 3D effects, such as the distortions mentioned above, to develop a complete EM code. We could think first to develop a pseudo 3D tool, starting from our 2D in-house tool. The idea will be to replace the reflection coefficients by the corresponding scattering matrices. This have been investigated for the validation of Urban Canyon V3 with the 3D EM tool FEKO. In this way, we could take into consideration all the characteristics of the canyon such as the 3D dimensions of the walls and the dielectric properties. In this first stage, the outputs will remain the same. The next step will be to develop a real 3D tool taking into account the positions of the sensor. We could at that point add a new output, such as the SAR image. Then, in the frame of determining the probability of detection of NLOS targets over an extended urban scene, we have to consider a realistic description of this scene. The development of a dedicated simulator is probably not possible in an academic laboratory. However, we could work on the characteristics of the urban environment scattering. Namely, this would imply to determine all the canonical urban structures, typically observed in the scene under study, their sizes as well as their distributions according to the sensor trajectory. The canonical structures and their associated distributions are expected to be highly dependant on the geographical localization: an european city is not similar to a american one. Finally, it appears that there is a quite important prior work to achieve before moving to the 3D analysis.

Moreover, our work focused on PEC canyon to begin with a simple and complete case, since no loss in the amplitude is expected and consequently, all the predicted mechanisms exist. Nevertheless, in realistic configurations, the urban structures are composed by dielectric materials that highly impact on the scattered EM field as well as on the interferometric signature as highlighted in the last chapter of the thesis. The difficulty is to characterize this wide variety of materials in urban areas, as well as the variation of their permittivity with the frequency and incidence angle. Nevertheless, a study of the dielectric properties of the most common materials in urban areas can be carried out and hence the effects of permittivity and roughness can be investigated using modified Fresnel reflection coefficients. In addition, we propose with this 3D EM tool to investigate the scattering in urban areas at X

band, since so far, there is an advanced knowledge concerning the EM behaviour of the dielectric materials at X-band comparing to the others bands (such as the Ka-band used for the outdoor measurements campaign presented in the last chapter where we encountered difficulties to find the permittivity of the concrete at the used frequency band.)

This prior study of the EM materials composing the scene is crucial since it strongly impacts on the interferometric signature: we highlighted the dependance of the interferometric signature on the materials composing the scene as their EM behaviour varies according to many parameters (the operating frequency, the polarization, the incidence angle..). Once the effect of the scene geometry and the material properties integrated in this 3D tool, the middle-term objective is to validate it. The validation will concern the effects that this tool is able to reproduce as well as the validation of the amplitude in order to use this 3D tool for NLOS target detection. We notice that at every extension on this code, the validation step becomes more and more complicated. Nowadays, we have to think about a strategy of validation if we aim to develop a 3D EM tool that can correctly model the most dominant effects happening in the complex multipath propagation environment of an urban area.

This lead us to define a long-term perspective that is to propose a SAR processing tool that corrects the artifacts in SAR images of an urban scene. In fact, once the impact of the geometric and EM characteristics of the scene on the scattered EM field investigated with the validated 3D EM tool, it is possible to understand the origin of some artifacts and hence to propose the adequate processing technique to correct them.

Moreover, until now, the SAR processing techniques assumed the isotropy of the scatterers on the imaging scene. This was denied in [Brigui 2010] where it was demonstrated that in the case of forest scenes, this assumption is no more valid. We could think that is also the case for urban areas due the multitude of interactions with a complex EM behaviour. Hence, it is necessary to propose a new SAR processing technique adapted to the non isotropic behaviour of the urban scenes.

Referring to the initial goal of this present thesis, which is the NLOS target detection, the results of the 3D EM tool can be used to determine rapidly with a prior study of the geometry of the urban structures as well the different materials composing it, the most relevant radar configuration allowing a high percentage of target detection. As shown through this work, the detection of the target depends on the geometry of the canyon in which it is located and necessary on the materials composing the walls of the canyon. This 3D tool will help to design future radar campaign and to define a strategy of city surveillance.

Appendix A

Range profile reconstruction

A.1 Scene definition

The scene model is composed of independant scatterers characterized by their reflection coefficients σ_i (that depends on the physical properties of the scatterer such as the conductivity, the permittivity, the roughness) and their range coordinates $x_{i(i=1,..n)}$. The radar is located at x=0 and illuminates the area where the target is located. It transmits a pulse $p(t)$ of duration T, generally shorter than the time taken for the emitted signal to go back to the radar. We are in the monostatic case since the transmitter and the receiver are located at the same coordinates.

A.2 Signal modelling

The emitted signal $p(t)$ reaches the first scatterer at t_1=x_1/c , c is defined as the speed of light. Thus, the signal that reaches the first scatterer is expressed as $p(t-t_1)$. After reflection, the signal goes back to the receiver and arrives at $x=0$ after t_1 seconds. The receiver records the signal $s_1(t)=\sigma_1 \times p(t-2t_1)$.

The resulting signal that corresponds to the summation of all the backscattered signal from all the scatterers in the scene is defined as:

$$s(t) = \sum_{i=1}^{n} s_i(t) \tag{A.1}$$

$$= \sum_{i=1}^{n} \sigma_i \times p(t-2t_i) \tag{A.2}$$

where $t_i = x_i/c$

A.3 Reconstruction of the image 1D: the radar range profile

The radar range profile allows to localize all the scatterers using $s(t)$ in order to identify the targets in the illuminated scene. Therefore, we write the Eq.A.2 using the convolution product as:

$$s(t) = \sum_{i=1}^{n} \sigma_i [p(t) \otimes \delta(t-2t_i)] \tag{A.3}$$

$$= p(t) \otimes [\sum_{i=1}^{n} \sigma_i \delta(t-x_i/a)] \tag{A.4}$$

where a is defined as $a = c/2$.

Using the fact that: $\delta(t - x_i/a) = a\delta(at - x_i)$,

We obtain:

$$s(t) = p(t) \otimes [a \sum_{i=1}^{n} \sigma_i \delta(at - x_i)] \tag{A.5}$$

$$= p(t) \otimes [aI_o(at)] \tag{A.6}$$

where $I_o(x) = \sum_{i=1}^{n} \sigma_i \delta(x - x_i)$

$I_o(x)$ is the radar range profile that provides the spatial distribution of the scatterers. It is expressed as the summation of the dirac distributions located at the scatterers coordinates with an amplitude equal to the reflection coefficients of the scatterers. Our goal is to reconstruct the radar range profile $I_o(x)$ from the received signal $s(t)$. The procedure then is to deconvoluate the signal in Eq.A.6. This deconvolution or model inversion is realized in steps:

- The first step is to apply the Fourier Transform to the signal in Eq.A.6. It will be defined in the frequency domain for a frequency f_j as:

  $$S(f_j) = P(f_j)H_o(k_{xj}) \tag{A.7}$$

  Where $k_{xj} = f_j/a = 2f_j/c$ is the dual variable of x by Fourrier Transform. It is defined as the spacial frequency, whereas f_j is defined as the temporal frequency. The previous equation establishes the relation between the spectrum of the received signal, the spectrum of the emitted signal and the spectrum of the radar range profile,
- Then the frequency spectrum of $I_o(x)$ denoted $H_o(k_{xj})$ can be obtained by:

  $$H_o(k_{xj}) = \frac{S(f_j)}{P(f_j)} \tag{A.8}$$

  However, we have to ensure that the spectrum of the emitted signal has a finite bandwith without any null value ($P(f_j) \neq 0 \; \forall f_j \in \Delta_f$). The spectrum $H_o(k_{xj})$ can be deduced by applying the Fourrier Transform to Eq.A.2 as follows:

  $$H_o(k_{xj}) = \sum_{i=1}^{n} \sigma_i e^{-2j\pi f_j (2x_i/c)} \tag{A.9}$$

  $$= \sum_{i=1}^{n} \sigma_i e^{-2j\pi k_{xj} x_i} \tag{A.10}$$

- $I_o(x)$ is then obtained by applying the Inverse Fourrier Transform applied to $H_o(k_{xj})$ such as:

  $$I_o(x) = TF^{-1}_{k_{xj} \to x}[H_o(k_{xj})] \tag{A.11}$$

  $$= \sum_{i=1}^{n} \sigma_i \times \delta(x - x_i) \tag{A.12}$$

In practice, the spectrum of the radar range profile $H_o(k_{xj})$ has a width of Δ_f and

is centered around a central frequency f_c:

$$P(f_j) = \begin{cases} \neq 0 \text{ if } f_j \in [f_c - \Delta_f/2, f_c + \Delta_f/2] \\ = 0 \text{ else} \end{cases} \tag{A.13}$$

The spectrum $H_o(k_{xj})$ of the radar range profile can not be determined directly using the formula in Eq.A.8, but, using the following equation:

$$H(k_{xj}) = \begin{cases} S(f_j)/P(f_j) \text{ if } k_{xj} \in [k_c - \Delta_k/2, k_c + \Delta_k/2] \\ 0 \text{ else} \end{cases} \tag{A.14}$$

where $\Delta_k = 2\Delta_f/c$ and $k_c = 2f_c/c$ Consequently, the radar range profile $I(x)$ is expressed as:

$$I(x) = TF^{-1}_{k_{xj} \to x}[H(k_{xj})] \tag{A.15}$$

$$= \sum_{i=1}^{n} \sigma_i \times \Delta_k \times sinc[\pi \Delta_k (x - x_i)] e^{+2j\pi k_c (x - x_i)} \tag{A.16}$$

Fig.A.1 shows the spacial distribution for a set of scatterers for a transmitting signal with a limited bandwidth and for a signal with an infinite bandwith.

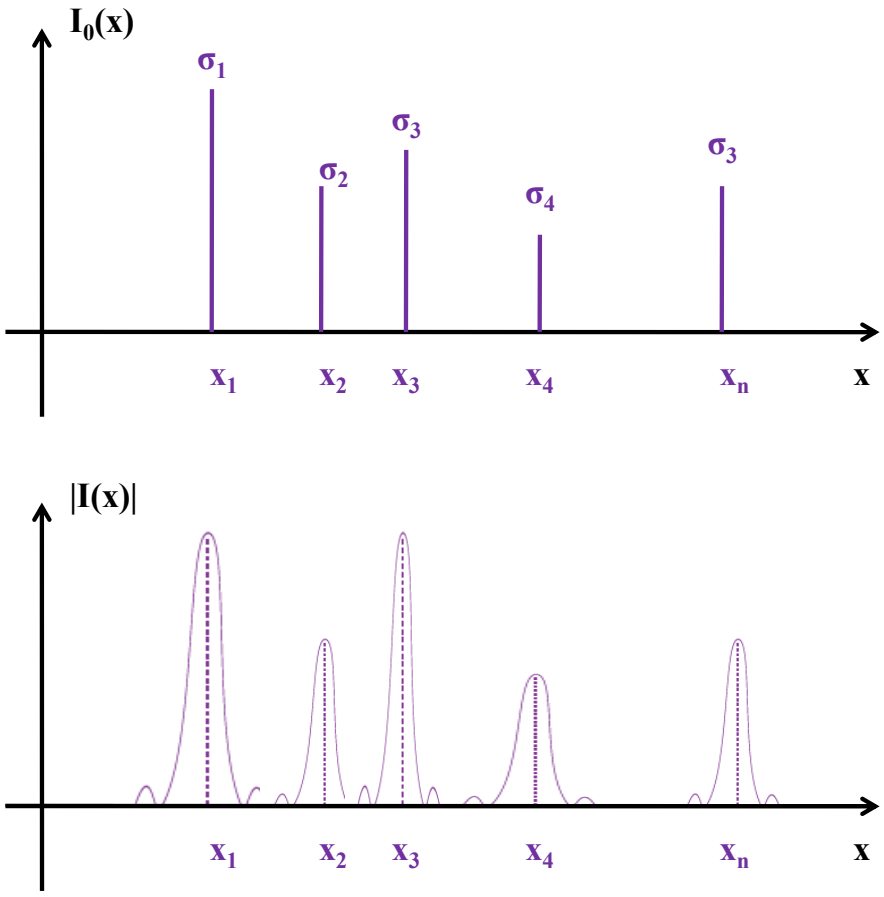

Figure A.1: Spacial distribution of the scatterers for the case where the signal has a limited bandwith (Top) and an infinite bandwith (Bottom).

Appendix B

Résumé

Introduction

Dans cette thèse, le thème principal est la détection de cibles en non visée directe du radar à l'intérieur d'une scène simple mais représentative (le canyon urbain défini comme étant deux bâtiments séparés par une route) en utilisant des images SAR, pour des applications militaires et civiles. Les applications dans le domaine de la détection des cibles cachées en utilisant des systèmes radar sont nombreuses: la reconnaissance mondiale se fait principalement par les systèmes satellitaires, des avions et des plates-formes à haute altitude transportant des capteurs pour l'observation de larges zones. En outre, il y a des équipements SAR miniature qui sont intégrés dans des drones pour la surveillance du champ de bataille. La résolution des systèmes SAR a été améliorée au cours des dernières décennies jusqu'à l'ordre du centimètre. De ce fait, des algorithmes de classification de haute performance sont maintenant en mesure d'identifier certains objets militaires cachés dans la scène d'étude.

Dans ce contexte, notre objectif principal n'est pas de développer des techniques de traitement d'images appliquées à la détection de cibles en non visée directe du radar mais plutôt d'acquérir des connaissances sur la phénoménologie électromagnétique (EM) de propagation à l'intérieur des canyons urbains. Une fois que la relation entre les paramètres du radar (fréquence, polarisation, angle d'incidence, ..), la composition de la scène (incluant la géométrie et les matériaux) et le signal renvoyé établie, une prédiction correcte de la détection d'une cible cachée peut être envisagée.

Cette thèse se compose de trois parties principales. La première partie est consacrée à une introduction générale à la problématique basée sur une étude de l'état de l'art afin de mettre en évidence notre contribution par rapport aux réalisations précédentes. Notre méthodologie pour aborder ce nouveau thème est également présentée (chapitre 1). En outre, une description des données de référence que nous avons à notre disposition pour analyser la phénoménologie EM de la diffusion à l'intérieur des canyons urbains à la fois pour des environnements contrôlés et réels, est présentée dans le chapitre 2. La deuxième partie de cette thèse présente la connaissance de la phénoménologie EM de propagation à l'intérieur du canyon que nous avons acquise suite à l'analyse des données en environnement contrôlé. Dans le troisième chapitre, nous présentons les différents outils EM commerciaux testés pour sélectionner un outil fiable qu'on utilisera pour analyser la diffusion à l'intérieur des canyons urbains réels. Le chapitre 4 est consacré à une présentation détaillée des données de la chambre anéchoÃ¯que sur lesquels nous avons effectué des simulations à l'aide des outils EM commerciaux. Dans le dernier chapitre de cette partie, les résultats des simulations des outils sont présentés avec les différentes conclusions que nous avons tiré suite à l'analyse de ces simulations sur des config-

urations en environnement contrôlé et réel. La troisième partie de la thèse est une présentation de notre code maison développé et validé pour la détection des cibles ponctuelles et étendues à l'intérieur des canyons urbains (chapitre 6 et 7). Enfin, un exemple d'application de ce code pour l'interprétation des données InSAR est proposé dans le dernier chapitre de la thèse.

Problème et méthodologie

Enoncé de la problématique

Les systèmes typiques du SAR sont conçus pour imager des cibles en visée directe du capteur. Cependant, dans un environnement où la cible en question (par exemple des objets fabriqués par l'homme, comme une voiture ou un camion) est cachée ou entourée par plusieurs diffuseurs (par exemple, des bâtiments), la détection de cette cible dans l'image SAR correspondante peut être erronée en raison de l'absence d'une réponse en visée directe. Un exemple typique de ce problème concernant la détection de cibles dans les images SAR en milieu urbain est illustré dans la Fig.B.1.

Figure B.1: (Gauche) Bâtiment d'étude avec une cible (cornet réflecteur) située en face (le point vert indique la position de la cible). (Droite) Image SAR correspondante acquise et traitée par l'ONERA durant une campagne de mesures impliquant la plate-forme moteur Busard équipé d'un radar routier. La bande de fréquences est de [33-37] GHz, et l'angle d'incidence est de 60°. Cette image contient un artefact: la cible située initialement en face de l'immeuble est synthétisée à la zone d'ombre située derrière le bâtiment (voir le rectangle rouge).

Etat de l'art

Détection des cibles en non visée directe du radar

Dans la littérature, les travaux portant sur la détection de cibles dans les zones urbaines peuvent être classés en deux groupes. Le premier groupe des travaux étudie la détection (ou suivi) des cibles mouvantes et le deuxième groupe est concerné par la détection des cibles statiques.

Détection des cibles mouvantes Suite à une étude de l'état de l'art sur le premier groupe de travaux, nous avons conclu que la propagation par les trajets multiples peut être exploitée pour étudier la détection des cibles mouvantes. Ainsi, basée sur cette hypothèse, plusieurs modèles ont été mis au point. Néanmoins, même si ces modèles ont montré des résultats satisfaisants, nous ne pouvons pas compter entièrement sur eux dans la mesure où on ne peut pas penser à utiliser des approches similaires ou à les adapter à notre cas d'étude. La raison est que la validation de ces modèles proposés n'est pas complète vu que la validation du paramètre d'amplitude manque. L'amplitude est un paramètre important dans le cadre spécifique de cette étude puisque dans certains cas de figure, il est possible de prédire la position d'une réponse qui peut ne pas exister, ce qui peut induire en erreur.

Détection des cibles statiques A l'encontre des travaux précédents qui exploitent la propagation par les trajets multiples comme information utile pour suivre correctement la cible, l'approche n'est pas la même pour les travaux concernant la détection d'une cible statique. En effet, pour le cas d'une cible statique située dans un riche environnement de diffusion, l'image SAR résultante contiendra des duplicats de la cible en plus de la réponse primaire (la réponse en visée directe). Par conséquent, la tâche de détection sera complexe car il sera difficile de distinguer la réponse en visée directe des réponses fantômes (duplicats de la cible). La propagation par les trajets multiples n'est plus exploitée, car elle représente un obstacle à une détection correcte. Par conséquent, les travaux actuels se concentrent sur le développement d'outils SAR de traitement d'images dédiées à supprimer les artefacts dus aux effets de non visée directe. Ces travaux ne peuvent pas être exploités dans le cadre de cette étude vu que notre premier objectif est de ne pas proposer une technique de traitement d'image pour corriger les artefacts dans les images, mais plutôt, de comprendre la phénoménologie EM de propagation à l'intérieur des canyons urbains qui peuvent expliquer l'origine de certains artefcats.

Les simulateurs SAR des zones urbaines

Les simulateurs SAR peuvent être calssés en deux groupes:

- des simulateurs basés sur la justesse radiométrique: Ces simulateurs utilisent des formules pour calculer une valeur d'intensité de haute qualité du champ EM diffusé. Ces modèles prennent en compte les paramètres de rugosité et les propriétés diélectriques des surfaces de la scène afin de calculer la diffusion. Cependant, le niveau de détail des modèles 3D à utiliser est limité. Ainsi, ces simulateurs peuvent correspondre à notre cas d'étude vu que nous traitons

également des structures canoniques simples (le canyon urbain). Néanmoins, même si l'intensité des champs diffusés a été bien calculée, elle n'a pas été validée avec des données expérimentales.

- des simulateurs basés sur la justesse géométrique: Ces simulateurs mettent l'accent sur la représentation des effets géométriques d'une scène détaillée. La qualité radiométrique est de moindre importance pour cette approche, de ce fait, on ne peut pas les utiliser pour la détection de la cible en non visée directe vu que la paramètre d'amplitude est primordial pour notre cas d'étude.

Spécification de l'objectif

Comme un simulateur SAR idéal dédié aux zones urbaines, qui relie à la fois la justesse géométrique et radiométrique, et qui est validé en termes d'amplitude et de phase, n'est pas réalisable pour le moment, nous devions développer notre propre simulateur tout en définissant une stratégie pour le valider. Comme notre objectif ultime est de prédire la détection éventuelle des cibles en non visée directe à l'intérieur du canyon, notre outil proposé doit être:

- dédié à la configuration du canyon urbain
- rapide en terme de temps de calcul
- efficace pour la simulation de la phase et de l'amplitude des réponses des diffuseurs
- validé à la fois en termes de phase et d'amplitude.

Méthodologie

Pour développer notre outil de simulation dédié à la détection de cibles en non visée directe à l'intérieur du canyon urbain, nous avons adopté la méthodologie suivante, basée sur deux étapes de processus de validation. Premièrement, nous avons effectué des mesures dans la chambre anéchoique servant à étudier la propagation EM dans un canyon avec et sans la présence de la cible. Une étude EM théorique a été réalisée afin de comprendre les phénomènes de diffusion pour un canyon présentant un ratio entre la dimension typique d de l'objet d'intérêt et la longueur d'onde λ imposée par les contraintes techniques de la chambre anéchoÃ¯que qui ne correspond pas au ratio réel. De ce fait, nous avons eu recours à des codes EM commerciaux capables de simuler des configurations avec un ratio réel. Une analyse comparative entre différents codes EM commerciaux a été effectuée pour sélectionner le code qui reproduit aux mieux la phénoménologie EM de propagation à l'intérieur du canyon dans le cas d'un environnement contrôlé. En effet, les comparaisons entre les différents résultats de la simulation de deux codes (FEKO et CST) et les résultats expérimentaux ont montré un bon accord à la fois pour la phase et de l'amplitude. Ensuite, ces deux codes ont été utilisés pour simuler la diffusion à l'intérieur des configurations plus réalistes (en termes de ratio d/λ). Toute cette étude concernant la validation des codes EM commerciaux est présentée dans la deuxième partie de cette thèse.

La troisième partie traite la deuxième étape de la validation. Il s'agit de la validation d'un code-maison développé simple et rapide dédié à la detection des cibles en non visée directe à l'intérieur des canyons urbains. En fait, se basant sur les résul-

tats de simulation de l'outil EM commercial validé appliqué à des configurations de cas réels, nous avons développé notre propre outil EM. Cet outil prédit pour toute configuration du canyon, les zones de détectabilité en non visée directe du radar (les zones où la cible peut être détectée), et dans le cas où la cible est présente si elle peut être détectée ou non, et la signature en distance du canyon. Puisque la validation directe (par comparaison directe avec les données expérimentales) n'est pas possible vu que le ratio d $/\lambda$ ne peut pas être respecté dans la chambre anéchoique, nous avons validé notre code avec l'un des codes EM sélectionnés. Un exemple d'application des résultats de notre code EM pour l'interprétation de données InSAR réels est proposé dans le dernier chapitre. Dans Fig.B.2, nous proposons un schéma résumant les différentes étapes de la méthodologie proposée.

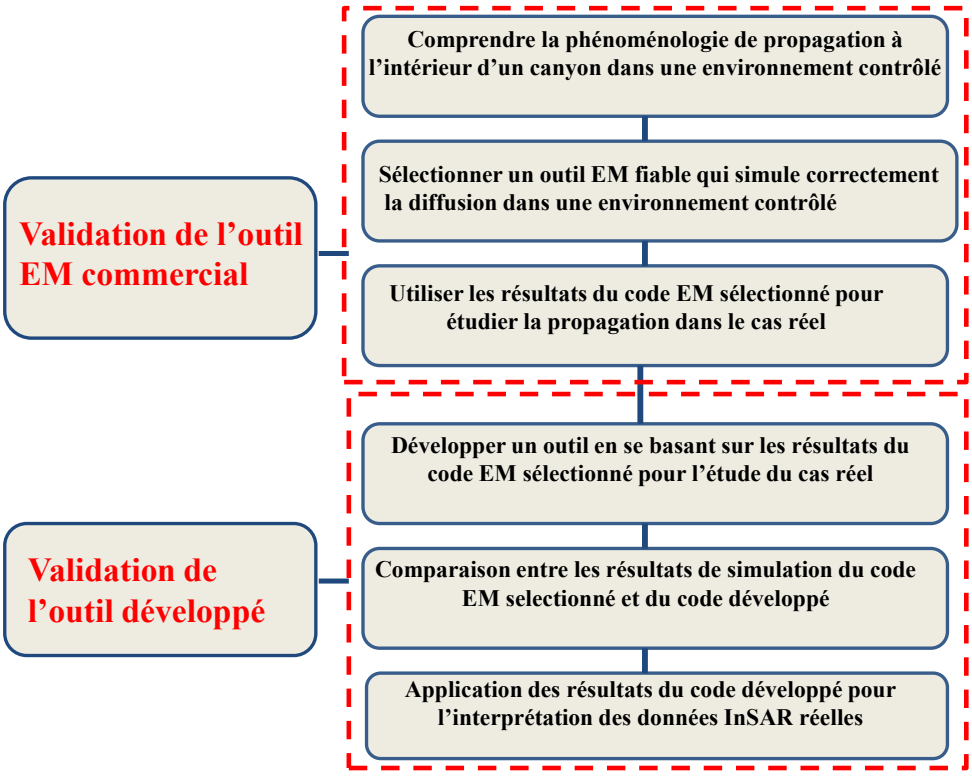

Figure B.2: Un schéma résumant les différentes étapes de la méthodologie suivie pour élaborer et valider notre outil de simulation EM dédié à la détection de cibles en non visée directe à l'intérieur des canyons urbains.

Données de référence

Données existantes

Surface Equivalente Radar (SER)

Le paramètre SER est utilisé pour valider les niveaux en amplitude des réponses collectées (par les simulations ou par les mesures). Pour certaines cibles typiques, comme l'expression théorique de la SER est déjà établie, ces cibles sont généralement utilisées pour calibrer les mesures en environnement contrôlé. En outre, dans le cadre spécifique de la détection des cibles en non visée directe du radar, la SER

a été utilisée pour valider les résultats de simulation des outils EM commerciaux permettant d'évaluer correctement l'amplitude des réponses des diffuseurs dans la scène. En effet, le paramètre SER est un prérequis fondamental qui sert à valider toute étude portant sur le calcul de l'amplitude du champ EM diffusé dans une scène.

Mesures en environnement contrôlé

Une première étude préliminaire sur la faisabilité de détecter des cibles en non visée directe du radar à l'intérieur d'un canyon urbain a été menée à l'aide de mesures en environnement contrôlé. Ces données ont été acquises dans le cadre d'une collaboration avec des chercheurs singapouriens de NTU en utilisant la chambre anéchoique du DSO. La configuration de la chambre anéchoÃ¯que présente un ratio entre les dimensions et la longueur d'onde utilisée, qui est proche du ratio réel. Cependant, la condition du champ lointain n'est pas réspecté et par conséquent, des effets de champ proche sont apparus dÃ»s à la variété angulaire en incidence.

Mesures réelles

Un deuxième ensemble de données pour étudier les phénomènes de la propagation multitrajets à l'intérieur d'un canyon urbain, a été acquise en bande Ka au cours d'une campagne de mesures menée par l'ONERA. Une partie de ces données a été analysée dans le dernier chapitre de la thèse.

Données nouvelles

La deuxième étude réalisée concernant la détection des cibles en non visée directe à l'intérieur du canyon en utilisant des mesures en environnement contrôlé a été effectuée en Juin 2012 dans le cadre de cette thèse. Ces mesures ont été collectées dans la chambre anéchoique BABI de l'ONERA afin d'acquérir des connaissances sur la phénoménologie EM de propagation l'intérieur d'un canyon dans le cas du champ lointain. Pour assurer la condition du champ lointain avec la meilleure résolution en distance, un très faible ratio d/ λ est obtenu. A moins d'utiliser une fréquence très élevée qui est techniquement irréalisable, le ratio réel ne peut jamais être respecté dans la chambre anéchoÃ¯que. Par conséquent, les effets EM se produisant à l'intérieur d'un canyon réel ne peuvent jamais être analysés à l'aide des données de la chambre.

Présentation des codes EM

L'objectif de l'analyse comparative entre codes est de sélectionner les outils EM qui sont capables de simuler correctement la phénoménologie EM de diffusion à l'intérieur d'un environnement contrôlé à la fois en termes de phase et d'amplitude. Ces outils EM, une fois validés, seront utilisés pour modéliser la diffusion avec des fréquences plus élevées assurant un ratio d/λ convergeant vers le ratio réel. De ce fait, l'étude de la phénoménologie EM de propagation pour le cas réel peut être effectuée et par conséquent on peut développer notre outil dédié se basant sur les résultats de cette étude. Quatre outils EM ont été utilisés, cependant, uniquement

deux d'entre eux ont été retenus. Dans ce qui suit, nous allons présenter les différents codes EM.

Wireless Insite (WI)

WI est un outil EM basé sur des méthodes de tracé de rayons pour l'analyse de la propagation radio dédié principalement pour les communications sans fil.

Nous avons rencontré quelques difficultés avec WI qui nous ont poussé à rejeter cet outil. Elles peuvent se résumer ainsi:

- Difficulté dans la défnition de la forme d'onde
- Difficulté dans le calcul du profil distance en utilisant les sorties de WI
- Difficulté dans la calibration radiométrique

WI a été rejeté du fait que l'amplitude n'a pas été validée.

MOCEM

MOCEM est un simulateur d'images SAR dans lequel l'utilisateur a la possibilité d'inclure les propriétés diélectriques des différents matériaux composant la scène d'étude. La validation du SER d'un trièdre a été possible avec MOCEM. Cependant, MOCEM présente un nombre d'inconvénients qui nous a poussé à considérer que cet outil n'est pas bien adapté à notre cas d'étude. Ces limitations se résument ainsi:

- Limitation en nombre d'intéractions
- Nécessité de connaître les propriétés diélectriques des matériaux
- Produit une image SAR et non pas des champs diffusés, ce qui rend la génération de profils distance difficile

MOCEM a été rejeté principalement du fait du nombre d'intéractions limité qu'il prend en compte, une caractéristique qui ne convient pas aux milieux urbains caractérisés par la propagation multi rebonds.

FEKO

FEKO est un code EM basé sur des méthodes exactes et des méthodes approchées pour la résolution des équations de Maxwell.

- Exemples de méthodes exactes: MoM
- Exemples de méthodes approchées: Théorie Uniforme de la Diffrcation (UTD), Optique Physique (OP), Optique Géométrique (OG)

Vu que FEKO est basé sur une méthode exacte pour le calcul des champs diffusés, les résulats obtenus peuvent être considérés comme des résultats de référence. Pour la méthode exacte (MoM) et certaines méthodes approchées (UTD, OP), le temps de simulation est long.

FEKO a été testé sur un canyon simple et sur un canyon avec cible et une bonne correspondance a été trouvée entre les résultats de simulation et les mesures en termes de phase et d'amplitude. De ce fait, FEKO a été considéré comme le premier outil validé.

CST

CST est un outil EM basé sur un solveur dans le domaine temporel. Il présente l'avantage majeur d'être rapide par rapport à FEKO. Cependant, CST devient long en temps de calcul si le volume contenant l'objet d'intéret devient important. CST a été testé sur un canyon simple et sur un canyon avec cible et une bonne correspondance a été trouvée entre résultats de simulation et mesures en termes de phase et d'amplitude. De ce fait, CST a été considéré comme le deuxième outil validé.

Présentation détaillée des nouvelles mesures

Présentation des données en environnement contrôlé

Mesures à la chambre anéchoique de NTU

L'objet d'intérêt est un canyon parfaitement métallique avec différents types de cibles incluses. La configuration de ces mesures est illustrée dans la Fig.B.3. La

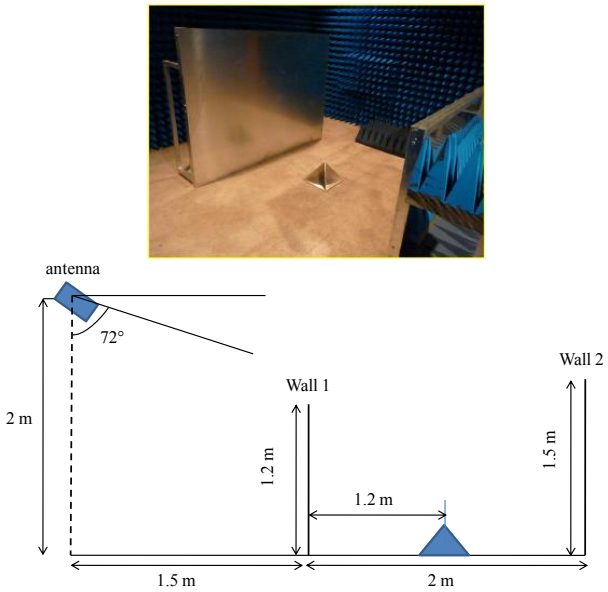

Figure B.3: Configuration des mesures dans la chambre anéchoique de NTU en bande Ka. L'angle d'incidence est 72° et la bande de fréquences est [33,37]GHz.

configuration de la chambre anéchoique présente un ratio entre les dimensions du canyon d'intérêt et la longueur d'onde utilisée qui est proche du ratio réel. Cependant, avec cette configuration, des effets de champ proche apparaissent.

Nouvelles mesures à la chambre anéchoique BABI de l'ONERA

Pour palier aux problèmes du champ proche, une configuration du canyon en champ lointain a été proposée à la chambre anechoique BABI de l'ONERA afin d'étudier la detectabilité des cibles en non visée directe du radar à l'intérieur du canyon urbain réel. Cette configuration est illustrée dans la Fig.B.4. A moins d'utiliser une fréquence très élevée, ce qui est techniquement impossible à l'intérieur de cette

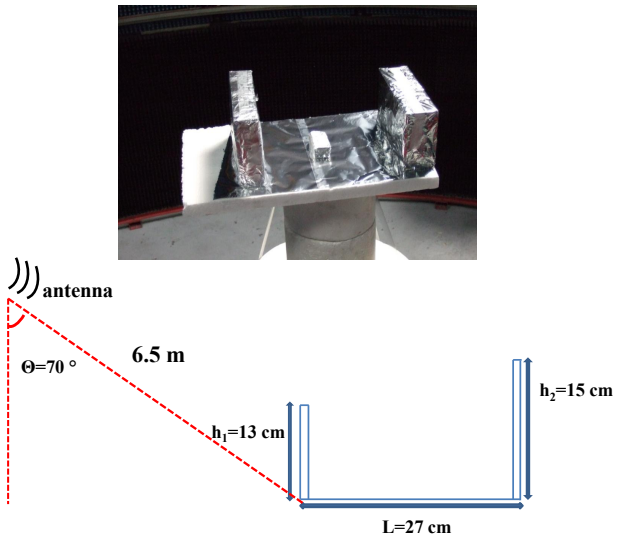

Figure B.4: Configuration de mesures dans la chambre anéchoÃ¯que BABI de l'ONERA. L'angle d'incidence est 70° et la bande de fréquences est [6,18] GHz.

chambre anéchoique, le ratio réel ne peut jamais être respecté dans la chambre anéchoÃ¯que. Par conséquent, de nouveaux effets dus à une variation angulaire en diffusion apparaissent. Ainsi, la phénoménologie EM de propagation à l'intérieur des canyons pour le cas réel, ne peut jamais être étudiée en chambre anéchoique.

Expoloitation des données de la chambre anéchoique

Les données expérimentales ont été analysées en calculant un profil distance qui indique la position des diffuseurs dans une scène suivant un ligne distance. La formule utilisé pour calculer un profil distance est la suivante:

$$\mathcal{F}^{-1}(\underline{E}(f)) \tag{B.1}$$

ou $\underline{E}(f_i)$ est le champ diffusé complexe et F^{-1} est la transformée de Fourrier Inverse.

Analyse des données de la chambre anéchoique

cas du canyon vide

Utilisant la configuration géométrique du canyon de la chambre anéchoique et la phase de chaque pic obtenu sur le profil distance expérimental, nous avons identifié par un calcul de la distance géométrique les mécanismes correspondant aux cinq premiers pics comme illustré sur les Fig.B.7 et Fig.B.8 . L'existence de nombreux pics dans le profil expérimental suppose l'existence de nombreux mécanismes géométriques qui peuvent être dus à une variation angulaire en incidence. Puisque nous avons assuré la condition du champ lointain, cette variation angulaire en incidence n'est plus possible vu que le diagramme d'antenne est assimilé à un faisceau étroit. Cela nous amène à penser à une variation angulaire possible dans la diffusion des rayons arrivant sur les murs du canyon. Pour cette raison, nous avons

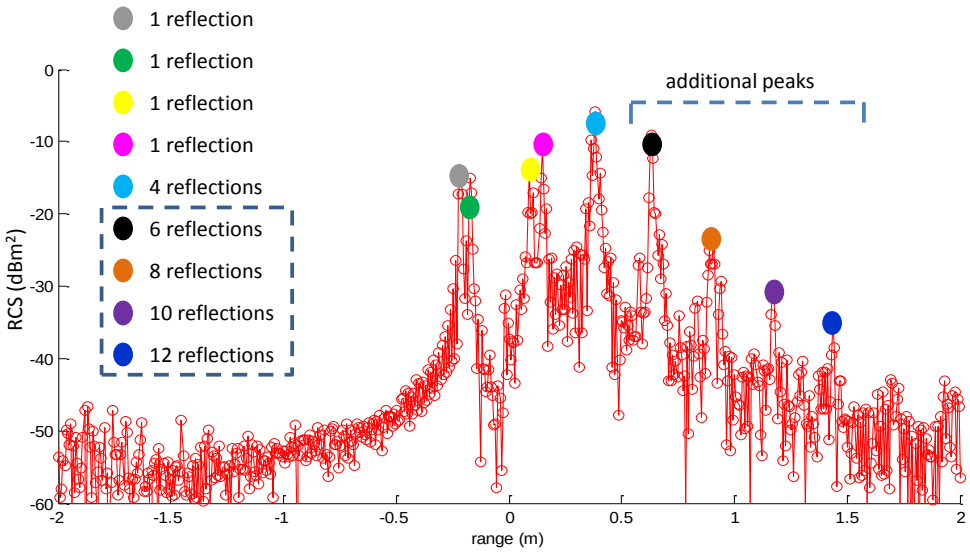

Figure B.5: Profil distance expérimental correspondant à la configuration du canyon vide de la chambre anchoique BABI de l'ONERA

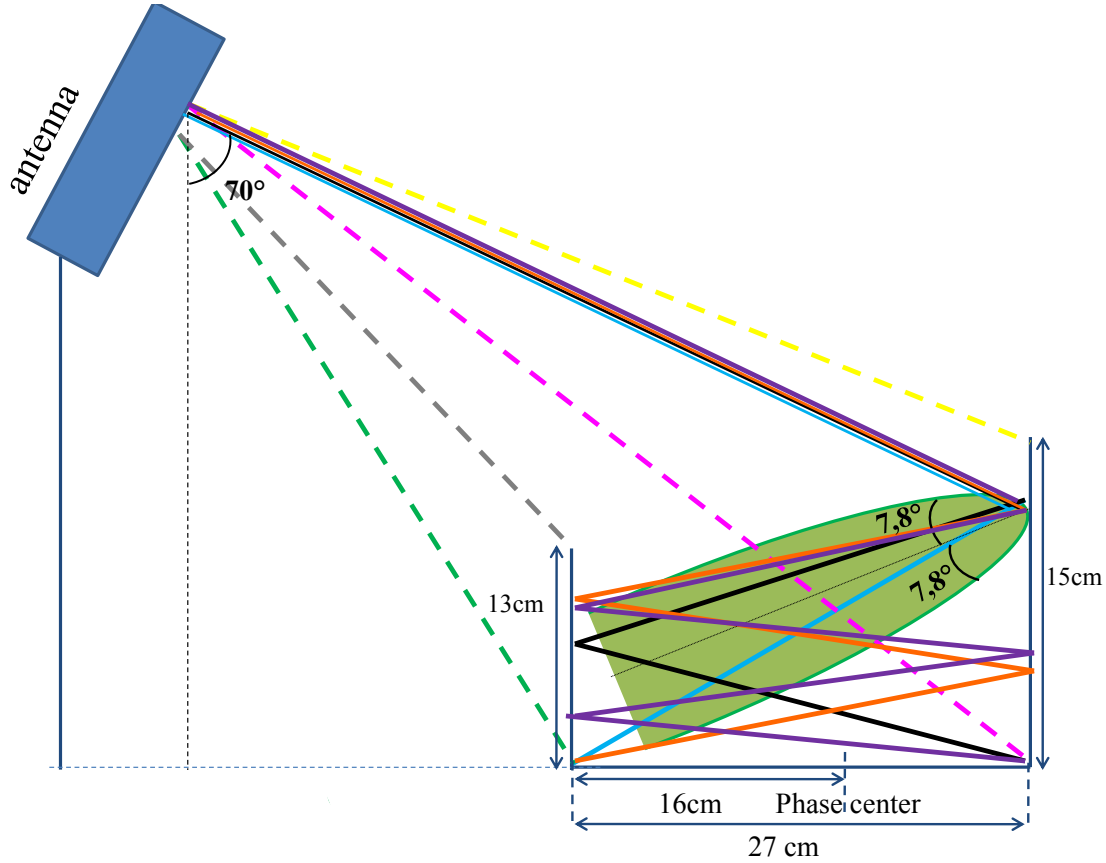

Figure B.6: Mécanismes géométriques correspondant à chaque pic du profil distance.

étudié la réponse EM d'une plaque ayant les mêmes dimensions que le second mur du canyon à la fréquence centrale de la chambre anéchoÃ¯que (12 GHz) et à une fréquence plus élevée (75 GHz) pour un angle d'incidence pareil que l'expérience. Nous pouvons conclu à l'issue de cette étude que cette plaque diffuse dans un lobe de 13° autour de la direction de réflexion spéculaire (110°) pour la fréquence de la chambre anéchoique, par contre pour une fréquence plus élevée, la diffusion se fait dans un lobe étroit. Cette variation angulaire en diffusion à la fréquence basse peut expliquer l'origine des pics supplémentaires dans le profil distance expérimental.

Conclusion

Vu que la ratio d/λ ne pourra jamais être respecté en chambre anéchoique, l'étude des effets EM du cas réel doit se faire à l'aide des codes EM commerciaux qui vont permettre une montée en fréquence, cependant, ces codes doivent être d'abord validés avec les données expérimentales.

Simulation et comparaison en utilisant FEKO

Validation de FEKO à la fréquence de la chambre anéchoique

Fig.B.7 et Fig.B.8 représentent une simulation FEKO en utilisant la méthode EM exacte MoM appliquée à la configuration du canyon vide de la chambre anéchoique BABI illustré dans Fig.B.4 et à la configuration du canyon avec cible, respctivement. Comme nous pouvons le constater, il y a un bon accord entre les profils distances simulés et expérimentales en terme de phase et d'amplitude.

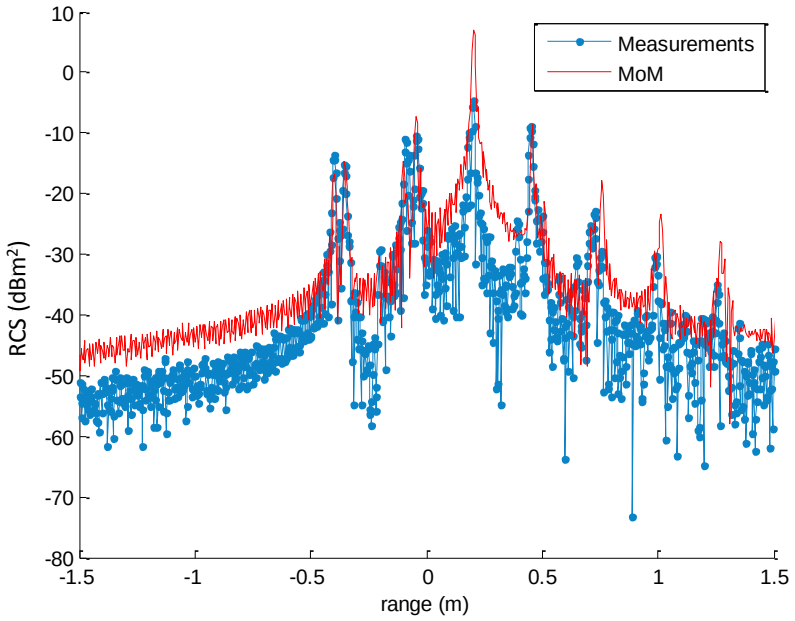

Figure B.7: Profil distance simulé avec Feko/MoM pour un canyon vide

Comme la MoM est une méthode couteuse en temps de calcul, nous avons opté pour des simulations avec des méthodes approchées comme l'Optique Géométrique

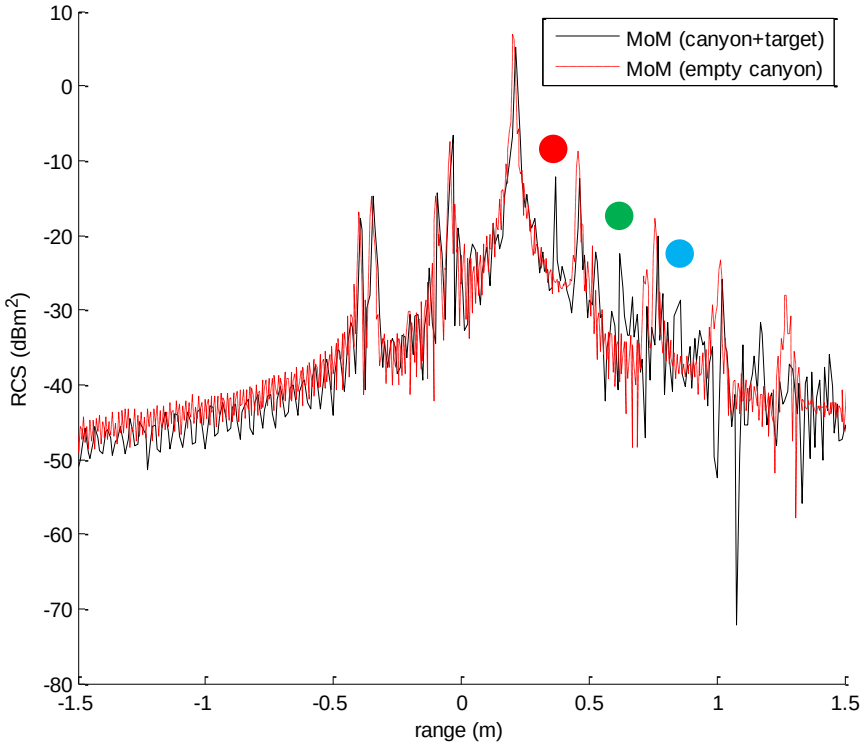

Figure B.8: Profil distance simulé avec Feko/MoM pour un canyon avec cible

(OG), la Théorie Uniforme de Diffraction (UTD) et l'Optique Physique (OP). D'après la Fig.B.9, nous avons conclu que:

- le nombre de pics ne varie pas en augmentant le nombre de réflections
- OG qui considère que la diffusion se fait dans un lobe étroit ne peut pas simuler les effets EM à la chambre anéchoique

D'après la Fig.B.10, nous avons conclu que:

- Il n'y a pas de différence entre le profil distance simulé avec l'OG et le profil distance simulé avec l'UTD et donc on peut conclure qu'il n'y a pas d'effets de diffraction.

D'après la Fig.B.11, nous avons conclu que:

- Il y a bon accord entre le profil distance simulé avec la MoM et celui avec la OP à 12 réflections, de ce fait, l'OP est une méthode efficace du moment que le nombre de reflections est correctement choisi, pour simuler tous les pics
- Le temps de calcul en utilisant l'OP augmente avec le nombre de réflections pour atteindre un temps de calcul pareil que la MoM avec un nombre de reflections égale à 12.

Comme on vient de constater, les méthodes approchées ne présentent pas d'avantages par rapport à la méthode de référence (MoM) ni par rapport à la justesse des résultats ni par rapport au temps de calcul, donc, nous avons utilisé la MoM pour simuler une montée en fréquence pour le canyon vide.

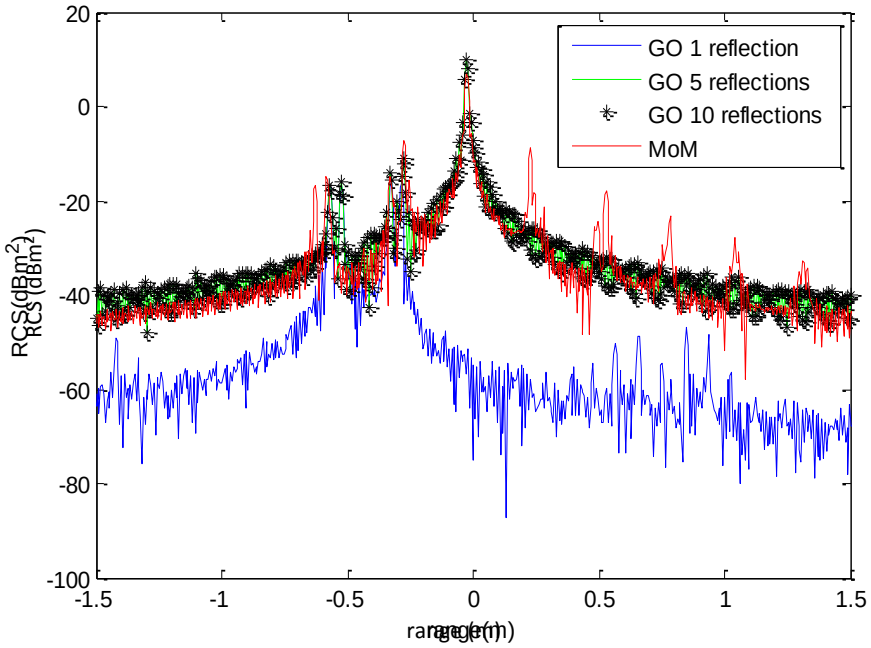

Figure B.9: Profil distance simulé avec Feko/OG.

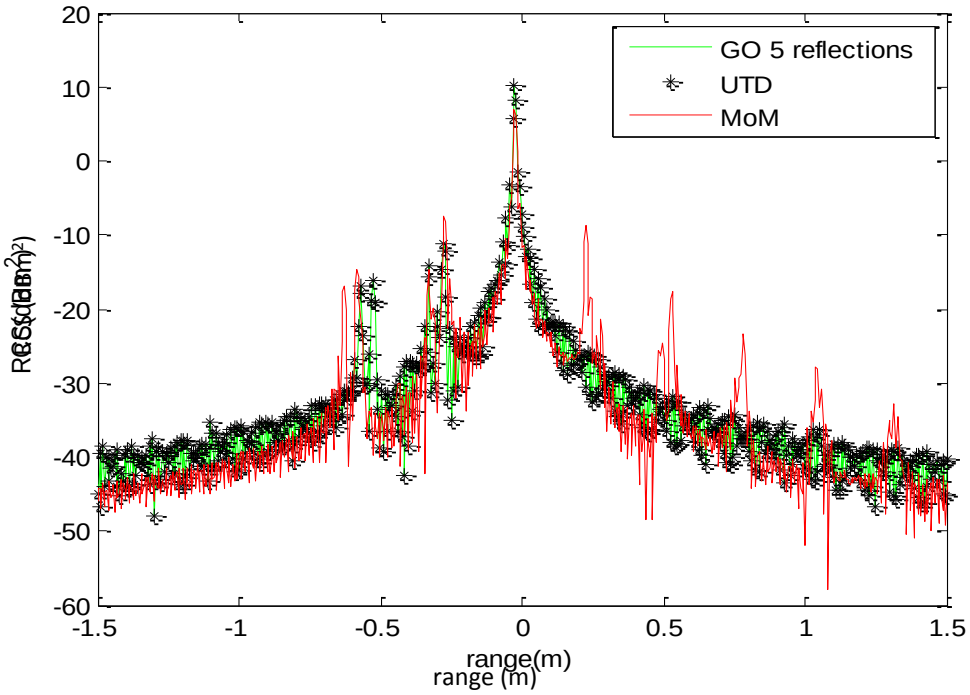

Figure B.10: Profil distance simulé avec Feko/UTD

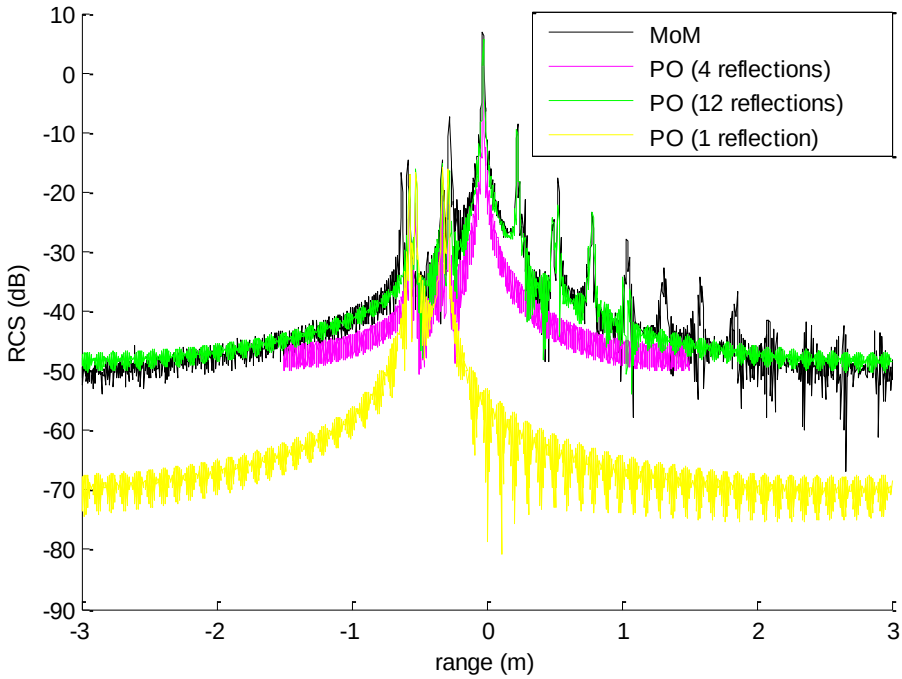

Figure B.11: Profil distance simulé avec Feko/OP

Validation de FEKO à une fréquence élevée

Comme notre objectif principal est d'étudier les effets EM dans des configurations de cas réels, nous devons assurer un ratio d/λ qui tend vers le ratio réel. Par conséquent, une augmentation de la fréquence est requise pour les simulations sur la configuration du canyon vide. Nous présentons dans Fig.B.12, les résultats de la simulation de la MoM et de l'OG à la fréquence de 78 GHz. Comme prévu par les résultats théoriques, le nombre de pics diminue puisque la diffusion se fait dans un lobe étroit. De cette simulation, nous pouvons conclure que l'OG, une méhode basée sur le tracé de rayons, offre un compromis satisfaisant entre la temps de calcul et la précision des résultats. Ainsi, elle peut être utilisé pour étudier la phénoménologie EM de propagation pour des cas réelles de scènes urbaines.

Présentation du codes développé

Le code EM développé est un code basé sur un tracé de rayons qui simule pour une succession de canyons, tous les rayons qui sont en mesure de revenir au récepteur et calcule le profil distance correspondant. les entrées de ce code sont:

- la hauteur des murs de chaque canyon
- la largeur des murs de chaque canyon
- la distance séparant les murs
- l'angle d'incidence

Les sorties du code:

- Les zones de détectabilité en non visée directe du radar
- Un profil distance radar

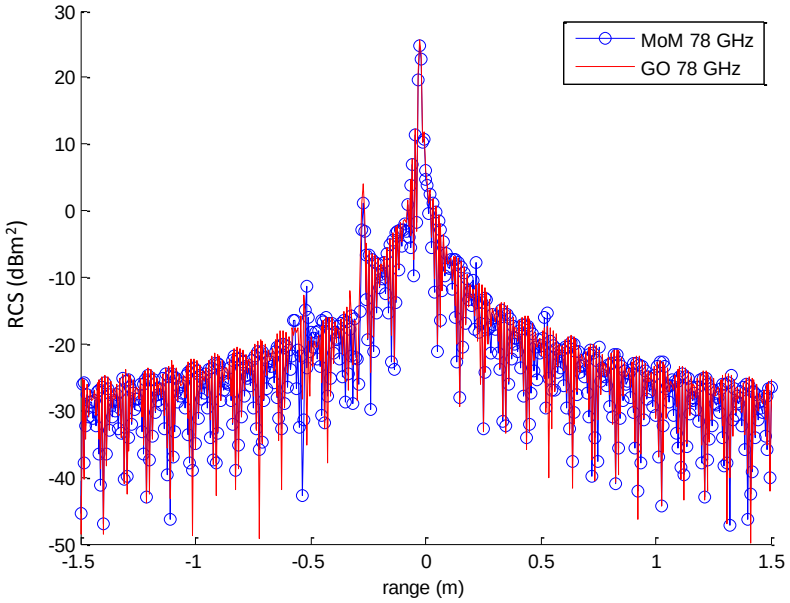

Figure B.12: Profil distance correspondant à une configuration du canyon vide simulé avec MoM et OG à la fréquence de 78 GHz.

Urban Canyon V1: analyse de la réponse d'un canyon vide

Urban Canyon V1 est la première version du code développé pour analyser la réponse d'un canyon vide. Il prend en entrée une configuration du canyon définie par la hauteur des deux murs, la distance les séparant et l'angle d'incidence et permet d'identifier:

- Les zones de détectabilité par mécanisme de réflection spéculaire
- le profil distance correspondant

Au cours de cette étude, nous avons souligné l'intérêt d'étudier les zones de détectabilité en non visée directe qui sont plus imporantes que les zones en visée directe permettant ainsi une meilleure détection de la cible. Ceci est illustré dans la Fig.B.13 où nous avons comparé le pourcentage des zones de détectabilité en non visée directe du radar par mécanisme de réflection spéculaire par rapport à ceux en visée directe (nul) pour un exemple de canyon donné.

Urban Canyon V2: analyse de la réponse d'un canyon avec une cible ponctuelle

Urban Canyon V2 est la deuxième version du code développé pour analyser la réponse d'un canyon avec une cible ponctuelle. Cette cible peut créer un nouveau mécanisme de détection en raison de sa propriété de diffusion. Dans le cas particulier de la détection des véhicules, deux mécanismes principaux doivent être pris en considération: le mécanisme de réflexion spéculaire par le toit et le mécanisme de rétrodiffusion par les deux côtés du véhicule. Pour cette raison, nous avons développé un second code EM nommé Urban Canyon V2 qui intègre ces deux mécanismes de rétrodiffusion supplémentaires. Il prend en entrée n'importe quelle configuration du canyon et permet d'identifier:

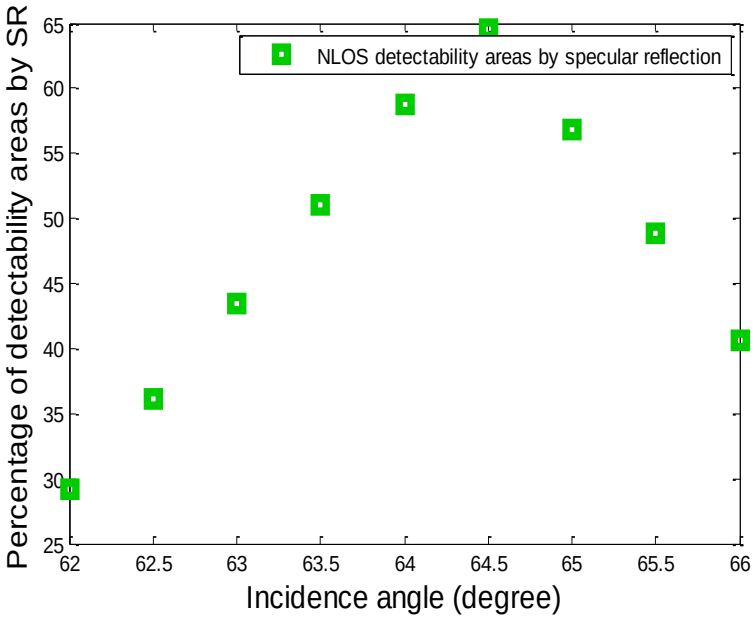

Figure B.13: Pourcentage de zones de détectabilité en non visée directe du radar par mécanisme de réflection spéculaire en variant l'angle d'incidence pour une configuration du canyon donnée.

- Les zones de détectabilité par mécanisme de rétrodiffusion
- le profil distance correspondant

Par une étude similaire que la précédente, nous avons démontré que les zones de détectabilité en non visée directe du radar par mécanisme de rétrodiffusion sont plus importantes que les zones détectabilité en non visée directe du radar par mécanisme de réflection spéculaire, d'où l'intérêt de les étudier. Aussi, vous avons pu démontrer par l'analyse du profil distance d'un canyon avec une cible à l'intérieur que nous pouvons déterminer:

- La position de la cible à l'intérieur du canyon
- l'orientation de la cible
- La nature de la cible: diffusant d'un coté ou des deux cotés.

Urban Canyon V3: analyse de la réponse d'un canyon avec une cible étendue: le parallélipipède

Cet outil est plus approprié pour étudier les configurations du canyon dans le cas réel, puisque le nombre de cibles étendues (voiture, camion ..) dépasse le nombre de cibles ponctuelles. Le code développé correspondant est nommé Urban Canyon V3 et constitue un code global car il comprend l'étude des canyons vides, des canyons avec des cibles ponctuelles et des canyons avec cibles étendues. En utilisant Urban Canyon V3, nous pouvons prédire pour toute configuration du canyon avec la présence d'une cible étendue, si la cible peut être détectée par son côté droit, par son côté gauche ou par le toit ainsi que le profil distance correspondant. Au terme de cette étude, nous avons conclu que le pourcentage de détection augmente encore avec la cible étendue. En effet, un profil distance pour un canyon avec une cible étendue peut contenir jusqu'à 8 pics:

- 2 pics correpondant aux murs du canyon
- 2 pics correspondant aux intéractions des côtés de la cible avec les murs du canyon
- 2 pics relatifs à la cible: côté droit et côté gauche
- 2 pics dÃ»s au toit de la cible

Validation de Urban Canyon v3 avec FEKO

Urban Canyon V3 ne peut pas être validé directement avec FEKO depuis FEKO est un outil 3D et Urban Canyon V3 est un outil 2D. La solution était de proposer une formule utilsant une matrice de diffusion au lieu d'un coefficient de reflection tel que :

$$\sigma_{feko}^{qp} = 20Log_{10}(S^{qp}) + \sigma_{ucv3} \tag{B.2}$$

où σ_{feko}^{qp} est la la composante de la matrice S Ã la polarisation qp, σ_{feko}^{qp} est la SER estimée de la réponse calculée par FEKO et σ_{ucv3} est la SER de la réponse calculée par Urban Canyon V3. Une méthode a été proposée pour calculer la matrice de diffusion, σ_{feko} et σ_{ucv3} ont été calculés sur un exemple de canyon vide et une différence de 3.76 dB a été retrouvée entre la valeur calculée et la valeur estimée. Cette différence est due aux:

- approximations dans l'estimation de la matrice de diffusion
- effets 3D considérés avec FEKO qui n'ont pas été pris en compte avec Urban Canyon v3

Cependant, on peut dire que les résultats de validation sont satisfaisant et peuvent être considéres comme une première étape d'extension de notre code 2D en code 3D.

Application du code développé: analyse de données interférométriques

Dans le cadre spécifique de l'analyse des données InSAR des zones urbaines, nous nous sommes proposés de donner une interprétation complète d'une image SAR radiométrique et interférométrique d'une scène urbaine réelle contenant un canyon avec des cibles simples et complexes. L'objectif principal est d'interpréter des données réelles InSAR d'un canyon avec tous les effets possibles survenant à l'intérieur, en utilisant notre code EM développé (Urban Canyon V3). L'utilisation de ce code sur des données réelles constitue une deuxième validation.

Description de la scène d'étude

Au cours d'une campagne de mesures dédié aux zones urbaines, l'ONERA a acquis des données SAR à la bande Ka et à la polarisation VV, avec une résolution de 30 cm sur une zone industrielle. L'image interférométrique illustrée dans Fig.B.16 contient deux bâtiments avec des cibles situées entre eux comme décrit dans Fig.B.14. Le premier bâtiment (bâtiment 1) est utilisé comme un masque tandis que la deuxième bâtiment (bâtiment 2) est utilisé comme un réflecteur. L'expérience consiste à illuminer les trois cornets réflecteur et le camion situés en face du deuxième bâtiment.

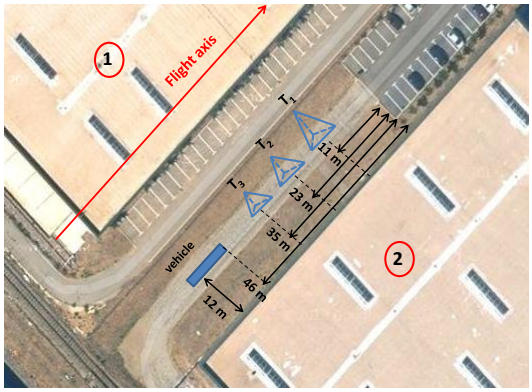

Figure B.14: Scène d'étude: deux bâtiments définissant le canyon d'étude. Trois cornet reflecteurs ($h_{t1} = 0.55$ m, $h_{t2} = 0.47$ m, $h_{t3} = 0.39$ m) et un camion ($h_t = 2.45$ m) sont placés en face du deuxième bâtiment.

Analyse de l'image radiométrique

Cette étude radiométrique a permis de:

- Identifier les différents attributs de l'image à l'aide de notre outil développé Urban Canyon V3
- Identifier les différents mécanismes géométriques correspondant à chaque attribut identifié
- Proposer une formule analytique pour le calcul des coefficients de rétrodiffusion pour les différents attributs et particulièrement pour le cas ou plusieurs mécanismes se superposent à l'intérieur de la même cellule de résolution. La formule est la suivante:

$$\sigma_{tot} = \left\langle \sum_{k=1}^{N} \sigma_k + 2Re \sum_{k=1}^{N} \left(\alpha_k \sum_{j=k+1}^{N} {\alpha_j}^* \right) \right\rangle \tag{B.3}$$

  où σ_k est le coefficient de rétrodiffusion du mécanisme k et α_k est défini comme suit:

$$\alpha_k = \lim_{R \to +\infty} \frac{E_k^s \sqrt{4\pi R^2}}{E_k^i \sqrt{A_k}} \tag{B.4}$$

- Validation de la formule par une étude statistique

Analyse de l'image interférométrique

L'analyse de l'image interférométrique de la Fig.B.16 consiste à prédire la phase et le module interférométrique relatifs à chaque zone délimitée par Urban Canyon V3 particulièrement pour les zones où il y a recouvrement de mécanismes. Cette étude interférométrique vise à:

- choisir des zones interférométiques d'étude: ce sont les zones ayant une signature interférométrique différente: ce sont les cinq zones déimitées par Urban Canyon V3
- Analyse de la cohérence interférométique de chaque zone
- Fournir une interprétation à la transition interférométrique

Analyse de la cohérence interférométrique de chaque zone

Il s'agit de proposer une formule pour le calcul du coefficient de cohérence pour les cinq zones d'étude, plus particulièrement pour les zones ou il y a superposition de N mécanismes. Cette formule est la suivante:

$$\gamma_{tot} \simeq \sum_{i=1}^{N} \gamma_i \frac{< \sigma_{i,1} >}{< \sigma_{tot} >} \tag{B.5}$$

La deuxième étape est de valider cette formule. Il s'agit de:

- Sélectionner une zone rectangulaire de chaque zone d'étude à partir de l'image de cohérence
- Dériver la distribution statistique de l'amplitude et de la phase de la cohérence dans chaque zone sélectionnée,
- Simuler les distributions de l'amplitude et de la phase des coefficients de cohérence en zone 1 et zone 5 (où un seul mécanisme de rétrodiffusion existe) et également dans les zones de repliement (zone 2, 3 et 4), ceci en utilisant la formule de l'Eq.B.5.
- Comparaison des distributions simulées avec les distributions réelles

A l'issu de cette validation, nous avons trouvé une bonne correspondance entre les distributions simulées et les distributions réelles de la phase et de l'amplitude.

Interprétation de la transition de phase interférométrique

Pour donner une interprétation à la transition de la phase interférométrique, nous avons comparé la distribution de la phase simulée de la cohérence dans la zone 2, 3 et 4 avec la distribution de la phase de la cohérence du toit et du sol. Nous avons conclu que:

- Pour la zone 2, l'intervalle de phase de la cohérence est situé entre l'intervalle de la phase du toit et l'intervalle de la phase du sol. On voit sur l'image interférométrique que dans cette zone, il y a un mélange de deux couleurs (le vert correspondant à la phase du sol et le bleu correspondant à la phase du toit). Cependant, l'intersection avec l'intervalle de la phase du sol est plus importante que l'intersection avec à l'intervalle de phase du toit, d'où la prédominance de la couleur verte.
- Pour la zone 3, l'intervalle de phase de la cohérence correspond exactement à celui du toit, donc la phase interférométrique associée est celle du toit.
- Pour la zone 4, nous gardons le même raisonnement que pour la zone 2. Comme l'intersection de l'intervalle de phase de la zone 4 est plus importante avec l'intervalle de phase du sol, ainsi, la couleur prédominante est le vert.

Par conséquent, en comparant la distribution de phase simulée de la zone 2, 3 et 4 avec la phase du sol et du toit, nous avons fourni une explication à la transition de phase interférométrique. Nous avons également mis en évidence l'impact des propriétés diélectriques des matériaux dans la signature interférométrique des zones de repliement. En effet, avec une valeur basse du coefficient de réflexion, un mécanisme disparaît en faveur d'un deuxième mécanisme qui devient dominant, et par conséquent définit la phase interférométrique des cellules de résolution dans les zones de repliement. Cet effet est présent dans la zone 3 où une faible valeur

du coefficient de reflection du beton dénoté R^c_{vv} à la polarisation utilisée (VV) et l'angle d'incidence (60°) (voir Fig.B.15) rend la contribution interférométrique du sol négligeable et par conséquent la phase interférométrique résultante est celle du toit.

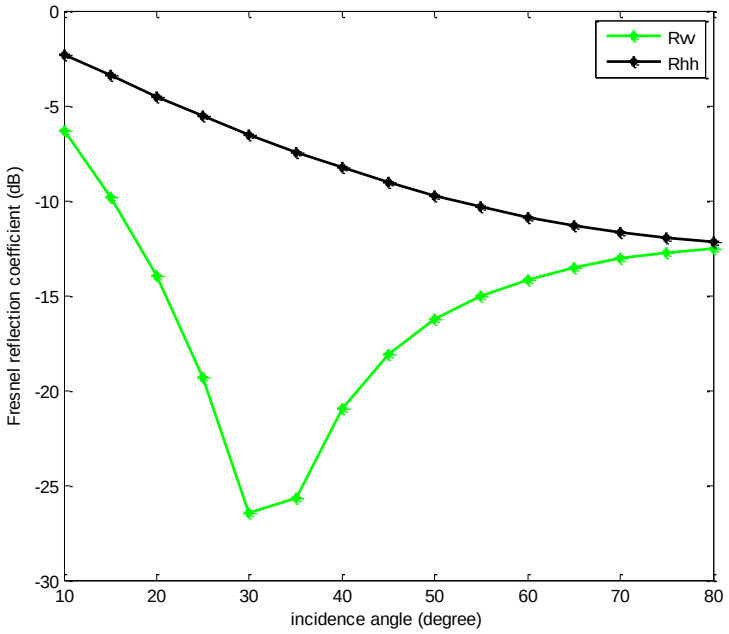

Figure B.15: Coefficient de réflection du béton en variant l'angle d'incidence pour une fréquence centrale de 35 GHz et une permittivité de 2.5+i 0.65.

Conclusion

L'objectif principal de cette thèse était d'étudier la détection des cibles en non visée directe du radar à l'intérieur d'une scène urbaine représentantative: le canyon urbain. Trois parties ont été proposées pour aborder ce nouveau sujet. La première partie est une introduction générale à la problématique qui présente l'état de l'art sur la détection des cibles à l'intérieur des scénarios urbains au moyen d'algorithmes de détection ou de simulateurs EM. La principale conclusion à la fin de cet état de l'art a été qu'il n'existe aucune méthode ou simulateur qui soit validé en ce qui concerne à la fois la phase et l'amplitude. Sur la base de cette constatation, nous avons mis toute notre contribution sur l'élaboration d'un outil EM dédié aux structures urbaines simples: le canyon urbain, qui soit validé.

Pour acquérir des connaissances sur la phénoménologie EM de propagation à l'intérieur des canyons urbains et afin d'évaluer correctement le paramètre d'amplitude, nous avons effectué des mesures en environnement contrôlé à l'ONERA. Cependant, il n'a pas été possible de respecter le ratio d $/\lambda$. L'idée était alors de considérer des fréquences plus élevées avec des outils EM commerciaux qui soient validés avec les mesures de la chambre anéchoique (la seconde partie de la thèse). Les résultats de cette étude nous ont servi pour développer notre outil dédié à la détection rapide des cibles en non visée directe à l'intérieur du

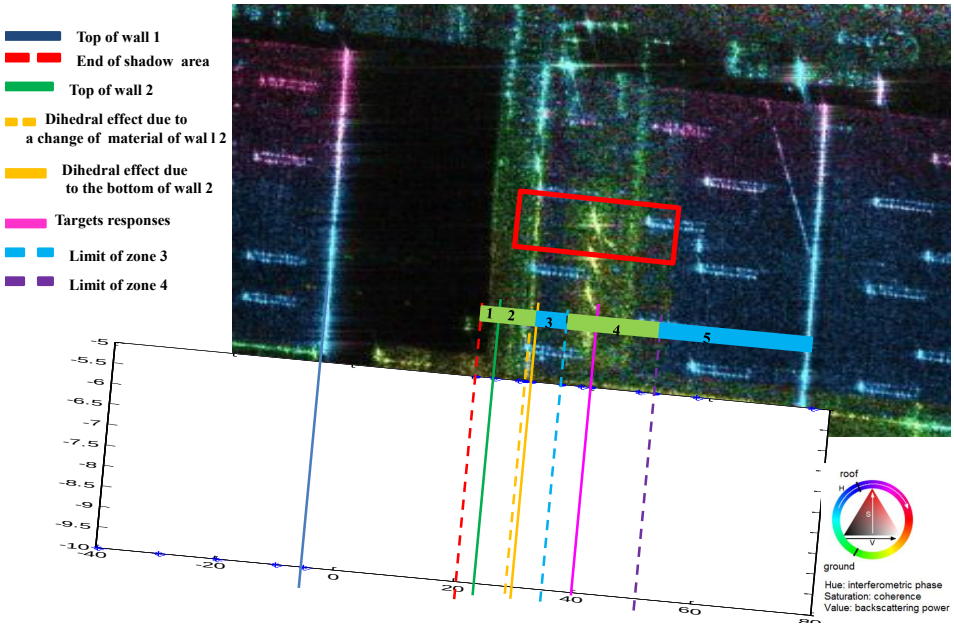

Figure B.16: L'image interférométrique correspondant à la scène d'étude avec le profil distance associé généré avec Urban Canyon V3 et un calcul de la distance géométrique: 5 zones d'étude délimités par les différentes réponses des diffuseurs avec des nombres différents de mécanismes, les pics illustrés avec un trait continu sont générés par Urban Canyon V3 et les pics illustrés par des traits en pointillés sont rajoutés à l'aide d'un calcul de la distance géométrique des différents mécanismes. Le rectangle rouge délimite la zone de transition de la phase interférométrique.

canyon. Le développement, l'analyse et la validation de cet outil ont été les sujets abordés à la troisième partie. Cet outil a permis de générer les profils distance de différentes configurations du canyon: pour un canyon vide et pour un canyon avec une cible ponctuelle ou étendue. Afin d'illustrer l'une des applications possibles de l'outil développé, nous avons finalement proposé une analyse d'une image InSAR d'un canyon urbain contenant différentes cibles, dont les réponses sont en non visée directe du radar.

Comme ce travail s'inscrit dans le cadre d'une étude préliminaire sur la détection de cible en non visée directe du radar en utilisant un outil EM simple, de nombreuses perspectives peuvent être envisagées. Une des perspectives à court terme est d'étendre notre outil 2D à un outil 3D pour mieux s'adapter aux conditions du cas réel où les canyons ne sont pas nécessairement orientés parallèlement à la trajectoire du capteur SAR.

De plus, notre travail a porté sur un canyon métallique afin de commencer avec un cas simple et complet, puisque aucune atténuation de l'amplitude ne peut exister, par conséquent, toutes les réponses prédites existent. Néanmoins, dans des configurations réalistes, les structures urbaines sont constituées par des matériaux diélectriques qui impactent hautement sur le champ EM diffusé ainsi que sur la signature interférométrique comme souligné précédemment. La difficulté est de caractériser cette grande variété de matériaux dans les zones urbaines, ainsi que la variation de leur permittivité avec la fréquence et l'angle d'incidence. Néanmoins, une étude des propriétés diélectriques des matériaux les plus courants dans les zones

urbaines peut être réalisée, aisi les effets de la permittivité et de la rugosité peuvent être étudiés en utilisant des coefficients de réflexion de Fresnel modifiés.

Cela nous conduit à définir une perspective à long terme qui est de proposer un traitement SAR qui corrige les artefacts dans les images SAR d'une scène urbaine. En fait, une fois que l'impact des caractéristiques géométriques et électromagnétiques de la scène maîtrisé à l'aide d'un outil 3D qu'on aura valider, il est possible de comprendre l'origine de certains artefacts et de proposer par la suite une technique adéquate de traitement afin de les corriger.

Bibliography

[Arnold-Bos 2007] A. Arnold-Bos, A. Khenchaf and A. Martin. *Bistatic Radar Imaging of the Marine Environment;Part I: Theoretical Background*. Geoscience and Remote Sensing, IEEE Transactions on, vol. 45, no. 11, pages 3372–3383, 2007. (Cited on page 17.)

[Auer 2009] S. Auer, X. Zhu, S. Hinz and R. Bamler. *3D analysis of scattering effects based on Ray Tracing techniques*. In Geoscience and Remote Sensing Symposium, 2009 IEEE International, IGARSS 2009, volume 3, pages III–17. IEEE, 2009. (Cited on page 26.)

[Auer 2010] S. Auer, S. Hinz and R. Bamler. *Ray-Tracing Simulation Techniques for Understanding High-Resolution SAR Images*. Geoscience and Remote Sensing, IEEE Transactions on, vol. 48, no. 3, pages 1445–1456, 2010. (Cited on pages 19 and 20.)

[Balanis 1989] C.A. Balanis. Advanced engineering electromagnetics, volume 205. Wiley New York, 1989. (Cited on page 68.)

[Balz 2004] T. Balz. *SAR simulation based change detection with high-resolution SAR images in urban environments*. ISPRS Archives, vol. 35, 2004. (Cited on page 18.)

[Balz 2006a] T. Balz. *Real-time SAR simulation of complex scenes using programmable graphics processing units*. In Proc.ISPRS TCVII Mid-Term Symp, 2006. (Cited on page 21.)

[Balz 2006b] T. Balz. *Real-time SAR simulation on graphics processing units*. EUSAR 2006, 2006. (Cited on page 20.)

[Balz 2009] T. Balz and U. Stilla. *Hybrid GPU-Based Single- and Double-Bounce SAR Simulation*. Geoscience and Remote Sensing, IEEE Transactions on, vol. 47, no. 10, pages 3519–3529, 2009. (Cited on pages 16, 19, 20 and 26.)

[Bennett 2003] A.J. Bennett and D. Blacknell. *The extraction of building dimensions from high resolution SAR imagery*. In Radar Conference, 2003. Proceedings of the International, pages 182–187, 2003. (Cited on page 176.)

[Berens 2006] P. Berens. *Introduction to synthetic aperture radar (SAR)*. Rapport technique, DTIC Document, 2006. (Cited on pages 3 and 178.)

[Berry 1988] F. Berry, B. De Roover, R. De Wulf and R. Goossens. *The Use Of SPOT-1 Imagery For Forest Classification In Flanders (Belgium)*. In Geoscience and Remote Sensing Symposium, 1988. IGARSS '88. Remote Sensing: Moving Toward the 21st Century., International, volume 2, pages 913–916, 1988. (Cited on page 2.)

[Bolter 1996] R. Bolter, M. Gelautz and F. Leberl. *SAR speckle simulation.* International archives of photogrammetry and remote sensing, vol. 31, pages 20–25, 1996. (Cited on page 17.)

[Botler 2001] R. Botler. *Detection and reconstruction of buildings from multiple view high resolution interferometric SAR data.* PhD thesis, University Graz, Austria, 2001. (Cited on page 176.)

[Brenner 2013] A.R. Brenner. *Improved radar imaging by centimeter resolution capabilities of the airborne SAR sensor PAMIR.* In Radar Symposium (IRS), 2013 14th International, volume 1, pages 218–223, 2013. (Cited on page 3.)

[Brigui 2010] F. Brigui. *Algorithmes d'imagerie SAR polarimétriques basés sur des mod è les sous-espace: application à la détection de cible sous couvert forestier.* PhD thesis, Université Paris Ouest Nanterre, France, 2010. (Cited on page 211.)

[Brunner 2010] D. Brunner, G. Lemoine, L. Bruzzone and H. Greidanus. *Building Height Retrieval From VHR SAR Imagery Based on an Iterative Simulation and Matching Technique.* Geoscience and Remote Sensing, IEEE Transactions on, vol. 48, no. 3, pages 1487–1504, 2010. (Cited on page 176.)

[Brunner 2011] D. Brunner, G. Lemoine, H. Greidanus and L. Bruzzone. *Radar Imaging Simulation for Urban Structures.* Geoscience and Remote Sensing Letters, IEEE, vol. 8, no. 1, pages 68–72, 2011. (Cited on pages 21 and 26.)

[Cellier 2007] F. Cellier. *Reconstruction 3D de batiments en interférometrie RSO haute resolution : approche par gestion d hypothèses.* PhD thesis, Ecole nationale supérieure des télécommunications, France, 2007. (Cited on pages 176 and 208.)

[Chakraborty 2011] B. Chakraborty, J.J. Zhang, A. Papandreou-Suppappola and D. Morrell. *Urban terrain tracking in high clutter with waveform-agility.* In Acoustics, Speech and Signal Processing (ICASSP), 2011 IEEE International Conference on, pages 3640–3643, 2011. (Cited on page 12.)

[Chu 1989] S.T. Chu and S.K. Chaudhuri. *A finite-difference time-domain method for the design and analysis of guided-wave optical structures.* Lightwave Technology, Journal of, vol. 7, no. 12, pages 2033–2038, 1989. (Cited on page 73.)

[Cloude 1996] S.R. Cloude and E. Pottier. *A review of target decomposition theorems in radar polarimetry.* Geoscience and Remote Sensing, IEEE Transactions on, vol. 34, no. 2, pages 498–518, 1996. (Cited on page 106.)

[Cochin 2008] C. Cochin, P. Pouliguen, B. Delahaye, D. Hellard, P. Gosselin and F. Aubineau. *MOCEM - An 'all in one' tool to simulate SAR image.* In Synthetic Aperture Radar (EUSAR), 2008 7th European Conference on, pages 1–4, 2008. (Cited on pages 62, 63 and 66.)

[Codjoe 2007] S.N.A. Codjoe. *Integrating remote sensing, GIS, census, and socioeconomic data in studying the population–land use/cover nexus in Ghana: A literature update.* Africa Development, vol. 32, no. 2, 2007. (Cited on page 7.)

[cst] *http://www.cst.com/.* (Cited on page 73.)

[Cumming 2004] I.G. Cumming, F.H. Wong and M. Dettwiler. Digital signal processing of synthetic aperture radar data: algorithms and implementation. Artech House Norwood, 2004. (Cited on page 2.)

[Delliere 2007] J. Delliere, H. Maitre and A. Maruani. *SAR measurement simulation on urban structures using a FDTD technique.* In Urban Remote Sensing Joint Event, 2007, pages 1–8, 2007. (Cited on pages 20 and 25.)

[Eltoft 2005] T. Eltoft. *The Rician inverse Gaussian distribution: a new model for non-Rayleigh signal amplitude statistics.* Image Processing, IEEE Transactions on, vol. 14, no. 11, pages 1722–1735, 2005. (Cited on page 18.)

[Eymard 2000] R. Eymard, T. Gallouët and R. Herbin. *Finite volume methods.* Handbook of numerical analysis, vol. 7, pages 713–1018, 2000. (Cited on page 67.)

[fek] *http://www.feko.info/.* (Cited on pages 66, 67, 68 and 69.)

[Franceschetti 1992] G. Franceschetti, M. Migliaccio, D. Riccio and G. Schirinzi. *SARAS: a synthetic aperture radar (SAR) raw signal simulator.* Geoscience and Remote Sensing, IEEE Transactions on, vol. 30, no. 1, pages 110–123, 1992. (Cited on pages 19, 20 and 25.)

[Franceschetti 1995] G. Franceschetti, M. Migliaccio and D.Riccio. *The SAR simulation: an overview.* In Geoscience and Remote Sensing Symposium, 1995. IGARSS '95. 'Quantitative Remote Sensing for Science and Applications', International, volume 3, pages 2283–2285 vol.3, 1995. (Cited on pages 19 and 20.)

[Franceschetti 2002] G. Franceschetti, A. Iodice and D. Riccio. *A canonical problem in electromagnetic backscattering from buildings.* Geoscience and Remote Sensing, IEEE Transactions on, vol. 40, no. 8, pages 1787–1801, 2002. (Cited on pages 11, 20 and 176.)

[Franceschetti 2003] G. Franceschetti, A. Iodice, D. Riccio and G. Ruello. *SAR raw signal simulation for urban structures.* Geoscience and Remote Sensing, IEEE Transactions on, vol. 41, no. 9, pages 1986–1995, 2003. (Cited on pages 20 and 25.)

[Fung 1992] A.K. Fung, Z. Li and K.S. Chen. *Backscattering from a randomly rough dielectric surface.* Geoscience and Remote Sensing, IEEE Transactions on, vol. 30, no. 2, pages 356–369, 1992. (Cited on page 17.)

[Fung 1994] A.K. Fung and K.S. Chen. *Microwave scattering and emission models and their applications.* 1994. (Cited on page 17.)

[Gallman 2005] P.G. Gallman. Radar reflectors for cruising sailboats: Why they work, what the limitations are, and how to evaluate them. Pine Orchard, Incorporated, 2005. (Cited on pages 30 and 31.)

[Gatesman 2001] A.J. Gatesman, T.M. Goyette, J.C. Dickinson, J. Waldman, J. Neilson and W.E. Nixon. *Physical scale modeling the millimeter-wave backscattering behavior of ground clutter*. Rapport technique, DTIC Document, 2001. (Cited on pages 192 and 194.)

[Gedney 2011] S.D. Gedney. *Introduction to the Finite-difference Time-domain (FDTD) Method for Electromagnetics*. Synthesis Lectures on Computational Electromagnetics, vol. 6, no. 1, pages 1–250, 2011. (Cited on page 73.)

[Gibson 2007] W.C. Gibson. The method of moments in electromagnetics. CRC press, 2007. (Cited on page 67.)

[Glassner 1984] A.S. Glassner. *Space subdivision for fast ray tracing*. Computer Graphics and Applications, IEEE, vol. 4, no. 10, pages 15–24, 1984. (Cited on page 15.)

[Guida 2008] R. Guida, A. Iodice, D. Riccio and U. Stilla. *Model-Based Interpretation of High-Resolution SAR Images of Buildings*. Selected Topics in Applied Earth Observations and Remote Sensing, IEEE Journal of, vol. 1, no. 2, pages 107–119, 2008. (Cited on page 18.)

[Guida 2010] R. Guida, A. Iodice and D. Riccio. *Height Retrieval of Isolated Buildings From Single High-Resolution SAR Images*. Geoscience and Remote Sensing, IEEE Transactions on, vol. 48, no. 7, pages 2967–2979, 2010. (Cited on page 176.)

[Guillaso 2005] S. Guillaso, L. Ferro-Famil, A. Reigber and E. Pottier. *Building characterization using L-band polarimetric interferometric SAR data*. Geoscience and Remote Sensing Letters, IEEE, vol. 2, no. 3, pages 347–351, 2005. (Cited on page 176.)

[Gutiérrez-Meana 2011] J. Gutiérrez-Meana, J. Martínez-Lorenzo and F. Las-Heras. *High Frequency Techniques: the Physical Optics Approximation and the Modified Equivalent Current Approximation (MECA)*. 2011. (Cited on page 69.)

[Hammer 2008] H. Hammer, T. Balz, E. Cadario, U. Soergel, U. Thoennessen and U. Stilla. *Comparison of SAR simulation concepts for the analysis of high-resolution SAR data*. In Synthetic Aperture Radar (EUSAR), 2008 7th European Conference on, pages 1–4, 2008. (Cited on pages 18, 21 and 115.)

[Hao 1989] L. Hao, R.C. Chou and L. Shung-Wu. *Shooting and bouncing rays: calculating the RCS of an arbitrarily shaped cavity*. Antennas and Propagation, IEEE Transactions on, vol. 37, no. 2, pages 194–205, 1989. (Cited on page 15.)

[Holtzman 1978] J. Holtzman, V.S. Frost, J.L. Abbott and V.H. Kaupp. *Radar Image Simulation.* Geoscience Electronics, IEEE Transactions on, vol. 16, no. 4, pages 296–303, 1978. (Cited on page 20.)

[Jagdhuber] T. Jagdhuber, I. Hajnsek and K.P. Papathanassiou. *Refined soil moisture estimation by means of L-BAND polarimetry.* A A, vol. 1, no. 2, page V12. (Cited on page 177.)

[Jakeman 1976] E. Jakeman and P.N. Pusey. *A model for non-Rayleigh sea echo.* Antennas and Propagation, IEEE Transactions on, vol. 24, no. 6, pages 806–814, 1976. (Cited on page 18.)

[Jin 2002] J.M. Jin, J. Jin and J.M. Jin. The finite element method in electromagnetics. Wiley New York, 2002. (Cited on page 67.)

[Jin 2009] Yuanwei Jin, J. Moura and N. O'Donoughue. *Experimental study of extended target imaging by time reversal SAR.* In Acoustics, Speech and Signal Processing, 2009. ICASSP 2009. IEEE International Conference on, pages 2109–2112, 2009. (Cited on page 14.)

[Johannessen 1995] J.A. Johannessen. *Overview of ERS-1 scientific results obtained from ocean and sea ice observations.* In Geoscience and Remote Sensing Symposium, 1995. IGARSS '95. 'Quantitative Remote Sensing for Science and Applications', International, volume 2, pages 1035–1037 vol.2, 1995. (Cited on page 2.)

[Johnson 2008] C.P. Johnson, B. Deshmukh and M. Kale. *Role of GIS and remote sensing in the sustainable development of Mauritius.* In Proceedings of the 10th GSDI International Conference for Spatial Data Infrastructure, 2008. (Cited on page 7.)

[Joseph 2005] G. Joseph. Fundamentals of remote sensing. Universities Press, 2005. (Cited on page 1.)

[Jutzi 2006] B. Jutzi and U. Stilla. *Range determination with waveform recording laser systems using a Wiener Filter.* ISPRS Journal of Photogrammetry and Remote Sensing, vol. 61, no. 2, pages 95–107, 2006. (Cited on page 17.)

[Keller 1962] J.B. Keller. *Geometrical theory of diffraction.* 1962. (Cited on pages 67 and 69.)

[Knott 2004] E.F. Knott, J.F. Shaeffer and M.T. Tuley. Radar cross sections. SciTech Publishing, 2004. (Cited on page 28.)

[Kouyoumjian 1974] R.G. Kouyoumjian and P.H. Pathak. *A uniform geometrical theory of diffraction for an edge in a perfectly conducting surface.* Proceedings of the IEEE, vol. 62, no. 11, pages 1448–1461, 1974. (Cited on page 69.)

[Krolik 2006] J.L. Krolik, J. Farrell and A. Steinhardt. *Exploiting multipath propagation for GMTI in urban environments.* In Radar, 2006 IEEE Conference on, pages 4 pp.–, 2006. (Cited on page 12.)

[Kunz 1993] K.S. Kunz and R.J. Luebbers. The finite difference time domain methods for electromagnetics. CRC press, 1993. (Cited on page 67.)

[Kyu-Young 1995] W. Kyu-Young, S. Ju-Won, C. Ji-Woong, K. Ji-Yun, C. Wan-Sup, P. Chong-Mok and S. Il-Yeol. *Octree-R: an adaptive octree for efficient ray tracing.* Visualization and Computer Graphics, IEEE Transactions on, vol. 1, no. 4, pages 343–349, 1995. (Cited on page 15.)

[Le Moigne 2007] V. Le Moigne and F. Tupin. *Statistical Polygonal Snakes for 3D building reconstruction using High Resolution SAR data.* In Urban Remote Sensing Joint Event, 2007, pages 1–5, 2007. (Cited on page 176.)

[Leberl 1990] Franz W Leberl. Radargrammetric image processing. Artech House Norwood, MA, 1990. (Cited on page 19.)

[Liao 2009] M. Liao, L. Zhang and T. Balz. *Post-earthquake landslide detection and early detection of landslide prone areas using SAR.* In Urban Remote Sensing Event, 2009 Joint, pages 1–5. IEEE, 2009. (Cited on page 177.)

[Linnehan 2009] R. Linnehan and J. Schindler. *Multistatic scattering from moving targets in multipath environments.* In Radar Conference, 2009 IEEE, pages 1–6, 2009. (Cited on page 12.)

[Linnehan 2010] R. Linnehan and J. Schindler. *Validating multipath responses of moving targets through urban environments.* In Radar Conference, 2010 IEEE, pages 1036–1041, 2010. (Cited on page 12.)

[Longshaw 1976] G. Longshaw, R.P. Viljoen and M.C. Hodson. *Photographic Display of LANDSAT-1 CCT Images for Improved Geological Definition.* Geoscience Electronics, IEEE Transactions on, vol. 14, no. 1, pages 66–78, 1976. (Cited on page 1.)

[Mametsa 2002] H.J. Mametsa, F. Rouas, A. Berges and J. Latger. *Imaging radar simulation in realistic environment using shooting and bouncing rays technique*, 2002. (Cited on pages 15, 19, 20, 26 and 209.)

[Margarit 2006] G. Margarit, J.J. Mallorqui, J.M. Rius and J. Sanz-Marcos. *On the Usage of GRECOSAR, an Orbital Polarimetric SAR Simulator of Complex Targets, to Vessel Classification Studies.* Geoscience and Remote Sensing, IEEE Transactions on, vol. 44, no. 12, pages 3517–3526, 2006. (Cited on pages 16, 20 and 21.)

[Margarit 2007] G. Margarit, J.J. Mallorqui and C. Lopez-Martinez. *Grecosar, a SAR simulator for complex targets: Application to urban environments.* In Geoscience and Remote Sensing Symposium, 2007. IGARSS 2007. IEEE International, pages 4160–4163, 2007. (Cited on pages 21 and 25.)

[Mattar 2003] K.E. Mattar, M.L. Yeremy and C. Livingstone. *Polarimetric Interferometric SAR: Literature Review and an Assessment of its Utility for DND: TIF Project Memorandum.* Rapport technique, DTIC Document, 2003. (Cited on page 8.)

[Mitra 2001] A.K. Mitra and T.L. Lewis. *Spectral analysis of high-frequency SAR data*, 2001. (Cited on page 8.)

[Monaldo 2003] F. Monaldo. *SEASAT sees the winds with SAR*. In Geoscience and Remote Sensing Symposium, 2003. IGARSS '03. Proceedings. 2003 IEEE International, volume 1, pages 38–40 vol.1, 2003. (Cited on page 2.)

[Montoya 2002] L. Montoya. *GIS and remote sensing in urban disaster management*. In 5th AGILE Conference on Geographic Information Science, Palma (Balearic Islands, Spain) April 25th-27th, 2002. (Cited on page 7.)

[Nadarajah 2008] S. Nadarajah and S. Kotz. *Intensity models for non-Rayleigh speckle distributions*. International Journal of Remote Sensing, vol. 29, no. 2, pages 529–541, 2008. (Cited on page 18.)

[Nguyen 2011] N.T.M. Nguyen, D. Lautru and H. Roussel. *A 3D model to characterize high-frequency scattering by urban areas for monostatic and bistatic radar configurations*. Progress In Electromagnetics Research B, vol. 30, pages 83–102, 2011. (Cited on pages 22 and 25.)

[Nicolas 2006] J.M. Nicolas. *Application de la transformée de Mellin: étude des lois statistiques de l'imagerie cohérente*. Rapport de recherche, 2006D010, 2006. (Cited on page 192.)

[Nouvel 2011] J.F. Nouvel. *NLOS signature analysis*. Rapport technique, ONERA, 2011. (Cited on pages 27 and 39.)

[Nunziata 2008] F. Nunziata, A. Gambardella and M. Migliaccio. *An educational SAR sea surface waves simulator*. International Journal of Remote Sensing, vol. 29, no. 11, pages 3051–3066, 2008. (Cited on page 18.)

[Paterson 1990] M.S. Paterson and F. Yao. *Efficient binary space partitions for hidden-surface removal and solid modeling*. Discrete & Computational Geometry, vol. 5, no. 1, pages 485–503, 1990. (Cited on page 15.)

[Pedrotti 2008] L.S. Pedrotti. *Basic physical optics*. Fundamentals of Photonics, Chandra Roychoudhuri, Ed. Bellingham: SPIE Press Book, page 137, 2008. (Cited on page 68.)

[Pedrotti 2012] L.S. Pedrotti. *Basic geometrical optics*. SPIE, 2012. (Cited on page 68.)

[Phong 1975] B.T. Phong. *Illumination for computer generated pictures*. Communications of the ACM, vol. 18, no. 6, pages 311–317, 1975. (Cited on page 17.)

[Rius 1990] J.M. Rius and M. Ferrando. *Real-time radar cross section of complex targets by physical optics graphical processing*. In Antennas and Propagation Society International Symposium, 1990. AP-S. Merging Technologies for the 90's. Digest., pages 1280–1283. IEEE, 1990. (Cited on page 21.)

[Rius 1993a] J.M. Rius, M. Ferrando and L. Jofre. *GRECO: graphical electromagnetic computing for RCS prediction in real time.* Antennas and Propagation Magazine, IEEE, vol. 35, no. 2, pages 7–17, 1993. (Cited on page 21.)

[Rius 1993b] J.M. Rius, M. Ferrando and L. Jofre. *High-frequency RCS of complex radar targets in real-time.* Antennas and Propagation, IEEE Transactions on, vol. 41, no. 9, pages 1308–1319, 1993. (Cited on pages 16, 19, 21 and 25.)

[Rübenkönig 2006] O. Rübenkönig. *The finite difference method (FDM)-an introduction.* Albert Ludwigs University of Freiburg, page 139, 2006. (Cited on page 67.)

[SAR 2011] N. SAR. Faisabilité de la détection d'une cible cachée dans un canyon urbain: analyse des profils distances radar. Master's thesis, IPSA, 2011. (Cited on pages 27 and 35.)

[Schön 2009] B. Schön, D.F. Laefer, M. Bertolotto and S. Morrish. *Three-dimensional spatial information systems: state of the art review.* 2009. (Cited on page 20.)

[Soergel 2001] U. Soergel, K. Schulz and U. Thoennessen. *Phenomenology-based segmentation of InSAR data for building detection.* In Pattern Recognition, pages 345–352. Springer, 2001. (Cited on page 176.)

[Soergel 2003] U. Soergel, U. Thoennessen and U. Stilla. *Reconstruction of buildings from interferometric SAR data of built-up areas.* International archives of photogrammetry remote sensing and spatial information sciences, vol. 34, no. 3/W8, pages 59–64, 2003. (Cited on pages 176 and 180.)

[Soergel 2010] U. Soergel. Radar remote sensing of urban areas, volume 15. Springer, 2010. (Cited on pages 19 and 20.)

[Sportouche 2009] H. Sportouche, F. Tupin and L. Denise. *Building detection by fusion of optical and SAR features in metric resolution data.* In Geoscience and Remote Sensing Symposium,2009 IEEE International,IGARSS 2009, volume 4, pages IV–769–IV–772, 2009. (Cited on page 176.)

[Stilla 2003] U. Stilla, U. Soergel and U. Thoennessen. *Potential and limits of InSAR data for building reconstruction in built-up areas.* ISPRS Journal of Photogrammetry and Remote Sensing, vol. 58, no. 1, pages 113–123, 2003. (Cited on page 176.)

[Tahmoush 2012] D. Tahmoush, J. Silvious and B. Bender. *Radar surveillance in urban environments.* In Radar Conference (RADAR), 2012 IEEE, pages 0220–0225, 2012. (Cited on page 12.)

[Takeuchi 2000] S. Takeuchi, Y. Suga, C. Yonezawa and A.J. Chen. *Detection of urban disaster using InSAR. A case study for the 1999 Great Taiwan Earthquake.* In Geoscience and Remote Sensing Symposium, 2000. Proceedings. IGARSS 2000. IEEE 2000 International, volume 1, pages 339–341. IEEE, 2000. (Cited on page 177.)

[Tison 2007] C. Tison, F. Tupin and H. Maitre. *A Fusion Scheme for Joint Retrieval of Urban Height Map and Classification From High-Resolution Interferometric SAR Images.* Geoscience and Remote Sensing, IEEE Transactions on, vol. 45, no. 2, pages 496–505, 2007. (Cited on page 176.)

[Trewartha 1961] G.T. Trewartha, A.H. Robinson and E.H. Hammond. Fundamentals of physical geography. McGraw-Hill, 1961. (Cited on page 1.)

[Tsingos 2001] N. Tsingos, T. Funkhouser, A. Ngan and I. Carlbom. *Modeling acoustics in virtual environments using the uniform theory of diffraction.* In Proceedings of the 28th annual conference on Computer graphics and interactive techniques, pages 545–552. ACM, 2001. (Cited on page 70.)

[Tupin 2003] F. Tupin. *Extraction of 3D information using overlay detection on SAR images.* In Remote Sensing and Data Fusion over Urban Areas, 2003. 2nd GRSS/ISPRS Joint Workshop on, pages 72–76, 2003. (Cited on page 176.)

[Ufimtsev 1971] P.Y. Ufimtsev. *Method of edge waves in the physical theory of diffraction.* Rapport technique, DTIC Document, 1971. (Cited on page 69.)

[Ulaby 1989] F.T. Ulaby and M.C. Dobson. Handbook of radar scattering statistics for terrain, volume 357. Artech House Norwood, MA, 1989. (Cited on page 28.)

[Ulaby 1990] F. Ulaby and C. Elachi. *Radar polarimetry for geoscience applications.* Norwood, MA, Artech House, Inc., 1990, 376 p. No individual items are abstracted in this volume., vol. 1, 1990. (Cited on pages 103 and 169.)

[Van Westen 2000] C.J. Van Westen. *Remote sensing for natural disaster management.* International Archives of Photogrammetry and Remote Sensing, vol. 33, no. B7/4; PART 7, pages 1609–1617, 2000. (Cited on page 7.)

[Voigt 2005] S. Voigt, T. Riedlinger, P. Reinartz, C. Künzer, R. Kiefl, T. Kemper and H. Mehl. *Experience and perspective of providing satellite based crisis information, emergency mapping & disaster monitoring information to decision makers and relief workers.* In Geo-information for Disaster Management, pages 519–531. Springer, 2005. (Cited on page 177.)

[Wald 2006] I. Wald and V. Havran. *On building fast kd-Trees for Ray Tracing, and on doing that in O(N log N).* In Interactive Ray Tracing 2006, IEEE Symposium on, pages 61–69, 2006. (Cited on page 15.)

[Yonezawa 2002] C. Yonezawa, N. Tomiyama and S. Takeuchi. *Urban damage detection using decorrelation of SAR interferometric data.* In Geoscience and Remote Sensing Symposium, 2002. IGARSS '02. 2002 IEEE International, volume 4, pages 2051–2053 vol.4, 2002. (Cited on page 18.)

[Yuanwei 2007a] J. Yuanwei and J.M.F. Moura. *TR-SAR: Time Reversal Target Focusing in Spotlight SAR.* In Acoustics, Speech and Signal Processing, 2007. ICASSP 2007. IEEE International Conference on, volume 2, pages II–957–II–960, 2007. (Cited on page 14.)

[Yuanwei 2007b] J. Yuanwei, J.M.F. Moura, N. O'Donoughue, M.T. Mulford and A.A. Samuel. *Time Reversal Synthetic Aperture Radar Imaging In Multipath*. In Signals, Systems and Computers, 2007. ACSSC 2007. Conference Record of the Forty-First Asilomar Conference on, pages 1812–1816, 2007. (Cited on page 14.)

[Zhang 2008] L. Zhang, J. Zhang, B. Zou and Y. Zhang. *Comparison of methods for target detection and applications using polarimetric SAR image*. Piers online, vol. 4, no. 1, pages 140–145, 2008. (Cited on page 103.)

Publications

Articles de revue :

- **A. Mokadem**, L. Thirion-Lefevre and E. Colin-Koeniguer, "Simple Modeling of Urban Canyon for Detection of Non Line of Sight Targets on SAR images of Urban Areas", submitted in IEEE Transactions on Geoscience end Remote Sensing.
- **A. Mokadem**, L. Thirion-Lefevre and E. Colin-Koeniguer, "SAR backscattering coefficient and interferometric coherence in complex areas mixing several scattering mechanisms", submitted in Progress In Electromagnetics Research.

Articles de conférences :

- **A. Mokadem**, M.Charbit and G.Chollet, "Age Regression Based on Local Image Features", PSIVT 2010.
- L. Thirion-Lefevre, E. Colin-Koeniguer, N. Sar and **A. Mokadem**, "Preliminary studies on the detection of a NLOS target in a 2D urban canyon using polinsar data", POLINSAR 2011.
- **A. Mokadem**, L. Thirion-Lefevre and E. Colin-Koeniguer, "Determination of the mechanisms that can occur in NLOS urban canyon-1-", EUSAR, 2012.
- **A. Mokadem**, L. Thirion-Lefevre and E. Colin-Koeniguer, "Determination of the mechanisms that can occur in NLOS urban canyon-2-", IGARSS, 2012.
- **A. Mokadem**, L. Thirion-Lefevre and E. Colin-Koeniguer, "Analysis of a NLOS canyon in an Insar image of an urban area at Ka band-1-", POLINSAR, 2013.
- **A. Mokadem**, L. Thirion-Lefevre and E. Colin-Koeniguer, "Analysis of a NLOS canyon in an Insar image of an urban area at Ka band-2-", IGARSS, 2013.
- **A. Mokadem**, L. Thirion-Lefevre, E. Colin-Koeniguer, R. Guinvarc'h and J. Nouvel, "Analysing urban areas in the frame of non line of sight target detection. Electromagnetic modelling, validation and application to real data in Ka-band", ICEAA, 2014.
- **A. Mokadem**, L. Thirion-Lefevre, E. Colin-Koeniguer and R. Guinvarc'h, "The polarimetric information in urban areas. The specific case of urban canyons", ASAR, 2014.